An integrative investigation of liquid metal embrittlement in the Fe-Zn system: From responsible mechanisms to mitigation strategies

by

Ali Ghatei Kalashami

A thesis
presented to the University of Waterloo
in fulfillment of the
thesis requirement for the degree of
Doctor of Philosophy
in
Mechanical and Mechatronics Engineering
Waterloo, Ontario, Canada, 2023

@ Ali Ghatei Kalashami 2023

Examining Committee Membership

The following served on the Examining Committee for this thesis. The decision of the Examining Committee is by majority vote.

External Examiner:	Professor Leijun Li Department of Chemical & Materials Engineering, University of Alberta, Canada
Supervisor:	Professor Norman Y. Zhou Department of Mechanical and Mechatronics Engineering, University of Waterloo, Canada
Internal Member:	Professor Adrian P. Gerlich Department of Mechanical and Mechatronics Engineering, University of Waterloo, Canada
Internal Member:	Professor Hamid Jahed Department of Mechanical and Mechatronics Engineering, University of Waterloo, Canada
Other Member(s):	Professor Walter W. Duley Department of Physics and Astronomy, University of Waterloo, Canada

Author's Declaration

This thesis consists of material all of which I authored or co-authored: see Statement of Contributions included in the thesis. This is a true copy of the thesis, including any required final revisions, as accepted by my examiners. I understand that my thesis may be made electronically available to the public.

Statement of Contribution

There are seven chapters in this thesis, including an introduction (Chapter 1) and a literature review (Chapter 2), followed by four chapters of data, all of which include published or submitted manuscripts by the candidate. The manuscripts have been revised to conform to the style of the thesis. In all manuscripts, the candidate is the primary author. The candidate performed all the calculations and most of the experiments (except as noted) including sample preparation, high-temperature tensile testing, welding of samples, mechanical testing, characterizations, and preparing the manuscript and all associated sections. Following is a list of co-authors who have contributed to the current work:

Professor Norman Zhou supervised the progress of the research program, advised on the direction of the research, and reviewed and edited the manuscripts.

Dr. Frank Goodwin from the International Zinc Association (IZA), Durham, USA contributed as an industrial supervisor, provided research materials, financial support, and feedback, and contributed to manuscript revisions.

Chapter 1 and **Chapter 2**: Ali Ghatei-Kalashami, Norman Y. Zhou, Progress in understanding zinc-assisted liquid metal embrittlement in advanced high strength steels: responsible mechanisms, crack susceptibility and mitigation strategies, draft review paper.

The candidate was the primary author of the review paper and prepared all sections of the manuscript. The role of Prof. Zhou was described above.

Chapter 3: Ali Ghatei-Kalashami, M. Shehryar Khan, Frank Goodwin, and Y. Norman Zhou, Investigating the mechanism of zinc-induced liquid metal embrittlement crack initiation in austenitic steel, submitted manuscript.

The candidate was the primary author of this manuscript, performing all calculations and experiments, analyzing the data, and preparing the manuscript and all associated sections. M. Shehryar Khan provided revisions and edits to the manuscript and contributed to the discussion. The roles of Prof. Zhou and Dr. Frank Goodwin were described above.

Chapter 4: Ali Ghatei-Kalashami, M. Shehryar Khan, Frank Goodwin, and Y. Norman Zhou, Investigating zinc-assisted liquid metal embrittlement in ferritic and austenitic steels: Correlation between crack susceptibility and failure mechanism, Published in Materials Characterization, Vol. 195, 2023.

The candidate was the primary author of this manuscript, performing experimental work, analyzing the data, and preparing the manuscript and all associated sections. M. Shehryar Khan provided revisions and edits to the manuscript, contributed to the discussion, and assisted in the confocal laser scanning microscope (CLSM) experiment. The roles of Professor Zhou and Dr. Frank Goodwin were described above.

Chapter 5: Ali Ghatei-Kalashami, M. Shehryar Khan, Mok-Young Lee, and Y. Norman Zhou, High-temperature phase evolution of the ZnAlMg coating and its effect on mitigating liquid-metal-embrittlement cracking, Published in Acta Materialia, Vol. 229, 2022.

The candidate was the primary author of the manuscript, performing all experimental work, analyzing the data, and preparing the manuscript and all associated sections. M. Shehryar Khan provided revisions and edits to the manuscript, contributed to the discussion, and assisted in the CLSM experiment. Dr. Mok-Young Lee from Welding & Joining Research Group, POSCO, Korea provided materials and supported the transmission electron microscopy. The roles of Prof. Zhou and Dr. Frank Goodwin were described above.

Chapter 6: Ali Ghatei-Kalashami, Ehsan Ghassemali, Chris DiGiovanni, Frank Goodwin and Norman Y. Zhou, The influence of initial microstructure on liquid metal embrittlement cracking behavior in iron-zinc (Fe/Zn) couple, Published in Materials Letters, Vol. 324, 2022.

The candidate was the primary author of the manuscript, performing all experimental work, analyzing the data, and preparing the manuscript and all associated sections. Prof. Ehsan Ghassemali from Jönköping University, Sweden supported the electron backscatter diffraction (EBSD) and contributed to the edition/revision of the manuscript. Dr. Christopher DiGiovanni contributed to the edition/revision of the manuscript. The roles of Prof. Zhou and Dr. Frank Goodwin were described above.

Abstract

Liquid metal embrittlement (LME) is a problematic phenomenon that results in the abrupt failure of a ductile metal that is exposed to a reactive liquid metal while simultaneously experiencing a tensile load. Despite extensive research efforts to understand this phenomenon, the underlying mechanisms driving LME remain unclear due to conflicting hypotheses and limited empirical evidence. The lack of fundamental knowledge consequently hinders efforts to investigate the influence of metallurgical factors on the severity of LME, resulting in challenges in devising effective solutions to mitigate or eliminate this catastrophic event. In this thesis, both fundamental and engineering aspects of LME are examined comprehensively in the iron-zinc (Fe-Zn) system by unraveling the underlying mechanisms of LME, exploring metallurgical factors contributing to its susceptibility, and investigating an effective strategy for mitigating LME.

The results showed that LME crack initiation entails several atomic-scale steps where the interdiffusion of Zn atoms into the grain boundaries led to the formation of a stress-induced diffusion wedge that significantly affects the kinetics of interdiffusion, as well as the mechanical integrity of the grain boundary being attacked. The results of a detailed characterization of the LME crack path revealed that stress-induced grain boundary diffusion was the most probable underlying mechanism for LME crack propagation. It was shown that LME crack propagation was strongly affected by the initial microstructural characteristics, in which the ferritic microstructure was more prone to LME crack initiation, while the austenitic microstructure had a significantly higher LME crack propagation rate. This led to the occurrence of a hybrid ductile/brittle failure in the ferritic microstructure but a completely intergranular brittle failure in the austenitic sample. The results showed that the ZnAlMg coating has exceptional resistance to LME cracking at high temperatures. Due to an increase in the testing temperature, the lamellar eutectic microstructure of the coating dissolved into the Zn-matrix, with the constituent elements, Al and Mg, segregating towards the steel substrate and the coating surface, respectively. This led to the in-situ formation of a uniform α-Fe(Zn, Al) layer at the steel/coating interface which prevented the direct contact of liquid metal with the steel substrate, resulting in complete suppression of LME at high temperatures.

The study presented an integrated perspective on LME crack formation in the Fe-Zn system and used numerical modeling and empirical results to offer fundamental insights that have so far been lacking in the literature. This study proposed a unified mechanism for the occurrence of LME crack, which is able to reconcile conflicting micro- and macro-scale experimental results reported in the literature. The study also facilitated the resolution of the long-standing debate regarding the LME mechanisms proposed in the literature while offering practically relevant knowledge that leads to the design of LME-resistant Fe-Zn couples.

Keywords: Liquid metal embrittlement (LME); Advanced high-strength steels; Zinc-coating, LME mechanisms; Grain boundary; Cracking mitigation strategies; ZnAlMg coating

Acknowledgments

First of all, I would like to express my sincere gratitude to my supervisor, ***Professor Norman Zhou***, for his valuable advice, encouragement, and patience throughout my Ph.D. program. I was extremely inspired by his extensive knowledge and expertise in a wide range of areas, including Material Science, Mechanical Engineering, Modeling, Welding, Joining, etc. during my Ph.D. program. In addition, I am extremely grateful to ***Dr. Frank Goodwin*** from the International Zinc Association (IZA), who sponsored and provided resources for this study. Furthermore, I would like to express my gratitude to the ***National Science and Engineering Research Council (NSERC) of Canada*** for its support of this research. It is my sincere gratitude to the ***American Welding Society (AWS)*** for selecting me for the prestigious AWS Graduate Fellowship and for supporting this research project.

I would like to express my sincere gratitude to ***Prof. Ehsan Ghassemali*** from Jönköping University in Sweden for all the assistance he provided in the conduct of the EBSD analysis. It would be my pleasure to thank the technical staff at the MME department, especially ***Mr. Mark A Whitney*** and ***Dr. Yuquan Ding***, for their assistance during the experimental works. I am deeply indebted to ***Dr. Mok-Young Lee*** from POSCO, Korea for his assistance with TEM analysis. I would also like to express my sincere thanks to the technical team at the ***Canadian Centre for Electron Microscopy (CCEM)***. Moreover, I wish to express my deepest gratitude to my dear friend ***Dr. Shehryar Khan*** for his support. I am grateful for the support and encouragement I have received from the ***Centre for Advanced Materials Joining (CAMJ)*** colleagues and friends: Dr. Chris DiGiovanni, Dr. Abdelbaset R.H. Midawi, Dr. Amirali Shamsolhodaei, Dr. Hadi Razmpoosh, Shiping Zhang, Xu Han, Mohammad Shojaee, and Mohammadreza Rouhi. During the past four years, I have had the pleasure of working with them.

I wish to take this opportunity to express my sincere gratitude to my family, especially my parents, ***Sima*** and ***Hadi***, as well as my dear sisters, ***Sanaz*** and ***Zahra***, my brother-in-law ***Mohsen*** and my lovely niece, ***Shayna***, who have shown me unconditional love, support, and faith throughout my life. I would like also to express my gratitude to my parents-in-law, ***Dr. Effat*** and ***Reza***, who have shown me endless love and support.

Above all, words cannot express my gratitude to my beautiful wife, ***Shadab***, who has been a constant source of support and love throughout these years. Thanks, ***Shadab***, for giving me the courage to try and for encouraging me to pursue my dreams. I owe you everything!

Dedicated to my beloved family; wife, mom, dad, and sisters.

For their unending love, support, and encouragement …

Table of Contents

List of Tables

List of Figures

Chapter 1 Introduction

1.1 Background

The catastrophic failure of metallic components by way of environmentally assisted cracking (EAC), i.e., stress corrosion cracking (SCC) [1], liquid metal embrittlement (LME) [2,3], and hydrogen embrittlement (HE) [4–6] is one of the leading causes for the deterioration and failure of global assets in a wide variety of industries. Among the different types of EAC, LME has been observed in several important metallic systems that are affected by a variety of processing treatments (e.g., hot-dip galvanizing, and hot-stamping), manufacturing setups (e.g., soldering, brazing, and welding), and their applications in the nuclear industry [7]. LME is a phenomenon caused by the penetration of a reactive liquid metal into the exposed grain boundaries of a solid metal leading to an abrupt failure in the bulk structure [8,9]. This phenomenon happens by the concurrent action of three factors: (i) the presence of an aggressive liquid metal (hereafter called the embrittler), (ii) a susceptible polycrystalline metal (e.g., Al, Ni, Cu, Fe), and (iii) tensile stress acting on the metal [7]. LME has been reported in different solid-liquid systems such as aluminum-gallium (Al-Ga [10]), nickel-bismuth (Ni-Bi [2]), copper-bismuth (Cu-Bi [11]), and iron-zinc (Fe-Zn) [12]. The Al-Ga system has been studied in-depth due to its high LME susceptibility and structural simplicity for atomistic modeling [7]. The Ni-Bi and Cu-Bi couples were investigated comprehensively through ab-initio modeling and high-resolution transmission electron microscopy (HRTEM) [2,13]. LME in the Fe-Zn couple has recently become highly relevant due to the significant challenges it poses to the lightweight and carbon emission goals of the global automotive industry [14–20]. LME of the Fe-Zn system has been less recognized than other systems, which has hindered the development of new generations of AHSS used in automotive structural components.

In recent years, several studies have been conducted to understand the LME phenomenon in the Fe-Zn system [7,21,22]. However, the underlying physical mechanisms of LME remain the subject of intense scientific debate. Furthermore, there is limited knowledge regarding the effect of metallurgical factors, such as the initial microstructure and alloying elements, on the severity of LME. The lack of systematic studies has hampered the development of effective strategies for mitigating this catastrophic phenomenon. In light of this, a detailed investigation of the LME in the Fe-Zn system from unraveling atomic-scale mechanisms to developing effective mitigation strategies is a step in the right direction because the literature on this subject is deficient.

1.2 Objectives

The aim of this study is to explore three major unexplored aspects of LME in the Fe-Zn system as shown in Figure 1.1. The main objectives of this thesis are as follows:

1. Investigating the atomic-scale mechanism of LME crack initiation using numerical modeling and empirical analysis
2. A systematic investigation of the LME crack propagation path to illuminate the underlying crack propagation mechanism
3. Studying the influence of metallurgical factors such as initial microstructure, grain boundary characteristics, and grain boundary chemistry on the severity of LME crack
4. Studying the LME crack susceptibility of ZnAlMg coated steel and establishing a correlation between high-temperature phase evolution and the LME cracking severity
5. Proposing an effective LME mitigation strategy using a ternary ZnAlMg coating system

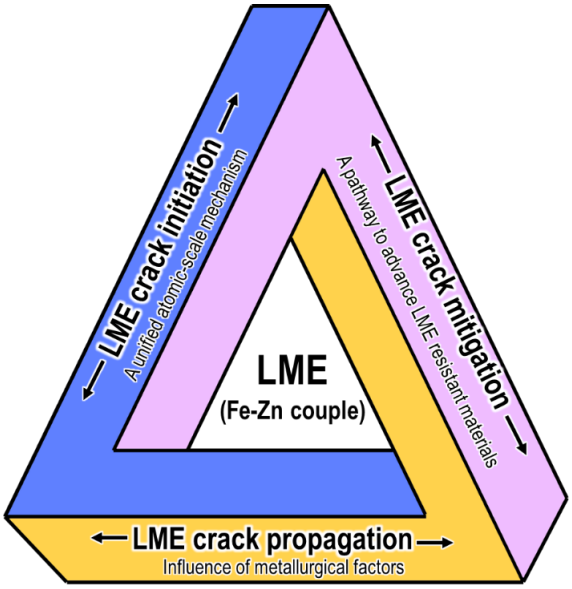

Figure 1.1 Illustration of the main objectives of the present study on the LME in the Fe-Zn system

1.3 Thesis outline

The thesis is divided into seven chapters. The main research conducted in this thesis is summarized in Figure 1.2. In Chapter 1, the motivation and objectives of the study are discussed. Chapter 2 discusses the most recent advances in knowledge concerning the mechanisms that lead to the formation of LME cracks from micro-, and atomic-scale viewpoints. Additionally, Chapter 2 discusses the impact of metallurgical characteristics and kinetic parameters involved in thermomechanical processes on the severity of LME cracking.

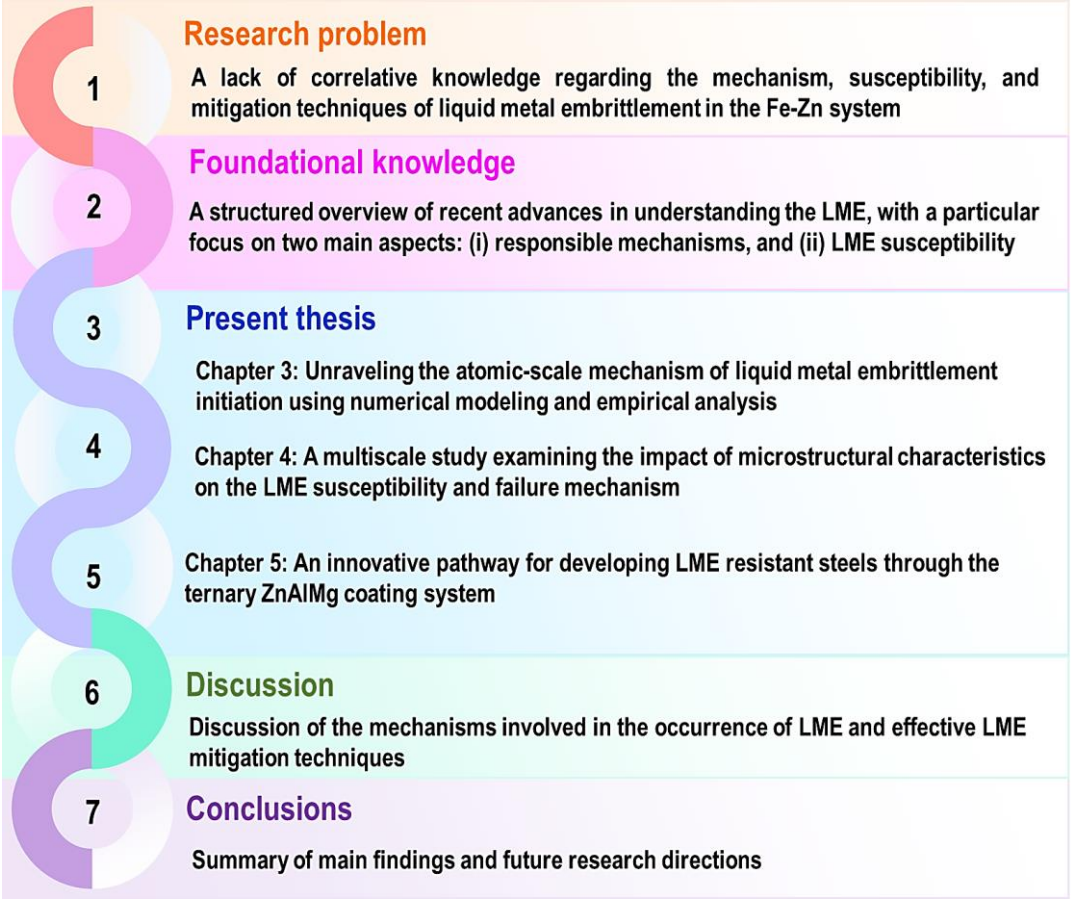

Figure 1.2 A diagram illustrating the different sections of the present thesis

From Chapter 3 to Chapter 6, the contents represent the research manuscripts that have been published or are currently submitted. Chapter 3 presents an integrated perspective on LME crack initiation in the Fe-Zn system and uses numerical modeling and atomistic empirical results to offer fundamental insights that have so far been lacking in the literature. Chapter 4 provides a systematic analysis of the LME crack propagation path in two ferritic and austenitic stainless steels and establishes a correlation between the underlying mechanisms of LME crack propagation and the influence of metallurgical factors such as initial microstructure, grain boundary characteristics, and grain boundary chemistry on the severity of LME cracking. Chapter 5 evaluates the LME crack susceptibility of ZnAlMg coated steel and establishes a correlation between high-temperature phase evolution and the LME cracking severity. Furthermore, Chapter 5 provides a new pathway for advancing LME resistant materials using ternary ZnAlMg alloy systems. In Chapter 6, a comprehensive discussion is presented to provide insights into the mechanisms underlying LME-induced cracks in the Fe-Zn system, as well as discuss effective methods for reducing this catastrophic phenomenon. Lastly, Chapter 7 summarizes the main findings of the current research and discusses future research directions.

Chapter 2 : Literature review

2.1 Overview

Advanced high strength steels (AHSS) have become extensively used in the automobile industry in an attempt to reduce vehicle weight and improve safety while maintaining relatively low manufacturing costs [16–20]. To maintain the integrity of vehicle structures, it is necessary to protect AHSS from corrosion. Zinc coating is a highly efficient and cost-effective technique for protecting steel sheets from corrosion [23,24]. Despite its excellent corrosion protection, the Zn coating may result in LME-induced cracks during different stages of manufacturing processes, including hot-stamping [25–29], brazing [30], laser welding [31–33], and resistance spot welding (RSW) [34–53]. Therefore, LME has emerged as a significant challenge in the development of new generations of high-strength lightweight steels in the automotive industry.

This chapter presents a comprehensive overview of recent advances in understanding the LME phenomenon in the Fe-Zn system. First, the general characteristics of the LME in the Fe-Zn system will be described. Next, the proposed hypotheses that aim to explain the mechanism leading to LME will be discussed from a historical perspective. Following this section, the underlying LME mechanisms in the Fe-Zn system will be discussed in detail, based on both experimental and analytical evidence In this section, emphasis will be placed on the correlation between empirical results and theoretical predictions. Lastly, the impact of factors such as metallurgical characteristics of steel substrate (e.g., initial microstructure, alloying elements, etc.) and thermomechanical process parameters (e.g., temperature, stress, strain rate, etc.) on the severity of LME cracking will be explored.

2.2 General characteristics of LME in the Fe-Zn system

The LME in the Fe-Zn system exhibits some distinctive characteristics that distinguish it from other LME couples. These complex characteristics complicate attempts to investigate the responsible LME mechanisms in the Fe-Zn system, which in turn results in the LME in this system being less recognized than in other couples. Figure 2.1 provides a general overview of the characteristics of LME in the Fe-Zn system. LME cracking in the Fe-Zn system occurs predominantly intergranular [7], in contrast to Fe-Pb and Fe-Pb(Bi) systems which show both transgranular and intergranular cracking [54]. Accordingly, the grain boundary characteristics of Fe-based substrates play a critical role in crack propagation behavior [7]. The LME crack propagation rate is rapid (up to m/s [55]), with an entire LME-induced failure occurring within 1-2 seconds [45]. The rapid LME crack propagation rate complicates the analysis of micro-scale events at the crack tip using empirical methods, such as in-situ high-resolution transmission electron microscopy (HRTEM). The occurrence of LME in the Fe-Zn couple occurs within a narrow temperature range (i.e., 700-940 °C) for most families of the Fe-Zn system. The impact of temperature on LME is evaluated by the "ductility trough" [56–58],

which indicates that the maximum reduction in tensile elongation occurs at this specific temperature range.

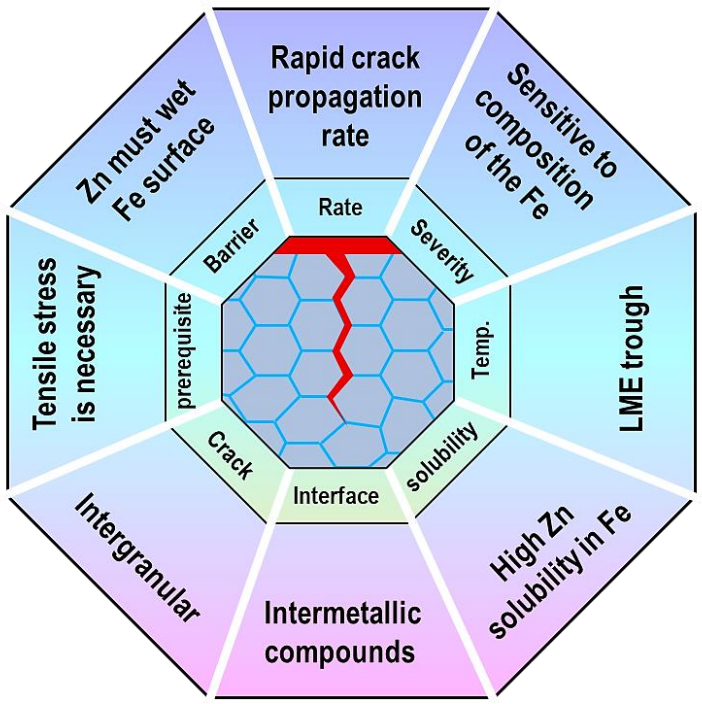

Figure 2.1 Illustration of the general characteristics of LME cracking in the Fe-Zn system

The solubility of Zn in Fe-based alloys is relatively high: 45.4 wt.% at 782 °C in Fe-BCC structure and 7.00 wt.% at 1150 °C in Fe-FCC [26]. The reaction of Fe and Zn at high temperatures results in multi-component systems consisting of several phases and intermetallic compounds. The Fe-Zn reaction at high temperatures can be described by using the binary phase diagram, as shown in Figure 2.2 (a) and (b). A schematic illustration of the metallurgical phase reactions at different temperatures is also presented in Figure 2.2 (c). The outer layer of the Zn coating is composed of pure Zn, identified as the η-eta phase with an HCP crystal structure. Several Fe-Zn intermetallic compounds are formed beneath this layer, as shown in the Zn-rich corner of the binary phase diagram (Figure 2.2 (b)). The first intermetallic compound (IMC) is zeta (ζ, $FeZn_{13}$, Monoclinic) which contains 3-6 wt.% Fe and is formed through a peritectic reaction at 530°C. The next IMC is the delta (δ, $FeZn_{10}$, HCP) with approximately 7.0-11.5 wt.% Fe and is formed through a peritectic reaction at 665°C [23,59]. The phase is divided into two forms: δ_{1k} ($FeZn_7$, HCP), and δ_{1p} ($FeZn_{10}/Fe_{13}Zn_{126}$, HCP), with slightly different crystal lattice sizes and compositions [60]. The next IMC is the $gamma_1$ (Γ_1, $Fe5Zn_{21}$, FCC) phase with an iron composition of 17-19.5 wt.% at 450˚C. As the last IMC, the gamma phase (Γ, Fe_3Zn_{10}, BCC) is formed after the peritectic reaction at 782°C and contains a high concentration of Fe (i.e., 23.5-28.0 wt.% Fe). The last phase preceding the steel substrate is α-Fe, which is a solid solution of Zn in the Fe matrix (Figure 2.2 (a)). As Zn is a strong stabilizer of ferrite [26], the reaction of Zn with Fe results in the formation of the ferritic α-Fe(Zn) phase.

It is evident that Fe-Zn IMCs exhibit distinctly different mechanical and physical properties owing to their different compositions and crystal structures. An illustration of the physical properties of IMCs as a function of the Fe content is shown in Figure 2.2 (d). Increasing Fe content increases resistance to decohesion at the coating/steel interface (i.e., flaking) while decreasing resistance to cracking (i.e., powdering) [61]. In addition, Fe-Zn IMCs are characterized by limited ductility due to their complex crystal structure [61]. In view of the general characteristics of LME described in this section, investigating the underlying mechanisms of LME crack formation has proven to be extremely challenging. Due to the micro/nanoscale size of IMCs, a detailed analysis of the impact of IMCs on LME cracking is complicated as ultra-thin specimens are required for advanced characterization methods.

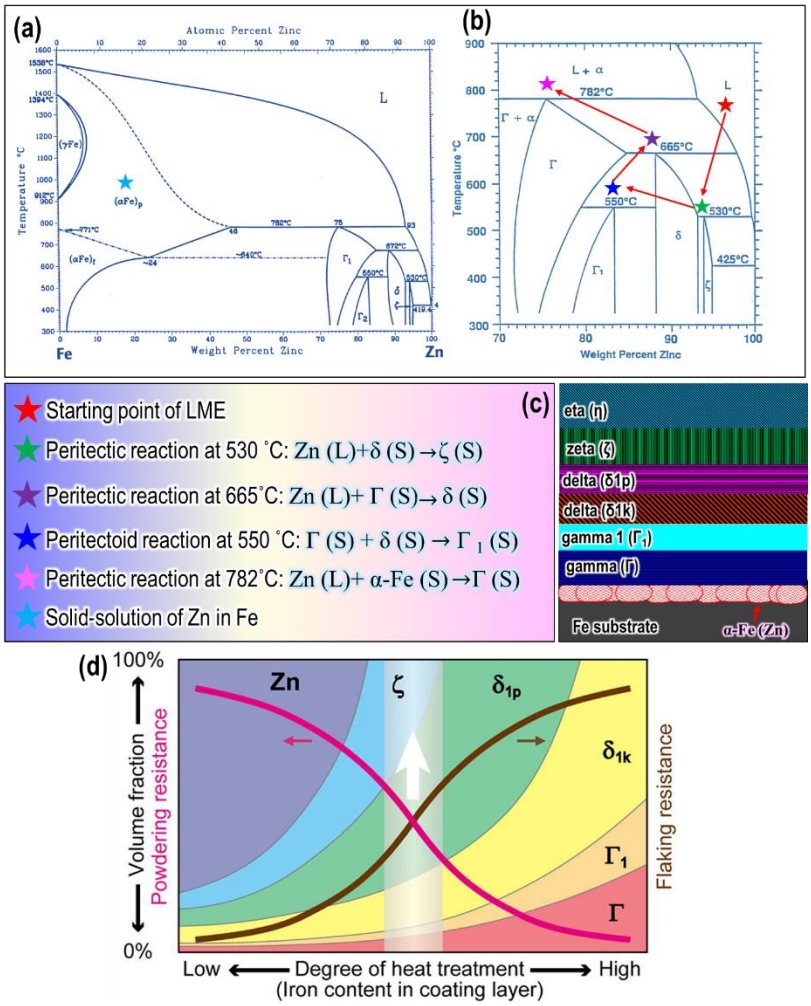

Figure 2.2 (a) The Fe-Zn binary phase diagram where the α-Fe phase has been identified by the blue star in the figure, (b) the Zn-rich corner of the Fe-Zn binary phase diagram showing the formation of different intermetallic compounds (adapted from Ref. [59]) (c) the corresponding metallurgical phase reactions during the formation of intermetallic compounds along with a schematic illustration of the sequence of the phases during Fe-Zn reaction, and (d) schematic illustration of the physical properties of Fe-Zn intermetallic compounds in the galvannealed (GA) coating as a function of Fe (Adopted from Ref. [61])

2.3 Theoretical models of LME mechanisms

Over the last decades, several models were proposed to explain the underlying mechanisms leading to LME in various solid-liquid systems [7,62–64]. Figure 2.3 presents a historical perspective on the proposed LME theories over the past decades. Theoretical models were also divided into three main categories [7,65]: (1) crack tip brittle fracture models, (2) crack tip plastic fracture propagation models (i.e., dislocation activity models), and (3) atomic grain boundary diffusion models. A brief overview of the proposed theoretical models is presented in this section to provide insight into the underlying LME mechanism in the Fe-Zn system. A detailed discussion of these models is beyond the scope of this study and comprehensive discussions can be found in references [64–66].

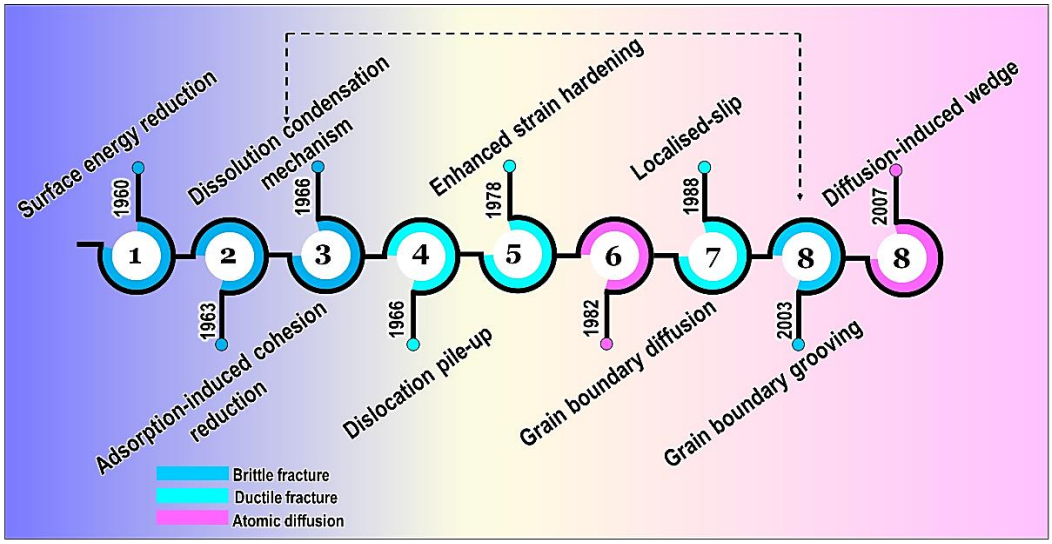

Figure 2.3 An overview of the proposed models for the underlying LME mechanisms in different solid-liquid systems. The theoretical models are classified into three main groups including (i) crack tip brittle fracture models, (ii) crack tip plastic fracture propagation models (i.e., dislocation activity models), and (iii) atomic grain boundary diffusion models.

2.3.1 Surface energy reduction

In this model, the responsible LME mechanism has been conceptualized as a reduction in surface energy caused by the adsorption of liquid metal atoms [54]. This model is linked with Griffith's theory for brittle fracture, which stated that the elastic strain energy during fracture is transferred into surface energy (γ_s) as described by $\sigma_c = \sqrt{\frac{2E\gamma_s}{\pi a}}$ [54], where σ_c is applied stress, E is Young's modulus of solid metal, and a is the half-length of an internal crack. This model predicts that the surface energy of solid metal is reduced by the penetration of liquid metal (i.e., $\gamma_{sl} < \gamma_s$, where γ_{sl} is surface energy at the liquid/solid interface), thereby resulting in reducing the critical stress required to cause the brittle fracture. Despite offering a simple explanation of LME-induced cracking, the surface energy reduction model fails to provide an accurate

prediction of the LME mechanism. The model provides no precise description of the atomic-scale events occurring during crack propagation [67]. Furthermore, measuring the surface energy during liquid metal penetration through experimental methods is quite complicated, making empirical support for this model challenging [54].

2.3.2 Adsorption-induced cohesion reduction (SJWK) model

The adsorption-induced cohesion reduction model proposed independently by Stoloff and Johnston [68] and Westwood and Kamdaras [67] (referred to as Stoloff-Johnson-Westwood-Kamdar (SJWK) model) [67,68] is an extension of the surface energy reduction model. This model presumes that the absorption of liquid metal atoms reduces the interatomic bond strength of the solid metal. Figure 2.4 (a) shows the schematic illustration of the atomic configuration at the crack tip in which the interatomic bonds to the left of A-A have been completely broken. The potential energy curve of the solid metal is shown in Figure 2.4 (b), where the minimum point of the energy curve represents the binding energy at the equilibrium atomic position. The stress required to separate the A-A bond is determined by taking the slope of the potential energy curve (i.e., dU/dr) as shown in Figure 2.4 (c). In the absence of the liquid metal, the solid metal has a potential energy curve of $U(r)_0$ and the binding energy (a_0) at the equilibrium atomic position. The presence of liquid metal atoms at the crack tip reduces the binding energy of solid metal to a_g, thereby reducing the stress required to overcome the potential energy barrier for fracture (i.e., from σ_{m_0} to σ_{m_g}) [68]. After breaking the atomic bonds, the embrittler atom is adsorbed to the newly formed surface, and the process is repeated until the crack propagates throughout the microstructure [63].

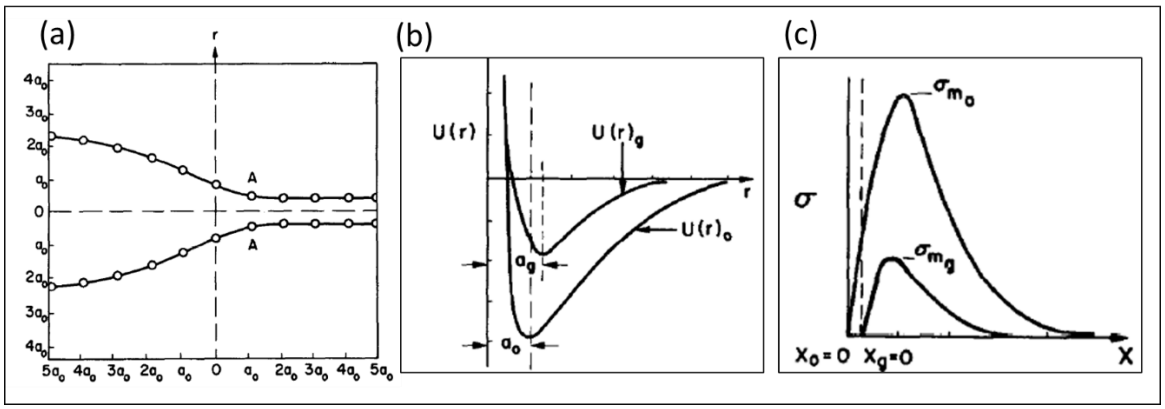

Figure 2.4 A schematic representation of the adsorption-induced cohesion reduction model (AICR); (a) Atomic configuration at the crack tip, where all atomic bonds to the left of A-A were completely broken; (b) schematic representation of the reduction in the interatomic potential curve; (c) stress required to overcome the potential energy barrier in the presence of liquid metal at the crack tip. Adapted from Ref. [68].

2.3.3 Dissolution condensation mechanism (DCM)

This model was first proposed by Robertson [69] and later further developed by Glickman and Goryunov [70], which is known as the Robertson-Glickman model [71]. A schematic representation of the primary concept of this model is shown in Figure 2.5 (a). According to this model, the stress increases the chemical potential of the solid metal at the crack tip and acts as a driving force for the localized dissolution of the solid metal atoms into the liquid metal (i.e, "dissolution" stage) [71]. Solid metal atoms subsequently deposit (i.e., "condensation" stage) onto the stress-free crack walls. Therefore, the liquid metal provides a fast transport medium for the diffusion of the dissolved solid metal atoms [71]. However, this model is not widely accepted because it has certain limitations [54]. For instance, the model predicts that embrittlement would be more severe for LME couples with high solubility of solid metal atoms in liquid metal [65]. However, the solubility of Fe in liquid Cs is only 2×10^{-4} wt.% at 400°C, yet LME in Fe-Cd systems is well documented in the literature [7,62,72]. In light of this, Glickman [73] devised a new version of DCM referred to as the grooving accelerated by local plasticity (GALP) model. Glickman [73] hypothesized that tensile stress and local plastic deformation near the tip of the groove (which has been filled with liquid metal) would lead to a decrease in diffusion length (L), ultimately leading to an increase in grain boundary grooving rate (i.e., groove rate (V_b) is inversely proportional to diffusion length, $V_b \propto \frac{1}{L^2}$). Figure 2.5 (b) shows a schematic representation of the multiple steps embrittlement process in the GALOP model. As a first step, the grain boundary groove with a primary dihedral angle of θ and width of w is filled by liquid metal. The sharp grain boundary groove acts as a stress concentration point, leading to localized plastic deformation and blunting of the groove tip and increasing the groove width from w to δ. The grain boundary groove continues to extend until the blunting distance reaches to the ΔL^*(parameter that indicates the increment in groove length between two subsequent blunting events). At this point, a new blunting event occurs, which results in a further increase in the grain boundary groove width. The occurrence of multiple (e.g., n times) grooving-blunting events ultimately results in grain boundary cracks with the total length of $L = n \times \Delta L^*$.

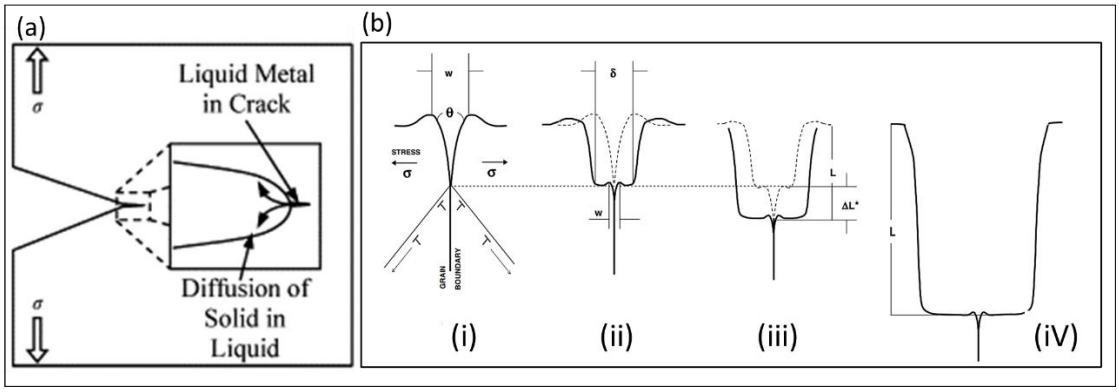

Figure 2.5 A schematic representation of (a) dissolution condensation model that explains LME based on the localized dissolution of the solid metal atoms into the liquid metal (adapted from Ref. [74]) and (b) multiple stages involved in the grooving accelerated by local plasticity (GALOP) model; (i) grain boundary groove with a primary dihedral angle of θ and width of w (ii) increasing the width of the groove from w to the δ as a result of blunting of groove tip, (iii) occurrence of grooving-blunting event and further increasing of groove width (ΔL^* is an adjustable parameter and represents the groove length increment between two consequent blunting events) and (iv) the formation of grain boundary crack with the total length of L due to the occurrence of "n-times" grooving-blunting events ($L = n \times \Delta L^*$). Adapted from Ref. [71].

2.3.4 Dislocation pile-up and enhance strain hardening models

The "dislocation pile-up" model was introduced by Hancock and Ives [75] in 1971 based on experimental observations in the Cu(Al)-Hg system. The main idea behind this model was to consider the role of dislocation activities in the crack tip. According to this model, crack propagation occurs as a result of an interaction between dislocation pile-ups and diffusion of liquid metal atoms along grain boundaries. The atomic diffusion ahead of the crack tip reduces grain boundary cohesion, and the stress concentration caused by the pile-up of dislocations facilitates crack propagation [75]. Accordingly, the model predicts that the LME crack propagates preferentially in an intergranular manner [54]. Furthermore, as the stress concentration at the crack tip is driven by dislocation pile-ups, the stacking fault energy (SFE) of the solid metal plays a significant role in the severity of the embrittlement [75].

The role of plastic deformation at the crack tip was also discussed by Popovich and Dmukhovskaya [76] when they proposed the "enhanced strain hardening" model. In this model, the absorption of liquid metal is postulated to affect the deformation behavior of the surface layer of the solid metal, which results in the intense strain hardening of this layer [76]. The limited strain hardening capability of the surface layer results in increased dislocation density at the interface between liquid and solid metal, leading to the development of microcracks in dislocation pileups and areas with stress concentrations [63,76]. The process of surface deformation, strain hardening, enhanced dislocation density, and microcrack formation is repeated until the LME crack propagates through the specimen.

2.3.5 Stress-assisted grain boundary diffusion model

Stress-assisted grain boundary diffusion was first introduced by Krishtal [77] and then developed further by Gordon and An based on experimental observations of delayed failure in the iron-indium (Fe-In) system [78]. In this model, embrittler atoms diffuse into solid metal grain boundaries and act as barriers for dislocation motion, causing dislocation pile-up ahead of grain boundaries. Upon building up a sufficient concentration of embrittler atoms at some critical depth (tens of atom diameters, according to Krishtal [77]), the stress reaches critical levels, causing crack initiation along the grain boundary. The “fractured” tip of the grain boundaries then allows the mass transfer of liquid metal into the crack, resulting in rapid crack propagation [79]. These authors examined the effect of temperature and stress on the kinetics of crack initiation and crack propagation stages, as shown in Figure 2.6 (a). For the temperatures below the melting point of embrittler (i.e., In), the phenomenon was referred to as solid-induced metal embrittlement (SIME). The crack initiation time (t_i) refers to the time when the crack becomes detectable by potential drop measurement test. Accordingly, t_i represents the point at which the dominant mechanism changes from crack initiation to crack propagation. According to Figure 2.6, the time for crack propagation is much shorter than for crack initiation; therefore, the LME crack formation is controlled by the crack initiation stage. The measured crack initiation time as a function of temperature is shown in Figure 2.6 (b), indicating that both SMIE and LME follow an Arrhenius-type behavior. Further, the initiation time increases with decreasing stress, indicating that SIME and LME (reffred as liquid-induced metal embrittlement (LMIE) in Figure 2.6) are influenced by stress levels. The impact of stress on crack initaion time is shown in Figure 2.6 (c). It is evident there exsits a "threshold" stress level below which no embrittlement occurs. The presence of stress is therefore an essential prerequisite for the occurrence of both SIME and LME phenomena. The stress-assisted grain boundary diffusion has been widely accepted as the underlying mechanism of LME in several studies [7,79–81]. Detailed information regarding the empirical evidence supporting this model in the Fe-Zn system will be discussed in the next sections.

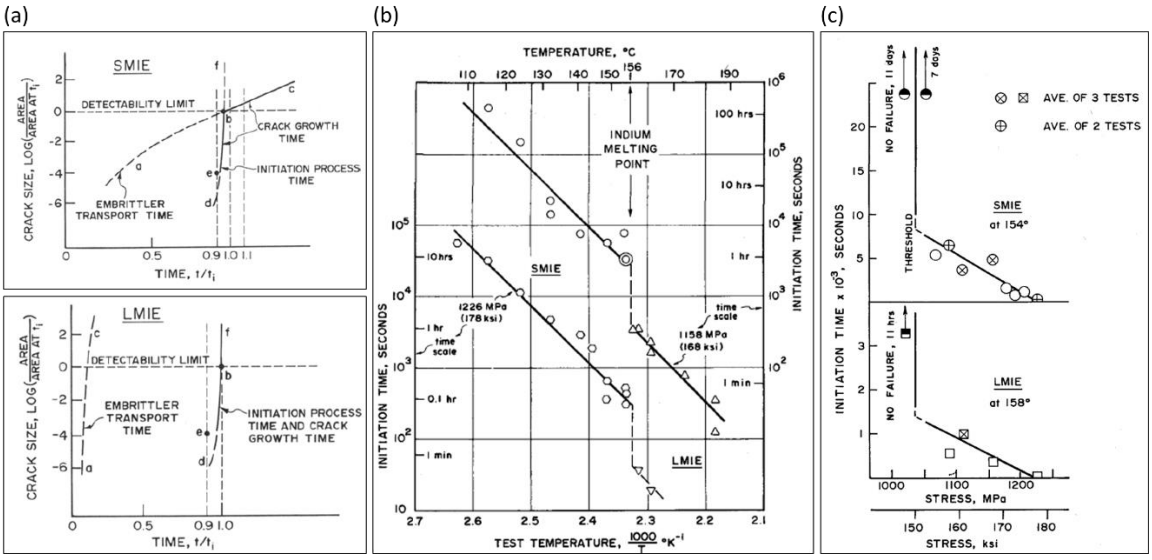

Figure 2.6 The effect of temperature and stress on crack initiation and propagation in solid metal-induced embrittlement (SMIE) and liquid metal-induced embrittlement (LMIE) phenomena; (a) schematic representation of LME crack initiation and propagation stages, with the line paths "abd" indicating the crack initiation stage and "dbc" indicating crack propagation stage, (b) variation of measured crack initiation time with temperature in SIME and LIME emphasizing the temperature-stress dependence of these two phenomena, (c) variation in initiation time as a function of stress emphasizing the critical stress required to trigger SIME and LIME. Adopted from Ref. [78].

2.3.6 Absorption-induced localized slip

The absorption-induced localized slip model was proposed by Lynch [66,82–84] to explain the role of dislocation activities and localized plastic deformation at the LME crack tip. An excessive fractography analysis was performed in order to illuminate the microscopic events that occur during the failure in an inert environment and the failure induced by LME. In an inert environment, crack propagation occurs when dislocation sources are activated on slip planes perpendicular to the crack. The dislocations emitted from other sources that do not meet this criterion, will not contribute to crack propagation, but rather will create strain fields ahead of the crack or result in crack blunting. Consequently, the crack propagation is accompanied by an excess plastic zone around the crack. This ultimately leads to extensive void nucleation and growth ahead of cracks, which are evident as dimples on the fracture surface. In contrast, the absorption of liquid metal atoms decreases the strength of the interatomic bond (i.e., chemisorption), indicating that a lower level of shear stress is necessary to initiate nucleation of dislocation at the crack tip. Since dislocation nucleation is less energetically favorable than dislocation movement, the local shear stress is considered sufficient for dislocation movement once nucleation takes place. Furthermore, void nucleation and growth occur in advance of the crack, and finally, the crack grows in conjunction with the voids. It must be noted that chemisorption indirectly reduces the degree of plasticity at the crack tip and, as a result, affects

the nucleation and growth of voids ahead of cracks. Consequently, one can expect that in the presence of liquid environments, strains and plastic zones around cracks are small.

2.3.7 Diffsuin-induced wedge formation

This model was developed by Klinger and Rabkin [80,81] from a mathematical standpoint and provides a detailed description of the atomic-scale events that occur during LME crack initiation. Figure 2.7 illustrates the schematic illustration of the model for a semi-infinite bicrystal of solid phase *B* subjected to tensile stress (σ_0) perpendicular to the grain boundary plane, where a droplet of liquid phase *A* is deposited on the surface of solid phase *B*. Due to the inequality in diffusion fluxes (i.e. $J_{Solid,B} \neq J_{\mathrm{Embrittler,A}}$), a stress-induced diffusion wedge is formed along the grain boundary. Further inward diffusion of liquid metal atoms causes a thickening of the diffusion wedge, thereby generating a stress field along the length of the grain boundary. It was shown that the geometrical characteristics of the diffusion wedge, including its width and length, as well as the stress-induced diffusion, play a significant role in the kinetics of grain boundary diffusion and the mechanisms involved in grain boundary decohesion [80,81].

Two different mathematical solution methods were used to integrate diffusion wedge into grain boundary concentration equations. In the first mathematical method, grain boundary diffusion coefficients and atomic volumes (Ω) of components *A* and *B* were assumed to be equal to determine the role of externally applied tensile stress (σ_0 in Figure 2.7 (a)) on the geometrical characteristics of the diffusion wedge [80]. Figure 2.7 (b) shows the change in concentration within the diffusion wedge as a function of time and applied stress. With an increase in the α value, i.e., a dimensionless parameter described by $\alpha = \frac{\sigma_0 \Omega}{kT}$, the width of the concentration wedge increases while its length remains unchanged. Figure 2.7 (c) illustrates the relative grain boundary concentration and penetration depth for different α values under various time intervals, where an $\alpha = 0$, $\alpha = 1$ and $\alpha = 5$ indicates no stress, low stress and high stress conditions, respectively. The grain boundary concentration profile follows a classical error function distribution in the absence of stress [80], similar to Fisher's grain boundary diffusion profile [85]. Moreover, the penetration rate of *A* atoms within the grain boundary is significantly increased by increasing the stress value, indicating that a high concentration of *A* atoms accumulates inside the diffusion wedge as the stress value is increased.

The Klinger-Rabkin [80] model illustrates the role of external stress in the kinetics of grain boundary interdiffusion, and it provides a persuasive explanation for the stress-assisted grain boundary diffusion model proposed by Gordon and An [78]. Although the Klinger-Rabkin model [80] provides an in-depth understanding of LME onset mechanisms, it is assumed that the grain boundary diffusivities of solid and liquid metal are equal which is not true for LME. Later, Klinger and Rabkin developed another model which included the differences in grain

boundary diffusivities of solid and liquid metal and proposed the concept of the Kirkendall effect during grain boundary interdiffusion [81]. Due to different intrinsic diffusivities between two components during diffusion, the diffusion fluxes are not balanced, resulting in the plating out of stress-induced diffusion wedge along the grain boundary. Figure 2.7 (d) and (e) show the stress-induced interdiffusion profile for two different grain boundary coefficient ratios (i.e. $\varphi = D_A/D_B$, where D_A and D_B are the grain boundary diffusion coefficients of matrix and liquid, respectively). For $D_A < D_B$ (i.e., the fast diffusion of B-embrittler atoms into the matrix during LME), a tensile stress zone develops close to the crystal surface, and compressive stress develops ahead of the diffusion wedge. The opposite occurs in the case $D_A < D_B$ (i.e., rapid diffusion of matrix atoms), and a zone of compressive stresses develops close to the surface. Furthermore, the amplitude of the stresses is determined by the ratio of diffusion coefficients and time. According to this model, the generated stress field during the interdiffusion process contributes significantly to the driving force of grain boundary diffusion. The magnitude of the stresses is sufficient to cause crack formation along grain boundaries, allowing further penetration of liquid metal into the crack and the formation of LME. This model describes the atomic scale events during the early stages of LME from a theoretical point of view, however, it remains without direct experimental evidence.

According to the literature review presented in this section, despite various hypotheses that have been proposed to explain the mechanism leading to LME, no consensus has been reached regarding the universal mechanism of LME. This is due to the complexity of the LME phenomenon, as well as the lack of empirical evidence to support the proposed hypotheses.

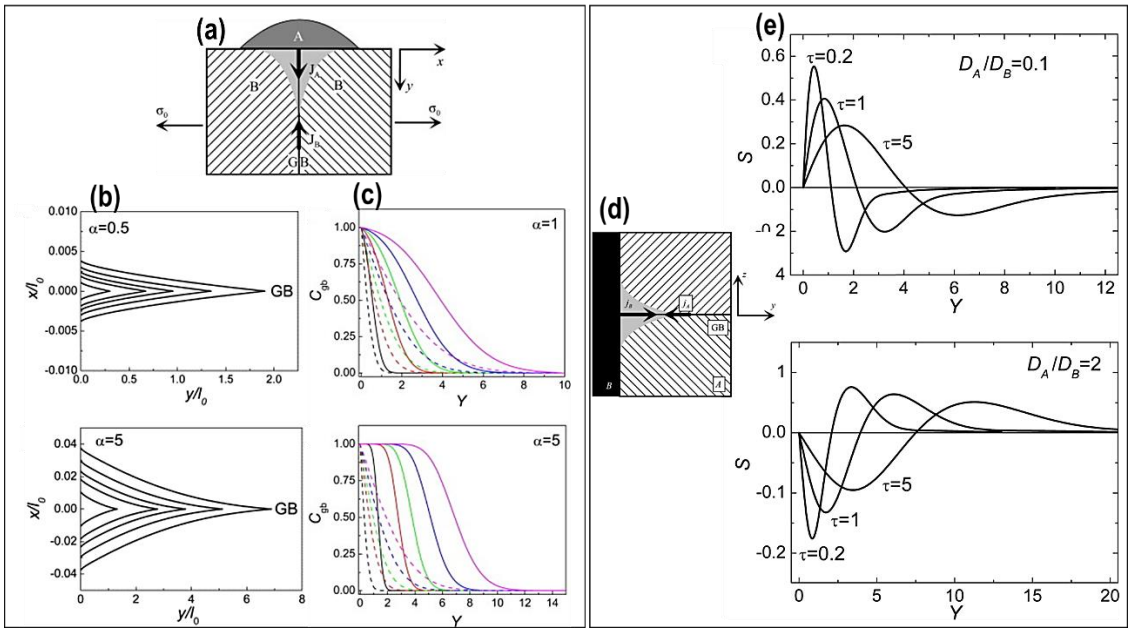

Figure 2.7 (a) Schematic illustration of a bicrystal of solid *B* subjected to an external stress σ_0 perpendicular to the grain boundary plane, where a droplet of liquid phase *A* was assumed to deposit on the surface of solid phase *B*, (b) distribution of concertation within the wedge at different times and applied stress ($\alpha = \frac{\sigma_0 \Omega}{kT}$ represents the applied tensile stress), (c) grain boundary concentration profiles at different times, and applied tensile stress where the concentration profile with no stress ($\alpha = 0$) condition is shown by dashed lines. Adopted from Ref. [80]. (d) bicrystal of solid *A* with a deposited layer of *B*. The difference in intrinsic diffusivities between *A* and *B* causes an imbalance of diffusion fluxes between the two components, which results in the formation of a diffusion wedge at the grain boundary, (e) the calculated stress-induced diffusion for different non-dimensional times ($\tau = 0.2, 1\ and\ 5$) and grain boundary coefficient ratios of $D_A/D_B = 0.1$ and $D_A/D_B = 2$. Adopted from Ref. [81].

2.4 The responsible LME mechanism in the Fe-Zn system

LME in the Fe-Zn system has several distinctive characteristics that limit the exploration and understanding of its underlying mechanism. As described in the previous section, the LME in the Fe-Zn couple occurs at high temperatures, i.e, between 700-900 °C [56,86]. This temperature range exceeds the critical temperature required to transform ferrite to austenite in most families of Fe-based substrates [18,53,87,88]. Due to the reorientation of atoms during non-equilibrium phase transformation at high temperatures, studying the mechanism behind LME is challenging. In light of this, a throughout understanding of the LME mechanism requires detailed experimental and theoretical analyses, investigating the crack path from a macroscopic, microscopic, and atomic-scale perspective. Over the past decade, extensive research has been conducted in an attempt to understand the LME occurrence mechanism during different thermomechanical processes. Figure 2.8 summarizes the proposed LME mechanisms in the literature in light of the evidence derived from empirical analysis. It is evident that the adsorption-induced cohesion reduction (SJWK) model [67,68] and (stress-assisted) grain boundary diffusion [78] models have been widely considered as leading

mechanisms responsible for LME in the Fe-Zn system. The proposed mechanisms are primarily based on empirical assessments in which the resolution of the characterization methods plays an imperative role in the accuracy of the LME mechanisms. As a result, the empirical analysis to study LME can be categorized into different groups, ranging from atomic- to mesoscale studies, as shown in Figure 2.9

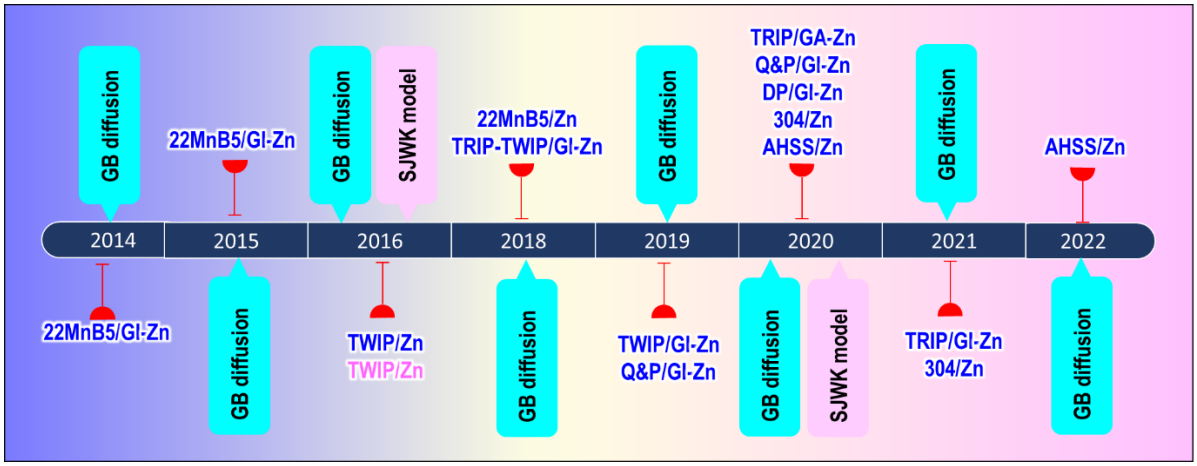

Figure 2.8 A diagram showing the research activities undertaken over the last decade in order to understand the underlying LME mechanism in different families of the Fe-Zn system during various hot-working processes, including hot-stamping, high-temperature tensile test, resistance spot welding (RSW), and laser welding. The adsorption-induced cohesion reduction (SJWK) [67,68] and stress-assisted grain boundary diffusion [78] were considered in the literature as responsible LME mechanisms in the Fe-Zn system (Zn-GI: Galvanized, Zn-GA: Galvannealed, TWIP: Twinning-induced plasticity, Q&P: Quenching and partitioning, TRIP: transformation induced plasticity, DP: dual phase, AHSS: advanced high strength steel 304: austenitic stainless steel)

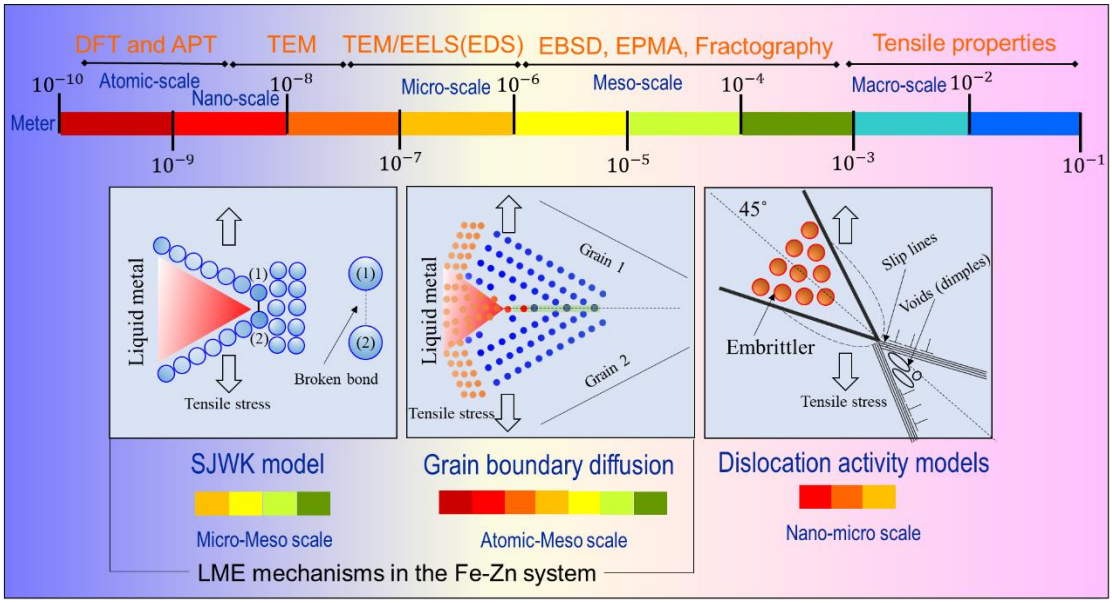

Figure 2.9 An illustration of the investigations on the LME crack occurrence mechanism in the Fe-Zn system by using empirical analysis and theoretical calculations at different length scales (DFT: density functional theory, APT: atom probe tomography, TEM: transmission electron microscopy, EELS: electron energy loss spectroscopy, EDS: energy-dispersive X-ray spectroscopy, EBSD: electron backscatter diffraction and EPMA: electron probe microanalyzer)

Several recent studies suggest that (stress-assisted) grain boundary diffusion (aka Gordon-An model [78]) is the most plausible mechanism for LME in the Fe-Zn system [22,41,65,79,89]. In this model, solid Zn atoms diffuse into the grain boundaries of the steel substrate leading to crack initiation. The "fractured" tip of the grain boundaries then allows the mass transfer of liquid metal into the crack, resulting in rapid crack propagation [79]. Cho et al. [26] investigated LME crack formation in 22MnB5 steel during the high-temperature tensile test. The authors claimed that LME-induced cracking occurred due to Zn diffusion along austenite grain boundaries which resulted in the transformation of austenite into ferrite. This transformation contributed to higher Zn diffusion rates along grain boundaries owing to the much higher bulk diffusion rate of Zn in ferrite compared to austenite. The experimental evidence in support of this hypothesis is presented in Figure 2.10. According to the SEM and EMPA analysis (Figure 2.10 (a) and (b)), the Zn content inside the LME crack was 70-80 wt.%, indicating the presence of the Γ-Fe_3Zn_{10} phase within the LME crack. EBSD-IPF map (Figure 2.10 (c)) showed an equiaxed grain structure within the LME crack, which indicates the presence of α-Fe(Zn) grains on both sides of the Γ-Fe_3Zn_{10} phase. The TEM micrographs and EDS analysis at the LME crack further confirmed the presence of Γ-Fe_3Zn_{10} (Zn content of 72 wt.%) and α-Fe(Zn) (Zn content of 10-40 wt.%) inside of the LME crack.

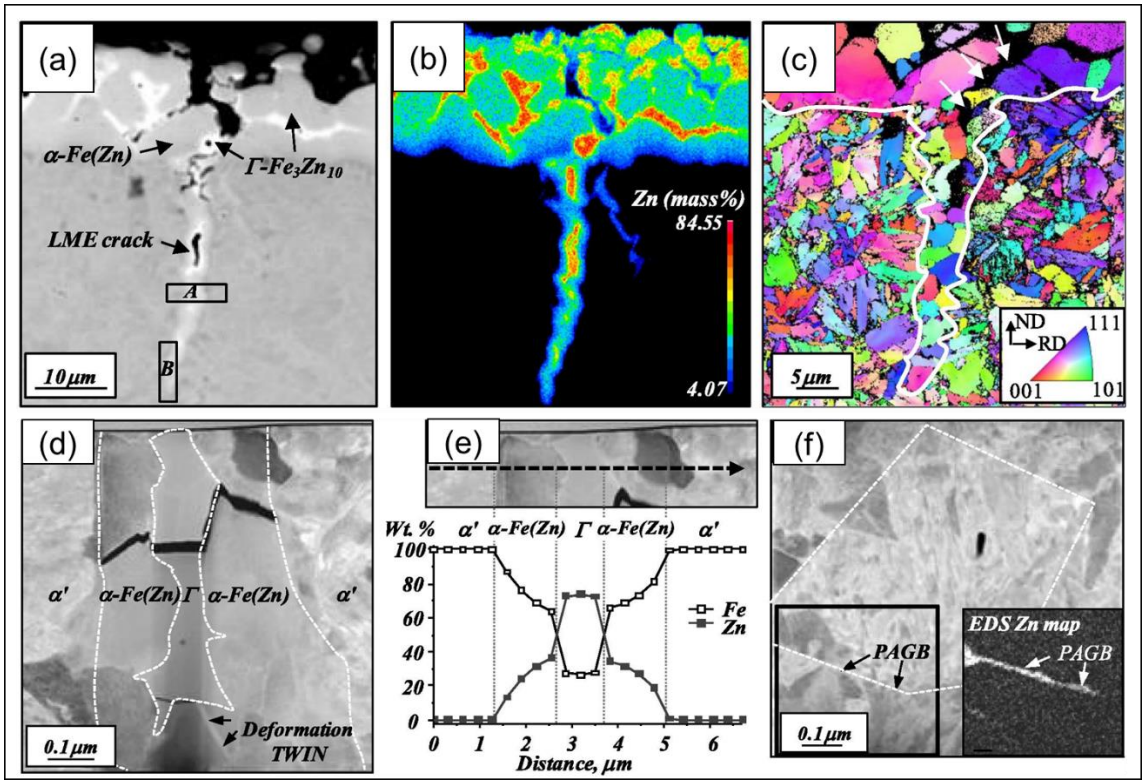

Figure 2.10 Microstructural and element characterization of the LME crack formed during the high-temperature tensile test at 900 °C in 22MnB5 steel; (a) SEM micrograph of the LME crack, (b) the corresponding EPMA analysis showing the Zn content at the LME crack tip reaches to the 70-80 wt.% indicating the presence of Γ-Fe_3Zn_{10} phase within the crack, (c) EBSD-IPF map which indicates the presence of α-Fe(Zn) grains inside of the crack, (d) Dark-field (DF) scanning TEM (STEM) image of the LME crack tip, (e) TEM-EDS analysis along the dashed line as indicated by the arrow and (f) DF-STEM image and the corresponding EDS-Zn map of the LME crack tip showing Zn diffusion along austenite grain boundaries. Adopted from Ref. [26].

Kang et al. [65] investigated Zn penetration mechanisms in TWIP steel during high-temperature tensile tests through TEM analysis in samples parallel to the normal direction (ND) and rolling direction (RD) of the Zn penetrated region, as shown schematically in Figure 2.11 (a). In this study, the quantitative measurement of the Zn content at the tip of the LME crack along the grain boundary was considered the most critical factor in determining the mechanisms involved in LME. Figure 2.11 (b) and (c) illustrate the TEM analysis of the ND specimen where the Γ-$(Fe, Mn)_3Zn_{10}$ islands were observed at the LME crack tip, which was surrounded by γ-(Fe, Mn)(Zn) grains. The EDS analysis revealed a maximum Zn content of 56 wt.% for the Γ-$(Fe, Mn)_3Zn_{10}$ phase and a range of 20-25 wt.% for the γ -(Fe, Mn)(Zn) grains, indicating that liquid Zn was penetrated along the austenite grain boundaries.

On the other hand, TEM analysis of the LME crack tip in the RD specimen (Figure 2.11 (d) and (e)) indicated only a small fraction of Γ-$(Fe, Mn)_3Zn_{10}$ phase (with 65.7 wt.% Zn) at the tip of the Zn penetration boundary. The EDS results (Figure 2.11 (f)) showed that the maximum

Zn content at the grain boundary was 4 wt.%, which is much lower than the maximum Zn solubility in steel.

In light of the measured Zn content at the crack tip of ND and RD specimens, Kang et al. [65] concluded that both stress-assisted grain boundary diffusion and adsorption-induced cohesion reduction (SJWK) models can be validated by experimental observations. In the case of the stress-assisted diffusion mechanism, Zn atoms react with the steel substrate at low temperatures to form a layer of the Γ-$(Fe, Mn)_3Zn_{10}$ phase at the interface between the steel and the coating. Upon increasing the temperature, the Γ-$(Fe, Mn)_3Zn_{10}$ phase is dissolved in the Fe substrate, allowing solid Zn atoms to diffuse into the steel grain boundaries through stress-assisted solid-state diffusion. When Zn reaches its maximum solubility in austenite, a small amount of liquid Zn islands are formed, due to which the grain boundary cohesion is lost, and cracks are formed. The low Zn content (i.e., 4 wt.%) at the tip of the Zn penetration region was considered evidence for a solid-state grain boundary diffusion mechanism. For the SJWK model, it was assumed that the Γ-$(Fe, Mn)_3Zn_{10}$ phase forms at low temperatures at the interface between the coating and the steel. As the temperature increases above the peritectic temperature reaction, the Γ-$(Fe, Mn)_3Zn_{10}$ phase transforms into a Zn-rich liquid that penetrates along austenite grain boundaries and eventually forms the LME crack. The model was validated through the detection of the Γ-$(Fe, Mn)_3Zn_{10}$ phase with high Zn content (~56 wt.%) at the tip of the LME crack [65].

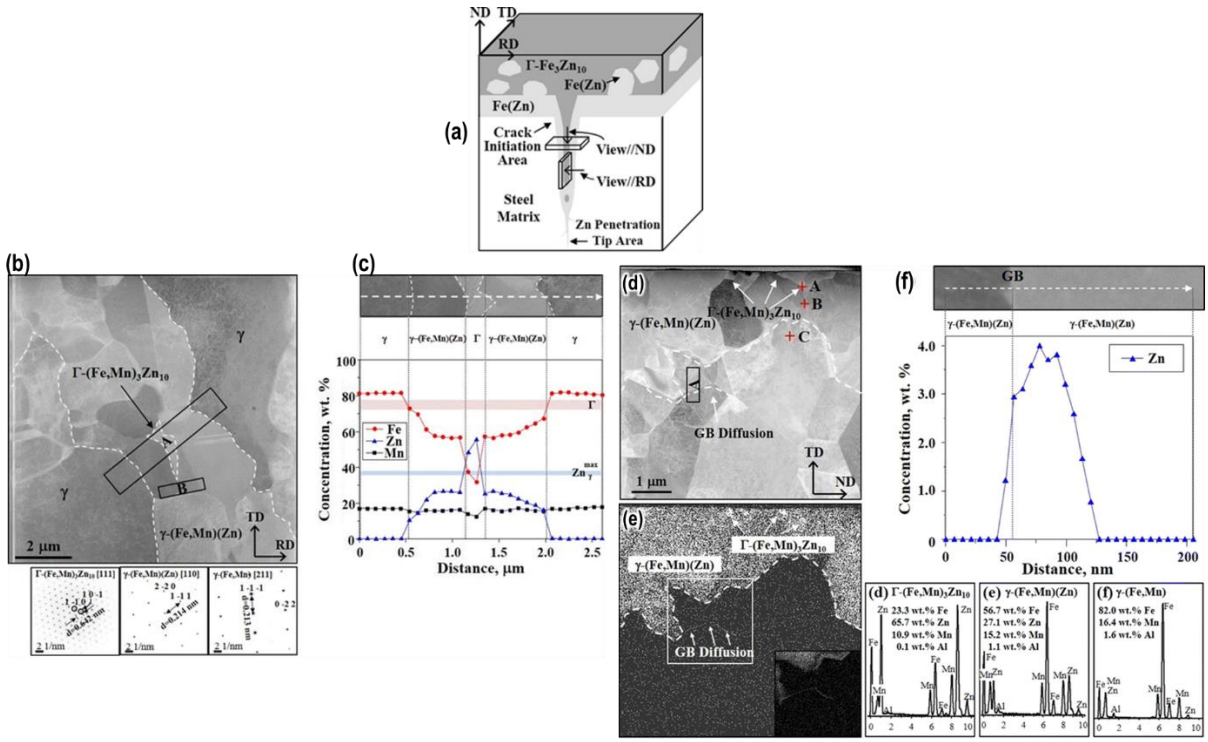

Figure 2.11 (a) Schematic illustration showing details of TEM sample preparation orientation parallel to normal direction (ND) and rolling direction (RD) of the Zn-penetrated grain boundary, (b) the TEM micrograph, and (c) EDS analysis of the ND specimen which showed the presence of the Γ-(Fe, Mn)$_3$Zn$_{10}$ phase within the LME crack, providing evidence to support the SJWK model, (d)-(f) TEM micrographs, and EDS analysis of the RD specimen which showed a low Zn content at the austenite grain boundary, providing evidence in support of the stress-assisted grain boundary diffusion model. Adopted from Ref. [65].

Although all discussed studies focused on (stress-assisted) grain boundary diffusion mechanisms, the role of stress on grain boundary diffusion was not explored. In light of this, DiGiovanni et al. [89] used numerical modeling (based on the Klinger-Rabkin model [80]) and experimental observation in order to investigate the effects of external tensile stress on Zn grain boundary penetration. Figure 2.12 shows the depth profile of Zn concentration based on numerical calculations (i.e., solid lines in Figure 2.12) and experimental measurements by EPMA (i.e., points in Figure 2.12). In the no-stress case, the concentration profile follows an error function distribution, but with an increase in stress levels, it deviates from the error function to form a distinct sigmoidal distribution. Accordingly, increasing stress levels act as an additional driving force for grain boundary diffusion and result in an increase in Zn penetration depth along grain boundaries. The results of this study provided a clear understanding of the effect of tensile stress on LME behavior in which under the no-stress condition, typical grain boundary diffusion behavior is observed, but that alone is not sufficient to facilitate the Gordon-An penetration zone required for LME crack formation. The application of external stress promoted the stress-assisted diffusion mechanism until the penetration zone develops into an LME crack [89].

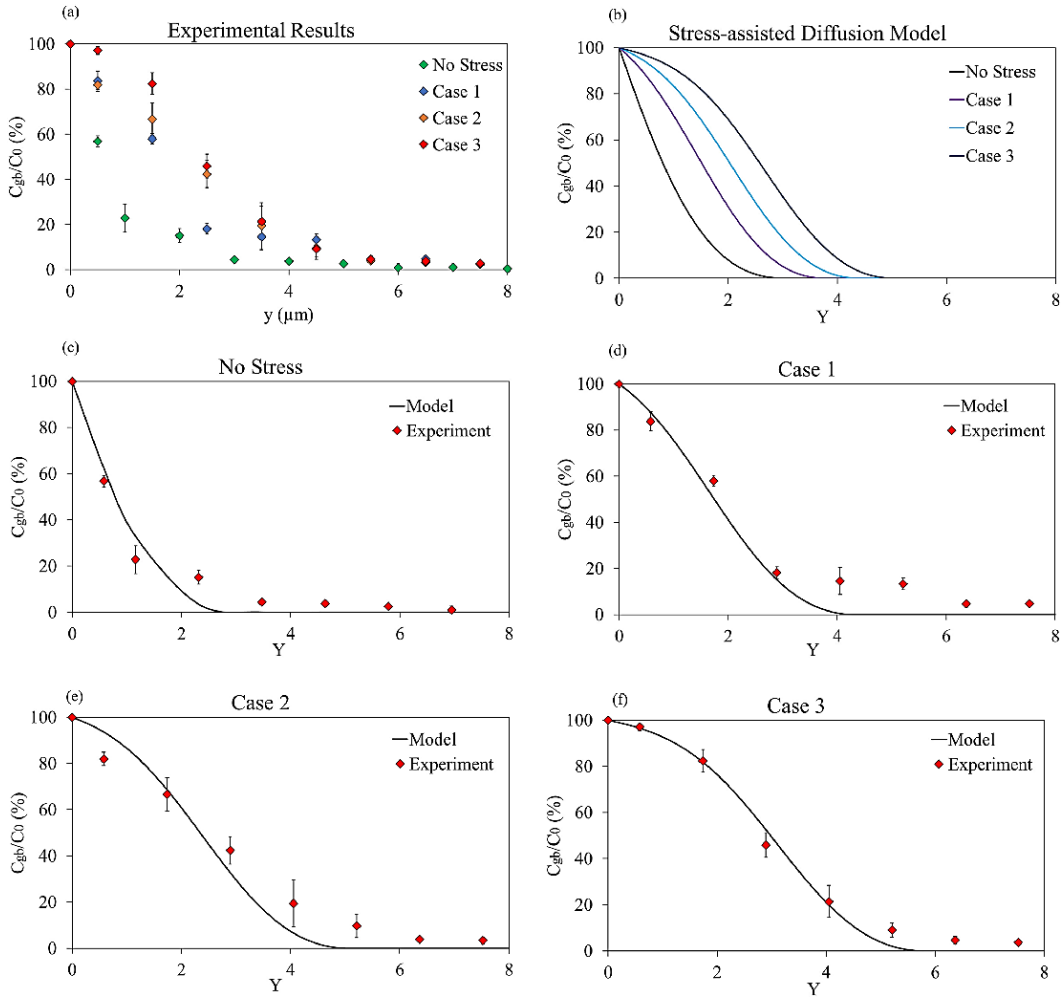

Figure 2.12 The calculated and measured Zn concentration profile under different stress levels during interrupted high-temperature tensile tests. Cases 1-3 correspond to 190 MPa, 305 MPa, and 406 MPa stress levels, respectively; (a) experimental measurements of Zn concentration depth profiles, (b) calculated Zn concentration profile, (c) a combination of numerical and experimental measurements for no stress condition, (d) combination of numerical and experimental measurements for case 1, (e) combination of numerical and experimental measurements for case 2, and (f) combination of numerical and experimental measurements for case 3. Reprinted from Ref. [89].

As discussed up to this point, all investigations were conducted on a meso- to micro-scale analysis, primarily based on microstructural characterization of Zn content at the LME crack tip. Although quantitative analysis of the crack tip provides a preliminary understanding of LME crack mechanisms (i.e., an indication for grain boundary diffusion or liquid Zn penetration), it does not reveal insight into the micro-scale events responsible for LME crack initiation or crack propagation. In light of this, atomic-scale analysis at the crack tip provides a more accurate picture of the mechanisms that lead to the formation of the LME crack. Razmpoosh et al. [79] examined the mechanism leading to LME cracking in austenitic steel using atom probe tomography (APT) analysis. The study provided evidence for the stress-assisted grain boundary diffusion model as the underlying mechanism of LME crack

propagation. Furthermore, the study shed light on the role of grain boundary chemistry on susceptibility to LME cracking. Figure 2.13 shows 3-dimensional (3D) APT maps as well as detailed composition profiles of the Zn-penetrated grain boundary. The results showed clear segregation of Cr and co-segregation of other alloying elements on one side of the Zn-penetration film. The observation led to the conclusion that the LME crack propagation involved a multi-step process where Zn-induced embrittlement led to a fracture on one side of the grain boundary. This is followed by the subsequent flow of fresh liquid Zn, in conjunction with the interdiffusion of Zn, Ni, and Fe along the grain boundary. This study revealed that the LME-induced cracking occurred through a solid-state grain boundary diffusion mechanism through which the segregation of alloying elements compromised the cohesive strength of the grain boundaries, resulting in grain boundary fracture before Zn penetration [79].

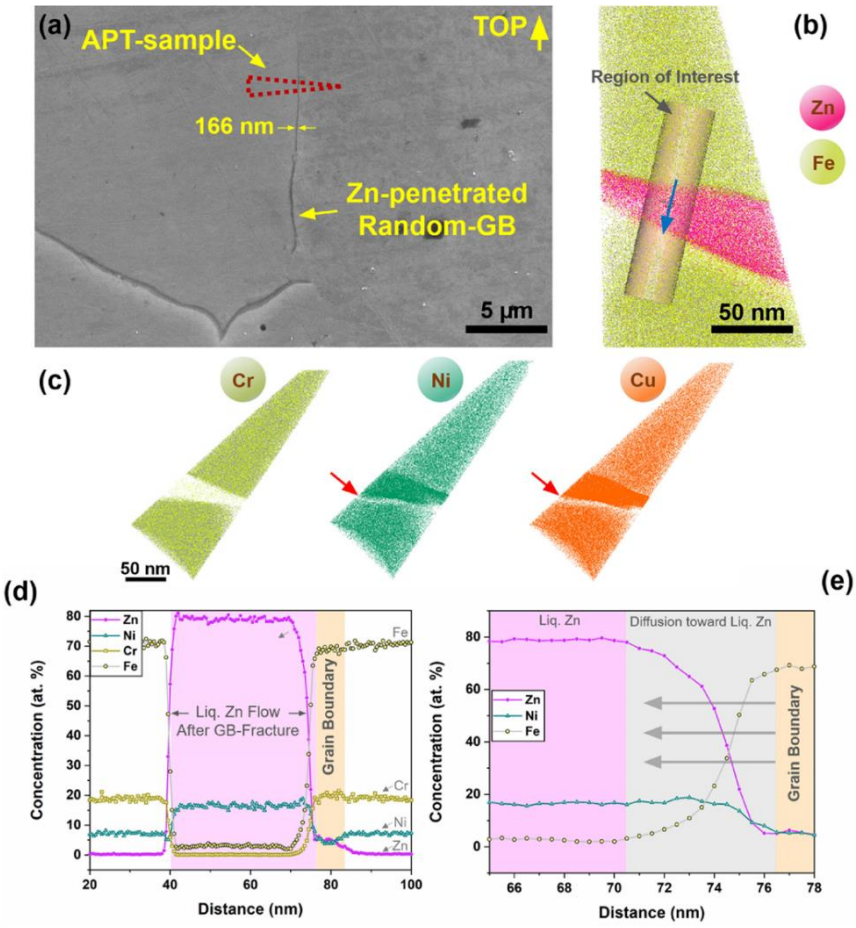

Figure 2.13 Atomic-scale analysis at the LME crack tip in austenitic steel using the atom probe tomography (APT) technique at a Zn-penetrated grain boundary; (a) location of the APT specimen at the Zn-penetrated random grain boundary, (b) 3-dimensional (3D) reconstruction of the APT analysis indicating the region of interest, (c) the chemical profile analysis of the Zn-penetrated grain boundary (outlined in orange) and the liquid Zn flow area following the fracture of the grain boundary (outlined in pink), and (e) enlarged view of the Zn-penetrated and subsequent liquid Zn flow region. Reprinted from Ref. [79].

While the studies discussed above provide persuasive evidence supporting the stress-assisted grain boundary diffusion mechanism, the adsorption-induced cohesion reduction mechanism (SJWK model [67,68]) has also been identified as the plausible LME mechanism in the Fe-Zn system [21,38,65,90]. According to the SJWK model, the liquid metal atoms at the crack tip reduce the interatomic bond strength as a result of chemisorption. When tensile stress is applied, the weakened bonds break and the crack propagates [7]. In light of the previous discussion, Kang et al. [65] indicated that this model is responsible for liquid metal penetration in TWIP steel, as evidenced by the presence of the Γ-$(Fe, Mn)_3Zn_{10}$ phase within the LME crack (Figure 2.11 (b) and (c)). A recent study conducted by Razmpoosh et. al [21] showed clear evidence of the Zn penetration along the grain boundaries of the austenitic steel. The TEM and EELS analysis at the tip of the LME crack (Figure 2.14) showed that liquid Zn penetrated the grain boundary. Furthermore, there is a severe segregation of Cr into small particles prior to the penetration of Zn along the grain boundary. In light of their observations, the authors concluded that the grain boundary opens prior to Zn-flow, thus supporting the SJWK model as the responsible mechanism of LME in the Fe-Zn system [21]. A study by Murugan et al. [38] examined Zn transport mechanisms in TRIP steel by using fractography analysis, which revealed a variety of Zn morphologies on the fracture surface, including continuous Zn films, and discontinuous Zn clusters between grains. As a result, the authors concluded that liquid Zn penetrated grain boundaries which supported the SJWK model as the mechanism for LME.

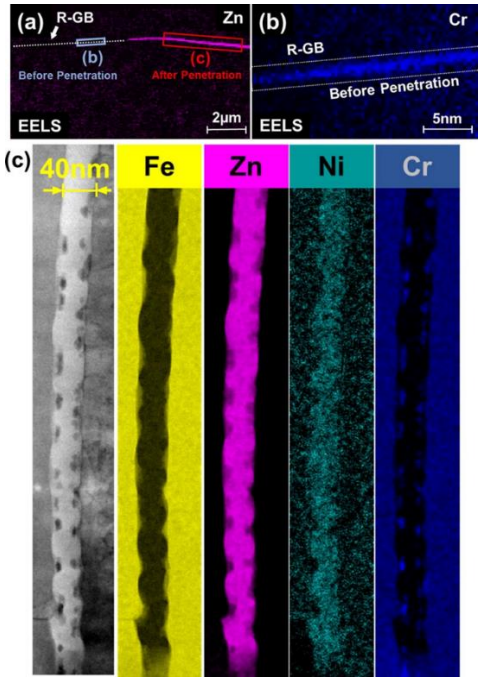

Figure 2.14 TEM and corresponding EELS elemental maps of the Zn-penetrated grain boundary in the austenitic steel; (a) the overall view of the representative grain boundary depicting the Zn-penetrated and non-Zn-penetrated regions, (b) the EELS-Cr map shows the corresponding side of the grain boundary before Zn penetration, and (c) high-resolution TEM and EELS maps of the Fe, Cr, Ni and Zn elements after Zn penetration. Reprinted from Ref. [21].

In light of the aforementioned discussions, the underlying mechanism responsible for LME remains insufficiently understood, such that no consensus can be reached regarding a unified mechanism, despite each providing a plausible explanation for LME. Therefore, it appears that there are some significant uncertainties regarding the mechanisms responsible for LME occurrence in the Fe-Zn system. For instance, the proposed mechanisms fail to distinguish between crack initiation and crack propagation stages. Currently, it is not yet clear whether stress-assisted grain boundary diffusion or liquid metal penetration is responsible for the initiation of LME cracks. In addition, the role of stress during the Zn diffusion process has not been thoroughly investigated. In regard to the mechanisms underlying LME crack propagation, there are still some disagreements in the literature. It is important to determine whether the propagation of LME cracks is caused by a brittle fracture at the crack tip or by dislocation activity and localized slip. While the TEM analysis at the LME crack tip did not indicate dislocation activity [21,65], a thorough analysis of the LME-induced failure – i.e., fractography analysis combined with characterization of the LME crack tip, is also necessary in order to identify the mechanisms responsible for LME crack propagation. Therefore, the LME mechanism has been concealed behind a number of contradictory hypotheses without any experimental support. In addition, the absence of a unified LME mechanism in the Fe-Zn system complicates the role of metallurgical factors in determining LME susceptibility.

2.5 LME susceptibility in the Fe-Zn system

Numerous factors contribute to the susceptibility of LME cracking in the Fe-Zn system. Generally, these factors can be divided into three categories as shown in Figure 2.15 [91]: (i) metallurgical characteristics of the steel, i.e., initial microstructure, alloying elements, etc. (ii) factors related to the Zn-coating, including its chemistry and intermetallic compounds, and (iii) kinetic parameters pertaining to the hot-working process. The influence of thermomechanical process parameters such as temperature [56,57,92], strain rate [58], holding time [42], and heating rate [86] has been extensively explored in the literature. However, the impact of the metallographic characteristics of steel substrates and Zn coatings on LME susceptibility has not been examined in depth.

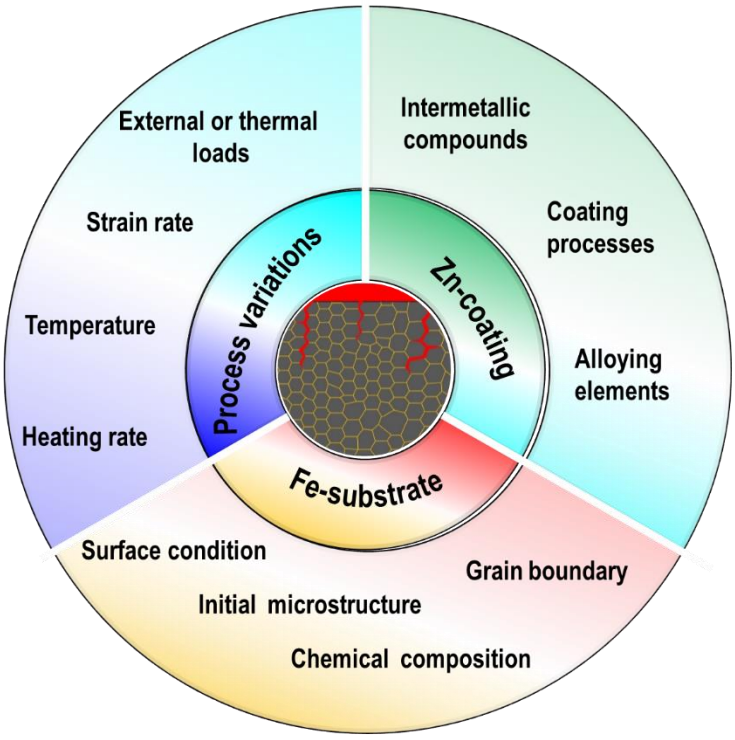

Figure 2.15 The factors affecting LME severity in the Fe-Zn system including metallurgical characteristics of the steel, factors related to the Zn-coating, and kinetic parameters pertaining to the hot-working processes

The parameters of the hot working process play an influential role in LME severity. Fe-based alloys can appear to be resistant to LME under a particular set of test conditions but suffer severe embrittlement under other test conditions [37,86,93]. Among the different hot working processes, the role of process parameters in RSW has been extensively investigated in the literature [35,37,38,42,44,46,94–96]. There are also a few studies that examine the impact of laser welding parameters on the severity of LME cracking [9,33]. As RSW is subjected to extreme non-equilibrium conditions, including high heating and cooling rates and extremely short welding times [35,37,46], the high temperature tensile test has also been conducted to assess the influence of temperature, strain rate, heating rate, etc., on LME cracking susceptibility [12,89,97]. Figure 2.16 summarizes the impact of RSW and high-temperature tensile test (HTT) parameters on LME severity. In the case of HTT, temperature is a critical determinant of LME severity. The impact of temperature on LME is evaluated by the "ductility trough" [22,56–58], which states that the severest reduction in tensile elongation occurs at a specific temperature range (i.e., 700-940 °C [56–58,86,98]). The severity of LME commonly increases with increasing temperature [22,47,56,57]. The impact of temperature on LME severity, however, is dependent upon other factors, such as the chemical composition of the steel or coating and HTT parameters, including strain rate, heating rate, and holding time [56,58,86]. For example, Beal et al. [56] showed that strain rate has a significant influence on the temperature range for the occurrence of LME in TWIP steel. At the lowest strain rate

(1.3×10^{-3} s^{-1}), no significant difference was observed between the tensile behavior of Zn-coated and uncoated specimens at all test temperatures between 600 and 1000 °C. By increasing the strain rate, the LME occurs at the temperature range between 775-950 °C, with the most severe embrittlement occurring at 800 °C and 850 °C. Additionally, it was shown that an increase in strain rate results in a wider range of embrittlement temperatures by decreasing the lower temperature limit (i.e., 775 °C for 1.3×10^{-2} s^{-1}, 700 °C for 1.3×10^{-1} s^{-1} and 600 °C for 1.3 s^{-1}) [56]. Similarly, Kang et al. [58] showed that lower strain rates reduced LME-induced ductility loss in high-Mn steel at 700 °C and 800 ° C.

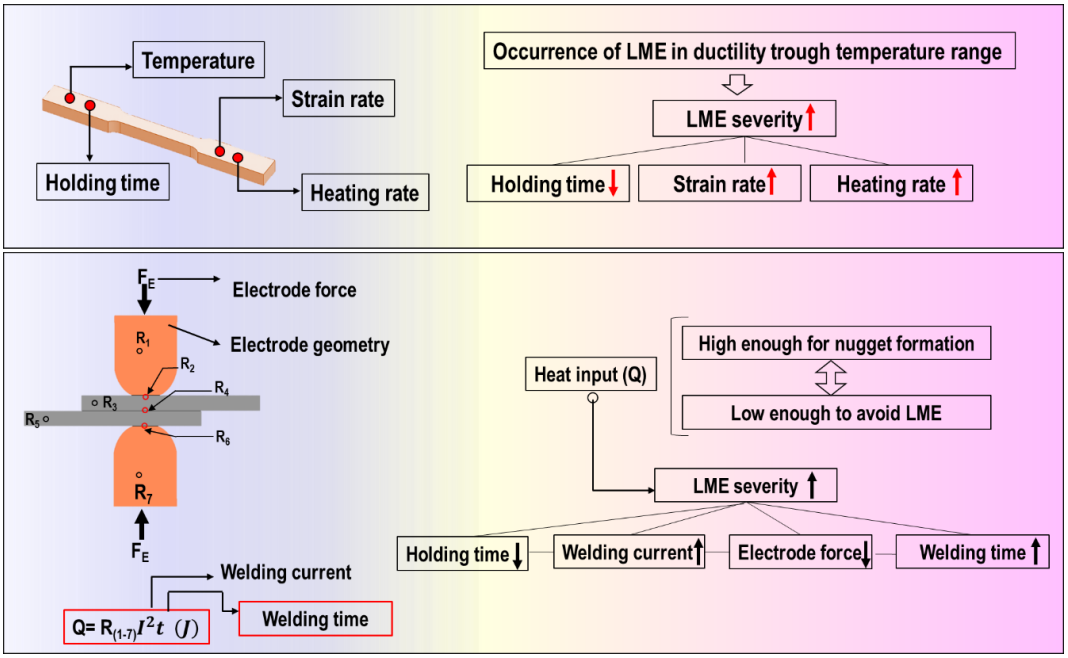

Figure 2.16 Overall impact of high-temperature tensile tests and resistance spot welding process parameters on the severity of LME cracking

Contrary to the hot-tensile process, the RSW process generates inhomogeneous distributions of temperature and stress in different regions of the specimen [35,37,46]. Heat input is one of the most significant factors influencing the severity of LME, as a reduction in heat input reduces the susceptibility to LME [37,96,99]. Meanwhile, an adequate amount of heat must be provided in order to meet the minimum nugget size required to achieve the integrity of the weldment under mechanical loads [15,100,101]. In light of this incongruity, RSW specimens with acceptable nugget sizes usually contain LME cracks.

The alloying elements in AHSS (e.g., Mn, Al, Si, Nb, V, N, etc.) can affect LME susceptibility through various mechanisms including (i) affecting the diffusion of Zn into Fe-substrates [45], (ii) segregation into grain boundaries (or co-segregation with Zn atoms) [21,79], and (iii) affecting the interaction between steel and liquid Zn to form different IMC and phases [12]. Among different alloying elements, only the effect of Si content on LME susceptibility has been studied in depth in literature. It is known that an increase in Si content increases the

susceptibility of the steel substrate to LME cracking [45,102–104]. A recent study showed that increasing Si has a significant effect on the microstructural characteristics of dual-phase steels [45]. According to this study, increasing Si content led to an increase in the density of internal oxides along grain boundaries and increased the depth of the decarburization layer. It is noteworthy that the intergranular internal oxides adversely impact grain boundary cohesion, which in turn affected the susceptibility of grain boundaries to LME cracking [14,45]. Additionally, the results showed that the severity of LME cracking was notably higher in the sample with higher decarburization layer depth (i.e., the sample with high Si content) [45]. This is consistent with the findings of recent investigations, which showed that increasing the Si content increases the depth of the decarburization layer and the density of internal oxides, thereby increasing the LME susceptibility [102,103]. However, the role of a fully ferritic layer on LME crack susceptibility is not in complete agreement with what has previously been discussed in the literature [7,28,65]. It has been frequently reported that the susceptibility of austenitic microstructures (such as TWIP steels [56,105]) to LME cracking is much higher than that of ferritic structures due to the much higher grain boundary diffusion coefficient of Zn in austenite as compared to ferrite [7,28,65]. This led to the conclusion that LME cracking can be prevented by using steel substrates with ferritic decarbonization layers [7]. However, the results presented earlier [22,45,91,102,103] indicated that LME can occur in fully ferritic microstructures. In this regard, there is no consensus regarding the role of initial microstructure in susceptibility to LME cracking. This lack of knowledge impedes the development of effective strategies for mitigating LME through the use of microstructural modification techniques.

The literature review of the mechanisms involved in crack initiation and propagation, as well as the role of metallurgical factors on LME susceptibility, revealed that different aspects of the LME phenomenon in the Fe-Zn system remain unexplored. It is evident that further research is required to identify the mechanisms responsible for the occurrence of LME. The advancement of research in this area leads to a better understanding of the factors that contribute to the susceptibility to LME, and, as a result, facilitates the development of strategies to mitigate this important concern from structural and engineering components.

Chapter 3 : Unraveling the atomic-scale mechanism of liquid metal embrittlement crack initiation in the Fe-Zn system[1]

3.1 Overview

Catastrophic brittle failure of ductile crystalline materials by liquid metal embrittlement (LME) is a widely documented phenomenon but the fundamentals of its initiation mechanism are poorly understood. The embrittlement of iron (Fe) by zinc (Zn) has recently become highly relevant due to the popularity of Zn-coated steels but the underlying mechanism driving LME in this couple remains unclear. The results of this study showed that the formation of a stress-induced diffusion wedge (SIDW) at the exposed grain boundary (GB) due to the interdiffusion of Zn-embrittler atoms was the trigger for LME. The formation of the SIDW facilitated the diffusion of the Zn-embrittler atoms into the GBs, which devastated their coherency and mechanical integrity. LME initiation entails several steps: (i) solid-state GB diffusion, (ii) formation of the SIDW, (iii) eventual melting of the SIDW, and (iv) opening of the liquid wedge due to interdiffusion and the application of externally applied stresses.

3.2 Background

In the last decade, LME in the iron-zinc (Fe-Zn) couple [12,22,44,91,95,106] has drawn considerable attention due to the development of Zn-coated advanced high strength steels (AHSS) used in the automotive industry to produce lightweight and crash-resistant structural components [107,108]. There are two continuous stages involved in LME cracking: crack initiation and crack propagation [78]. The LME susceptibility of a material is a crack initiation-controlled phenomenon, i.e., once cracks are initiated, they propagate into the bulk substrate as fast as several tens of micrometers per second [54]. To date, there have been several proposed hypotheses that aim to explain the mechanism leading to LME [64–66], but despite these efforts, there is no clear consensus in the existing literature. This is due to the complexity of the LME phenomenon, which makes it difficult to model the LME behavior based on the proposed theories due to a lack of experimental data and the difficulty associated with gathering empirical evidence pertaining specifically to the instances that mark the onset of LME.

Two distinct hypotheses have been considered to explain the mechanism leading to the onset of LME in the Fe-Zn couple. Some studies argue that strain-activated chemisorption of liquid-metal atoms (commonly known as the Stoloff-Johnson-Westwood-Kamdar (SJWK) model [67,68]) is the governing mechanism for LME [21,38,65,90]. The SJWK model states that the liquid metal atoms at the crack tip reduce the interatomic bond strength as a result of chemisorption, which causes the interatomic potential curves to have lower barrier energy

[1] A modified version of this chapter is submitted to Acta Materialia, Ali Ghatei-Kalashami, M. Shehryar Khan, Frank Goodwin, and Y. Norman Zhou

needed to break the bonds at the crack tip. When tensile stress is applied, the weakened bonds break and the crack propagates [7]. On the other hand, several recent studies suggest that stress-assisted grain boundary diffusion (which is commonly known as the Gordon-An model [78]) is the most plausible mechanism for LME [22,65,79,89]. In this model, embrittler atoms diffuse into the grain boundaries of the substrate leading to crack initiation. The "fractured" tip of the grain boundaries then allow the mass transfer of liquid metal into the crack, resulting in rapid crack propagation [79]. However, the Gordon-An [78] model does not account for the occurrence of micro/atomic scale events that contribute to the initiation of LME. For example, the diffusion of the embrittler atoms along grain boundaries (i.e., grain boundary interdiffusion) has not been included in this model. Furthermore, there is no clear understanding of how the application of stress affects the interdiffusion process and how the atomic diffusion leads to crack initiation resulting in the subsequent decohesion of the grain boundaries.

To study the effects of stress on grain boundary diffusion, Klinger and Rabkin [80] developed a grain boundary interdiffusion model in a semi-infinite bicrystal system under applied external stress to the grain boundary plane. According to this model, due to the inequality in diffusion fluxes (i.e. $J_{Solid} \neq J_{\text{Embrittler}}$), a stress induced diffusion wedge is generated along the grain boundary [80]. This diffusion wedge creates an extra diffusion flux which provides the driving force for grain boundary interdiffusion. In the Klinger-Rabkin [80] model, however, the grain boundary diffusivities of solid and liquid metal were assumed to be equal, which is not true for LME. Later, Klinger and Rabkin developed another model which included the differences in grain boundary diffusivities of solid and liquid metal and proposed the concept of the Kirkendall effect during grain boundary interdiffusion [81]. According to this model, interdiffusion of the embrittler atoms along grain boundaries can generate a stress field along the grain boundary, which acts as the thermodynamic driving force for diffusion. While this model attempts to describe the atomic-scale events involved in the early stages of LME, there is still lack of experimental evidence supporting the model, making it difficult to draw definitive conclusions.

In light of this, an atomic-scale experimental investigation of LME in the highly relevant Fe-Zn couple would be a progressive step toward unraveling this complex phenomenon. This chapter examines atomistic processes at grain boundary leading to the initiation of the LME crack and validates the proposed hypothesis of grain boundary (GB) interdiffusion as the most plausible mechanism for LME crack initiation. The results show that the interdiffusion of the Zn-embrittler atoms into the grain boundaries of the Fe-substrate led to the development of a stress-induced diffusion wedge that significantly affects the kinetics of interdiffusion, and the mechanical integrity of the grain boundaries being attacked by the liquid metal; ultimately leading to LME-induced crack initiation. This chapter is extremely relevant to the ongoing discussion on LME crack initiation events, with the results presented in this chapter providing some much-needed clarity to better understand this complex phenomenon. The present study

seeks to provide a deeper and more comprehensive understanding of the factors contributing to the onset of LME, offering important insights into developing potential strategies for eliminating LME in the Fe-Zn couple.

3.3 Material and method

3.3.1 Numerical modeling

A numerical model of a semi-infinite bicrystal, originally developed by Klinger and Rabkin [81], was used to study the interdiffusion process in the Fe-Zn binary system. The model assumes that diffusion occurs only through the GB, with bulk diffusion being neglected [81]. Due to the different GB diffusivities of Zn and Fe, their corresponding diffusion fluxes (shown as $J_{Zn}$and J_{Fe} in Figure 3.1) are also different. The divergence of diffusion fluxes leads to the insertion of a diffusion wedge (referred to as extra wedge material in [81]) as shown in Figure 3.1. Gao et al. [109] claimed that the diffusion wedge can be represented as an array of edge dislocations, which allows the stress at the GB to be calculated using Eshelby's analysis for edge dislocations near a surface. The analysis shows the build-up of a stress concentration at the tip of the diffusion wedge, acting as an effective contributor to the driving force for GB diffusion [80,81,110]. The wedge in the present study is referred to as a stress-induced diffusion wedge (SIDW), which emphasizes that it was formed as a result of the atomic GB diffusion.

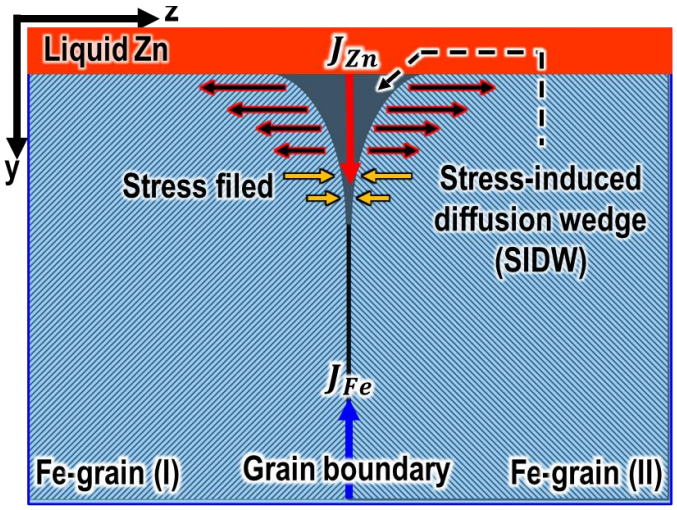

Figure 3.1 Schematic illustration of the Fe-Zn binary couple used; the inequality of diffusion fluxes ($J_{Zn}$and J_{Fe}) leads to the formation of a stress-induced diffusion wedge (SIDW). (W represents the width of the SIDW and S shows a schematic representation of the wedge-induced stress)

The chemical potential gradient is the driving force for diffusion. For a given binary system, the activity (a^i) is determined by the following equation:

$$\mu^i - \mu^0 = kT ln\, a^i \qquad \text{Equation 3.1}$$

Where μ^0 is the chemical potential of component i at the standard state (25 ºC and 1 atmospheric pressure), k is Boltzmann constant, and T is temperature. Herring [111] showed that in the presence of a stress gradient, diffusional flows move in directions that relieve the inequality of stress. In the presence of a normal stress (σ), the chemical potential of any atom of volume Ω would change as:

$$\mu^i - \mu^0 = kT ln\, a^i \pm \sigma\Omega \qquad \text{Equation 3.2}$$

The atomic fluxes along the GB are associated with the diffusion of Zn atoms into Fe-substrate (J_{Zn}) and the diffusion of Fe-atoms towards Zn (J_{Fe}) and can be represented as:

$$J_{Zn} = -\delta D_{gb}^{Zn} \frac{\partial C_{gb}^{Zn}}{\partial y} - \frac{\Omega \delta D_{gb}^{Zn}}{kT} C_{gb}^{Zn} \frac{\partial \sigma}{\partial y} \qquad \text{Equation 3.3 (a)}$$

$$J_{Fe} = -\delta D_{gb}^{Fe} \frac{\partial C_{gb}^{Fe}}{\partial y} - \frac{\Omega \delta D_{gb}^{Fe}}{kT} C_{gb}^{Fe} \frac{\partial \sigma}{\partial y} \qquad \text{Equation 3.3 (b)}$$

where, δ is the thickness of the GB, $C_{gb}^{i=Fe,Zn}$ is the GB concentration term, and $D_{gb}^{i=Fe,Zn}$ is the GB diffusivity term. It is assumed that GB diffusivities are independent of pressure (p) and concentration (C), e.g.:

$$\frac{\partial D(\sigma)}{\partial p} \equiv 0 \qquad \text{Equation 3.3 (c)}$$

$$\frac{\partial D(C)}{\partial C} \equiv 0 \qquad \text{Equation 3.3 (d)}$$

Based on Fick's second law, the GB concentration profile can be written as follows (see Appendix A for the complete derivation of the equation in supplementary materials):

$$\frac{\partial C_{gb}^i}{\partial t} = \delta D_{gb}^i \frac{\partial^2 C_{gb}^i}{\partial y^2} + \frac{\Omega \delta D_{gb}^i}{kT} \frac{\partial C_{gb}^i}{\partial y} \frac{\partial \sigma}{\partial y} + \frac{\Omega \delta D_{gb}^i}{kT} C_{gb}^i \frac{\partial^2 \sigma}{\partial y^2} \quad , i = Zn \text{ and } Fe \qquad \text{Equation 3.4}$$

To solve Equation 3.4, the stress profile along the GB, $\sigma(y,t)$ must be defined. Since the SIDW can be represented as a continuous array of edge dislocations [109], the normal traction at each position of y along the GB can be represented as [109]:

$$\sigma_{gb}(y,t) = E^* \int_0^\infty K(y,x) \frac{\partial w(x,t)}{\partial x} dx \qquad \text{Equation 3.5 (a)}$$

$$K(y,z) = \frac{1}{y-z} - \frac{1}{y+z} - \frac{2z(y-z)}{(y+z)^3} \qquad \text{Equation 3.5 (b)}$$

where, $E^* = \frac{E}{4\pi(1-\nu^2)}$ is the effective elastic modulus, E is Young's modulus, and ν is Poisson's ratio). It should be noted that the presence of SIDW with a width of w (x, y) must be taken into account in the diffusion equations (see Appendix A). Therefore, the GB concentration with the application of stress-induced interdiffusion is described as follows:

$$\frac{\partial C_{gb}^{Zn}}{\partial t} = \delta D_{gb}^{Zn}\frac{\partial^2 C_{gb}^{Zn}}{\partial y^2} + \frac{\Omega\delta D_{gb}^{Zn}}{kT}\frac{\partial C_{gb}^{Zn}}{\partial y}\frac{\partial \sigma}{\partial y} + \frac{\Omega\delta D_{gb}^{Zn}}{kT}C_{gb}^{Zn}\frac{\partial^2 \sigma}{\partial y^2} - C_{gb}^{Zn}\frac{\partial w}{\partial t} \quad \text{Equation 3.6 (a)}$$

$$\frac{\partial C_{gb}^{Fe}}{\partial t} = \delta D_{gb}^{Fe}\frac{\partial^2 C_{gb}^{Fe}}{\partial y^2} + \frac{\Omega\delta D_{gb}^{Fe}}{kT}\frac{\partial C_{gb}^{Fe}}{\partial y}\frac{\partial \sigma}{\partial y} + \frac{\Omega\delta D_{gb}^{Fe}}{kT}C_{gb}^{Fe}\frac{\partial^2 \sigma}{\partial y^2} - C_{gb}^{Fe}\frac{\partial w}{\partial t} \quad \text{Equation 3.6 (b)}$$

Equations 3.6 (a) and (b) are valid only when the SIDW grows with increasing time (i.e., $\frac{\partial w\,(x,y)}{\partial t} > 0$). This condition corresponds to $D_{gb}^{Zn} > D_{gb}^{Fe}$ (or J_{Zn}>J_{Fe}, which happens explicitly during the LME phenomenon). Assuming $C_{gb}^{Zn} + C_{gb}^{Fe} = 1$, we get:

$$\frac{\partial w\,(y,z)}{\partial t} = \delta\frac{\partial^2 C_{gb}^{Zn}}{\partial y^2}\left(D_{gb}^{Zn} - D_{gb}^{Fe}\right) + \frac{\Omega\delta}{kT}\frac{\partial C_{gb}^{Zn}}{\partial y}\frac{\partial \sigma}{\partial y}\left(D_{gb}^{Zn} - D_{gb}^{Fe}\right) + \frac{\Omega\delta}{kT}\frac{\partial^2 \sigma}{\partial y^2}\left(D_{gb}^{Zn}C_{gb}^{Zn} + D_{gb}^{Fe}C_{gb}^{Fe}\right) \quad \text{Equation 3.7 (a)}$$

$$\frac{\partial C_{gb}^{Zn}}{\partial t} = \left(D_{gb}^{Zn}C_{gb}^{Fe} + D_{gb}^{Fe}C_{gb}^{Zn}\right)\frac{\partial^2 C_{gb}^{Zn}}{\partial y^2} + \frac{\Omega\left(D_{gb}^{Zn}C_{gb}^{Fe} + D_{gb}^{Fe}C_{gb}^{Zn}\right)}{kT}\frac{\partial C_{gb}^{Zn}}{\partial y}\frac{\partial \sigma}{\partial y} + \frac{\Omega C_{gb}^{Zn}C_{gb}^{Fe}\left(D_{gb}^{Zn} - D_{gb}^{Fe}\right)}{kT}\frac{\partial^2 \sigma}{\partial y^2} \quad \text{Equation 3.7 (b)}$$

The following dimensionless variables were used to solve Equation 3.7:

$$W = \frac{w}{\delta} \quad \tau = \frac{D_{gb}t}{L^2} \quad Y = \frac{y}{L} \quad Z = \frac{z}{L} \quad S = \frac{\sigma\Omega}{kT} \quad L = \frac{\delta\Omega E^*}{kT} \quad \text{Equation 3.8}$$

where W is the dimensionless width of the SIDW (see Fig. 1), S is the dimensionless stress distribution along the GB, and τ represents time. Equation 3.8 was substituted into Equation 3.5 and Equation 3.7 to obtain the following set of equations representing the width of the SIDW, GB concentration, and the wedge-induced stress as a result of Zn atoms diffusing into the Fe-substrate GB:

$$\frac{\partial W}{\partial \tau} = (1 - \theta)\frac{\partial^2 C_{gb}^{Zn}}{\partial Y^2} + (1 - \theta)\frac{\partial C_{gb}^{Zn}}{\partial Y}\frac{\partial S}{\partial Y} + (C_{gb}^{Zn} + \theta C_{gb}^{Fe})\frac{\partial^2 S}{\partial Y^2} \quad \text{Equation 3.9 (a)}$$

$$\frac{\partial C_{gb}^{Zn}}{\partial \tau} = \left(C_{gb}^{Fe} + \theta C_{gb}^{Zn}\right)\frac{\partial^2 C_{gb}^{Zn}}{\partial Y^2} + \left(C_{gb}^{Fe} + \theta C_{gb}^{Zn}\right)\frac{\partial C_{gb}^{Zn}}{\partial Y}\frac{\partial S}{\partial Y} + C_{gb}^{Zn} C_{gb}^{Fe}(1 - \theta)\frac{\partial^2 S}{\partial Y^2} \quad \text{Equation 3.9 (b)}$$

$$S(Y,\tau) = \int_0^{\infty} K(Y,X)\frac{\partial W(X,\tau)}{\partial X} dX \quad \text{Equation 3.9 (c)}$$

$$K(Y,Z) = \frac{1}{Y - Z} - \frac{1}{Y + Z} - \frac{2Z(Y - Z)}{(Y + Z)^3} \quad \text{Equation 3.9 (d)}$$

where $\theta = D_{gb}^{Fe}/D_{gb}^{Zn}$, which defines the ratio between GB diffusivity of Fe relative to Zn. Equations 3.9 (a)-(d) were solved numerically using the finite difference method as described in detail in Appendix *B*.

3.3.2 Experimental procedure

An austenitic stainless steel (AISI 304) with a chemical composition of 0.08C-2.00Mn-0.75Si-(8-12)Ni-(18-20)Cr (wt.%)) and a thickness of 1.0±0.1 mm was used in this study. The as-received stainless steel was Zn-coated with an average thickness of 10 µm through an electro-galvanizing process. The LME cracks were induced by thermomechanical processing using a high-temperature uniaxial tensile test carried out on a Gleeble 3500 thermomechanical simulator machine under standard atmospheric conditions, referred henceforth as hot-tensile tested (HTT) samples. Copper (Cu)-grips were used to hold the tensile samples at high temperature and the temperature of the samples was controlled by the K-type thermocouple welded at the center of the samples. More comprehensive details regarding the preparation of the tensile test samples can be found elsewhere [12]. The HTT samples were heated to the target temperature of 800 °C at a heating rate of 1000 °C/s and held at that temperature for 0.5 s before subjecting the sample to a tensile load, with a constant crosshead speed of 1 mm/s. The HTT process parameters including temperature, heating rate, and holding time were selected to replicate the most severe thermomechanical conditions encountered in the Fe-Zn LME [89]. To study LME initiation, the HTT samples were interrupted right before failure was initiated. The interrupted samples were cut using a high-precision metallurgical saw and prepared for microstructural examination. The electron transparent lamellae were cut parallel to the grain boundaries using the focused ion beam (FIB) Thermo scientific Helios G4 PFIB machine. The atomic-scale investigation of the FIB-milled electron transparent lamellae specimen was carried out using high-resolution transmission electron microscopy (HRTEM) and energy-dispersive X-ray spectroscopy (EDS) on the FEI Titan 80-300 HB double aberration-corrected TEM system.

3.4 Results

3.4.1 Numerical modeling of the interdiffusion process

Figure 3.2 illustrates the calculated width of the SIDW (Figure 3.2 (a)), the wedge-induced stress (Figure 3.2 (b)), and the GB concentration profiles (Figure 3.2 (c)) at various (non-dimensional) times, τ. It is clear that the width of the SIDW increases with increasing time as seen in Figure 3.2 (a). It has been suggested that the concentration of embrittler atoms at the base of the SIDW can reach the solubility limit in the GB, which implies that the SIDW shares a coherent atomic structure with its surrounding bulk at the initial stage of the interdiffusion process [80]. This is in agreement with the results on the Al-Ga couple where it was found that the Ga atoms (acting as the embrittler) did not affect the atomic structure of the GB in the Al matrix [112]. As the SIDW grows to a critical size such that the concentration of embrittler atoms exceeds the solidus concentration, the SIDW melts [80]. This occurrence is similar to the analogous scenario described by Gordon and An [78] who referred to this phenomenon as the "incubation time" before the onset of LME. The incubation time was experimentally observed in the Al-Ga couple in which it was found that there was a variable delay between the time the sample reached the melting temperature of Ga and the detection of its first traces in the GB (ranging from about 120-180 s) [113]. In the Fe-Zn system, the LME-induced failure process occurs within a very short period of time (less than 1-2 seconds [91]), which makes it extremely challenging to determine the incubation period experimentally. However, the calculations of incubation time and SIDW thickness will be discussed in the next section.

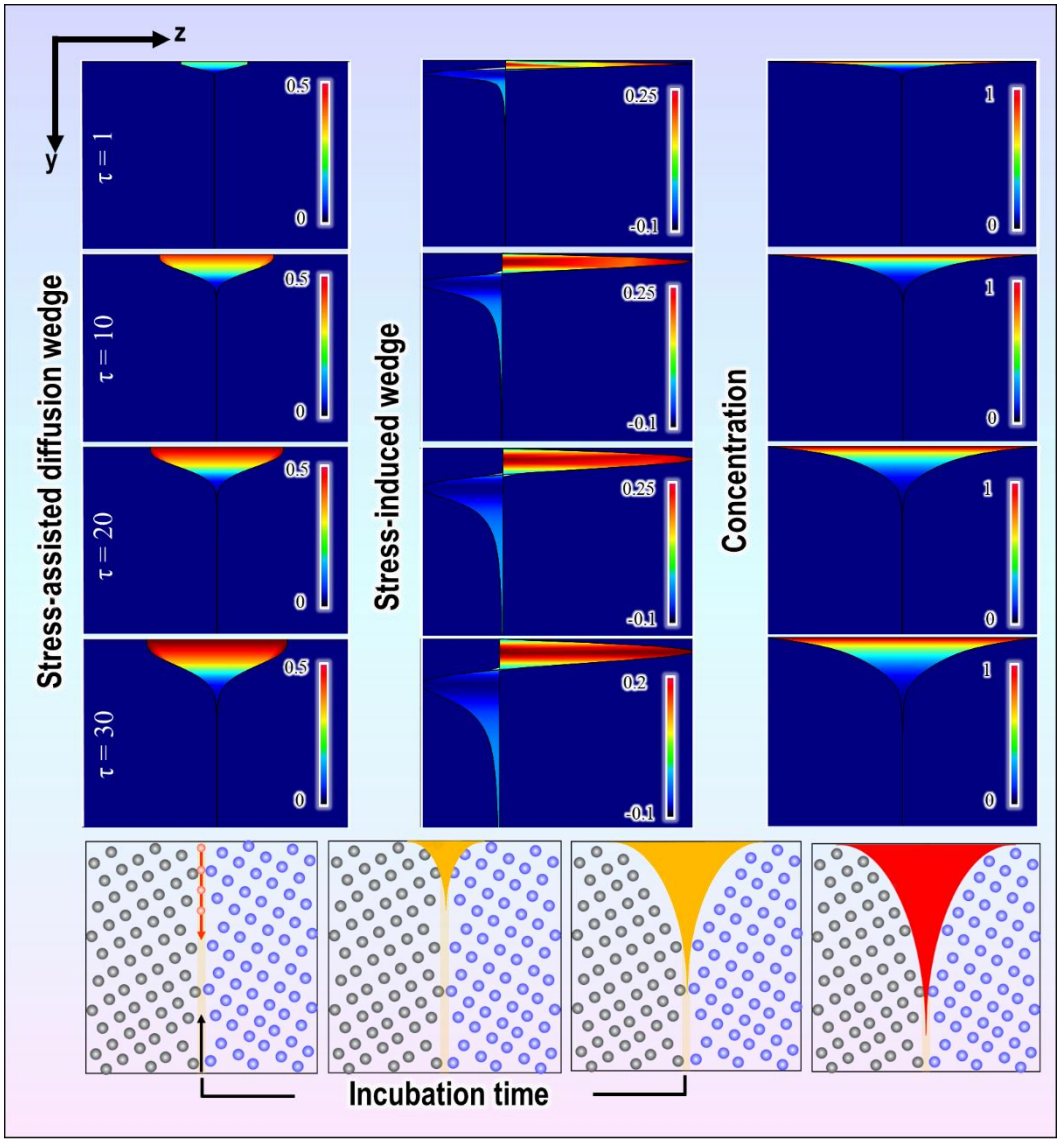

Figure 3.2 The calculated width of the stress-assisted diffusion wedge (SIDW), generated stress field, and grain boundary concentration at various non-dimensional times ($\tau = 1 - 30$) for the grain boundary ratio $\theta = 0.1$ (The $\theta = D_{gb}^{Fe}/D_{gb}^{Zn} < 1$ indicates that $D_{gb}^{Zn} > D_{gb}^{Fe}$ (or J_{Zn}>J_{Fe}) which happens explicitly during the LME phenomenon). The formation of the SIDW resulted in the generation of a sinusoidal stress field with both tensile and compressive components acting along the length of the grain boundary. The schematic representation provides an understanding of the incubation time prior to the initiation of the LME crack. The time period between the start of atomic grain boundary diffusion and the melting of the stress-assisted diffusion wedge is considered the incubation time prior to LME crack initiation.

The formation of the SIDW resulted in the generation of a sinusoidal stress field with both tensile and compressive components acting along the length of the GB, as shown in Figure 3.2 (b). The tensile stress acts near the surface, while the compressive stress acts closer to the tip of the SIDW. Over prolonged times, as the size of the wedge increases, the magnitude of the compressive stress tends to decrease. The results also show the changes in the GB concentration profile (Figure 3.2 (c)), with the GB concentration of the embrittler atoms increasing as time

increases. This trend is a clear indication of an increased amount of embrittler atoms diffusing into the GB.

The depth of the GB under stress is another geometrical characteristic of the SIDW that affects the interdiffusion process. The GB depth under tension is a representation of the length of the SIDW, which is determined by the point of zero stress and the crystal surface (Figure 3.3 (a)). Figure 3.3 (b) illustrates the variation in the normalized length of the SIDW ($L_{Tensile}/L$) at different times. It is evident that $L_{Tensile}/L$ follows a parabolic behavior with increasing time, clearly indicating that the tensile stress zone is initially confined to the bulk Fe matrix, progressively pulling it apart to facilitate the diffusion of the Zn-embrittler atoms into the Fe GB.

The applied tensile stress during interdiffusion along the GB plane was calculated using Equation 3.8 for a common Fe-based alloy with $E = 190\ GPa$, $\nu = 0.33$, $\Omega = 10^{-29}\ m^3$, and for different temperatures ranging from 500K to 900K. The variation of maximum tensile stress with D_{gb}^{Fe}/D_{gb}^{Zn} at different temperatures has been shown in Figure 3.3 (c). The maximum tensile stress acting on the GB increases rapidly with decreasing the value of D_{gb}^{Fe}/D_{gb}^{Zn} less than 0.001, but it remains relatively constant for values of D_{gb}^{Fe}/D_{gb}^{Zn} less than 0.001. Furthermore, the results show that as the temperature increases, the magnitude of the tensile stress increases for the same value of D_{gb}^{Fe}/D_{gb}^{Zn}. Klinger and Rabkin [81] proposed that the generated stresses induced by the interdiffusion process were sufficiently high to cause crack initiation at the GB. The results presented in this study validate the original hypothesis and therefore, we can conclude that LME is, in fact, initiated due to GB diffusion, leading to the formation of a SIDW that causes the subsequent crack initiation event.

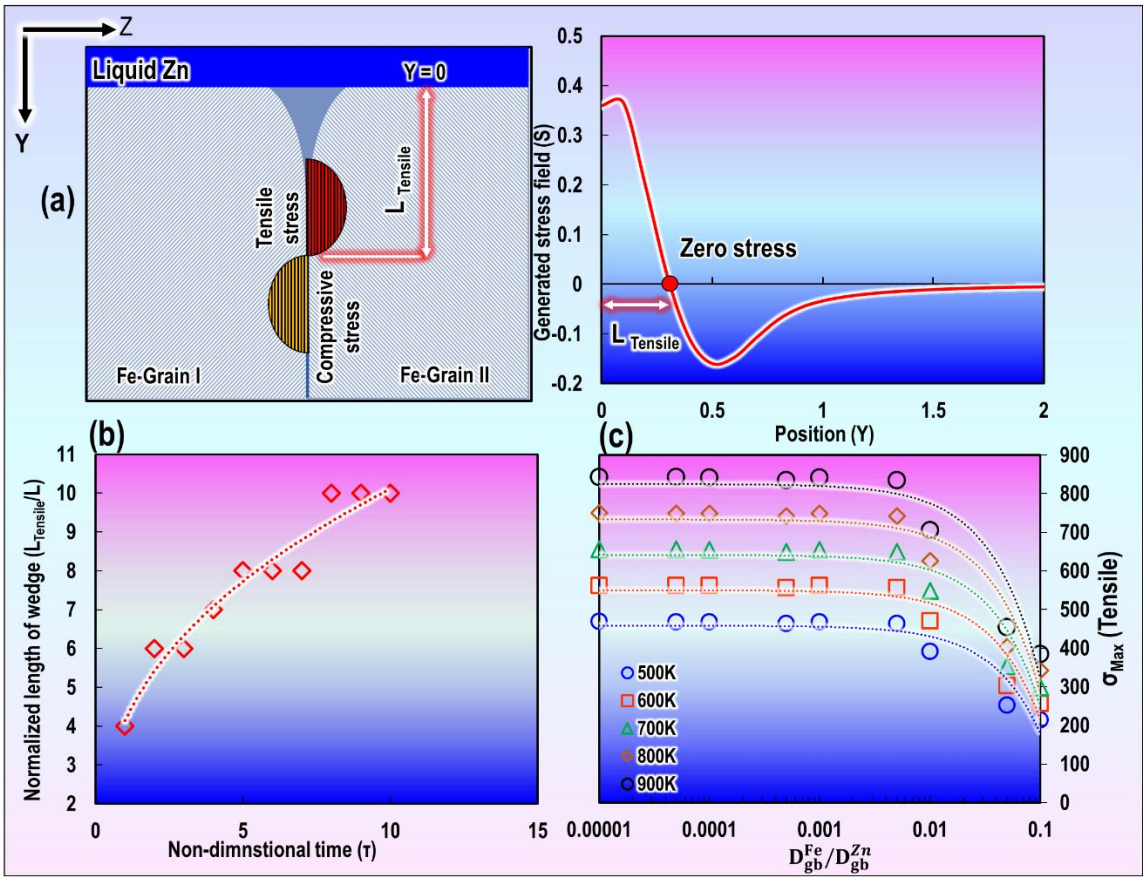

Figure 3.3 (a) Schematic illustration of the Fe-Zn binary couple along with the calculated stress field as a function of position (Y axis) at non-dimensional time of $\tau = 5$ and grain boundary coefficient ratio of $\theta = D_{gb}^{Fe}/D_{gb}^{Zn} = 0.1$. The grain boundary under tension is a representation of the length of the stress-assisted diffusion wedge ($L_{Tensile}$) and is determined by the point of zero stress and the crystal surface, (b) Variation of the normalized length of stress-assisted diffusion wedge ($L_{Tensile}/L$) with non-dimensional time, and (c) The calculated maximum tensile stress acting on the grain boundary plane with respect to grain boundary coefficient ratio ($\theta = D_{gb}^{Fe}/D_{gb}^{Zn}$) for a common Fe-based for different temperatures ranging from 500K to 900K.

3.4.2 HRTEM analysis of the Zn-penetrated grain boundaries

The TEM micrographs along with the high-angle annular dark-field (HAADF) image and the corresponding Zn-EDS map of the initial stages of Zn penetration into the GBs of steel substrate are shown in Figure 3.4 (a)-(c). The first region of interest (identified as (I) in Figure 3.4 (c)) was associated with the point of initiation of LME cracking when the wedge had been filled with liquid Zn, but it had not resulted in bulk liquid penetration into the GB. In the second region (identified as (II) in Figure 3.4 (c)), Zn had completely penetrated into the GB, and LME had been fully realized.

Figure 3.4 (d) and (e) show that the interface between the Zn and Fe has a clear wedge-shaped profile. Figure 3.4 (e) also shows the corresponding fast Fourier transformation (FFT)

diffractogram from the tip of the pre-penetration wedge (labeled as (III)). The inverse Fourier filtered transformation (IFFT) image shown in Figure 3.4 (e), identifies the lattice fringes from the corresponding region. The IFFT image indicates that the tip of the pre-penetration wedge shows a significant degree of lattice distortions with an array of lattice dislocations (shown with the "⊥" symbol). The HRTEM observations of the earliest stage of LME onset are important because they allow the identification of a relationship between the experimentally observed wedge and that discussed in the numerical modeling section.

The root cause for the formation of the SIDW is the difference in diffusion fluxes between the Zn and the Fe which causes the solid wedge to form at the exposed GBs of the substrate [80,81,109]. The matrix of SIDW loses its coherency as it becomes larger (i.e., approaches a critical size), while at the same time, the presence of the notch at the tip of the wedge, intensifies the effect of the tensile stress across the length of the GB. As the cohesiveness of the structure is compromised by the increased embrittler content in the wedge, LME is initiated as the liquid metal is able to quickly penetrate along the GB. Similar results have been reported in the atomic-resolution TEM analysis of LME in the Al-Ga system, which revealed that a critical thickness of solid-state embrittler atoms (at least a double monolayer of Ga) was required for liquid metal to penetrate the GB [112], similar to the critical size of the wedge being proposed in this study. Ludwing et al. [113] studied the in-situ GB penetration in the Al-Ga couple and observed that the liquid Ga penetration layer had an almost wedge-like shape with an opening angle of a few 10^{-5} rad. The MD simulation in the Al-Ga couple indicated that the interaction between external stresses and Ga penetration causes a chain of dislocations to form that climb down the GB at a relatively constant rate [10,114].

Interestingly, there is a striking resemblance between the shape of the SIDW and the GB groove [80]. The thermodynamic driving force (F_D) responsible for the formation of the GB groove is the reduction of the total GB area (i.e., $\mathrm{F_D} = \gamma_{\mathrm{GB}} - 2\gamma_{\mathrm{SL}}$) where γ_{GB} is the GB interface energy and γ_{SL} is solid/liquid surface energy [113]. When $2\gamma_{SL} < \gamma_{GB}$, spontaneous GB penetration is thermodynamically favorable, leading to GB replacement by liquid metal [54]. This means that liquid metal may penetrate along the GBs even in the absence of extrinsic stress, as observed in the Al-Ga system [115]. In the case where $2\gamma_{SL} > \gamma_{GB}$ (i.e., Fe-Zn system) [54], the replacement of the GB by a liquid film is not energetically favorable, resulting in an energy barrier for cracking. Glickman [73] proposed the grooving accelerated by local plasticity (GALOP) model where macro LME cracks are formed by a series of repetitive "grooving-blunting" events. In the Fe-Zn system, however, experimental observations revealed no dislocation activity or plastic deformation at the LME crack tip [21,65], which makes it clear that the formation of the GB groove does not lead to the onset of the LME crack.

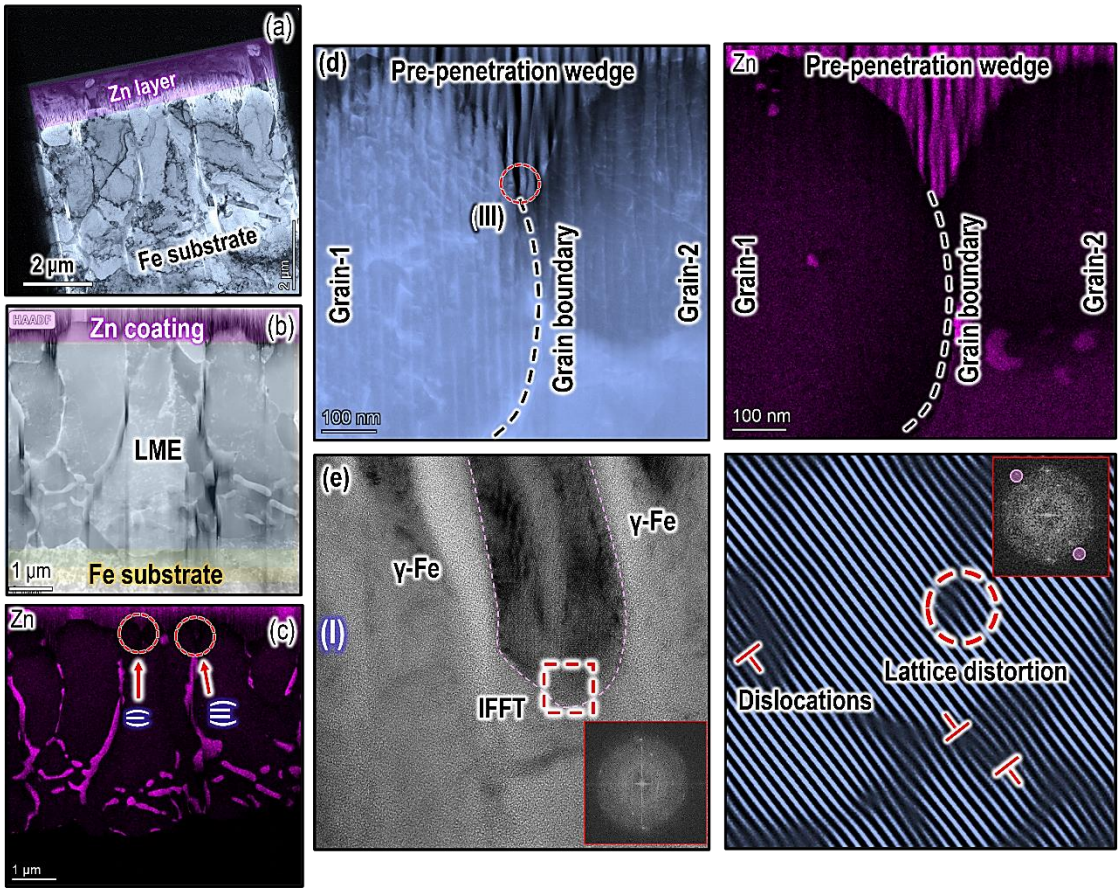

Figure 3.4 (a) TEM micrograph of the electron transparent lamellae from the interrupted high-temperature tensile test specimen showing three main regions including Zn coating, liquid metal embrittlement (LME) region, and Fe substrate, (b) high-angle annular dark-field (HAADF) image along with (c) Zn-EDS map showing the Zn penetration along grain boundaries; two regions were selected for high-resolution transmission electron microscopy (HRTEM) analysis, (d) the corresponding TEM micrograph along with Zn-EDS map of the "(I): pre-penetration wedge" at the earliest stage of LME initiation when the grain boundary of Fe-substrate has not been intact; Region (III) was selected for HRTEM analysis as indicated in the TEM micrograph, (e) the corresponding HRTEM of the region (III) along with fast Fourier transformation (FFT) diffractogram and the inverse Fourier filtered transformation (IFFT) image which shows the lattice fringes from the corresponding region demarcated by the red box (The IFFT image was obtained by applying the filter masks on the diffraction spots).

The representative TEM micrograph and the corresponding EDS-Zn map of the Zn-penetrated GB (region (II) in Figure 3.4 (c)) are presented in Figure 3.5 (a) along with the HRTEM micrograph and the FFT diffractogram and IFTT lattice image corresponding to the tip of the Zn-penetrated GB shown in Figure 3.5 (b). A high degree of lattice distortion and a high density of lattice dislocations can be clearly seen at the tip of the penetration area. The HRTEM analysis of the interface between the Zn-penetrated GB and the γ-Fe grain is shown in Figure 3.5 (c). The IFFT image of the Fe-Zn interface clearly shows the incoherency in the lattice caused by the penetration of Zn into the GBs, leading to the subsequent decohesion of

the GB structure which inevitably reduced the strength of the matrix, making it highly susceptible to intergranular cracking. The results offer definitive proof that the SIDW is, in fact, a precursor to the penetration of liquid Zn into Fe grain boundaries and the root cause for the initiation of LME.

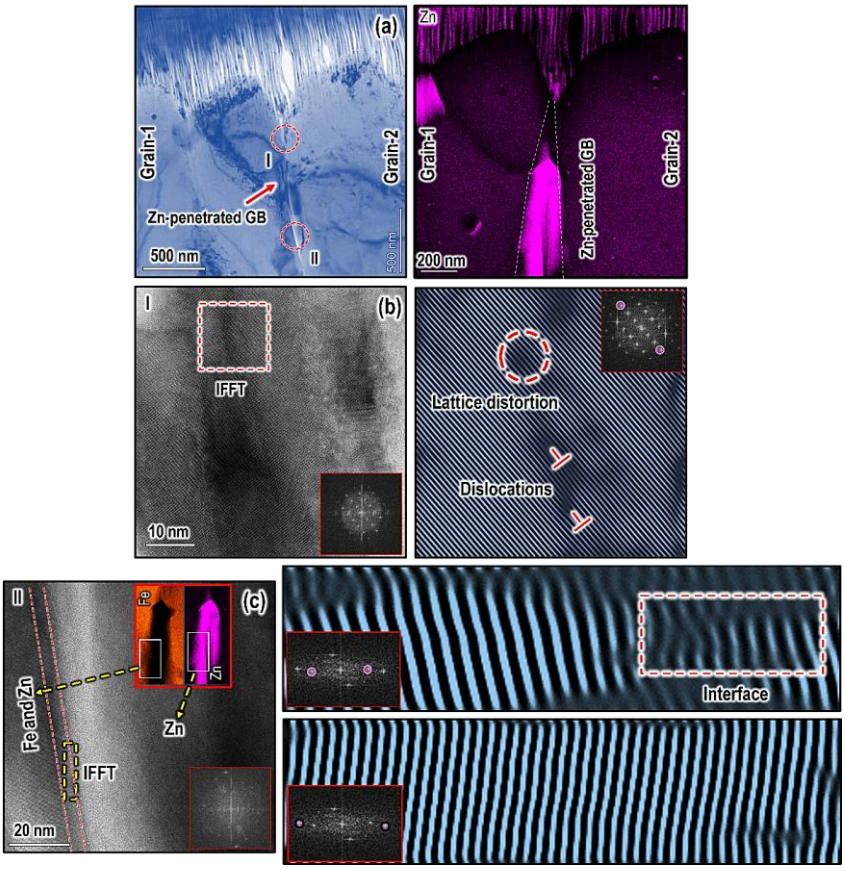

Figure 3.5 (a) TEM micrograph along with Zn-EDS map of the Zn-grain boundary penetrated (see the region "(II): Zn-penetrated grain boundary" in Fig. 3 (c)) when LME has been fully initiated. Two regions were selected for atomic-scale HRTEM analysis as indicated by (I): the tip of the Zn-penetrated grain boundary and (II): the interface between the Zn-penetrated grain boundary and the Fe substrate, (b) HRTEM micrograph alongside the fast Fourier transformation (FFT) diffractogram and the inverse Fourier filtered transformation (IFFT) lattice image corresponding to the tip of the Zn grain boundary penetration (region (I)), (c) The HRTEM analysis of the interface between the Zn-penetrated grain boundary and the Fe grain (region (II)). The FFT diffractogram reveals two sets of diffraction spots corresponding to Fe and Zn at the interface.

3.5 Discussion

This work provides novel insights into the atomic-scale events leading to the initiation of LME cracking in the Fe-Zn system. The schematic illustration of the LME crack initiation events is shown in Figure 3.6. The liquid Zn coating and solid Fe-substrate are initially subjected to external tensile stress at a high temperature, which provides the additional driving

force needed for greater interdiffusion of Zn atoms towards the Fe-substrate by the stress-assisted GB diffusion mechanism.

In the first stage of LME initiation, a SIDW is formed by way of interdiffusion at the exposed surface of the substrate along the GB, as shown by the schematic illustration of the LME crack initiation events in Figure 3.6. The SIDW becomes larger and begins to reach a critical size whereby losing its structural coherency. Melting occurs when the concentration of embrittler atoms in the SIDW exceeds the solidus concentration [80]. The transition from the formation of the solid SIDW to its eventual melting is a complicated phenomenon due to the microscale nature of the solid wedge. The current model, however, can be used to approximate the critical size of the wedge before its melting. According to the calculated phase diagram for the Fe-Zn binary system, the Zn solidus concentration at 800 °C (see experimental methodology section) is approximately 40 wt.% (~36 at.%) [116], which is the Zn content needed to ensure complete melting of the SIDW. The length of the SIDW (c.f. Figure 3.3 ($L_{Tensile}$)) was considered as the point at which the Zn content reaches the critical concentration required for the melting of the wedge.

The concentration profile was calculated for the common Fe-based alloy with $D_{gb}^{Zn} = 7.51 \times 10^{-12}\ m^2/s$ at 725 ˚C [117] using Equation 3.8 as shown in Figure 3.7 (a) in which the length of the SIDW is indicated by dashed lines. The SIDW does not reach a critical concentration of Zn required for melting when the exposure time is less than 188 ms. Upon exceeding this time threshold, the results show that sufficient Zn accumulates in the solid wedge, which results in the melting of the wedge. Due to the relative volume of the wedge compared to the volume of the surrounding substrate and the Zn layer, it can be assumed that the melting of a portion of the wedge implies that the entire wedge has melted.

The time interval between the formation of the wedge and its melting corresponds to the incubation time, as shown schematically in Figure 3.6. Despite the rough estimation of the incubation time, the results are quite consistent with the experimental observations made in the Fe-Zn system where the LME-induced failure occurs within less than 1-2 s [91], in contrast to the delayed failure observed in other LME systems [80].

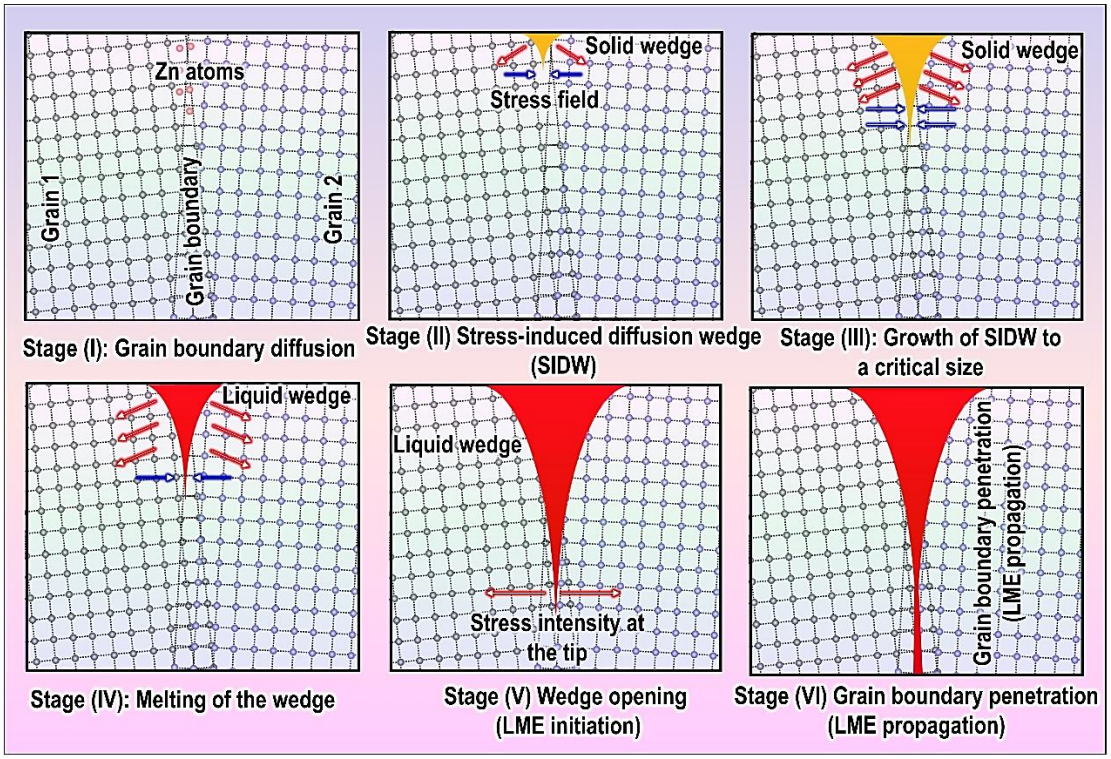

Figure 3.6 Schematic illustration of mechanisms leading to LME crack initiation; Due to the inequality of diffusion fluxes during Zn diffusion into the Fe-substrate grain boundary, a stress-induced diffusion wedge (SIDW) is formed at the grain boundary. The formation of the SIDW generates a sinusoidal stress field along the grain boundary plane. As the SIDW becomes thicker and deeper, it loses its coherency, resulting in the SIDW melting. The tensile stress is applied near the Fe/Zn interface leading to the wedge opening, while the wedge retains its wedge-shaped profile due to the presence of compressive stresses at the tip. This stage is known as the LME crack initiation stage. The further penetration of the liquid metal into the deep area of the GB will then cause LME propagation.

The maximum width of the SIDW (i.e., $w\ (y = 0, t)$) at various times was also calculated as shown in Figure 3.7 (c). The results confirm that it is impossible for the width of the SIDW to exceed the thickness of the GBs [80]. This is completely reasonable given that the present model is based on Fisher's GB model [85], in which the thickness of the GB is assumed to be independent of time and temperature [80,81]. In contrast, the maximum wedge width observed in the HRTEM micrograph is considerably larger (~400 nm according to Figure 3.4) than that predicted by the theoretical model. This apparent inconsistency in the predicted and experimentally observed size of the wedge is not unusual as can be seen in the Al-Ga case [113] where the wedge observed using in-situ TEM analysis was much larger than the size that was predicted numerically. One possible explanation for this difference between theoretical and experimental measurements is the role of stress on the width of the wedge. The stresses generated during interdiffusion are sufficient to cause phenomena like plastic deformation [118], creep [119], and bending [120].

The application of the tensile stress near the Fe/Zn interface can lead to the formation of the wedge, which retains its wedge-shaped profile due to the presence of compressive stresses present at its tip (Figure 3.7 (d)). The externally applied tensile stress also contributes to the widening of the wedge. It should be noted that due to the rapid formation of SIDW with only a few monolayers of embrittler atoms, atomic-scale characterization techniques, such as in-situ HRTEM, are not feasible as they are unable to detect the formation of an ultra-thin solid wedge. Nevertheless, the wedge-shaped penetration layer observed in this study offers concrete evidence to support the hypothesis that the formation of a diffusion-induced wedge is a prerequisite for the initiation of LME. The pre-penetration wedge, shown in the HRTEM micrographs, is formed due to the presence of the tensile stress and the high content of embrittler atoms in the wedge. As the wedge grows larger – approaching a critical size – its coherency is compromised leading to the eventual melting of the wedge, which is the official initiation of LME that can finally result in the aggressive penetration of liquid metal from the surface into the GBs.

Further penetration of the liquid metal into the GBs will then cause the cracks to propagate throughout the microstructure, with the tip of the wedge acting as a sharp notch which increases the stress intensity factor (K_I) at the tip higher than the threshold stress intensity required for crack formation ($K_{I,\ Th}$) [113], whereby contributing to crack nucleation at the GB and facilitating liquid metal penetration into the substrate. Interestingly, the mechanism discussed here also has philosophical implications for LME crack formation theory according to the classical Griffith framework, whose theory of fracture mechanics states that crack initiation is associated with the creation of free surfaces [109]. A fracture criterion is defined as a balance between the strain energy released at the crack tip and the surface energy required for the creation of the new surfaces, such that the surface energy becomes a dominant component of the energy balance. Due to the wedge-shaped profile and its associated stress distribution, it is straightforward to conclude that crack nucleation is more energetically favorable in the presence of a wedge compared to a flat surface [109].

The mechanisms described here offer much needed insights into unresolved issues regarding the LME initiation mechanism in the Fe-Zn system. The present model shows that the LME initiation mechanism involves multiple steps starting with solid-state diffusion along the exposed GBs at the liquid Zn and solid Fe-substrate interface, followed by the formation of a wedge-shaped profile that grows to a critical size, triggering crack nucleation at the GB, which results in the bulk penetration of liquid Zn into the Fe-substrate. The models described here are capable of explaining the experimental observations as they incorporate both solid-state diffusion [65,79,89] and direct liquid metal penetration [21,38,65,90] along the GB. This study, therefore, offers a unified explanation for the initiation of LME in the Fe-Zn system by discussing both solid-state diffusion and liquid metal penetration scenarios.

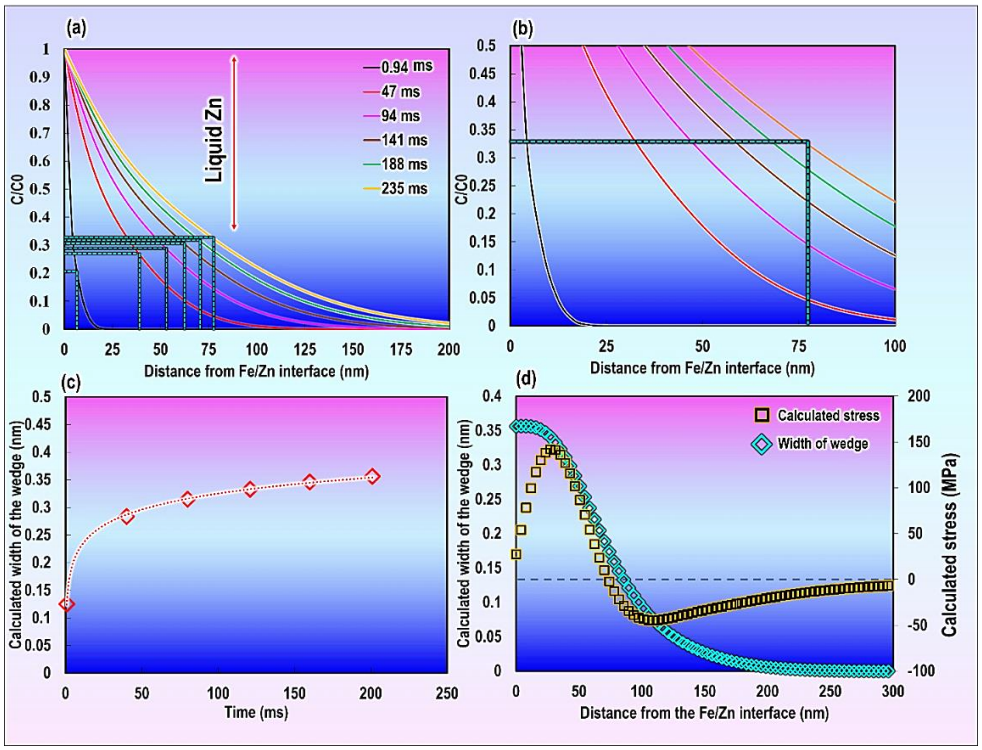

Figure 3.7 (a) The calculated concentration profile for the common Fe-based alloy. The length of the stress-induced diffusion wedge ($L_{Tensile}$) was considered as the point at which the Zn content reaches the critical concentration required for the melting of the wedge, which is indicated by dashed lines, (b) An enlarged section of the diagram of the grain boundary concentration at 201 ms, (c) the calculated width of the stress-induced diffusion wedge (SIDW) over various times, indicates that it never exceeds the thickness of the grain boundary, (d) the calculated stress and width of the SIDW at time of 201 ms.

3.6 Summary

In this chapter, numerical modeling and atomic-scale experimental analysis were used to provide insights into the atomic-scale events describing the initiation of LME in the Fe-Zn couple. This work provided experimental evidence for the stress-assisted grain boundary interdiffusion model as the precursor leading to LME initiation. The results revealed that LME initiation entails several steps, including (i) solid-state GB diffusion, (ii) formation of the stress-induced diffusion wedge (SIDW), (iii) melting of the SIDW after reaching a critical size, and (iv) opening of the liquid wedge due to interdiffusion and the application of externally applied stresses. The tip of the wedge acts as a sharp notch which increases the stress intensity at the GB, further facilitating the penetration of Zn at the GB. The results of this study are a crucial step in understanding the fundamental complexities associated with the LME phenomenon in the Fe-Zn couple.

Chapter 4 : Crack susceptibility and failure mechanism of zinc-assisted liquid metal embrittlement in ferritic and austenitic steels[1]

4.1 Overview

The theoretical models that have been developed to explain the micro-scale events that lead to the LME are unable to provide a clear explanation of the mechanism of LME crack propagation once the crack has been initiated. This lack of knowledge makes it significantly complicated to analyze the effect of initial microstructure on LME susceptibility and failure mechanism for the iron-zinc (Fe-Zn) system. Thus far, research activities on the role of microstructure on LME susceptibility have either provided conflicting results or failed to establish any correlation between crack susceptibility and the failure mechanism. In this chapter, steels with fully ferritic and austenitic microstructures were subjected to the same thermomechanical processing treatment to gain insight into how relevant features of the initial microstructure such as grain boundary distribution and local chemistry influence LME crack susceptibility and failure mechanism. The results showed that both ferritic and austenitic microstructures were sensitive to the LME crack formation. The ferritic microstructure was more prone to LME crack initiation with relatively low LME crack propagation rate resulting in a much higher frequency of smaller cracks observed in the sample. The austenitic microstructure was resistant to crack initiation but had a significantly higher LME crack propagation rate resulting in fewer cracks which were much larger in size. This led to the occurrence of a hybrid ductile/brittle type failure in the ferritic microstructure but a completely intergranular brittle failure in the austenitic sample. The results offer clear evidence of LME crack susceptibility in ferritic and austenitic steels, which can be used to guide microstructural modification strategies when developing novel methods to eliminate Zn-assisted LME cracking in steels.

4.2 Background

LME is a complex phenomenon; at present, there is no unified explanation for the crack propagation mechanism, especially on an atomic scale [54]. Over the last few decades, several models were proposed to explain the occurrence mechanism of this abnormal phenomenon as discussed in Chapter 2. Despite a rich body of literature on the subject, the underlying mechanism for LME crack propagation remains unclear. Regarding LME in the Zn-coated steels, there is currently no clear understanding of the mechanism by which liquid metal quickly penetrates the grain boundaries of the steel substrate through the nanosized crack tip originating at the steel-coating interface. In some studies, the emphasis was placed on the atomic grain

[1] This chapter consists of the published manuscript in Materials Characterization, Ali Ghatei-Kalashami, M. Shehryar Khan, Frank Goodwin, and Y. Norman Zhou, Vol. 195, 2023.

boundary diffusion mechanism [41,65,79,89], while others provide some evidence in support of the mass transport along grain boundaries [21,38,65,90]. As a result, the mechanism of LME crack propagation has been clouded by several contradictory and divergent hypotheses, with very little experimental support to offer any additional clarity. Consequently, an understanding of crack propagation during LME requires a detailed experimental analysis, investigating the crack path from a macroscopic, microscopic, and atomic perspective. Despite the significant challenges of observing the in-situ atomistic processes occurring at the LME crack tip [113], a detailed analysis of the LME crack path and its relationships to metallurgical characteristics would offer invaluable insights into the accuracy of the proposed theoretical mechanisms that may be involved in the LME process in the Fe-Zn system.

The metallurgical features of the steel substrate such as initial microstructure, grain boundary characteristics, and chemical composition of the alloy play a critical role in controlling LME crack propagation [22]. However, experimental studies have produced contradictory findings regarding the influence of initial microstructure on LME cracking and the resulting impact on mechanical properties. Generally, the effect of metallurgical features on LME susceptibility in the Fe-Zn system (e.g., initial microstructure or different content of alloying elements) is assessed by either quantitative crack analysis (i.e., crack number and crack length) [45,104] or by the holistic effect of LME on the degradation of tensile properties (i.e., loss of ductility) [97]. While it is obvious that LME-induced failure analysis is an excellent indicator of the LME crack propagation mechanism [54], this aspect has not been extensively examined in the literature for the Fe-Zn system, due to the many metallurgical features that may affect the LME crack propagation mechanism.

There is a lack of correlation between LME crack characteristics, mechanical properties, and failure behavior in the literature, which has made it challenging to investigate the role of metallurgical features on LME cracking susceptibility in the Fe-Zn system. For example, it has been reported that LME occurs only in the austenitic microstructures during the hot stamping of Zn-coated boron steels [28], which has led to conclusions that LME cracking may be eliminated by using steel substrates that have a ferritic microstructure at higher temperatures during hot-stamping [7]. Although austenite-containing microstructures have been frequently reported as the most susceptible to LME cracking [47,65], recent research has found that increasing decarburization depth (i.e., increasing the ferritic layer) leads to greater LME susceptibility in dual phase (DP) steels [45]. The presence of LME in the fully ferritic decarburized layer was also confirmed more recently during RSW of quench and partitioned (Q&P) steels [102,103]. Furthermore, in a recent study, it was shown that a fully ferritic microstructure is quite sensitive to LME cracking, as evidenced by the high number of LME cracks observed during the RSW process [22]. Bhattacharya et al. [97] compared the LME cracking behavior in different initial microstructures including martensitic, Q&P, TRIP-assisted

bainite-ferrite (TBF), and ferritic-martensitic steels during high-temperature tensile testing and concluded that the degree of LME severity was not significantly affected by microstructural components such as retained austenite or carbide-free bainite. Based on the literature it is clear that a comprehensive and rigorous understanding of the influence of the initial microstructure on LME crack susceptibility is necessary for the full understanding of the responsible mechanisms for LME crack propagation in the two main allotropes of Fe: alpha iron (α-Fe) and gamma iron (γ-Fe), i.e., analyzing the LME cracking behavior in fully ferritic and austenitic microstructures. This type of study holds the promise to facilitate the development of strategies that will mitigate and eliminate LME in the Fe-Zn system.

Therefore, the purpose of this chapter is to provide a detailed experimental investigation covering two critical aspects of LME in the Fe-Zn system that remain unexplored in the literature. This study offers a thorough examination of the sensitivity of LME crack formation to microstructural characteristics in fully ferritic and austenitic microstructures and presents a new perspective on defining LME susceptibility by correlating quantitative characteristics of cracks with the associated failure mechanism. The comprehensive discussion based on the results of this study illuminates the potential crack propagation mechanism during LME in fully ferritic and austenitic microstructures. Furthermore, this study discusses how proposed theoretical models can accurately predict a unified crack propagation mechanism in light of different Fe-substrates' metallurgical characteristics. The results of this section not only provide a detailed understanding of the LME crack propagation mechanism in the Fe-Zn system but also disclose the impact of metallurgical factors on the LME crack propagation path by providing a definitive definition of the LME crack susceptibility. Consequently, this study opens the pathway to developing LME-resistant Fe-Zn couples that are effective under different hot working conditions.

4. 3 Materials and methods

The as-received materials investigated in this study were 439-type ferritic (nominal chemical composition: 0.03C-1.00Mn-1.00Si-0.20Ti-(17-19)Cr (wt.%) per ASTM A240 [121]) and 304-type austenitic (nominal chemical composition: 0.08C-2.00Mn-0.75Si-(8-12)Ni-(18-20)Cr (wt.%) per ASTM A240 [121]) stainless steels (referred to henceforth as α-Fe and γ-Fe, respectively) with a thickness of 1.0±0.1 mm. An electro-galvanizing (EG) process was utilized to apply a Zn coating to the steel panels. The thickness of the Zn coating layer was 10 μm. More details regarding the initial microstructures of the as-received materials can be found in Ref. [22,91]. It is worth noting that LME in the Fe-Zn system occurs at high temperatures and within a narrow temperature range (i.e., 700 °C and 900 °C) [56,86], which exceeds the critical temperature needed to transform ferrite to austenite in most families of Fe-based substrates [22]. Due to the severe reorientations of atoms during non-equilibrium phase transformations at elevated temperatures, the role of metallurgical features in LME cracking behavior is uncertain.

The ferritic and austenitic stainless steels were specifically selected as the base materials for this study to ensure no high temperature phase transformation occurred during the hot-tensile test (HTT) as confirmed by the dilatometry analysis presented in Ref. [22], which showed that the austenite to ferrite transformation in the α-Fe specimen started at 1000˚C, which was significantly higher than the temperature range required for the initiation of LME in the samples (i.e., 700 °C and 900 °C).

High-temperature uniaxial tensile tests were carried out using a Gleeble 3500 thermomechanical simulator machine under standard atmospheric condition. Copper (Cu)-grips were used to hold the tensile specimens during testing at high temperatures. The temperature of the tensile test specimens was controlled by the K-type thermocouple welded at the center of the samples. Force, displacement, and temperature were recorded using 1 ms frequency during the HTT. The HTT samples were cut into a dog-bone shape using the ProtoMax Abrasive Waterjet Cutter. The hot-tensile tests were conducted on uncoated and Zn-coated specimens to study the effect of LME cracking on tensile properties of the α-Fe and γ-Fe specimens. For the preparation of the uncoated specimens, the Zn was completely removed by submerging the HHT specimens in a solution of 50% hydrochloric acid and 50% water for 20 s. For the preparation of the Zn-coated HHT specimens, the gauge area of the specimens was first covered with M-masking tape (S-6540). Afterward, the coating was stripped from all surfaces except for the gauge area on the one side where the masking was applied. This sample preparation method for the Zn-coated HTT specimens prevents Zn from sticking to the Cu grips and the thermocouples during the high-temperature tensile test. The samples were subsequently cleaned with isopropanol and dried using an air knife. As the masking tape was peeled off the Zn-coated specimens after drying, only the gauge area showed an intact coating. Figure 4.1 illustrates the process of preparation of uncoated and Zn-coated specimens. The thermomechanical processing for the LME crack study was heating the samples to 800 ˚C at a heating rate of 1000 °C/s. The specimens were held at 800 ˚C for 0.5s before being strained at a constant crosshead speed of 10 mm/s until final failure. The testing parameters were chosen to replicate common thermomechanical conditions experienced in Fe-Zn LME [89].

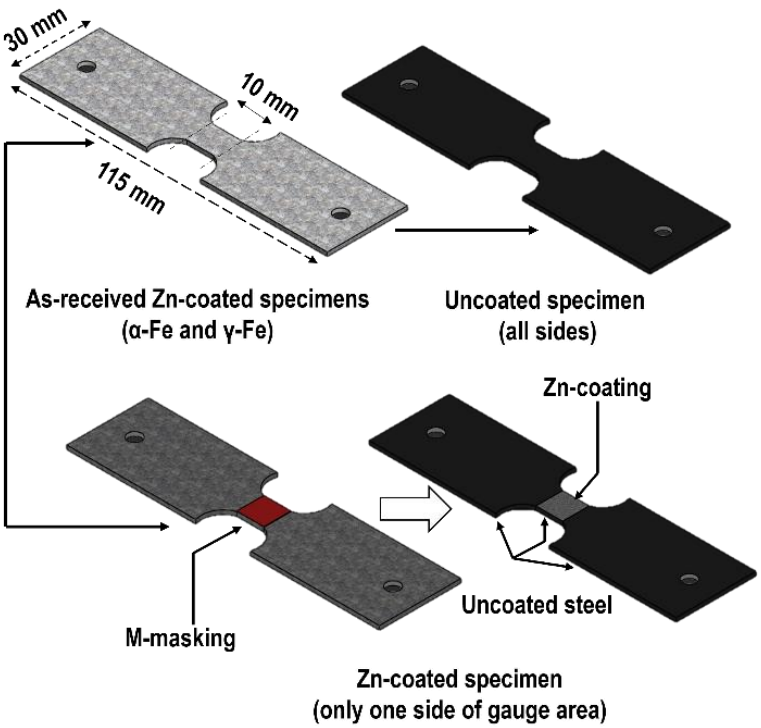

Figure 4.1 The preparation of the uncoated and Zn-coated specimens for the high-temperature tensile test (HTT); the Zn was completely removed from all surfaces of the uncoated HTT specimen. In the case of the Zn-coated HTT specimen, the Zn was removed from all surfaces of the specimen except for one side of the gauge area.

Microstructural characterization was conducted by scanning electron microscope (SEM, JSM7001F), energy-dispersive spectroscopy (EDS), and electron backscatter diffraction (EBSD) methods. The EBSD samples were prepared with a conventional sample preparation procedure and a final vibratory polishing step. A high-speed Hikari CCD camera was used for pattern acquisition ranging from 1.0-0.2 μm step size. EBSD data was analyzed using the MTEX [122] toolkit in MATLAB. For each of the EBSD data, the inverse pole figure (IPF), grain reference orientation deviation (GROD), and grain orientation spread (GOS) were utilized to reconstruct the microstructures of the samples. The GROD measures the misorientation between a reference point (or the mean misorientation) and the other points [123]. The GOS is defined as the average deviation in orientation between each scan point contained within a grain and the average orientation of the grain. Through the use of the GOS, all scan points within a grain are given the same value [123]. The range of color bar was between 0˚∼50˚ for GROD and 0˚∼20˚ for GOS maps. The transmission electron microscope (TEM) equipped with EDS and electron energy loss spectroscopy (EELS) was used for LME crack characterization. TEM samples were prepared via focused ion beam (FIB) with the Thermo Scientific Helios G4 PFIB machine. High-angle annular dark-field (HAADF) micrographs were captured using an FEI Titan 80-300HB operating at 300 keV. The electron channeling contrast imaging (ECCI) was conducted using a Quanta 250 FEG SEM system with a Gemini-type field emission gun and a

four-quadrant backscatter electron detector. The accelerating voltage and working distance were 20 keV and 2.6 mm, respectively.

Fractography analysis was performed on the Zn-coated α-Fe and γ-Fe specimens after failure to assess the effect of LME cracking on the failure mechanism of the specimens. It is worth noting that the contamination of fracture surfaces by liquid Zn poses a significant challenge to fractography [38]. To remove the Zn contamination from fracture surfaces, the Zn-coated fracture specimens were immersed in a solution of $\mathrm{HCl}\ (30\ \mathrm{vol.\%}) + \mathrm{H_2O}\ (70\ \mathrm{vol.\%})$ for 10 s. Subsequently, the samples were cleaned with isopropanol, dried using an air knife, and stored in low oxygen containers. The SEM analysis was conducted immediately following the cleaning of the samples to prevent the fracture surface from oxidizing when exposed to the air. The Keyence VK-X250K confocal laser scanning microscope (CLSM) was used to characterize the surface morphology of LME cracks on the surface of the samples.

4.4 Results

4.4.1 Impact of LME on tensile properties

Figure 4.2 shows the representative engineering stress-stress curves for the uncoated and Zn-coated α-Fe (Figure 4.2 (a)) and γ-Fe (Figure 4.2 (b)) samples after HTT at 800 ˚C. The corresponding reduction in ductility of the Zn-coated samples, with respect to their uncoated counterparts, has been also shown in Figure 4.2 (c). The results show that Zn-coated α-Fe and γ-Fe samples displayed a noticeable reduction in ductility when compared to their uncoated state. The difference in tensile properties observed between the Zn-coated and uncoated samples is a result of LME during the HTT. As displayed in Figure 4.2 (c), the γ-Fe steel exhibited a significantly higher loss in ductility (i.e., 72%) compared to the α-Fe (i.e., 18%) specimen. This indicates that the detrimental impact of LME cracking on tensile properties was significantly higher for the γ-Fe steel compared to the α-Fe steel.

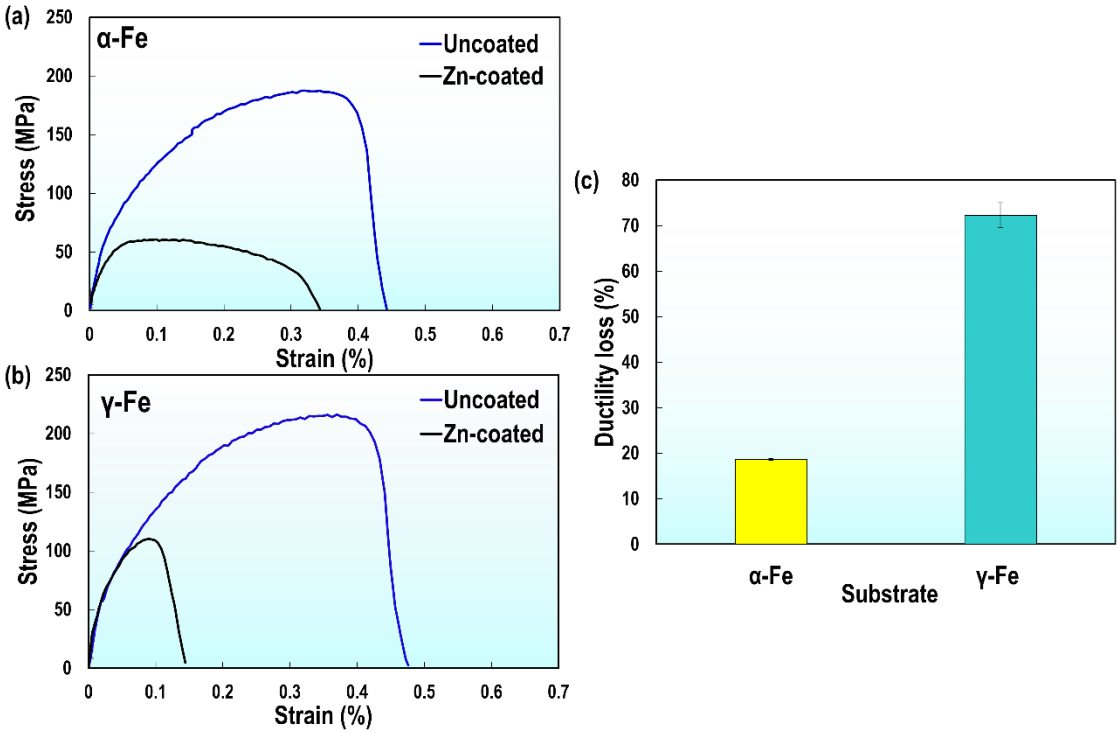

Figure 4.2 Engineering stress-strain curves of the uncoated and Zn-coated (a) ferritic (α-Fe) and (b) austenitic (γ-Fe) samples after HTTing at 800˚C, (c) the corresponding ductility loss of the samples (ductility loss $= \frac{\text{Strain}_{(\text{bare})} - \text{Strain}_{(\text{coated})}}{\text{Strain}_{(\text{bare})}}$).

Figure 4.3 (a) shows the SEM images of the cross-section of the Zn-coated α-Fe specimen after failure. It is evident that the fractured sample exhibited two distinct regions; the first region is associated with ductile fracture in which a high degree of plastic deformation and necking happened during the tensile test. This region is identified as 'Region I' in Figure 4.3 (a), where the presence of voids near the fracture surface is abundantly clear. The second region is associated with a flat-shaped fracture surface showing a completely brittle failure with no sign of plastic deformation or necking as indicated by 'Region II' in Figure 4.3 (a). Additionally, several LME cracks are observed in the vicinity of the brittle fracture surface, where the high magnification SEM micrographs of LME cracks are shown as 'Region III' in Figure 4.3 (a). This observation indicates that the α-Fe sample experienced a hybrid-type failure with a combination of ductile fracture that showed void nucleation/void coalescence and brittle fracture which was associated with rapid LME crack propagation. Furthermore, Figure 4.3 (a) indicates that the LME crack propagation rate was low, which meant that LME cracking was not the dominant failure mechanism in this sample. Consequently, it can be concluded that this sample showed a hybrid failure mechanism which consisted of void nucleation/void coalescence from the uncoated side, accompanied by the LME-induced cracking from the coated side.

The LME cracking and failure behavior of the α-Fe specimen can be further examined by the topographic maps shown in Figure 4.3 (b), which were acquired by CLSM from the top surface of the specimen on the Zn-coated side. Numerous LME cracks can be observed on the surface of the sample, consistent with the results of the SEM analysis (Figure 4.3 (a)). In fact, the degree of plastic deformation and the size of the plastically deformed zone close to the fracture surface can be observed through the height difference between the deformed and undeformed regions of the tested specimen [124]. The region that is affected by the LME cracks clearly indicates their relatively brittle nature, while the underlying regions of the sample that are still intact, exhibit plastic deformation during additional loading (blue areas in Figure 4.3 (b)), confirming the hybrid nature of failure in this sample.

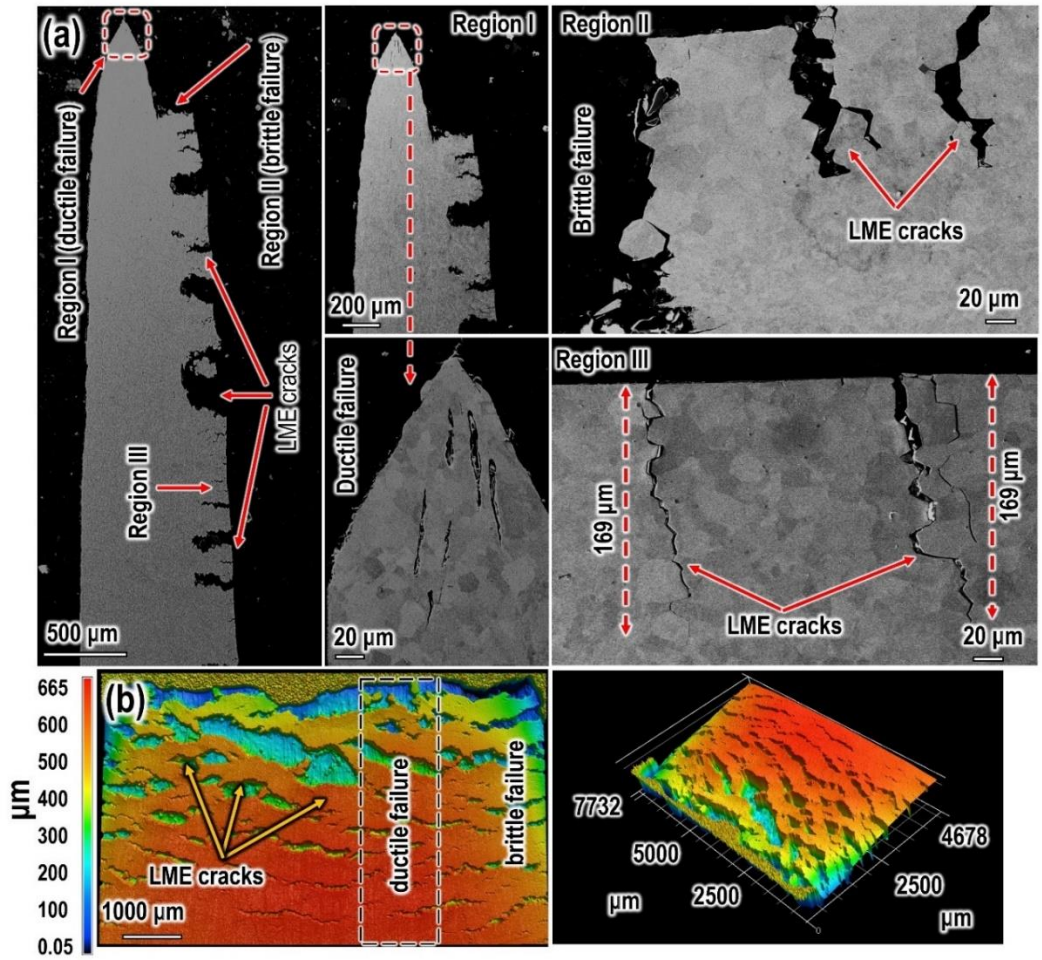

Figure 4.3 (a) SEM micrographs illustrating the cross-section of the ferritic (α-Fe) specimen after HTTing at 800˚C. There are two distinct fracture surfaces; 'Region I' which corresponds to ductile fracture, and 'Region II' which indicates brittle failure. The high magnification micrographs of the LME cracks are displayed in 'Region III', (b) the height-colored confocal laser scanning microscope (CLSM) maps of the top of the α-Fe fractured specimen. The α-Fe sample exhibited hybrid failure behavior in which an LME-induced failure occurred from the Zn-coated side of the sample and a ductile fracture occurred at the center.

The brittle and ductile fracture regions observed in the α-Fe specimen were studied by EBSD, as shown in Figure 4.4 (a) and (b). The IPF map from the ductile region (Figure 4.4 (a)) clearly indicates that grains were elongated in the tensile direction. The correlation between EBSD data and plastic strain of grains was carried out by utilizing two specific EBSD misorientation parameters, GROD and GOS, as shown in Figure 4.4. The values for GROD and GOS were quite high for the ductile region of the fracture surface, which indicates that a high degree of plastic deformation was applied to the region during tensile deformation. Conversely, equiaxed grains were observed on the IPF maps in the brittle region of the fracture surface (Figure 4.4 (b)). The EDS-Zn map clearly shows that Zn was present at the fracture surface due to liquid Zn penetration through grain boundaries. Additionally, the GROD and GOS values in this region were almost zero, indicating that minimal plastic deformation occurred along the fracture surface during high-temperature tensile testing. This observation further confirms that the α-Fe specimen failed by way of a hybrid mechanism, with both ductile and brittle fracture features observed in the HTT samples.

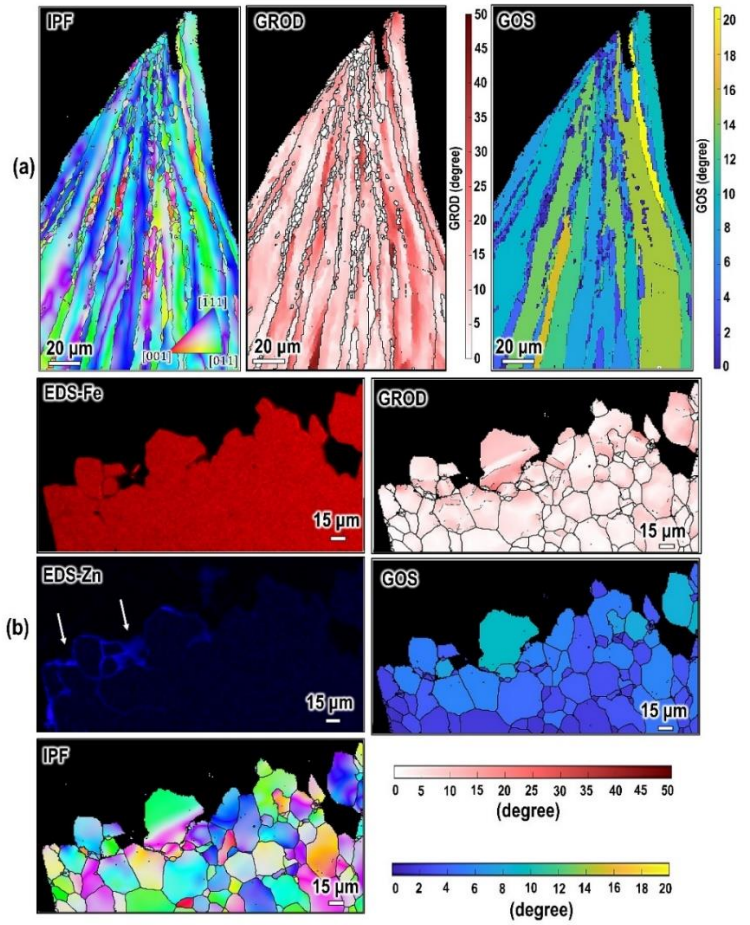

Figure 4.4 EBSD-IPF, GROD, and GOS maps from the cross-section fracture surface of the ferritic (α-Fe) specimen after HTTing at 800˚C; (a) EBSD maps of the ductile region in the fracture surface and (b) EBSD, EDS-Fe and EDS-Zn maps of the brittle region (IPF: inverse pole figure, and GOS: grain orientation spread).

Figure 4.5 (a) depicts SEM images of the cross-section of the Zn-coated γ-Fe specimen after failure. It is evident that the γ-Fe specimen failed in a completely brittle manner, associated with LME-induced cracking, with no signs of plastic deformation or necking observed along the fracture surface. In contrast to the α-Fe specimen, a significantly lower number of LME cracks were observed in the area near the fracture surface of the specimen. However, the length of the LME crack was much larger in the γ-Fe specimen (i.e., 400 μm) compared to the α-Fe substrate (i.e., 160 μm). The topographic maps showing the top surface of the γ-Fe specimen, shown in Figure 4.5 (b), indicate that no surface height difference was observed at the surface of the fractured specimen. Thus, no plastic deformation was applied to this sample and the failure was completely brittle in nature. Moreover, the zigzag pattern along the fracture surface is a clear indication that the fracture occurred because of LME caused by the penetration of liquid Zn through the microstructure.

Figure 4.6 shows the EBSD and EDS analysis of the cross-section of the Zn-coated specimen after failure from the corresponding region demarcated by the red box in Figure 4.5 (a). The EBSD-IPF and Zn-EDS maps make it clear that failure in these samples was associated with rapid LME crack propagation through the γ-Fe grain boundaries. The GROD and GOS maps indicate that there is no plastic strain within the grains along the fracture surface, further confirming the occurrence of brittle failure in the γ-Fe specimen.

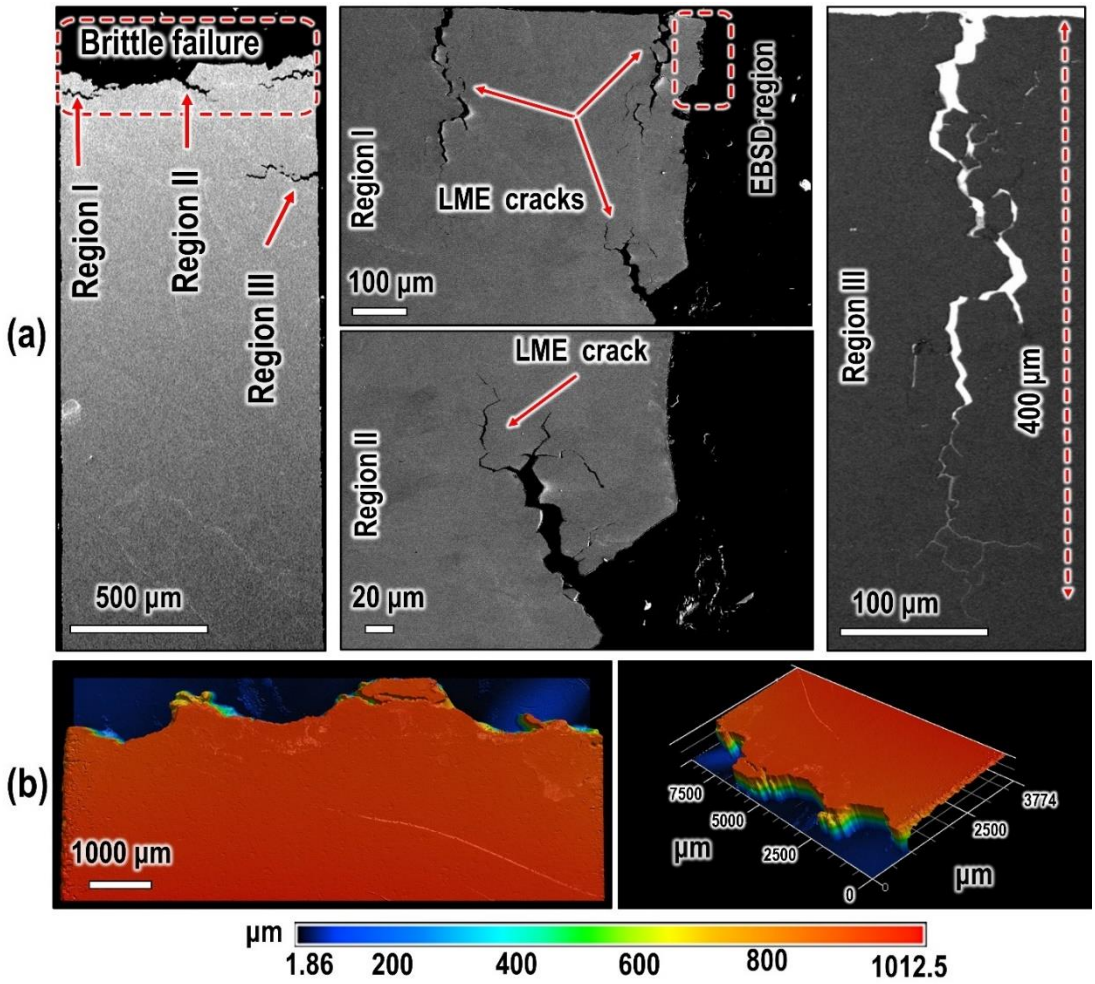

Figure 4.5 (a) SEM micrographs of the cross-section of the austenitic (γ-Fe) specimen after HTT at 800˚C, showing the brittle failure along with the presence of LME cracks (The SEM image in Region III is represented from the backscattered electron (BSE) mode), (b) the height-colored confocal laser scanning microscope (CLSM) maps of the top of the γ-Fe fractured specimen.

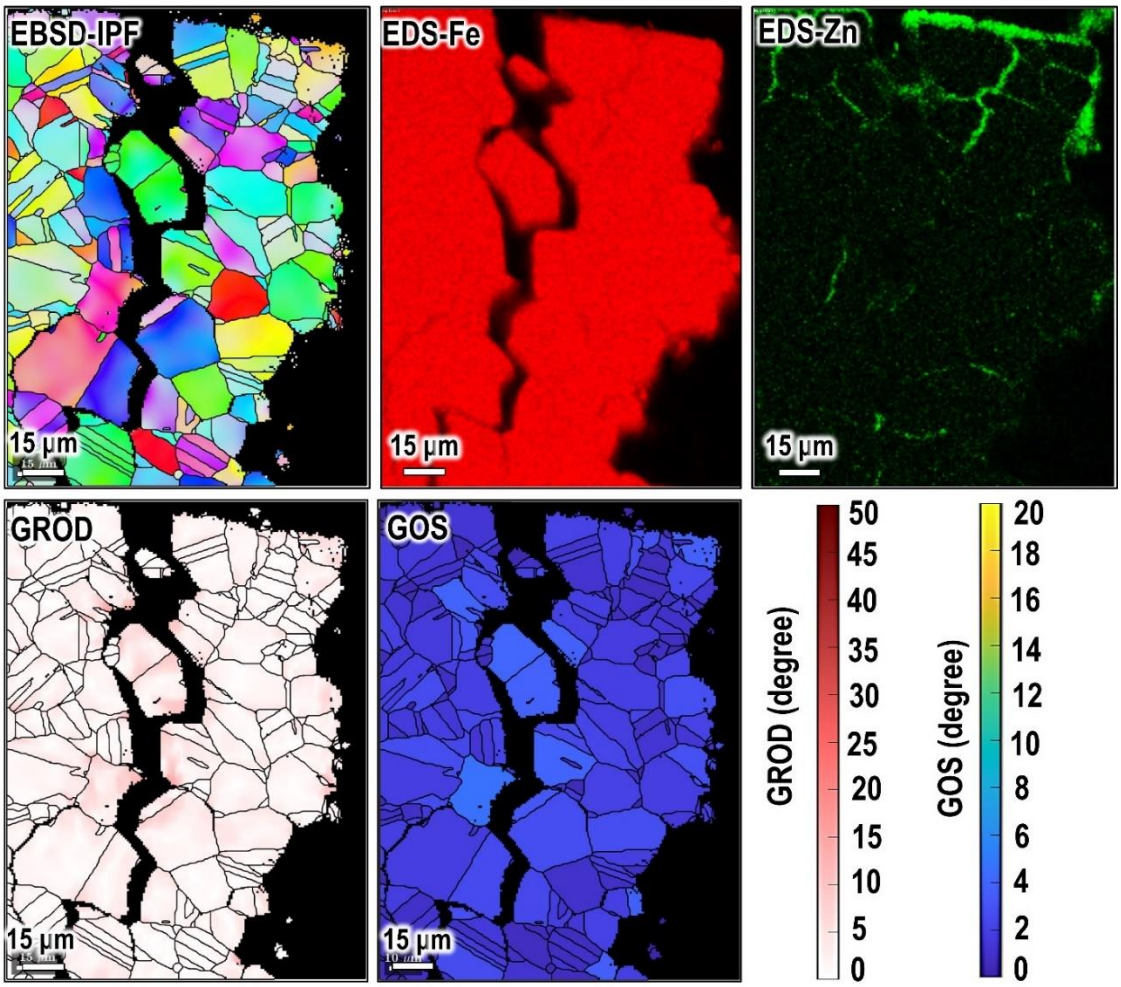

Figure 4.6 EBSD-IPF, EDS-Fe, and EDS-Zn maps along with GROD and GOS maps of the cross-section of the austenitic (γ-Fe) specimen after HTT at 800˚C showing that there is no plastic strain within the grains, confirming the occurrence of brittle failure in the γ-Fe specimen (IPF: inverse pole figure, GROD: grain reference orientation deviation, and GOS: grain orientation spread).

The results presented in this section clearly show that LME cracking was observed in both the α-Fe and γ-Fe samples. However, since the crack propagation rate in the α-Fe sample was much lower compared to the γ-Fe sample, the final failure happened through a hybrid mechanism consisting of both brittle and ductile characteristics at the fracture surface. For the γ-Fe specimen, the predominant failure mechanism was completely brittle in nature due to the rapid propagation of the LME crack through the substrate.

4.4.2 Fractography analysis

Figure 4.7 illustrates the representative SEM images of the fracture surfaces of the Zn-coated α-Fe samples. The fracture surface showed a hybrid transitionary fracture characteristic with three distinct regions labeled as the (i) ductile zone, (ii) transition zone, and (iii) brittle (intergranular) zone. The presence of voids in the ductile zone of the fracture surface indicates that the failure in this particular region occurred in a ductile manner, which is further validated by the necking observed in the cross-section of the ductile region of the fractured specimen (shown as Region I in Figure 4.3). The SEM image of the transition zone shows a distinct chevron fracture pattern, clearly indicating the direction of crack growth along the chevron ridges. The SEM images of the brittle zone revealed intergranular cracks, with the grain contours clearly visible on the fracture surface. This observation clearly indicates that LME cracks propagated through the grain boundaries resulting in an intergranular fracture morphology.

The SEM images of the fracture surface of the Zn-coated γ-Fe specimen are shown in Figure 4.8. In contrast to the α-Fe specimen, the fracture morphology of the γ-Fe specimen was entirely intergranular, emphasizing the dominant effect of the LME cracking on failure behavior. The results show that the fracture surface is made up of undeformed γ-grains without any signs of plastic deformation. Additionally, the twinning features that were observed in the as-received microstructure were also observed within the 3D γ-grains that were observed along the fracture surface. These results indicate premature fracture in these samples and are completely in agreement with the significant reduction in ductility of the γ-Fe sample shown in Figure 4.2.

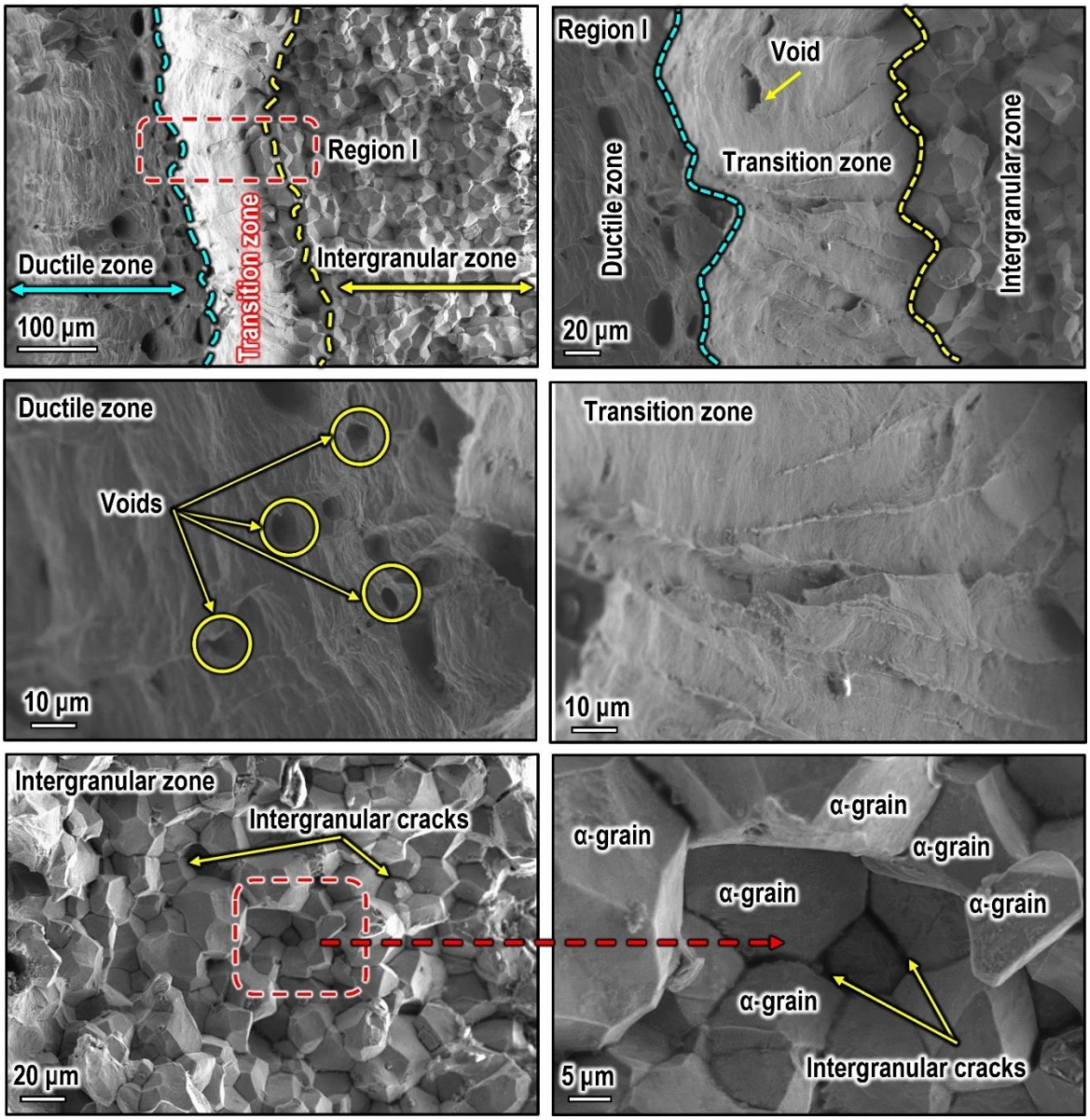

Figure 4.7 SEM micrographs of the fracture surface of the Zn-coated α-Fe specimen; the fracture surface has three distinct zones, including (i) the ductile zone, (ii) the transition zone, and (iii) the brittle zone.

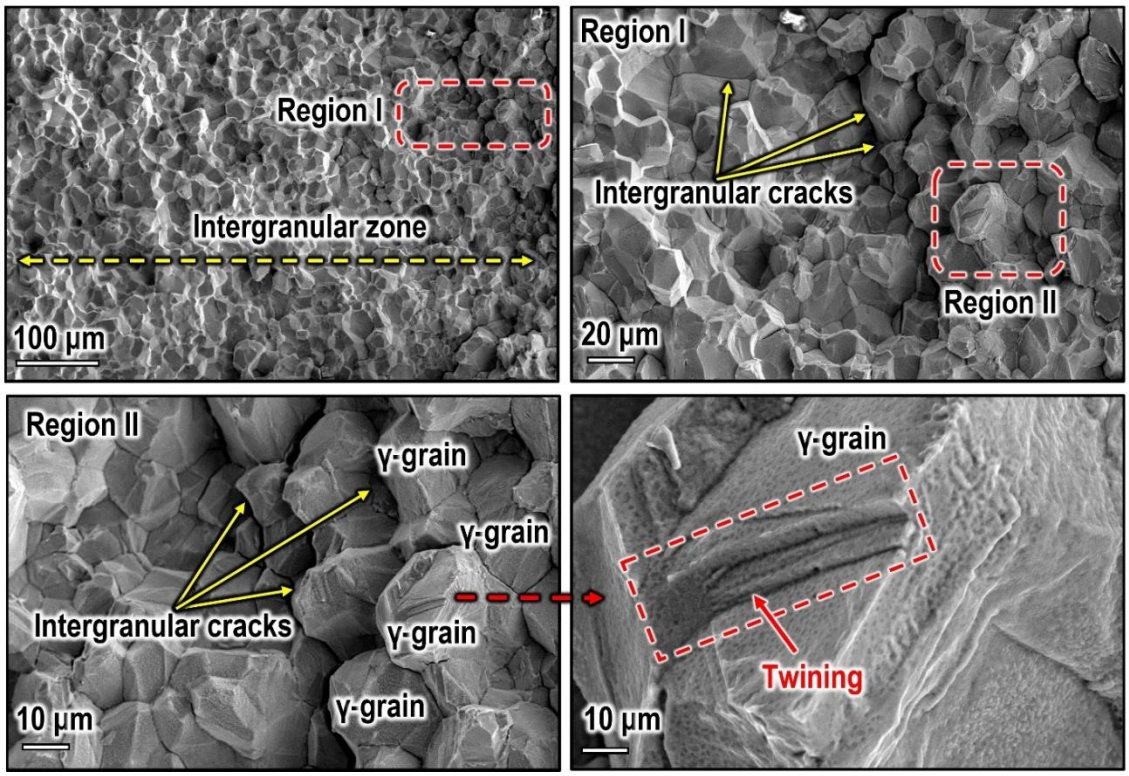

Figure 4.8 SEM micrographs of the fracture surface of the Zn-coated γ-Fe specimen showing the entirely intergranular fracture morphology.

4.4.3 LME crack characterization

Figure 4.9 illustrates the EDS-Zn and EBSD-IPF maps in the vicinity of the LME cracks in the α-Fe and γ-Fe samples. The EDS results confirm that Zn penetrated the grain boundaries resulting in LME-induced intergranular cracking, which is consistent with the fractography analysis shown in Figure 4.7 and Figure 4.8. The EBSD results show that LME cracks propagated through high-angle grain boundaries (HAGBs) in both α-Fe and γ-Fe samples. Razmpoosh et al. [21] showed that liquid metal penetration occurred only on random grain boundaries where its propagation was determined by the misorientation angle and the stress component perpendicular to the grain boundary (GB) plane. It was shown that at low GB misorientation, high stresses were needed for liquid metal penetration; however, a lower stress component was required to trigger Zn penetration at greater misorientation angles [21].

The GB characteristics, particularly the GB misorientation angle distribution and GB character distribution (GBCD), play a crucial role in LME propagation [8,21]. Figure 4.10 (a) shows GB angle/axis distributions in the investigated samples. As seen, the α-Fe specimen has an almost uniform GB angle distribution, in which the majority of the GBs were HAGBs and distributed between the <111> and <110> directions. In contrast, the GB angle/axis in the γ-Fe specimen revealed that a significant proportion of GBs (~25%) were Σ3 coincidence site lattice (CSL) boundaries with a 60˚/<111> misorientation. These boundaries were also evident in the

misorientation axis distribution, with the axis vectors clustered around the <111> direction. Figure 4.10 (b) shows the GBCD of the α-Fe and γ-Fe samples, whose triple junctions with at least two CSL boundaries were determined using the MTEX toolbox and are identified by red circles in the figure. The colored lines in Figure 4.10 (b) indicate the CSL boundaries, while the black lines indicate random boundaries. The results show that the majority of HAGBs in the γ-Fe sample are CSL boundaries, with a distinct distribution of triple junctions with CSL boundaries observed in the microstructure. Given that Razmpoosh et al. [21] showed that the low-Σ CSL boundaries were resistant to LME in γ-Fe steel, and it has been shown that triple junctions with at least one CSL boundary were effective in suppressing LME crack propagation [8]. The presence of LME-resistant GBs within the γ-Fe microstructure explains the lower number of cracks observed in this sample. However, the crack propagation rate was much higher in the γ-Fe sample compared to the α-Fe sample, which had a completely random GB distribution. This observation is somewhat counterintuitive, and as such, further analysis is required to shed light on the differences in LME crack propagation behavior in these samples.

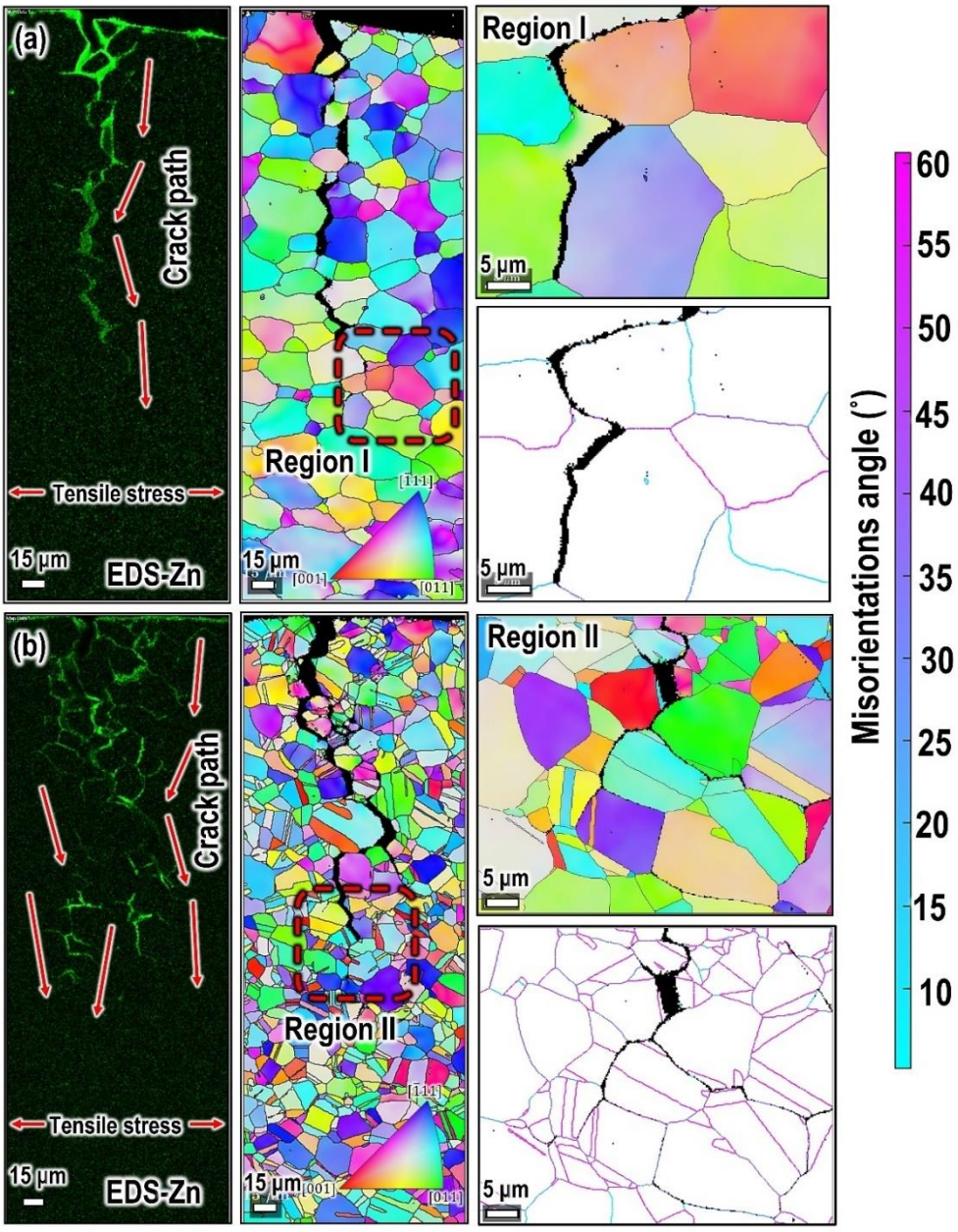

Figure 4.9 (a) EDS-Zn and EBSD-IPF and grain boundary misorientation maps at the vicinity of LME cracks in the (a) α-Fe and (b) γ-Fe samples. The high magnification EBSD maps along with grain boundary misorientation angle have been shown in "Region (I) and Region (II) for the α-Fe and γ-Fe samples (for interpretation of the references to color in this figure legend, the reader is referred to the web version of this article)

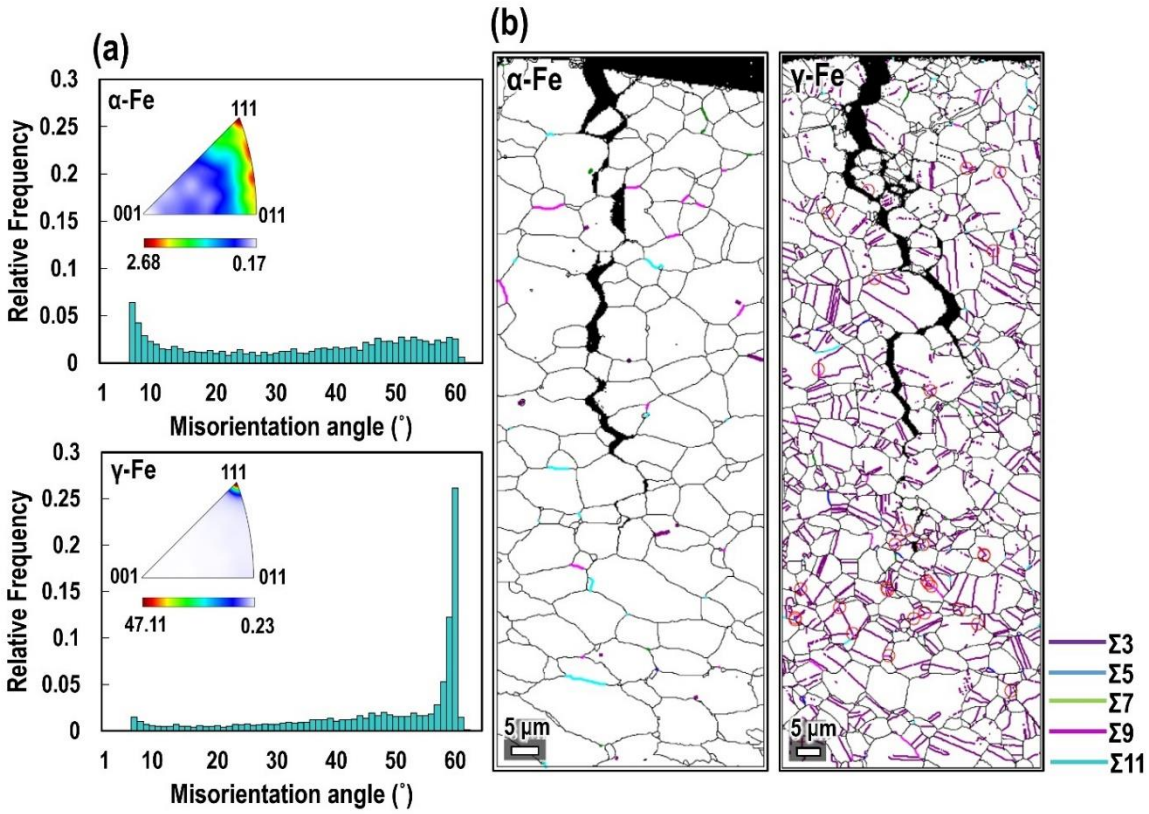

Figure 4.10 (a) The misorientation angle distribution of the EBSD maps in the vicinity of LME crack along with grain boundary axis distribution (between 2°-70° misorientation) and (b) the distribution of coincidence site lattice (CSL) boundaries in the investigated α-Fe and γ-Fe samples; The triple junctions with at least two CSL boundaries are identified by red circles in the EBSD maps (for interpretation of the references to color in this figure legend, the reader is referred to the web version of this article)

It is well known that the segregation of alloying elements at the GB directly influences GB decohesion, which consequently, affects the LME crack propagation behavior [79,91]. To analyze the segregation of alloying elements near Zn-penetrated GBs of the α-Fe specimen, the TEM-EDS and EELS analyses were performed on three regions of the LME crack tip as shown in the HAADF micrograph in Figure 4.11. According to the EDS analysis, Zn penetrated along the GB where local depletion of Cr had already occurred. Further confirmation can be obtained by the EELS analysis presented in "EELS-1" and "EELS-2" in Figure 4.11, where Zn penetration was clearly observed only in the regions of the GB where Cr and Mn had depleted. This observation is consistent with results presented in Ref. [91], in which we showed that liquid metal penetration could only be observed in regions with a high degree of Cr depletion.

The TEM and EELS analysis at the LME crack tip in the γ-Fe specimen has been shown in Figure 4.12. It is evident that in the Zn-penetrated area, severe depletion of Cr and Mn can be observed along the crack boundaries. The results also showed that Ni segregated adjacent to the edge of the LME crack in the γ-Fe sample which was not observed in the α-Fe sample, most

likely due to the relatively higher Ni-content of the γ-Fe alloy. A similar observation was made by Razmpoosh et al. [21,79], who found that Cr had a greater tendency to segregate to the random GBs in the γ-Fe sample compared to the LME-resistant GBs, facilitating the flow of liquid Zn penetration into the bulk microstructure. Razmpoosh et al. [79] used atom probe tomography (APT) analysis in three representative grain boundary types; (i) Zn-penetrated GB, (ii) random boundary without Zn penetration, and (iii) CSL boundary to show that severe depletion of Cr, Ni, and Cu occurred at the Zn-penetrated grain boundary, whereas only Cr was segregated at the random boundary. In addition, no segregation of alloying elements was observed at the CSL boundary. The authors stated that severe Cr-segregation along with co-segregation of other alloying elements at random boundaries compromised the cohesive strength of the grain boundaries, resulting in grain boundary fractures before Zn penetration [79].

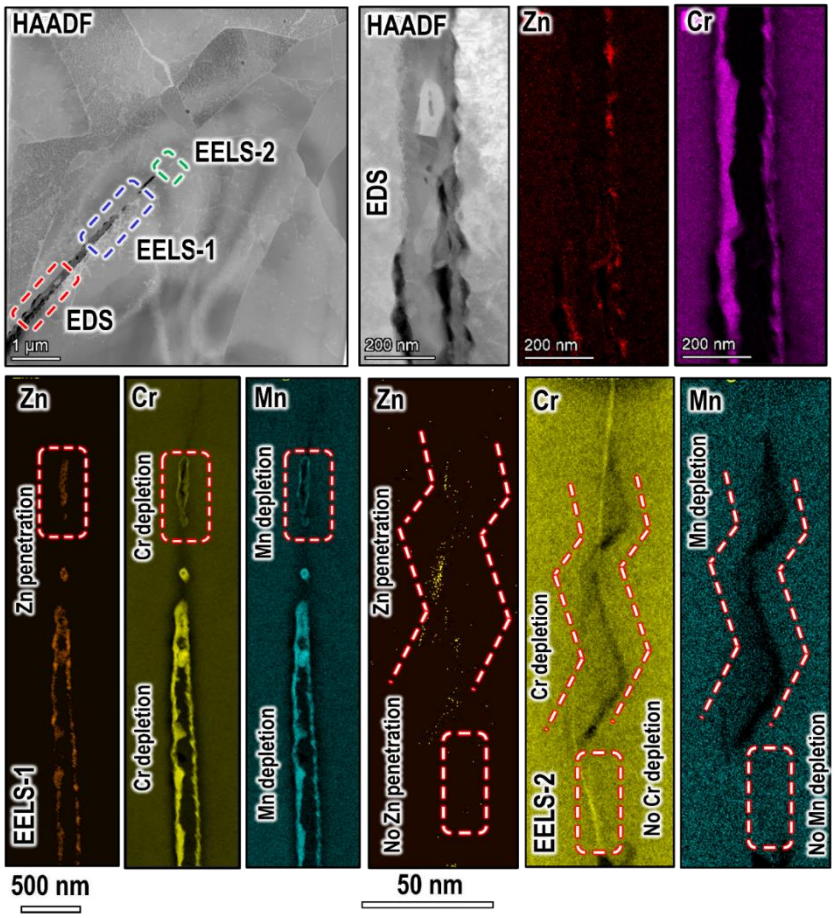

Figure 4.11 HAADF micrographs along with EDS and EELS elemental distribution maps of the LME crack tip in the α-Fe specimen; Three different regions of the LME crack tip were selected for the elemental distribution analysis. Maps for Region (I) were acquired by EDS analysis, while maps for Regions (II) and (III) were acquired by EELS analysis maps (for interpretation of the references to color in this figure legend, the reader is referred to the web version of this article)

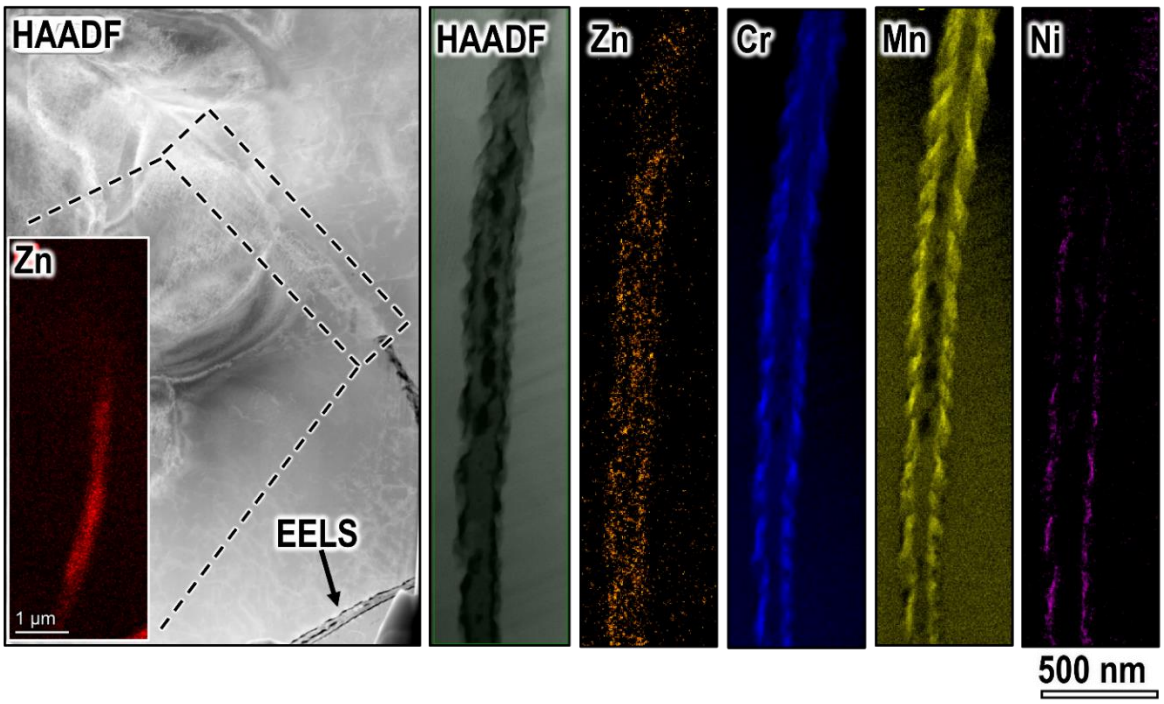

Figure 4.12 HAADF micrographs along with EDS and EELS elemental distribution maps of the LME crack tip in the γ-Fe specimen, showing the segregation of Cr, Mn, and Ni along the grain boundary (for interpretation of the references to color in this figure legend, the reader is referred to the web version of this article)

Cr depletion at the GBs is considered to be one of the mechanisms leading to various types of intergranular cracking, including stress corrosion cracking [125–127], and hydrogen embrittlement [128]. It is widely accepted that Cr depletion occurs primarily by precipitation of Cr-carbides at elevated temperatures, which results in a Cr-depleted zone along the GBs [129–131]. Recent research by Hu et al. [132] proposed a new mechanism for Cr depletion in which Cr atoms segregated extensively at GBs (along with co-segregation of other solute atoms) without any precipitation of Cr-carbides. Razmpoosh et al. [79] observed a similar behavior and showed that Cr-depletion and co-segregation of other elements, such as Ni and Cu, occurred before LME crack propagation, which led to GB decohesion, serving as the precondition necessary for LME to occur. It appears that co-segregation of the alloying elements makes the GB more susceptible to fracture, which eventually results in GB cracking, allowing liquid Zn to be infiltrated into the fracture area. Although the EELS analysis clearly indicated that Cr depletion occurred in both ferritic and austenitic specimens, the degree of Cr depletion cannot be directly compared. The degree of Cr depletion strongly depends on temperature, GB characteristics, and GB chemistry [133,134]. However, it is difficult to perform a quantitative and accurate analysis of the segregation of alloying elements in the Fe-Zn system using EELS. This is mainly due to the difficulty in preparing ultra-thin specimens for high-end TEM analysis by FIB technique because Fe and Zn have different sputtering rates [135]. It is nevertheless possible to study the effects of alloying elements on the embrittlement

of GB using thermodynamic calculations. In light of this, Gibson and Schuh [136] developed a quantitative model to assess the impact of the solute fraction on GB cohesive energy for a wide range of binary systems. According to this model, the GB is embrittled when the breaking of bonds across the GB becomes more energetically favorable to the blunting mechanisms (i.e., dislocation emission). The authors [136] developed a quantitative model to assess the impact of the solute fraction on GB cohesive energy for a wide range of binary systems. For GB decohesion, the energetic barrier is the GB cohesive energy (E_{GBC}) defined by Equation 4.1 [136]:

$$E_{GBC} = E_{Surface} - E_{GB} \qquad \text{Equation 4.1}$$

Where $E_{Surface}$ and E_{GB} are the internal surface and GB energies, respectively. A change in the GB cohesive energy can be calculated based on the difference between the cohesive energies of the alloyed and pure states [136]:

$$\Delta E_{GBC} = E_{GBC}^{Alloy} - E_{GBC}^{Pure} \qquad \text{Equation 4.2}$$

The Gibson-Schuh model [136] provides comprehensive thermodynamic information describing the embrittling process of a binary alloy such that the $\Delta E_{GBC} > 0$ indicates a net increase in decohesion resistance, while the $\Delta E_{GBC} < 0$ indicates a tendency for embrittlement. According to this model, change in cohesive energy (ΔE_{GBC}^{Alloy}) due to the presence of a solute (i.e., B) at the GB of a given matrix (i.e., A) can be obtained using Equation 4.3 [136]:

$$\Delta E_{GBC}^{Alloy} = 5X_{GB}/3[\gamma_s^B - \gamma_s^A] - \frac{zt_{GB}}{4\Omega} X_{GB}(1 - X_{GB})\omega_{GB} \qquad \text{Equation 4.3}$$

Where X_{GB} is the GB fraction of the solute, γ_s is the surface energy, t_{GB} is the thickness of the GB, Ω is the atomic volume and ω_{GB} is GB interaction energy which can be calculated by the following set of equations [136]:

$$\Delta H_0^{seg} = z\left(1 - \frac{\nu}{2}\right)\left[\omega_b - \omega_{GB} - \frac{\Omega}{zt}(\gamma_s^{Zn} - \gamma_s^{Fe})\right] \qquad \text{Equation 4.4 (a)}$$

$$\Delta H_0^{seg} = \Delta E_{Elastic} + \frac{\omega}{zt}(\gamma_s^{Zn} - \gamma_s^{Fe})\left(1 - \frac{\nu}{2}\right) \qquad \text{Equation 4.4 (b)}$$

$$\Delta H^{mix} = z\omega_b \qquad \text{Equation 4.4 (c)}$$

Where the ΔH_0^{seg} is dilute heat of GB segregation, ΔH^{mix} is dilute heat of mixing, ω_b is the bulk interaction energy, $\Delta E_{Elastic}$ is the elastic energy and ν is the transitional bond fraction and will be taken as 0.5 for numerical calculations [137]. A detailed mathematical description of this model can be found in Ref. [136]. In order to quantify the changes in GB cohesion of the Fe matrix due to the presence of different solute atoms (e.g., Cr, Mn, Si, Ti, etc.), the normalized GB cohesive energy ($E_{GBC}^{Alloy}/E_{GBC}^{Pure}$) was calculated based on the thermodynamic data presented in Ref. [136]. Figure 4.13 shows the plots of $E_{GBC}^{Alloy}/E_{GBC}^{Pure}$ as a function of surface energy ratio of the solute (e.g., Cr, Mn, Si, etc.) to the matrix (i.e., Fe) based on the chemical compositions of α-Fe and γ-Fe samples. For the binary couples with $(E_{GBC}^{Alloy}/E_{GBC}^{Pure}) < 1$, the solute atoms result in the embrittlement of the GB. Moreover, binary systems containing a greater amount of cohesive alloying elements (i.e., $(\gamma_S^{Solute}/\gamma_S^{Fe}) > 1$) are less likely to result in a decrease in GB cohesive energy [136]. In the case of γ-Fe specimen, the presence of Mn and Si can lead to GB embrittlement. This is consistent with the literature as experimental results indicated that the susceptibility to Zn-induced LME cracking significantly increases with increasing Si content [45,102,103]. Furthermore, Cr and Ni rarely cause embrittlement in the γ-Fe matrix. Accordingly, depletion of GB from these elements may lead to cracking and mass transfer of liquid metal to GB, as observed previously in the literature [79]. In the case of an α-Fe specimen, the Si can cause GB embrittlement similar to its effect in the γ-Fe specimen. As the Mn content in the α-Fe specimen is lower, this element does not appear to cause embrittlement in the α-Fe matrix. Moreover, alloying elements such as Nb and Ti do not contribute to GB embrittlement. It has been recently shown that the presence of the Nb atom can enhance the GB cohesion of the Fe-matrix [138].

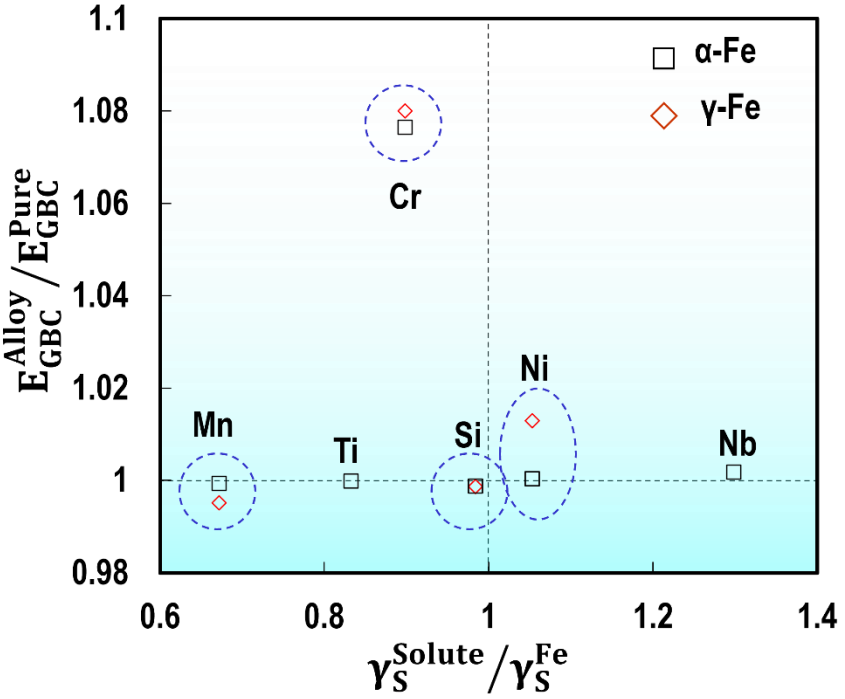

Figure 4.13 The normalized grain boundary cohesive energy upon alloying versus the ratio of surface energies of the major alloying elements in the chemical composition of the α-Fe and γ-Fe steels (e.g., Cr, Mn, Ni, Nb, Si, and Ti) and Fe-matrix.

4.5 Discussion

4.5.1 LME crack propagation mechanism

The morphology of LME-induced fracture surfaces is a significant indicator of the crack propagation mechanism [54]. Generally, the LME-induced fracture surfaces are characterized in two main ways [84]: (i) fracture surfaces that have shallow dimples, extensive slip lines, and intergranular cracks, (ii) fracture surfaces with no evidence of plastic deformation, containing mostly intergranular cracks. The primary explanation for the difference in fracture morphology originates from several proposed hypotheses that aim to explain the mechanism leading to LME crack propagation: (i) adsorption-induced dislocation emission (AIDE) [84], (ii) strain-activated chemisorption of liquid-metal atoms (commonly known as the Stoloff-Johnson-Westwood-Kamdar (SJWK) model [67,68]), and (iii) stress-assisted GB diffusion [78]. The AIDE model accounts for the presence of dimples on the LME-induced fracture surfaces during LME crack propagation. In this model, it is assumed that the interatomic bond strength around the crack tip is reduced due to the adsorption of liquid metal by which dislocations are emitted at the crack tip, leading to crack propagation governed by localized plasticity and void formation [66,84]. The SJWK model assumes that liquid metal at the crack tip weakens the interatomic bond strength of the GB. This results in the breakage of the bond and the mass transport of the liquid metal to the crack tip [67,68]. In this regard, the fracture surface is characterized by the presence of intergranular cracks and the absence of dimples. The stress-

assisted GB diffusion model postulates that liquid metal atoms diffuse into substrate GBs, leading to micro-crack formation [78]. The presence of this micro-crack along the exposed GB triggers the mass transfer of liquid metal into the GB through the crack tip which results in rapid intergranular crack propagation leading to catastrophic failure. According to this model, the associated LME-induced fracture surface consists of intergranular cracks without plastic deformation.

The fractography analysis in Figure 4.7 and Figure 4.8 clearly showed that intergranular cracking was the dominant feature of the fracture surfaces in both α-Fe (albeit only in the brittle zone) and γ-Fe samples. The fracture surface analysis did not reveal any evidence of slip lines or plastic deformation. ECCI analysis was conducted at the LME crack tip of the γ-Fe specimen to gain a better understanding of the LME crack propagation mechanism, as shown in Figure 4.14. ECCI provides a quantitative analysis of dislocation activities and nanoscale microstructural features such as deformation twins with a wide field of view [139]. As can be seen from the ECCI, there are no dislocations observed at the LME crack tip. In fact, the results showed that LME had only propagated along random boundaries and no LME was observed along twin boundaries. Additionally, EBSD analysis at the crack tip (Figure 4.14 (b)) showed no plastic deformation in the vicinity of the LME crack in both α-Fe and γ-Fe samples. Figure 4.14 (c) also shows TEM micrographs from the LME cracks tip of α-Fe and γ-Fe specimens, showing no evidence of dislocation activity in the vicinity of the LME crack, which is in complete agreement with previous studies [21,65]. Based on these observations, it can be concluded that LME crack propagation is associated with brittle intergranular cracking without any plastic deformation.

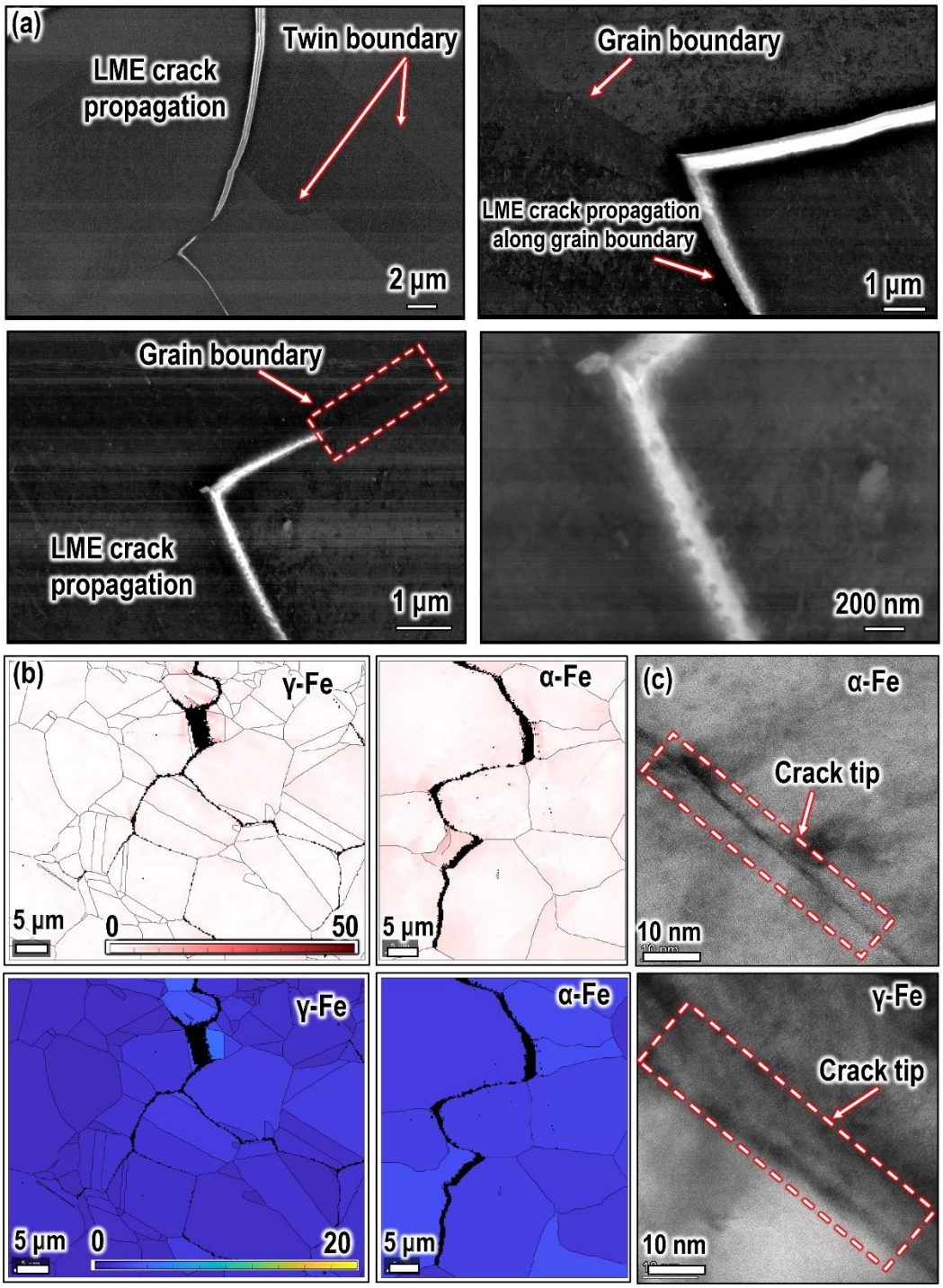

Figure 4.14 (a) ECCI of the LME crack tip the in the γ-Fe specimen, indicating no evidence of plastic deformation and dislocation during the propagation of the crack, (b) high magnification grain reference orientation deviation (GROD) and grain orientation spread (GOS) maps at the vicinity LME crack, and (c) HRTEM analysis at the LME crack tip in α-Fe and γ-Fe specimen.

On the other hand, GB chemistry analysis revealed severe segregation of alloying elements, which makes the GB region more susceptible to LME cracking. This resulted in the decohesion of the GB followed by the formation of the LME crack, and the penetration of liquid Zn into

the fractured area. As a result of the segregation of alloying elements prior to the liquid penetration, it can be concluded that it is most likely that LME crack propagation occurs by the GB diffusion mechanism. The results also indicate that despite the presence of LME-resistant GB features in the γ-Fe microstructure, such as the distribution of the CSL boundaries and triple junctions with at least one CSL boundary, the austenitic microstructure had a significantly higher LME crack propagation rate compared to the ferritic sample. Since GB diffusion is the most likely cause of LME in the Fe-Zn couple, the higher LME crack propagation rate in the austenitic sample can be explained by the difference between the diffusivity of Zn in austenitic and ferritic GBs. It is well known that the Zn GB diffusivity in austenite is much higher compared to ferrite [65], which, according to the GB diffusion theory of LME, would lead to a much higher crack propagation rate in γ-Fe when compared to the α-Fe substrate.

It is important to note that GB diffusion by itself cannot be considered to be the only mechanism for determining crack propagation rate. If one assumed that the LME crack propagation rate was $v_{crack} = 0.1\ cm/s$ [140] (which can be reached up to m/s according to Ref. [55]) and the Zn grain boundary diffusivity was assumed as $D_{GB} = 10^{-8}\ cm^2/\mathrm{s}$ (which has been calculated as $D_{GB} = 7.51 \times 10^{-8}\ cm^2/\mathrm{s}$ at 725 ˚C in α-Fe [117]), the length of the LME crack would be calculated as $L = D_{GB}/v_{crack} = 10^{-3}\ \mu m$. Evidently, the value for the calculated LME crack length is significantly smaller compared to the average LME crack length observed in previous studies [22,91] and the results reported here, i.e., $\sim 160\ \mu m$ for α-Fe and $\sim 400\ \mu m$ for the γ-Fe. Consequently, it becomes important to also consider the role of stress in assisting GB diffusion that leads to LME. It has been shown that the external stress applied to the GB plane can add a thermodynamic driving force to the diffusion process [80]. It was shown by DiGiovanni et al. [89] that increasing the degree of external stress enhanced the penetration of Zn atoms along the GB. As shown in Figure 4.2, the stress at which failure occurred was different for the Zn-coated α-Fe and γ-Fe samples. For the α-Fe specimen, the failure occurred at approximately 50 MPa, whereas for the γ-Fe specimen, it occurred at around 100 MPa. The difference in peak load during the HTT confirms that the γ-Fe sample was more resistant to LME crack initiation allowing the substrate to withstand a higher load. However, the application of this higher load during the deformation process resulted in higher GB diffusion whereby facilitating the crack propagation rate associated with LME. As a result of these observations, it can be concluded that the stress-assisted GB model can be considered as the underlying mechanism for the LME crack propagation in both ferritic and austenitic steels.

4.5.2 LME crack susceptibility in ferritic and austenitic steels

According to the results presented in this study, there is a clear distinction between LME-induced crack susceptibility of ferritic and austenitic microstructures as shown schematically in Figure 4.15. Subjecting the samples to high-temperature tensile test results in the melting of Zn and its subsequent penetration through the GBs based on the stress-assisted GB diffusion

mechanism. In the case of the α-Fe, numerous LME cracks formed on the Zn-coated side of the specimen, but the rate of crack propagation through the microstructure was very low as confirmed by the shallow depth of the cracks observed in the micrographs. During tensile deformation, the Zn-coated side showed LME cracks with very shallow penetration through the microstructure while a high degree of ductile (i.e., plastic) deformation was observed along the uncoated side that was unaffected by LME cracks. This resulted in a hybrid failure of the sample that involved LME-induced intergranular failure on the Zn-coated side that led to shallow LME cracks and ductile failure on the uncoated side where LME played no role during deformation. In comparison to the α-Fe specimen, very few LME cracks were observed at the surface of the γ-Fe specimen during the HTT, but the relative size and depth of each crack showed that the rate of crack propagation through the austenitic microstructure was extremely rapid. As a result of the high crack propagation rate observed in the γ-Fe, the entire sample displayed LME-induced catastrophic intergranular failure, without any signs of plastic deformation. In terms of a quantitative measure of LME cracking, it is evident that the α-Fe sample is more susceptible to LME crack initiation (i.e., the average number of cracks per sample). In contrast, the γ-Fe microstructure had a much lower number of LME cracks, but a significantly higher rate of LME crack propagation. Indeed, based on the results of the failure analysis and fracture morphology presented in this study, it appears that the austenitic microstructure is more susceptible to LME than ferrite; however, this does not imply that ferrite is not susceptible to LME, as clearly shown by the results. The numerous LME cracks that formed on the coated side of the ferritic samples may adversely affect the mechanical properties under special loading conditions (e.g., fatigue, etc.) that have not been explored in the existing literature. Further research is required to gain a thorough understanding of the role of LME cracks on a broad spectrum of mechanical properties of ferritic steels.

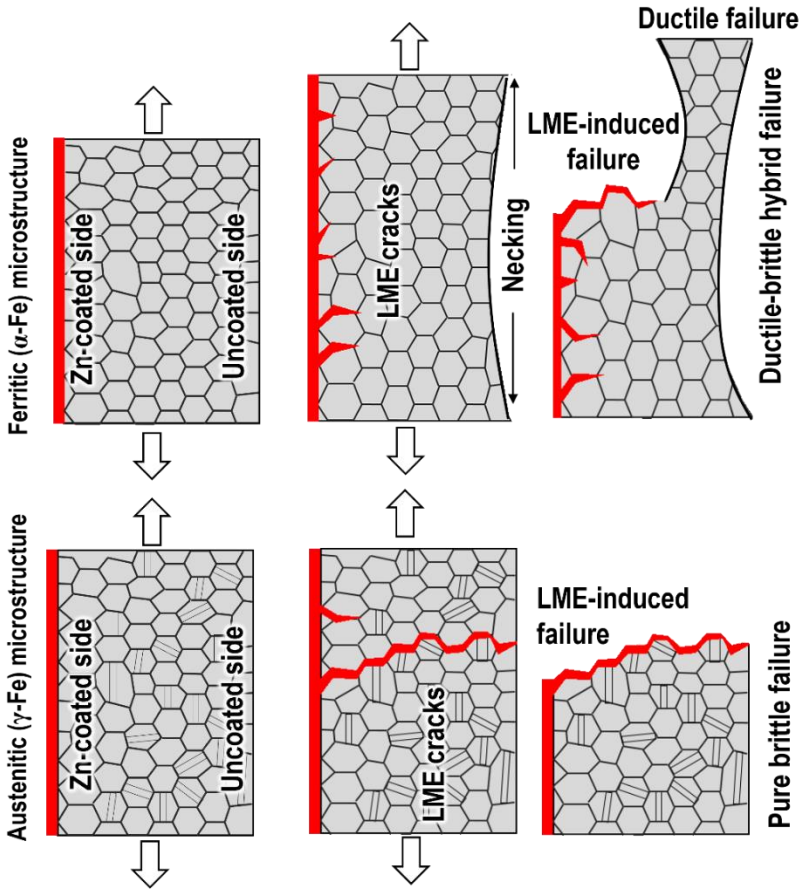

Figure 4.15 Schematic illustration of the LME crack susceptibility in two initial ferritic (α-Fe) and austenitic (γ-Fe) microstructures. Initially, ferritic and austenitic samples are subjected to high-temperature tensile deformation by which LME cracks are formed and propagate through the microstructure. Numerous LME cracks were formed in the α-Fe microstructure with a low crack propagation rate, resulting in a hybrid failure mechanism involving both LME-induced intergranular failure on the Zn-coated side and ductile failure on the uncoated side. The γ-Fe specimen showed only a few LME cracks, but their propagation rate was extremely rapid, resulting in a dominant intergranular failure caused by LME.

4.6 Summary

This chapter provided a detailed analysis of the Zn-induced LME cracking behavior in fully ferritic and austenitic microstructures to gain insight into the role that the initial microstructure plays in LME crack susceptibility and failure mechanism. Additionally, the results of this study contributed insight into the undefined term "LME susceptibility," and resolve the existing debate in the literature regarding the role of the initial microstructure on the severity of the LME cracking in the Fe-Zn system. A comprehensive analysis of the LME-induced fracture surfaces and LME crack morphology revealed that stress-induced grain boundary diffusion was the most probable underlying mechanism for LME-induced crack propagation in both ferritic and austenitic microstructures. The results showed that the ferritic microstructure has a higher sensitivity to LME crack initiation (i.e., LME crack number); however, the austenitic specimen displays a significantly higher LME crack propagation rate. Eventually, different LME cracking

behaviors lead to the occurrence of distinctive failure mechanisms, which can be used to evaluate the susceptibility to LME cracks in these initial structures. Despite the austenitic microstructure appearing to be more susceptible to LME cracking, this does not mean that LME is not a problematic issue in the ferritic microstructure. Given that the ferritic microstructure is highly sensitive to the LME cracking number, the impact of LME on the other loading conditions on this microstructure should be thoroughly examined.

Chapter 5 : High-temperature phase evolution of the ZnAlMg coating and its effect on mitigating liquid-metal-embrittlement cracking[1]

5.1 Overview

Ternary zinc-aluminum-magnesium (ZnAlMg) alloy coatings are the focus of significant attention in the automotive and steel industries due to several advantages over traditional Zn-based coatings. Currently, the literature on this type of coating is limited and focuses mainly on their corrosion resistance and room temperature tensile properties. To assess the relevance of ZnAlMg coatings in current manufacturing processes such as hot stamping and welding of advanced high strength steels (AHSS), it is essential to understand their high-temperature performance, particularly their resistance to liquid metal embrittlement (LME) cracking. This study showed that the ZnAlMg coating had complete resistance to LME cracking at a temperature of about 900 °C, which is traditionally recognized as the temperature at which the highest levels of LME susceptibility are observed in the different families of AHSS. Elemental distribution analysis confirmed that due to an increase in the testing temperature, the lamellar eutectic microstructure of the coating dissolved into the Zn-matrix, with the constituent elements, Al and Mg, segregating towards the steel substrate and the coating surface, respectively. This led to the in-situ formation of a uniform α-Fe(Zn, Al) layer at the steel/coating interface which prevented the direct contact of liquid metal with the steel substrate, resulting in complete suppression of LME at high temperature. Numerical calculations of interdiffusion flux were used to investigate the diffusion behavior of the elements of interest at the interface which indicated that the α-Fe(Zn, Al) layer formed due to the high diffusion rate of Al towards the Fe substrate at 900 °C. The effectiveness of the α-Fe(Zn, Al) layer in mitigating LME was evaluated by calculating the work of adhesion, which showed that this layer preserved its integrity under an applied tensile load, successfully mitigating the initiation of LME. The findings of this study offer valuable insights into developing new avenues for advancing LME resistant coatings by utilizing ternary Zn-based alloy systems.

5.2 Background

Recent developments in ternary ZnAlMg coatings applied to advanced high strength steels have shown that they offer enhanced, cutting-edge corrosion resistance properties compared to conventional Zn coatings [141–144]. Depending on the alloy composition, ZnAlMg coatings contain binary and ternary eutectic phases comprising η-Zn lamella, α-Al clusters, and intermetallic compounds such as $MgZn_2$ and Mg_2Zn_{11} [145,146]. However, the complex

[1] This chapter consists of the published manuscript in Acta Materialia, Ali Ghatei-Kalashami, M. Shehryar Khan, Mok-Young Lee, and Y. Norman Zhou, Vol. 229, 2022.

microstructural morphology has been shown to adversely affect the mechanical properties of the coatings, specifically their room temperature cracking resistance [147].

Despite the corrosion protection of Zn-based alloy coatings, liquid-metal-embrittlement (LME) cracking during high-temperature manufacturing processes such as hot-stamping [25–28], and resistance spot welding (RSW) [14,22,45,53] is a well-known problematic issue. LME occurs when an embrittler (aggressive liquid metal, such as Zn) penetrates the grain boundary network, leading to rapid brittle failure [10,79–81]. LME is a temperature-dependent phenomenon [78]. The impact of temperature on LME is evaluated by the "ductility trough" [22,56–58], which states that the severest reduction in tensile elongation occurs at a specific temperature range (i.e., 700-940 °C for most families of the Fe/Zn system [56–58,65,86,98]). Additionally, the severity of LME increases with increasing temperature, with 900 °C being recognized as the most critical temperature with the highest level of LME susceptibility [22,47,56,57].

The Fe-Zn reaction at high temperatures results in the formation of multi-component systems consisting of several phases and intermetallic compounds (IMCs) [23,148], which can have a significant impact on LME crack severity, depending on their melting temperature, and mechanical properties [92,149]. It is believed that the formation of IMCs with a relatively higher Fe-content (leading to a higher peritectic temperature) reduces the exposure of the Fe-substrate to liquid Zn, which in turn minimizes the susceptibility to LME [58]. In light of this, several attempts have been made to suppress LME by using low heating rates [86], prolonged holding times [25,42,98], and slow strain rates [58]. The suppression of LME under these conditions is believed to be due to diffusion of Fe towards the Zn-layer and the formation of IMCs such as Γ_1- $Fe5Zn_{21}$, Γ-Fe_3Zn_{10}. However, these layers can be broken into small particles under the application of tensile stress at high temperatures (i.e., temperatures above 800 °C), minimizing the effectiveness of the inhibition layer in suppressing LME [25]. Furthermore, it is worthy to note that most hot-working processes (e.g. hot-stamping or RSW) involve extreme conditions such as high heating and strain rates [89], which implies that using slow heating and strain rates to suppress LME cannot be effective or practically relevant in an industrial environment. As such, there is a need to develop LME-resistant coatings that can form effective inhibition layers at the coating/steel interface under extreme hot-working conditions.

In light of that, an investigation of the phase evolution and LME crack susceptibility of ternary ZnAlMg coatings at high-temperature (e.g. 700-900 °C) is a step in the right direction because the literature on this subject is deficient. Consequently, this sui generis study provides a systematic analysis of the phase evolution of the ZnAlMg coating at elevated temperatures to examine its LME cracking behavior. The results showed that there was a correlation between the coating phase evolution and the LME crack severity such that by increasing the hot tensile testing (HTT) temperature, the susceptibility to LME cracking was significantly decreased

which defies the established convention. This study holds an extremely high relevance to the ongoing debate on LME crack susceptibility of Zn-coated steels as it provides a new pathway for advancing the state-of-the-art in LME resistant Zn-based coatings using ternary alloy systems in hot-working applications.

5.3 Materials and methods

5.3.1 As-received material and Hot tensile testing

The as-received material was Zn (97wt.%)-Al(1.5wt.%)-Mg (1.5wt.%) coated interstitial free (IF) steel with a sheet thickness of 1.5 mm. High-temperature uniaxial tensile tests (aka hot tensile tests) were carried out using a Gleeble 3500 thermomechanical simulator machine under standard atmospheric conditions. Copper (Cu)-grips were used to hold the tensile samples at high temperatures and the temperature of the samples was controlled by the K-type thermocouple welded at the center of the samples. Force, displacement, and temperature were recorded using a 1 ms frequency during high-temperature tensile (HTT). The HTT samples were cut into a dog-bone shape using the ProtoMax Abrasive Waterjet Cutter. HTT was conducted on bare and ZnAlMg coated samples under the same processing parameters and the tensile curves of the ZnAlMg coated samples were compared to the bare samples to quantify LME severity. In the case of the bare samples, the ZnAlMg coating on the as-received samples was completely removed by submerging them in a solution of 50% hydrochloric acid and 50% water for 20 s. For the preparation of the ZnAlMg coated tensile test samples, the gauge area of the coated samples was covered on one side with M-masking tape (S-6540) and the coating was stripped from all the other surfaces except for the gauge area on the side where the masking tape was applied. This prevented the coating from sticking to the Cu-grips and the thermocouples during HTT. The samples were subsequently cleaned with isopropanol and dried using an air knife with the gauge area having a fully intact coating after the masking tape was peeled off. Five individual samples in the coated and uncoated conditions were heated to the target temperature of 700, 800, and 900 °C, respectively, at a heating rate of 1000 °C/s. The samples were held at the target temperature for 0.5s before being undergoing tensile loading at a constant crosshead speed of 10 mm/s until failure. The strain was measured using the "L-Gauge" technique which utilizes a jaw-to-jaw transducer to measure the length change of the specimen. The built-in Quiksim software that the Gleeble 3500 comes equipped with converted the load-displacement data directly to stress-strain data using the predefined geometry of the tensile coupons. The testing parameters for HTT were chosen to replicate the most severe thermomechanical conditions experienced in Fe/Zn LME [89].

5.3.2 Materials Characterization

Microstructural characterization was conducted by field emission scanning electron microscope (FE-SEM, JSM7001F), energy-dispersive spectroscopy (EDS), and electron

backscatter diffraction (EBSD) methods. The EBSD samples were prepared using a conventional sample preparation technique with a final vibratory polishing step. A high-speed Hikari charge-coupled device (CCD) camera was used for pattern acquisition at 0.7 μm step size and orientation imaging microscopy (OIM) analysis software was used for analyzing the EBSD results. To characterize the concentration of alloying elements across the ZnAlMg coated samples, time-of-flight secondary ion mass spectroscopy (ToF-SIMS) technique was used. The ToF-SIMS depth profiling was performed in the standard spectroscopy mode in an ION-ToF-SIMS V instrument using a 30 keV Bi_3^+ primary ion beam with an area of 150μm×150μm. The sputtering ion was Cs at 1kV rastered over 300μm×300μm. A transmission electron microscope (TEM) was used for detailed characterization of the coating evolution and the formation of different IMC phases at different testing conditions. TEM foils were prepared via focused ion beam (FIB) using an FEI VERSA 3D with 30 keV Ga ions until the appropriate sample thickness was achieved. Scanning transmission electron microscopy (STEM) micrographs were captured using Hitachi HF5000 operating at 200 keV. The Keyence VK-X250K confocal laser scanning microscope (CLSM) was used to characterize the differences in morphology and roughness of the fracture surfaces.

5.3.3 Analysis of interdiffusion flux

A numerical model was set up to calculate interdiffusion flux in the laboratory-fixed frame for unidimensional diffusion based on the model that was initially proposed by Dayananda [150]. In this model, the interdiffusion flux ($\widetilde{J_\iota}$) for a multi-element system consisting of *n* elements and n-1 independent concentration gradient can be expressed by [150]:

$$\widetilde{J_\iota} = -\sum_{j=1}^{n-1} \widetilde{D}_{ij}^{n} \frac{\partial C_j}{\partial x} \ (i = 1,2, \dots, n-1) \qquad \text{Equation 5.1}$$

Where $\frac{\partial C_j}{\partial x}$ is the independent concentration gradient and $\widetilde{D}_{ij}^{n}$ is interdiffusion coefficient. For a ternary system (i.e., $n = 3$), the interdiffusion flux of the independent components "*1*", "*2*", and "*3*" can be expressed as [151]:

$$\tilde{J}_1 = -\widetilde{D}_{11}^{3} \frac{\partial C_1}{\partial x} - \widetilde{D}_{12}^{3} \frac{\partial C_2}{\partial x} \qquad \text{Equation 5.2 (a)}$$

$$\tilde{J}_2 = -\widetilde{D}_{21}^{3} \frac{\partial C_1}{\partial x} - \widetilde{D}_{22}^{3} \frac{\partial C_2}{\partial x} \qquad \text{Equation 5.2 (b)}$$

$$\tilde{J}_1 + \tilde{J}_2 + \tilde{J}_3 = 0$$ Equation 5.2 (c)

For the given ternary systems, four interdiffusion coefficients $\widetilde{D}_{11}^{3}$, $\widetilde{D}_{12}^{3}$, $\widetilde{D}_{21}^{3}$ and $\widetilde{D}_{22}^{3}$ were calculated. The interdiffusion flux of each component was determined as a function of distance (X^*) away from the concentration profile based on the following equation [151]:

$$\tilde{J}_i\,(X^*) = -\frac{(C_{(i+1)} - C_{(i-1)}}{2t}\Bigg[(1 - Y_{C_i}^*)\int_{x^{-\infty}}^{X^*} Y_{C_i} dx + Y_{C_i}^*\int_{X^*}^{x^{+\infty}} (1 - Y_{C_i}) dx\Bigg]$$ Equation 5.3 (a)

$$Y_{C_i} = \frac{C_{(i)} - C_{(i-1)}}{C_{(i+1)} - C_{(i-1)}}$$ Equation 5.3 (b)

where $C_{(i+1)}$ and $C_{(i-1)}$ refer to the terminal alloy compositions, $Y_{C_i}^*$ refers to the location of the Matano plane and *t* is the diffusion time [152]. Further details about the model can be found elsewhere [150,151].

5.4 Results

5.4.1 The impact of LME on mechanical properties

Figure 5.1 (a) shows the representative engineering stress-strain curves at 700, 800, and 900 °C for the bare and ZnAlMg coated samples. The coated samples were observed to have a significant loss in ductility at 700 °C and 800 °C compared to the bare samples. In contrast, HTT at 900 °C did not reveal any significant difference in the mechanical properties of the bare and coated samples. The ductility loss of the samples was plotted as a function of temperature, as shown in Figure 5.1 (b). It was observed that as the testing temperature was increased, the ductility loss decreased from about 80% at 700 °C to less than 5% at 900 °C. The results shown in Figure 5.1 make it clear that the ZnAlMg coating had a significant role to play in the brittle failure of the coated samples at 700 °C and 800 °C. This indicated that the susceptibility to LME cracking in ZnAlMg coated steels decreased with increasing temperature. This finding is quite remarkable because in traditional Zn-based coated steels, the susceptibility to LME cracking generally increases significantly with increasing temperature, regardless of other HTT parameters such as strain rate [58], heating rate [86], or holding time [98].

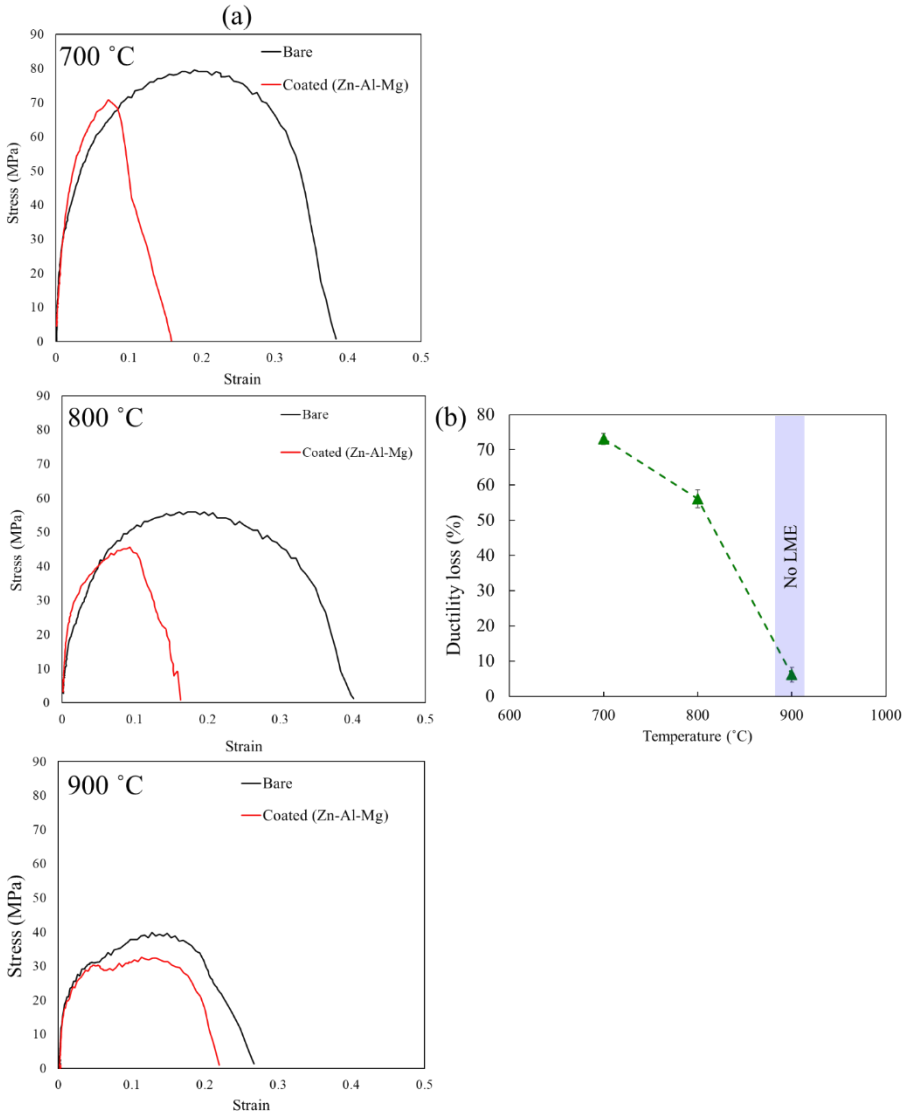

Figure 5.1 (a) Engineering stress-strain curves of the bare and ZnAlMg coated steels during HTTs at 700 ˚C, 800 ˚C, and 900 ˚C, (b) ductility loss the samples as a function of temperature (ductility loss $= \frac{\text{Strain}_{(\text{bare})} - \text{Strain}_{(\text{coated})}}{\text{Strain}_{(\text{bare})}} \times 100$).

Figure 5.2 displays SEM micrographs of the longitudinal cross-sections of the fractured samples. The coated samples tested at 700 °C and 800 °C showed no reduction in the cross-sectional area prior to failure, which is a clear indication that the samples failed due to catastrophic brittle fracture. Moreover, a high propensity of LME cracks was detected in the vicinity of the fractured area for the samples tested at 700 °C and 800 °C, further confirming that the failure was the result of LME-induced cracking. By contrast, necking was clearly visible in the longitudinal cross-sectional SEM image of the specimen tested at 900 °C, showing that this specimen failed by ductile fracture. There is no evidence of LME cracks at the fracture surface at this testing temperature clearly indicating the resistance of the coating to LME crack formation and propagation at this temperature. Figure 5.3 depicts EDS/EBSD analysis of the

LME cracks of the samples tested at 700 °C and 800 °C. It was observed that Zn and Al infiltrated the steel along the grain boundaries, leading to the formation of LME cracks. There was no Mg observed at the location of the LME cracks, as shown in the EDS map in Figure 5.3. The inverse-pole figures (IPF) and phase maps (PM) for both temperatures indicate a single-phase BCC microstructure in the vicinity of the LME cracks. The EBSD maps showed that the propagation of LME cracks happened through the high angle grain boundaries for both testing temperatures, similar to what has been reported in the literature [21].

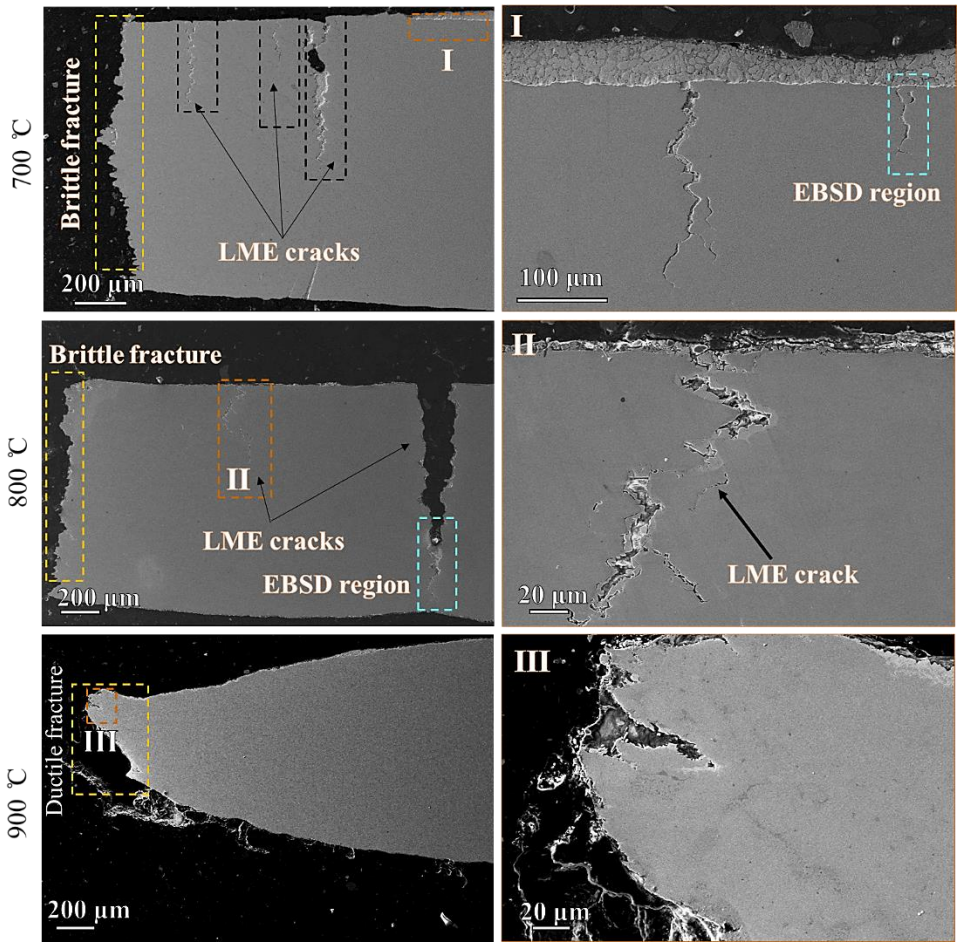

Figure 5.2 SEM micrographs of the cross-section of ZnAlMg coated specimen after HTT at 700 °C, 800 °C, and 900 °C (the right-side SEM images show magnified regions labeled as (I), (II), and (III), the blue rectangles in the SEM micrographs of 700 °C, 800 °C samples show the region for EBSD analysis)

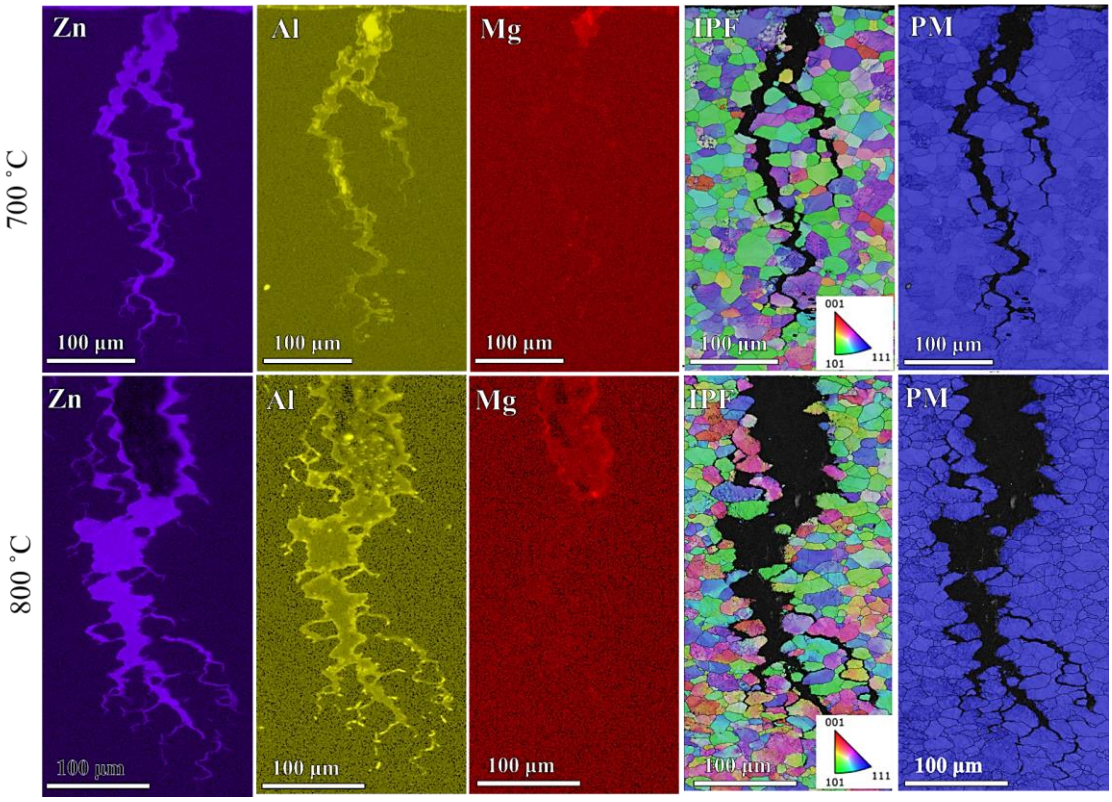

Figure 5.3 EDS elemental maps of Zn, Al, and Mg elements, along with EBSD inverse-pole figure (IPF) and phase map (PM) specimen after HTT at 700 °C and 800 °C.

The role of LME cracking on the failure behavior of the samples tested at different temperatures was further investigated using SEM micrographs of the fracture surface, as shown in Figure 5.4. The micrographs of the fracture surfaces showed two distinct regions: the bare surface and the coated surface as illustrated by EDS analysis (regions (I)-(V) in Figure 5.4). Failure began with intergranular LME cracking from the coated side, leading to sudden fracture for the samples tested at 700 °C and 800 °C. The fracture surfaces were characterized by clear signs of intergranular cracking, which is known to be the predominant fracture mechanism in LME-induced failure samples rather than the so-called "quasi-cleavage" fracture mode [153]. The fracture surface of the specimen tested at 900 °C exhibited dimples, indicating that the failure occurred by ductile fracture mechanism through void nucleation, void growth, and void coalescence. The fractured samples were further characterized by CLSM technique as shown in Figure 5.4 (b). Samples tested at 700 °C and 800 °C showed evidence of concave and convex macroscopic contours clearly indicating a catastrophically damaged fracture surface. On the other hand, dimples were observed at the center of the fracture surface of the specimen tested at 900 °C with a macroscopic morphology clearly resembling a ductile fracture surface.

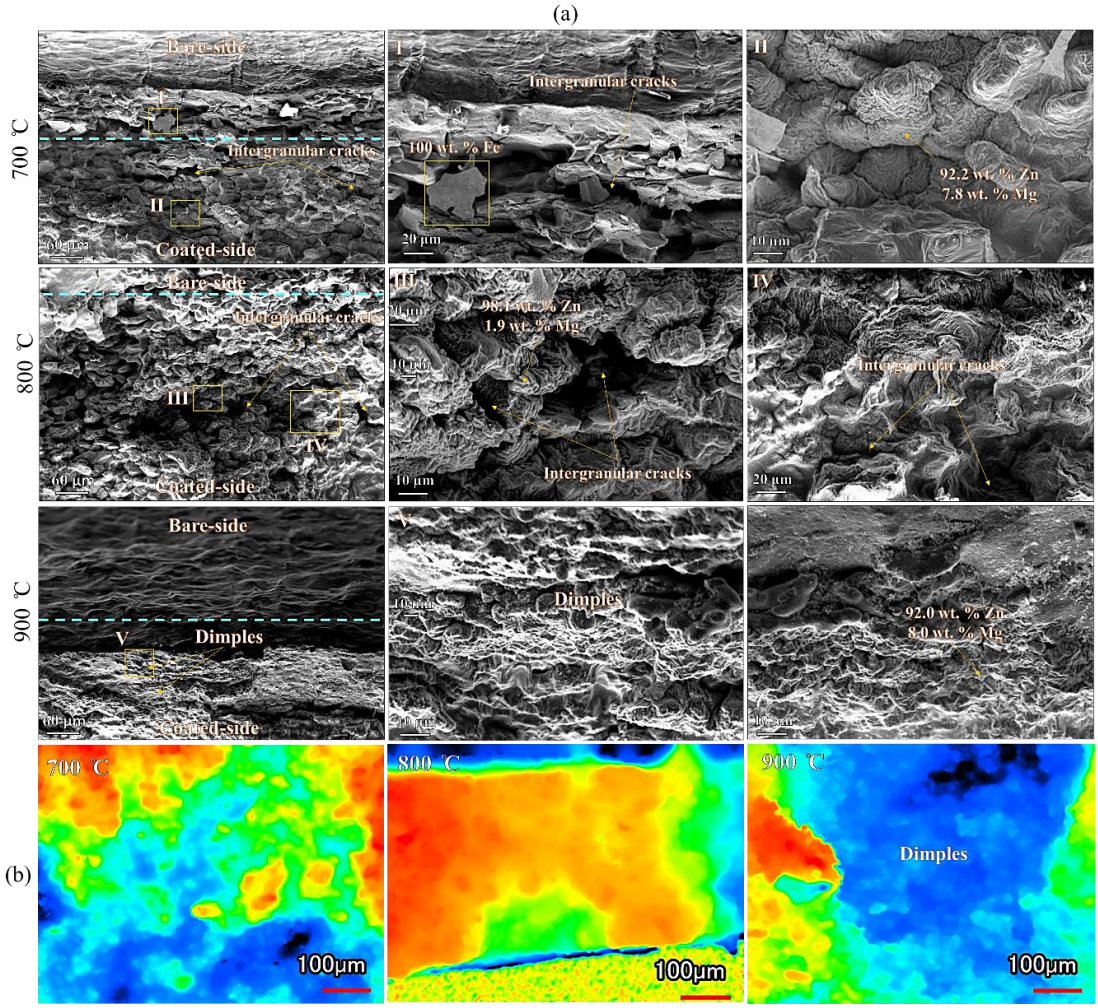

Figure 5.4 (a) SEM micrographs along with EDS analysis of the fracture surfaces of the ZnAlMg coated samples after HTT at 700 ˚C, 800 ˚C, and 900 ˚C, (b) the representative confocal laser scanning microscope (CLSM) images of the fracture surfaces by of the ZnAlMg coated samples.

5.4.2 High-temperature phase evolution

SEM micrographs along with the EDS analysis of the as-received ZnAlMg coating are shown in Figure 5.5 (a). The ZnAlMg coating was observed to be a heterogeneous layer that consisted of globular η-Zn grains with binary and ternary zones. The binary eutectic has been reported to be a lamellar structure made up of η-Zn and the intermetallic Laves phase (binary eutectic: η-Zn/$MgZn_2$), whilst the ternary eutectic consists of primary η-Zn, α-Al, and an intermetallic phase (ternary eutectic: η-Zn/$MgZn_2$/α-Al) [144,154]. The composition of each phase presented in Figure 5.5 is shown in Table 5.1. ToF-SIMS analysis was carried out as shown in Figure 5.5 (b), to observe the three-dimensional (3D) distribution of elements throughout the coating. Zn^+ was uniformly distributed across the thickness of the coating as shown in the two-dimensional (2D) and 3D images. The Al^+ and Mg^+ elements, on the other hand, had an inhomogeneous distribution across the thickness of the coating. The 2D and 3D images showed that Al^+ and Mg^+ were distributed in the coating as lamellar structures, linked

to the binary and ternary eutectic structures that have been previously reported in the literature [144,154].

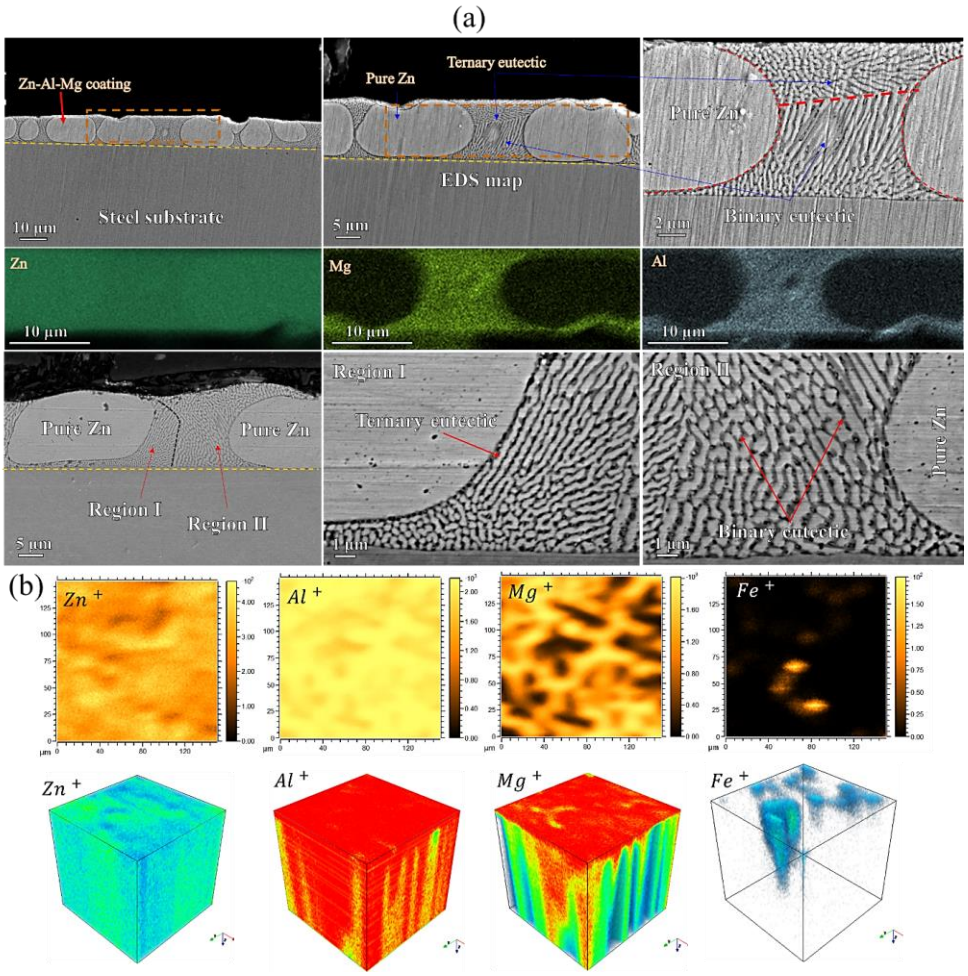

Figure 5.5 (a) SEM micrograph along with EDS analysis of the as-received ZnAlMg coating (The microstructure of the coating consists of three regions: globular zinc grains (pure Zn), binary eutectic, and ternary eutectic structures), (b) The positive ion ToF-SIMS analysis of Zn^+, Al^+, Mg^+, and Fe^+ elements in the as-received coating (The coding scale showing the distribution of elements at the surface and through the thickness of the coating in 2D and 3D images, respectively).

Table 5.1 Composition of phases present within ZnAlMg as-received coating obtained using EDS analysis.

Region	Zn (wt.%)	Al (wt.%)	Mg (wt.%)	Fe (wt.%)
Globular grains	100.00	-	-	-
Binary eutectic	89.6±1.9	4.8±1.1	5.5±0.9	-
Ternary eutectic	87.5±1.2	5.4±0.8	5.3±0.2	1.7±1.5

The microstructure of the coating at 700 °C is shown in Figure 5.6. As can be seen in the SEM micrographs (Figure 5.6 (a)), the coating displayed similar morphological features to the as-received coating, with globular η-Zn grains sandwiching a relatively coarser eutectic

structure. The ToF-SIMS analysis (Figure 5.6 (b)) showed a change in the distribution of Al^+ and Mg^+ compared to the as-received state: Al^+ tended to segregate towards the substrate interface and Mg^+ segregated towards the surface of the coating, while the Fe^+ present in the coating segregated towards the surface of the coating. The STEM images with the corresponding EDS elemental maps of the eutectic structure are shown in Figure 5.6 (c). The EDS data for the different regions have been summarized in Table 5.2. The elemental maps showed that the eutectic structure was composed of alternative layers of Zn and Mg, while Al was located at the interface between the two layers. As shown in Figure 5.6 (c), a thin and discontinuous layer of Fe-Al (see region (I)) was clearly visible at the interfacial region between the substrate and the coating, shown by the red arrow.

Figure 5.7 shows the corresponding selected area diffraction (SAD) patterns of the different regions of the coating at 700 °C. The SAD pattern isolated from Region (I) showed two types of diffraction spots in which the strong spots corresponded to α-Al//$[\bar{1}12]$ and the faint spots were indexed as the Fe_2Al_5 phase. In the presence of a small amount of Al (~0.2 wt%), an extremely thin layer of Fe_2Al_5 can be formed between the steel substrate and the coating that delays the formation of Fe–Zn phases at the substrate interface [155–157]. The SAD pattern from η-Zn and Mg (Regions (II) and (III) in Figure 5.7, respectively) confirmed the presence of η-Zn and Mg grains in the eutectic structure. It was also confirmed that the C14 Laves phase (hexagonal, $MgZn_2$) was present in the eutectic structure (Region (IV)), which is known to form during cooling at non-equilibrium conditions [154], and this phase has been observed in previous studies in typical industrial ZnAlMg coatings [145,146,154]. It is worth noting that ZnAlMg alloys are known to show a strong sensitivity to cooling rate on microstructural transformation because undercooling causes preferential nucleation of $MgZn_2$ over Mg_2Zn_{11} in metastable solidification [158].

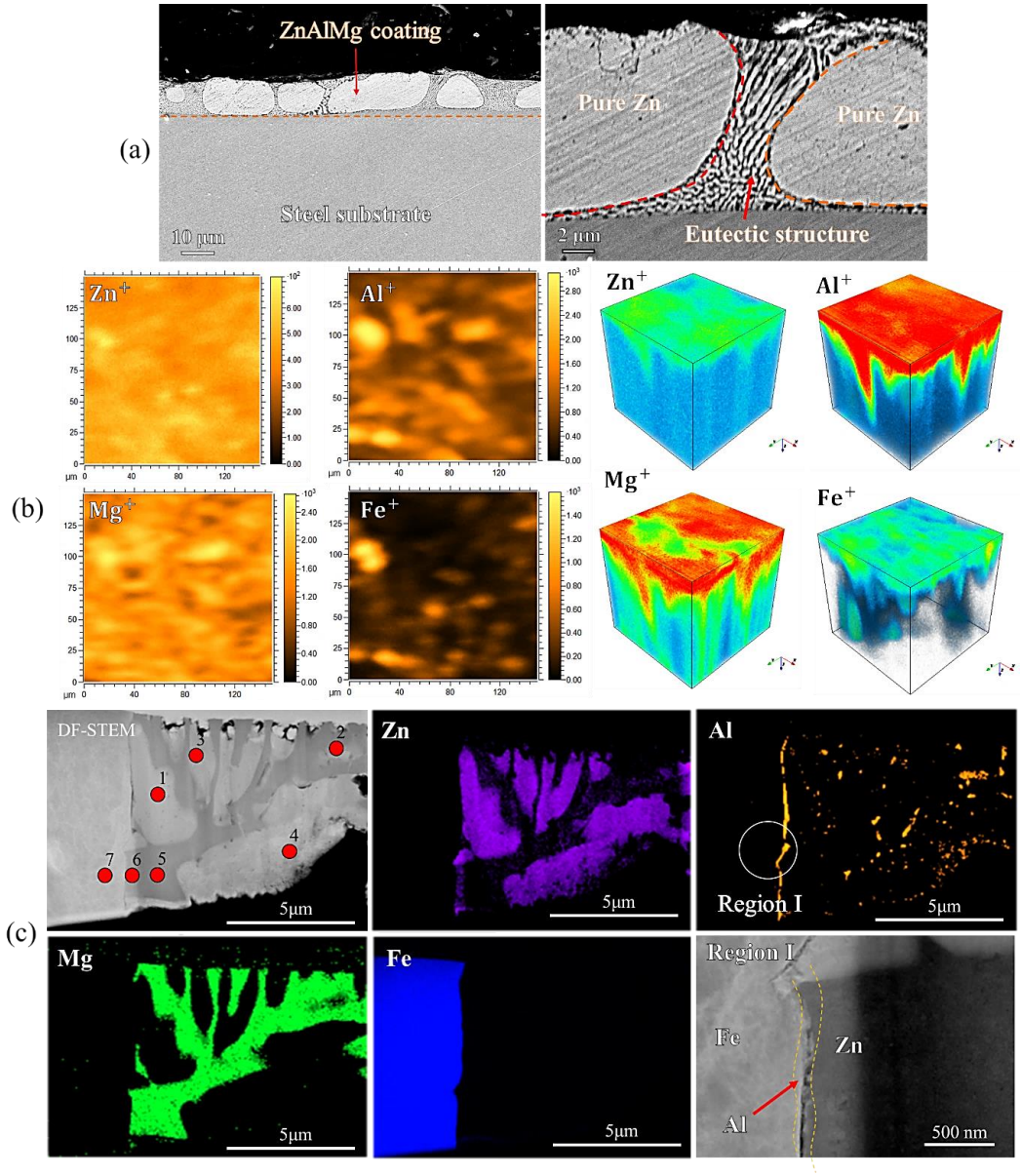

Figure 5.6 (a) SEM micrograph of the sample after HTTing at 700 ˚C, (b) the corresponding ToF-SIMS analysis of Zn^+, Al^+, Mg^+, and Fe^+ elements in the coating sample, and (c) STEM image along with EDS elemental analysis of the ZnAlMg coated (Region I shows bright-field STEM (BF-STEM) micrograph of the Fe-Al layer)

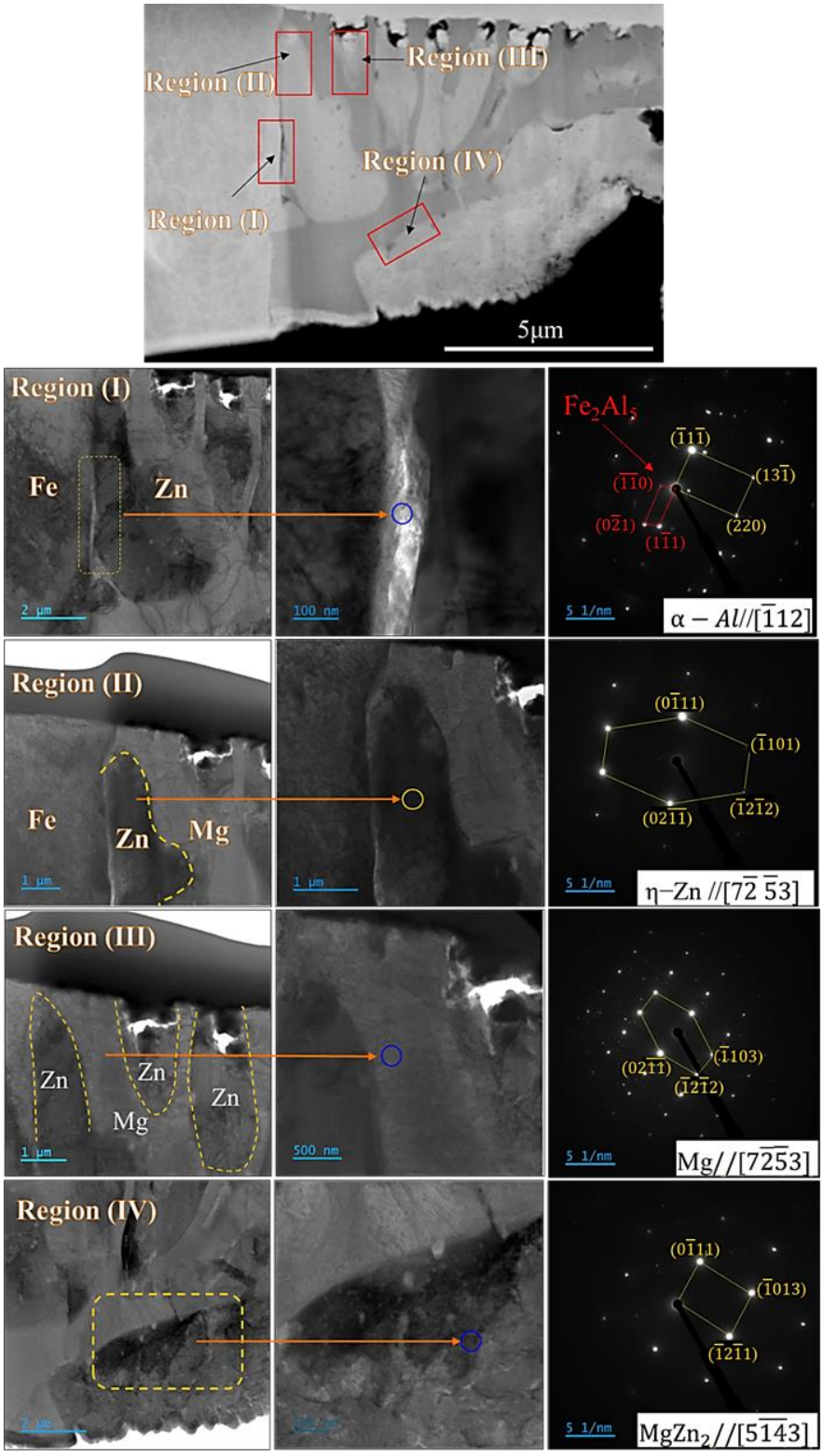

Figure 5.7 High magnification bright-field STEM (BF-STEM) images and corresponding selected area diffraction (SAD) patterns at different regions of the eutectic structure for the sample deformed at 700 °C.

Table 5.2 Composition of various areas of the sample test at 700 °C obtained using EDS analysis (see Figure 5.6 (c) for the location of each point)

Region	Zn (wt.%)	Al (wt.%)	Mg (wt.%)	Fe (wt.%)
1	98.75	0.2	0.08	0.98
2	90.88	1.35	7.43	0.33
3	98.03	0.42	1.03	0.53
4	98.53	0.64	0.30	0.53
5	87.70	0.73	10.17	0.73
6	91.51	0.87	5.71	1.91
7	0.00	0.07	0.06	99.87

The SEM micrographs of the coating at 800 °C are shown in Figure 5.8 (a), revealing the presence of pure Zn grains, eutectic structures, and a darker ribbon-like feature forming at the interfacial area (shown as Region I in Figure 5.8 (a)). The ToF-SIMS analysis, shown in Figure 5.8 (b), indicated that Al^+ segregation increased towards the steel substrate, while Mg^+ continued to segregate towards the coating surface. Additionally, it was evident that the ribbon-like feature was formed by Zn-Al-Fe elements at the interface. The TEM and EDS analyses of the sample at 800 °C have been shown in Figure 5.8 (c) and Table 5.3, respectively. In contrast to the sample tested at 700 °C, the STEM/EDS analysis indicated that a uniform inhibition layer had developed between the coating and steel interface. High magnification STEM images of the Fe-Al inhibition layer, as well as the Mg/Zn lamellas, are also shown in Figure 5.8 (c). In two regions of the inhibition layer (regions (I) and (II)), the SAD patterns confirmed the presence of the FeAl phase at the interfacial region between the coating and steel. This phase has a simple cubic (B2-type) crystal structure and can be present in the microstructure through the decomposition of Fe_5Al_8 IMC ($Fe_5Al_8 \rightarrow FeAl_2 + FeAl$) [159]. Additionally, the SAD pattern obtained from the eutectic phase showed two sets of points, with the indexed planes confirming Mg_2Zn_{11} along the $[\bar{2}33]$ zone axis. Compared to the analysis of the coating at 700 °C it was clear that the metastable $MgZn_2$ had transformed into the stable Mg_2Zn_{11} at the elevated temperature.

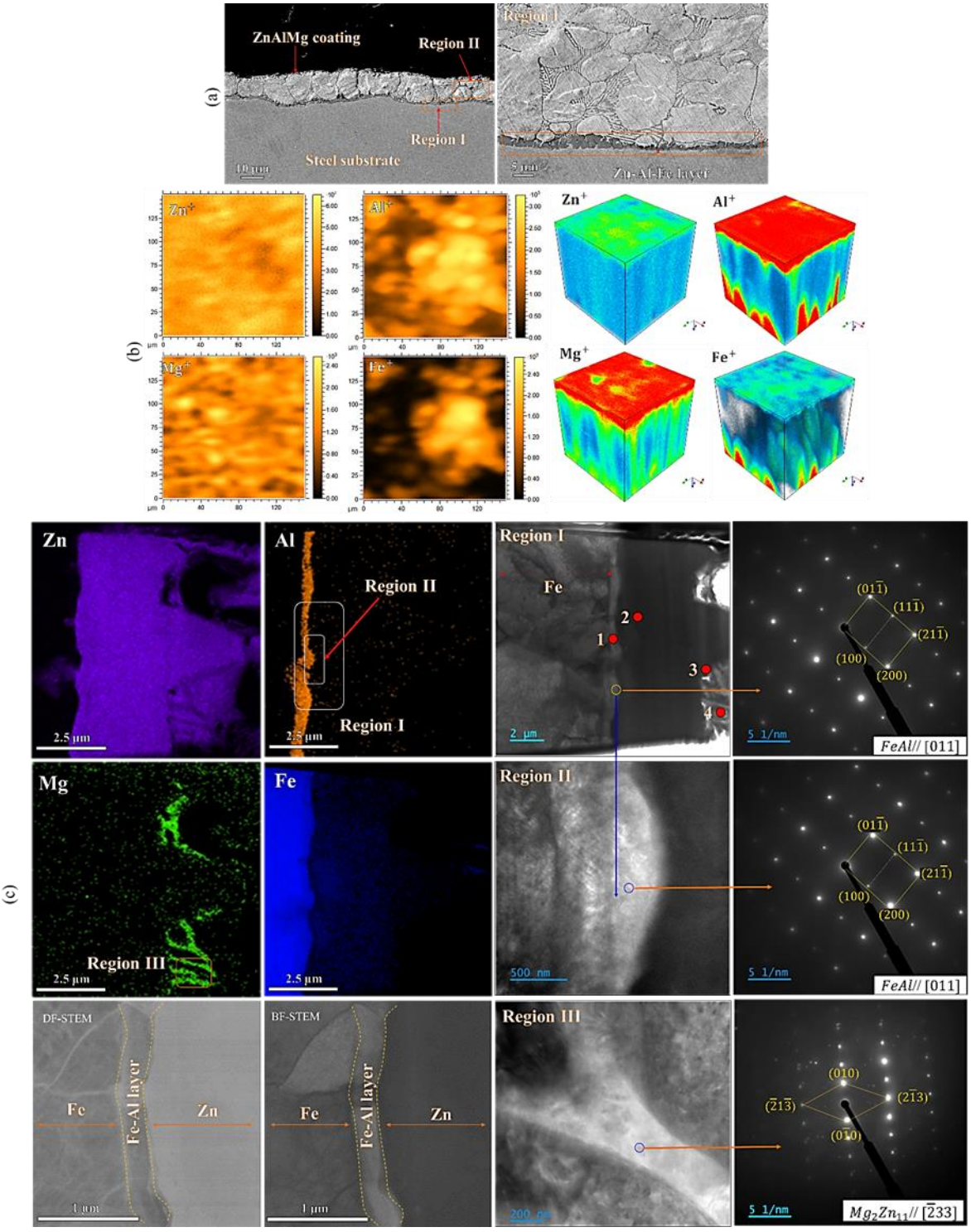

Figure 5.8 (a) SEM micrograph of the sample after HTTing at 800 °C, (b) the corresponding 2D and 3D ToF-SIMS analysis of Zn^+, Al^+, Mg^+, and Fe^+ elements in the coating sample, and (c) STEM micrographs and EDS elemental analysis and corresponding selected area diffraction (SAD) patterns at different regions of the coating near the fracture surface.

Table 5.3 Composition of various areas of the sample test at 800 °C obtained using EDS analysis (see Figure 5.8 (c), Region (I) for the location of each point)

Region	Zn (wt.%)	Al (wt.%)	Mg (wt.%)	Fe (wt.%)
1	35.87	2.79	0.04	61.29
2	85.62	0.31	0.07	13.99
3	91.89	0.50	1.21	6.40
4	94.70	0.00	1.78	3.53

Figure 5.9 (a) shows the SEM micrographs of the coating at 900 °C. The eutectic structure that was observed in the coating at 700 °C and 800 °C had completely coalesced and dissolved into the bulk structure of the coating at 900 °C. The microstructure of the coating contained dark, spherical grains (composed of Zn, Al, and Fe, as determined by EDS analysis) dispersed throughout the Zn matrix. Most importantly, an inhibition layer containing Fe, Zn, and Al was observed at the interfacial area between the coating and the steel substrate. As observed by ToF-SIMS analysis (Figure 5.9 (b)), the interfacial region contained a significantly higher concentration of Fe^{+} in the coating compared to what was observed at the previous temperatures. Additionally, the highest concentration of Al^{+} had segregated towards the coating/steel interface while Mg^{+} was highly concentrated towards the coating surface. The coating at 900 °C was analyzed using TEM, as shown in Figure 5.9 (c). In contrast to the previous testing temperatures, no eutectic phase was observed in the coating at this testing temperature, confirming that the lamellar eutectic structure dissolved into the coating matrix with the Mg and Al elements segregating towards the coating surface and the interfacial layer, respectively. The microstructure of this sample can be divided into three regions; (i) η-Zn, (ii) α-Fe, and (iii) Fe-Zn-Al interfacial area. EDS-point analysis of the different regions of the coating has been summarized in Table 5.4.

Table 5.4 Composition of various areas of the sample test at 900 °C obtained using EDS analysis (see Figure 5.9 for the location of each point)

Region	Zn (wt.%)	Al (wt.%)	Mg (wt.%)	Fe (wt.%)
1	0.00	0.00	0.00	100
2	6.7	0.11	0.04	93.15
3	16.24	0.20	0.00	83.57
4	73.83	0.16	0.00	26.00
5	2.28	0.08	0.00	97.63
6	26.29	0.67	0.00	73.04

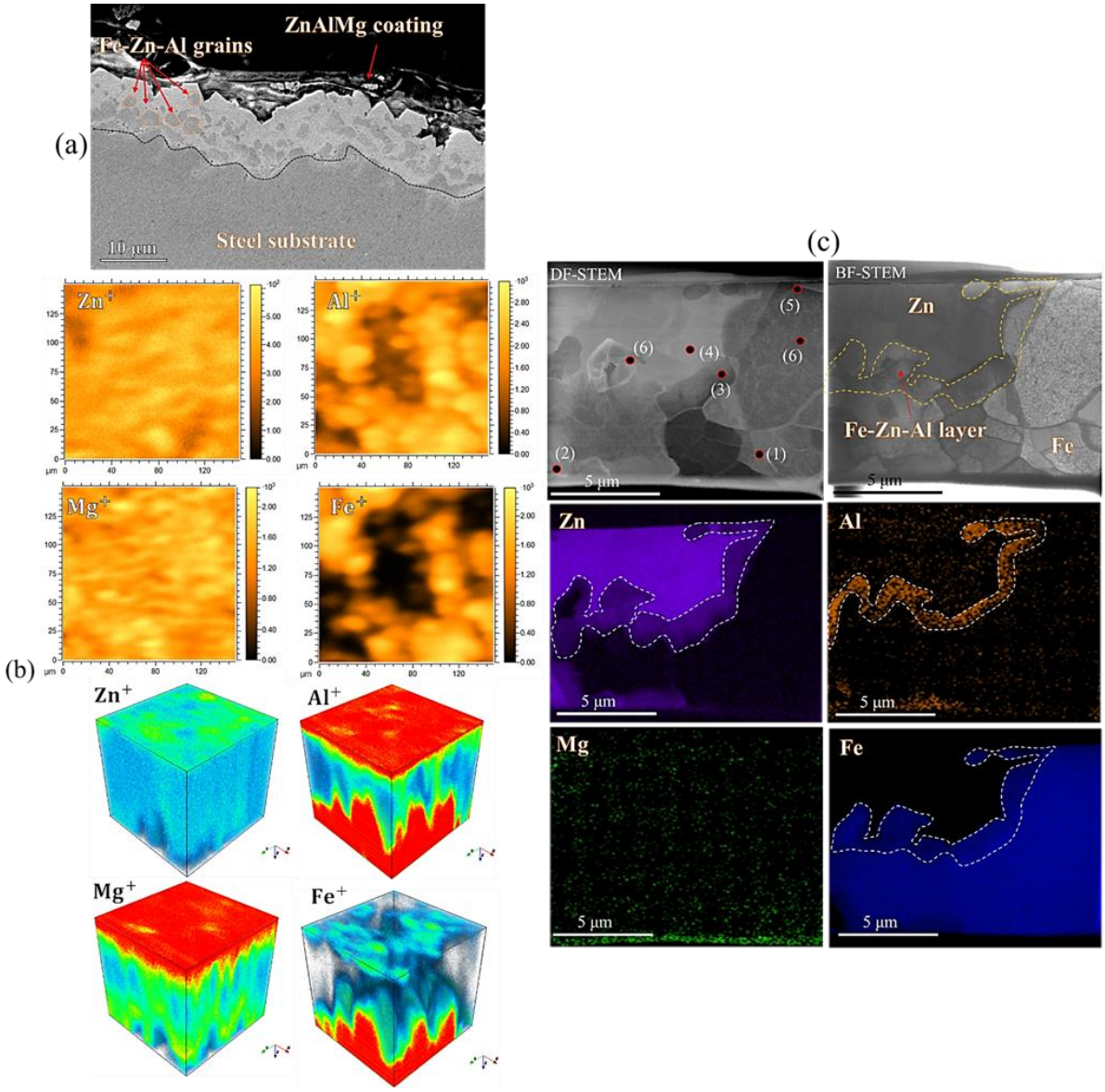

Figure 5.9 (a) SEM micrographs of the sample after HTTing at 900 °C, (b) ToF-SIMS analysis of Zn^+, Al^+, Mg^+, and Fe^+ elements by 2D and 3D images, and (c) dark-field STEM (DF-STEM) and Bright-field STEM (DF-STEM) images along with EDS elemental analysis of the ZnAlMg

The SAD patterns isolated from the regions of interest from within the coating have been shown in Figure 5.10. The SAD pattern acquired from Region (I) confirms the presence of the α-Fe(Zn, Al) phase. The α-Fe phase has been observed in Fe-Al and Fe-Zn binary systems with a cubic ($Im\overline{3}m$) lattice structure [160]. It has previously been shown in the literature that the α-Fe(Zn) layer can form during HTT by diffusion of Zn into Fe-substrates under extremely low strain rates (0.01 s^{-1}) [58] and prolonged holding times (20 minutes at 850 ˚C) [25]. However, the α-Fe(Zn, Al) layer observed in the present study has been formed at an exceedingly high heating rate (i.e., 1000 °C/s), high strain rate (i.e., 10 mm/s crosshead speed), and extremely short holding time (i.e., 0.5 s). The formation of the α-Fe(Zn, Al) phase in ZnAlMg coated steels at temperatures exceeding 850 °C, is a direct consequence of the severe segregation of

Al towards the Fe-substrate. The SAD pattern from the magnified area in Region (I) shows two distinct spots as shown in Figure 5.10 (Region (II)). The strong diffraction spots were indexed as α-Fe(Zn, Al) phase, similar to that observed in Region (I) Figure 5.10. The faint spots (identified by red arrows) are nano-sized precipitates that show an orientation relationship with the α-Fe(Zn, Al). On the other hand, Region III was acquired from the spherical dark grains which were dispersed in the η-Zn matrix (see SEM images in Figure 5.9), which were identified as the $Fe_8Zn_{87}Al_4$ phase, which possesses the γ′-brass structure with the space group $F\bar{4}3m$ [161].

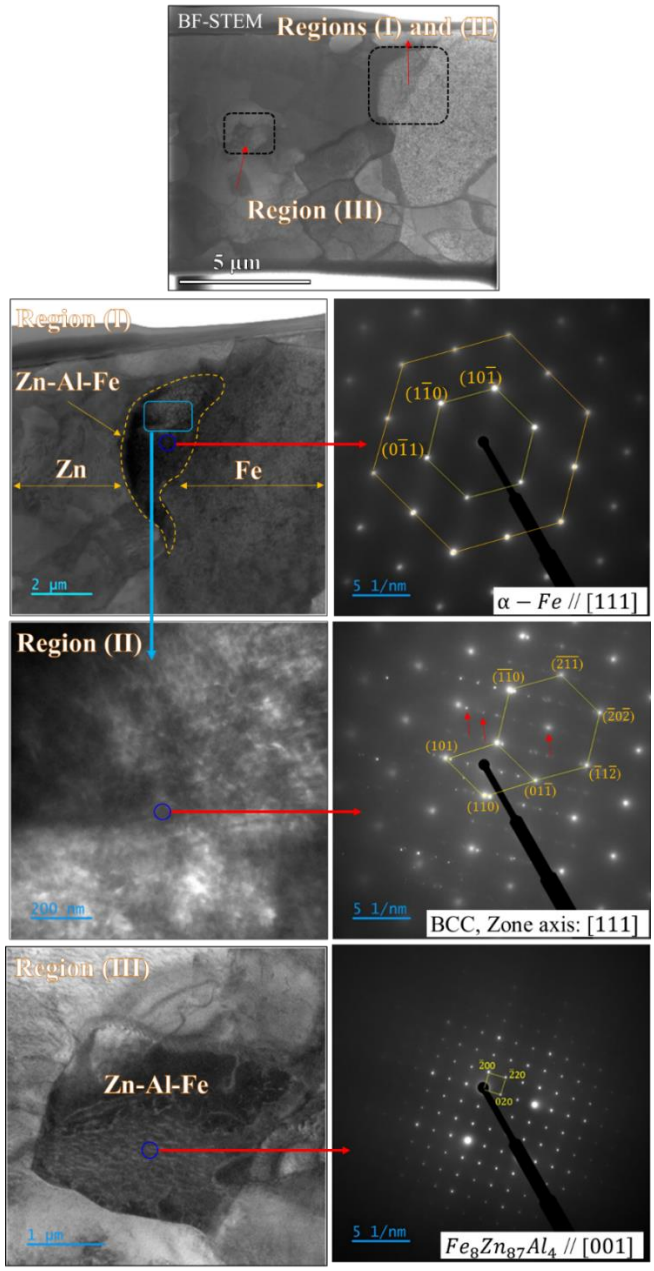

Figure 5.10 High magnification bright-field STEM (BF-STEM) images and corresponding selected area diffraction (SAD) patterns at different regions of the ZnAlMg coated sample after HTTing at 900 °C.

5.5 Discussions

It is known that direct contact between liquid metal and steel grain boundaries is essential for initiating LME because diffusion through the liquid phase occurs much more rapidly than it does in the solid-state [78,84,162]. Accordingly, the coating/steel interfacial region plays a critical role in defining the severity of LME cracking. It is well understood that the interfacial phase between the coating and substrate should generally possess two specific characteristics to act as an effective inhibition layer that prevents direct contact between liquid metal and the substrate. First, the interfacial phase should possess a high melting point, and second, it should maintain its integrity under the application of tensile stress. Figure 5.11 presents a schematic illustration of the microstructural evolution during HTT along with the interfacial reactions that lead to the formation of LME cracks at various temperatures. Upon solidification at 700 ˚C, a thin and irregular Al/Fe_2Al_{15} layer was formed at the coating/steel interface. When the temperature was increased to 800 ˚C, a uniform AlFe layer was identified at the interfacial area instead. Finally, it was observed that the eutectic structure of the coating completely dissolved into the Zn-matrix and was replaced by a composite structure consisting of $Fe_8Zn_{87}Al_4$ particles embedded in the Zn matrix following solidification at 900 °C, with the formation of a coherent interfacial α-Fe(Zn, Al) layer between the substrate and coating.

From the results presented in this work, it is clear that the thin and uneven α-Al/Fe_2Al_5 layer that formed at 700 °C did not provide an effective inhibition layer which could prevent the direct contact of liquid metal with the steel substrate. Furthermore, the LME results confirmed that the FeAl layer that formed at 800 °C had better performance than the α-Al/Fe_2Al_5 layer in mitigating LME but it was unable to withstand the hot tensile testing conditions at this temperature, resulting in the Fe substrate being exposed to the liquid metal leading to LME. However, the presence of the uniform α-Fe(Zn, Al) inhibition layer at the interface of the coating and substrate at 900 °C completely prevented contact between the liquid metal and the underlying steel, leading to complete suppression of LME. Additionally, the presence of dispersed $Fe_8Zn_{87}Al_4$ particles with a significantly higher melting temperature kept the α-Fe(Al, Zn) layer intact during tensile loading, effectively preventing the liquid Zn from coming into contact with the steel substrate. It is pertinent to note that the previously reported α-Fe(Zn) layer was formed by the bulk diffusion of Zn in Fe, triggered by extremely slow heating rates, prolonged holding times, and slow strain rates, resulting in a layer that could not prevent LME at high temperatures and was broken into small particles under the application of a tensile load [86]. The newly observed α-Fe(Zn, Al) inhibition layer, analyzed as part of this study, was a solid solution of Al and Zn in the Fe-substrate, which acted as a highly effective barrier between the molten Zn and the steel substrate, significantly minimizing the risk of LME at elevated temperatures during extreme hot-working conditions.

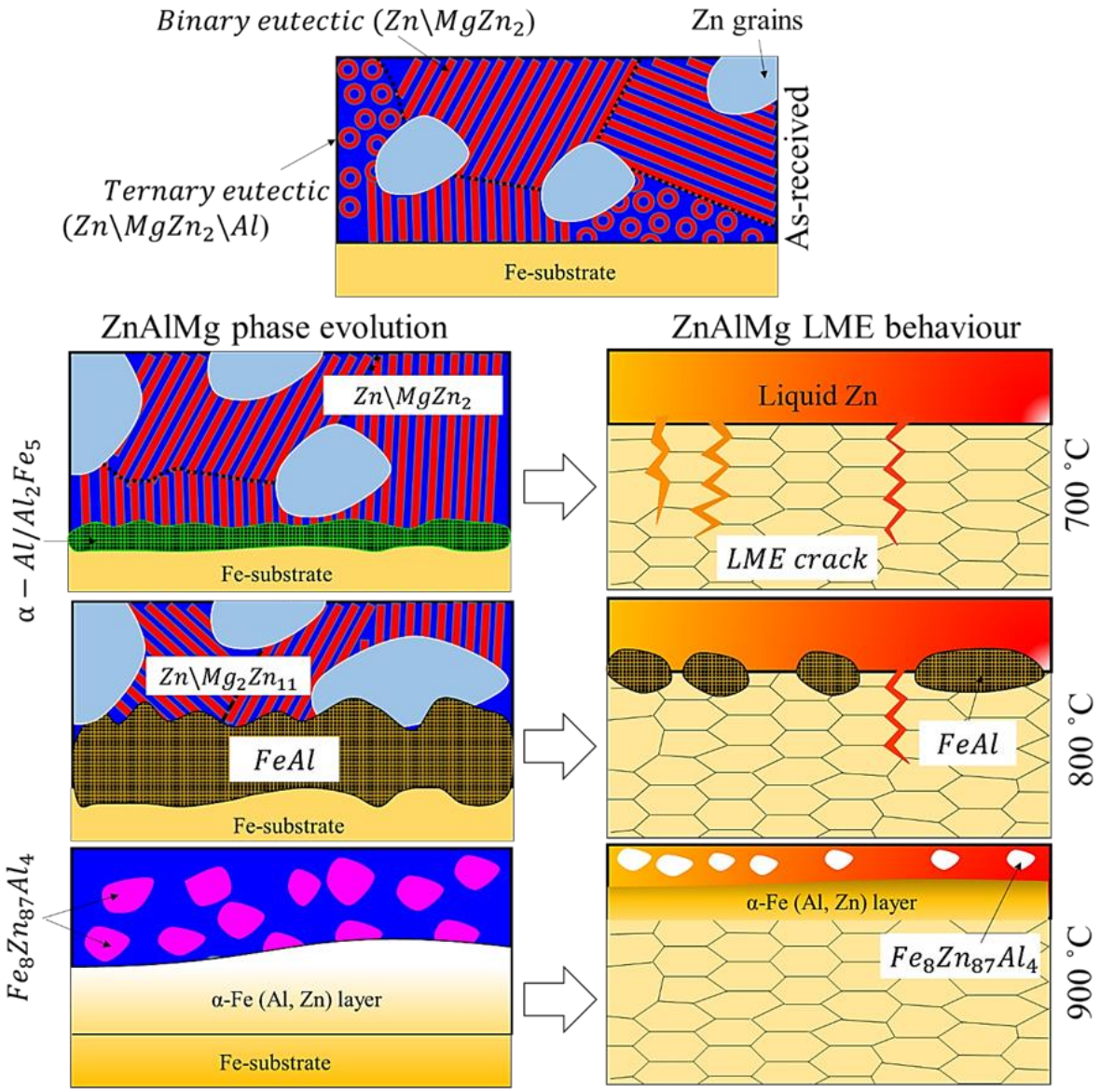

Figure 5.11 Schematic representation of the evolution of the coating's microstructure at various hot-tensile temperatures and its impact on LME crack formation; Images on the left demonstrate the high-temperature phase evolution of the ZnAlMg coating, while images on the right illustrate the effect of various inhibition layers on the formation of LME cracks. In the case of the α-Fe(Zn, Al) inhibition layer, direct contact has been prevented between the liquid Zn and the Fe-substrate. This has resulted in the complete mitigation of LME at 900 °C.

The role of interfacial layers between the coating and substrate on their respective potential for reducing LME was analyzed using thermodynamics and adhesion. The interdiffusion fluxes in the ternary ZnAlFe system were calculated with Fe as the dependent component (c.f. Equation 5.3). Figure 5.12 shows the concentration profiles and the calculated diffusion fluxes for the temperatures of interest. The interdiffusion flux of Zn was positive, while it was negative for the Fe at all temperatures, implying that the overall diffusion path in this system goes from the Zn-coating towards the Fe-substrate, due to the concentration gradient of these elements. In the case of Al, however, the interdiffusion flux had positive and negative values in either

direction of the thermodynamic gradient. During the transition from negative to positive values, the interdiffusion flux went through a zero value (i.e., region of zero flux), commonly referred to as a zero-flux plane (ZFP) [152,163,164]. The ZFP indicates that the flux of one component can be zero and it can change directions at different locations due to thermodynamic and kinetic interactions with other components [150]. Effectively, the idea of the ZFP shows that an element in a multi-element alloy system can inter-diffuse in either direction up to its thermodynamic gradient [164]. As shown in Figure 5.12, the value of the interdiffusion flux for Al is low in both the negative and positive directions at 700 °C. However, at 800 °C, the values of interdiffusion fluxes in both directions of the ZFP are higher than at 700 °C, indicating that Al has a greater tendency to diffuse along its thermodynamic gradient at this temperature. These results are consistent with the ToF-SIMS analysis (Figure 5.8), which clearly showed that Al segregated toward the surface of the coating as well as towards the Fe substrate. At 900 °C, the value for the negative interdiffusion flux of Al was less than the positive value, indicating that interdiffusion occurred predominantly towards the Fe-substrate. Thus, the higher interdiffusion rate of the Al component towards the Fe substrate contributed to the formation of the α-Fe(Zn, Al) interfacial phase. Using the information obtained directly from the ZFP compositions, the ratio of interdiffusion coefficient can be calculated. Since the interdiffusion flux was zero at the ZFP, Equation 5.3 can be written as follows [165]:

$$\tilde{J}_{Al} = -\widetilde{D}^{Fe}_{AlZn}\frac{\partial C_{Zn}}{\partial x} - \widetilde{D}^{Fe}_{AlAl}\frac{\partial C_{Al}}{\partial x} = 0 \qquad \text{Equation 5.4 (a)}$$

$$\frac{\partial C_{Zn}}{\partial C_{Al}}\Big]_{ZFP} = -\frac{\widetilde{D}^{Fe}_{AlZn}}{\widetilde{D}^{Fe}_{AlAl}} \qquad \text{Equation 5.4 (b)}$$

The slope of the interdiffusion path at the ZFP point yields the ratio of the interdiffusion coefficients, which was determined as -1.79 and -5.8 for 700°C and 800°C, respectively. Those values indicate that the interdiffusion coefficient of $\widetilde{D}^{Fe}_{AlZn}$ is larger in magnitude, but opposite in sign compared to the main coefficient $\widetilde{D}^{Fe}_{AlAl}$. This showed that the interdiffusion of Al in the positive direction along a Zn gradient is strongly favored, whereas the Al flow down the Zn gradient is considerably reduced. This results in the development of regions showing a change in the sign of $\tilde{J}_{Al}$, as shown in Figure 5.12.

On the other hand, diffusion is not the only factor that affects LME, as the adhesion of the interfacial layer under applied tension stress must also be considered. The adhesion of different IMC phases to the steel substrate at the coating/steel interface is one of the most important factors controlling the mechanical degradation of the coating during deformation [156,166].

The adhesive energy between the Zn-coating and the Fe-substrate can be determined by using the work of adhesion (W_{Ad}) [156,166]:

$$W_{Ad} = \gamma_A^S + \gamma_B^S - \gamma_{A-B}^I \qquad \text{Equation 5.5}$$

Where γ_A^S and γ_B^S are the surface energy of the coating (A) and substrate (B), respectively. The γ_{A-B}^I is the interfacial energy between A and B and the surface energy is defined as [156,166]:

$$\gamma_{A_1 \ldots A_m}^S = \sum_{i=1}^{m} C_{A_i}^S \gamma_{A_i}^S - \sum_{i=1}^{m-1} \sum_{j=i+1}^{m} C_{A_i}^S C_{A_j}^S \frac{\Delta H_{A_i \, in \, A_j}^I}{C_0 V_{A_i}^{2/3}} \qquad \text{Equation 5.6}$$

where $C_{A_i}^S$ is the surface fraction of the atom A_i, $\Delta H_{A_i \, in \, A_j}^I$ is the enthalpy change upon the solution of one mole of A_i in A_j, V_i is the volume fraction of element i and C_0 is a constant that relates the atomic volume to the atomic surface area in an atomic cell. For a given A-B interface, the enthalpy change can be defined as [166]:

$$\Delta H_{A \, in \, B}^I = \frac{V_A^{2/3}}{\left(n_{WS}^{-1/3}\right)_{ave}} \left[-P(\Delta\phi^*)^2 + Q \left(\Delta n_{WS}^{\frac{1}{3}} \right)^2 \right] \qquad \text{Equation 5.7}$$

Where ϕ is the electronegativity and n_{WS} is electron density. A negative enthalpy change indicates that an alloy AB is formed, while a positive enthalpy change indicates that the formation of alloy AB is unfavorable [166]. The value of $\Delta H_{A \, in \, B}^I$ for Al and Zn in Fe are $-79 \, kJ/mol$ and $-13 \, kJ/mol$, respectively [167]. Consequently, when Al and Zn are incorporated into an Fe-substrate, interfacial energy (γ_{A-B}^I) decreases, which ultimately increases the work of adhesion between Al/Fe and Zn/Fe interfaces (c.f. Equation 5.5). On the contrary, the value of $\Delta H_{A \text{ in } B}^{\text{I}}$ for Mg in Fe is $+54 \, kJ/mol$, indicating that Mg decreases the surface energy while generating positive interaction energy, whereby decreasing the work of adhesion. The results of this analysis were entirely consistent with the elemental distribution analysis shown by ToF-SIMS results, where it was observed that as the temperature was increased, Al showed a strong tendency to segregate towards the Fe substrate whereas Mg tended to segregate towards the surface of the coating.

Using Equation 5.4 and Equation 5.5 and the associated EDS data, the value of W_{Ad} was calculated to assess the effectiveness of the interfacial layers for LME crack suppression at

different temperatures. For the Fe-substrate with α-Al/Al_2Fe_5, FeAl, and α-Fe(Zn, Al), the W_{Ad} values were calculated to be 4.62 J/m^2, 5.73 J/m^2 and 7.70 J/m^2, respectively. Song et al. [166] indicated that the coating will delaminate from the substrate if the energy release rate (G) was greater than the fracture energy at the interface (Γ). The interfacial fracture energy for a metallic coating system includes two types of energies: elastic energy, Γ_e, and the plastic energy, Γ_p, (i.e. $\Gamma = \Gamma_e + \Gamma_p$), with Γ_e representing the energy required to create free surfaces in both materials without any plastic deformation, which can be equal to W_{Ad}, such that $\Gamma = W_{Ad} + \Gamma_p$. Since it is well known that the plasticity of the steel substrate (Γ_p^S) is greater than that of the brittle IMC layer forming at the interface it can be said that the W_{Ad} determines the fracture energy between the interfacial layer and the steel substrate. As shown clearly by the calculations, the α-Fe(Zn, Al) layer had the highest W_{Ad} value compared to other interfacial layers. Consequently, it can be concluded that this layer was the most effective in preventing the direct contact between liquid metal from the coating with the steel substrate during hot working conditions because it has the highest tendency to remain intact when exposed to elevated temperatures and stress conditions.

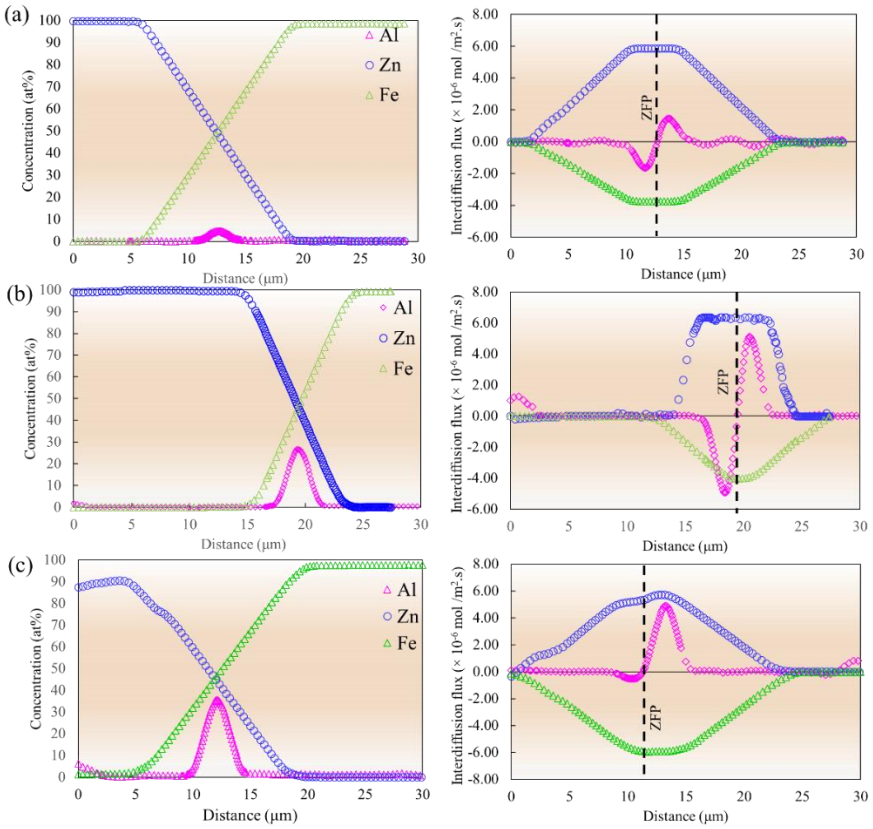

Figure 5.12 Composition profiles and calculated interdiffusion fluxes mass of Zn at different hot-tensile testing temperatures; (a) 700 ˚C, (b) 800 ˚C, and (c) 900 ˚C (ZFP refers to as zero-flux plane)

5. 6 Summary

The present study provides a comprehensive analysis of the phase evolution of ZnAlMg coated steel at elevated temperatures to investigate the LME cracking behavior of the coating. Although the ZnAlMg coating was highly susceptible to LME cracking at 700 °C, the coating offered extremely high resistance to LME cracking at 900 °C, which is traditionally recognized to be the most critical temperature for LME susceptibility for the Fe-Zn couple. This significant reduction of LME susceptibility was due to the unique phase evolution of the ZnAlMg coating at high temperatures. The findings of this work highlight the importance of protective Zn-based coatings that have a tendency to produce effective inhibition layers at the coating/steel interface at high temperatures which assist in greatly diminishing the severity of LME in automotive steels. By investigating the reasons behind the strong resistance to LME-induced cracking in ZnAlMg coated steels at high temperature, the study provides an effective roadmap that can be used in the future design and production of Zn-based coatings that are LME resistant.

Chapter 6 : Discussion on the correlation between the crack mechanism and crack susceptibility[1]

6.1 Overview

This chapter aims to establish a correlation between all the points covered in the preceding chapters to explore the application of the proposed model to study LME cracking during resistance spot welding (RSW), which is one of the most widely used welding technologies for joining advanced high-strength steels in the automotive industry. This chapter also provides a detailed description of the underlying mechanism of LME to explain the role of certain metallurgical characteristics of steel substrates in determining the susceptibility to LME cracking.

6.2 Study LME cracking in ferritic and austenitic steels during RSW process

6.2.1 Background and experimental procedure

This section presents a systematic analysis of the LME cracking behavior of fully ferritic and fully austenitic microstructures under the same thermomechanical conditions during the RSW process. The as-received materials were electro-galvanized 439-type (0.03C-1.00Mn-1.00Si-0.20Ti-(17-19)Cr (wt.%)) and 304-type (0.08C-2.00Mn-0.75Si-(8-12)Ni-(18-20)Cr (wt.%)) stainless steels with a nominal thickness of 1.0±0.1 mm. Samples were subjected to a thermomechanical cycle of RSW using an electrode force of 4 kN, welding time of 250 ms, and holding time of 167 ms. Cu-Cr dome radius type electrodes with a 6 mm tip diameter with a constant cooling water rate of 6 L min^{-1}. Microstructural characterization was conducted by scanning electron microscope (SEM, JSM7001F), energy-dispersive spectroscopy (EDS), and electron backscatter diffraction (EBSD) methods. A high-speed Hikari CCD camera was used for pattern acquisition at 0.1 μm step size. A transmission electron microscope (TEM) equipped with an electron energy loss spectroscopy (EELS) analytical facility was used for further LME crack characterization. TEM samples were prepared via focused ion beam (FIB) with an NVision 40 from Zeiss with 30 keV Ga ions. High-angle annular dark-field (HAADF) micrographs were captured using an FEI Titan 80-300HB operating at 300 keV.

6.2.2 Results and discussions

Figure 6.1 (a) depicts EBSD micrographs of the as-received steels. The image quality (IQ) map shows that the fraction of low-angle (red lines) and high-angle (blue lines) grain boundaries (GB) in Fe-BCC is approximately 24% and 76%, respectively. Furthermore, most of the GB (i.e. 96 %) present in the Fe-FCC sample are high-angle of which 51% of them are characterized

[1] This chapter (Section 6.2) consists of the published manuscript in Materials Letters, Ali Ghatei-Kalashami, Ehsan Ghassemali, Chris DiGiovanni, Frank Goodwin and Norman Y. Zhou, Vol. 324, 2022.

as $\sum 3 : < 111 > 60^{\circ}$ boundaries (green lines). Inverse pole figure (IPF) maps show single ferritic and austenitic phases with an average grain size of 21.1(±10.2) µm and 7.73(±5.27) µm, respectively. The EBSD maps in the vicinity of LME cracks (Figure 6.1 (b)) show that LME cracks have propagated along high-angle GB in both microstructures. Moreover, the crack has not propagated between the $\sum 3$ boundaries, similar to what has been reported in the literature [79]. Figure 6.1 (c) provides a qualitative LME crack analysis in terms of the average crack number and average crack length. The Fe-BCC specimen has a higher crack number, whereas the Fe-FCC sample has a much longer average crack length. As described in the previous chapters, LME cracking occurs in two distinct stages: (i) crack initiation and (ii) crack propagation. Upon initiation stage, embrittler atoms diffuse into GB, decreasing GB cohesion and leading to LME crack formation. At this stage, the average number of LME cracks can represent the severity of crack initiation. Once the crack is formed and liquid Zn flows into the crack, embrittler atoms transport from the crack tip to the GB, where the LME crack spreads rapidly throughout the entire GB network. Accordingly, the average LME crack length can be used as an indication of the LME crack propagation rate. According to Figure 6.1 (c), the Fe-BCC specimen exhibited higher severity to crack initiation and a lower crack propagation rate than that of the Fe-FCC specimen. The results are completely consistent with those presented in Chapter 4.

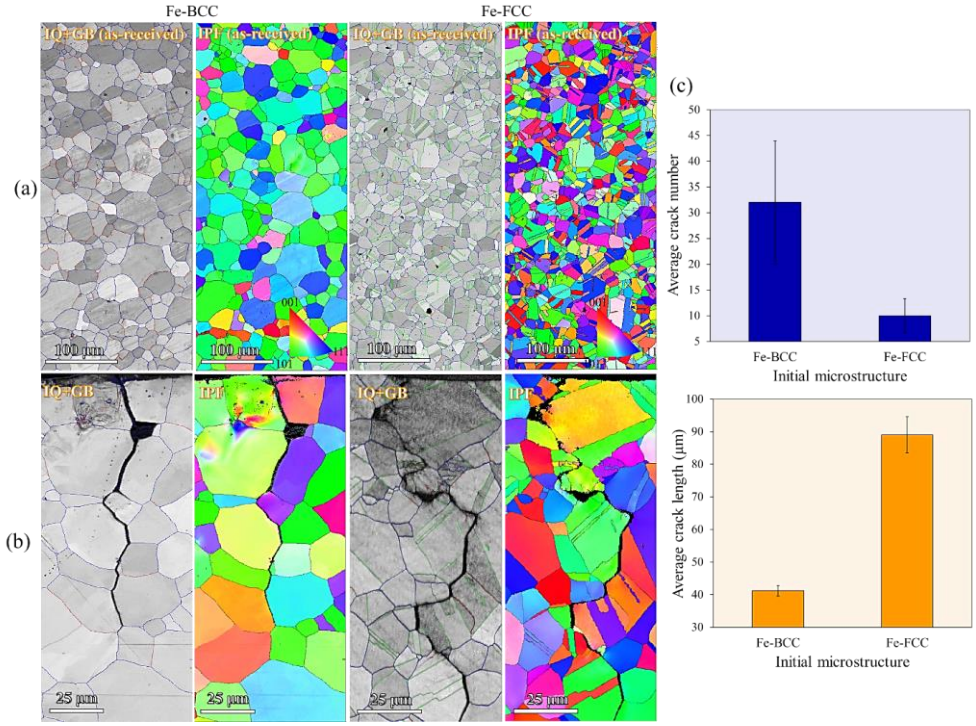

Figure 6.1 (a) EBSD maps of the as-received ferritic (Fe-BCC) and austenitic (Fe-FCC) steels, (b) EBSD maps in the vicinity of LME cracks, and (c) comparison in average LME crack number and LME crack length in investigated ferritic and austenitic steels under the same thermomechanical cycle

The dissimilar joint configuration (ferritic/austenitic) was studied to determine whether the crack propagation path is influenced by ferritic or austenitic microstructures. Figure 6.2 depicts the EBSD and EDS-Zn maps of the Fe-BCC/Fe-FCC interfacial area. While cracks are present on both sides, the crack on the Fe-FCC side is much longer than that of the Fe-BCC side. Additionally, the EBSD phase map shows the presence of a fully ferritic structure (green regions) within the LME crack at the Fe-FCC side. The EBSD-IPF and the corresponding EDS-Zn maps confirm the Fe-BCC structure is the α-ferrite (α-Fe(Zn)) layer inside of the Fe-FCC side. Since Zn is a strong ferrite stabilizer, its diffusion into austenite GB results in the austenite-to-ferrite transformation [26]. It was shown that the Zn bulk diffusivity in Fe-BCC is higher than that in Fe-FCC [26,65], hence, the austenite to ferrite transformation accelerates the rate of Zn diffusion and facilitates crack propagation rate.

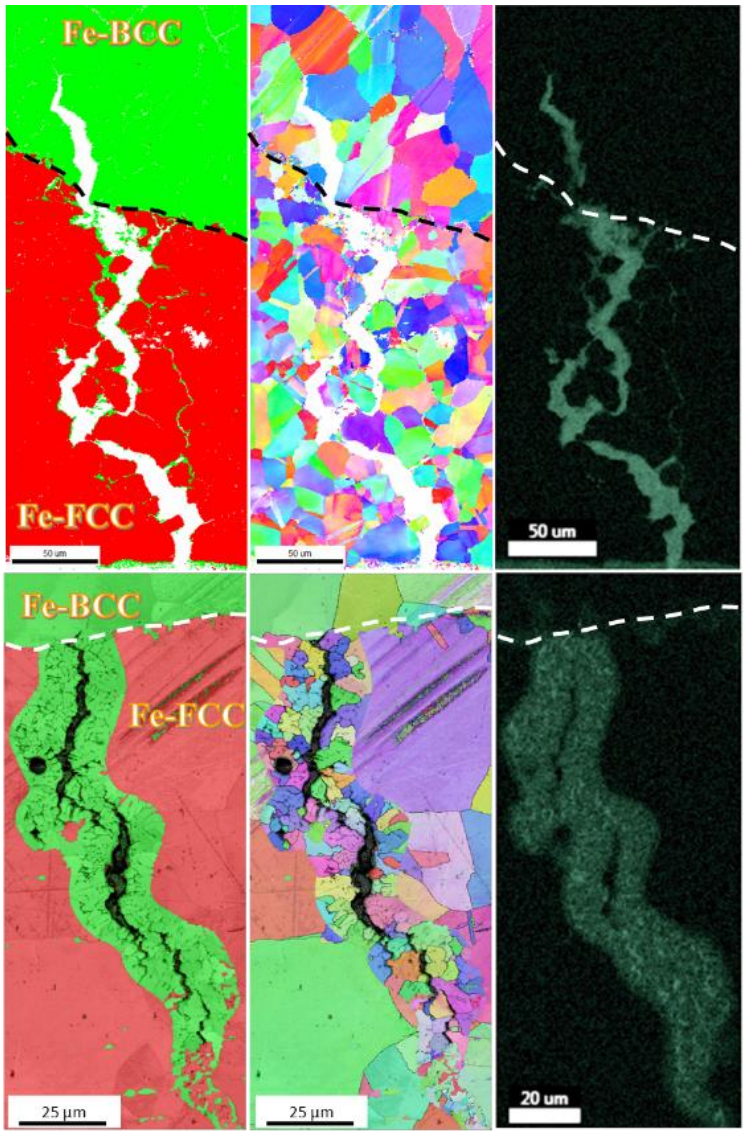

Figure 6.2 EBSD-IPF and the corresponding EDS-Zn maps of the interfacial area in ferritic/austenitic dissimilar joint

To characterize elemental distribution along LME crack in Fe-BCC steel, HAADF imaging, and EELS analysis were conducted as depicted in Figure 6.3. It is seen that the Zn penetration is only observed in regions with Cr-depletion and that no penetration of Zn can be detected in the area containing Cr (white arrows in Figure 6.3). It can also be observed that Ti is completely segregated on the edge of GB, while Ni is completely dissolved into Zn.

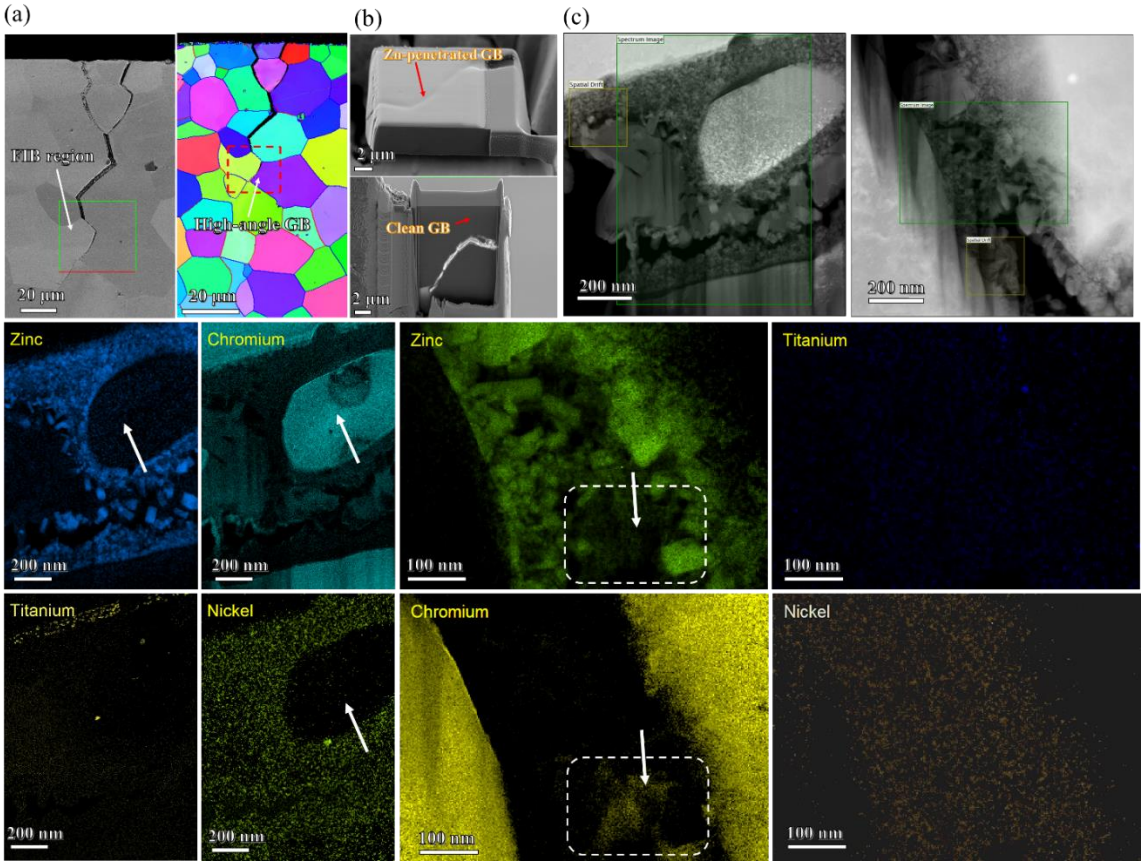

Figure 6.3 (a) SEM micrograph and corresponding EBSD-IPF map in the vicinity of LME crack in Fe-BCC, (b) The FIB in-plane sample, and (c) TEM micrograph and corresponding EELS maps of Zn-penetrated boundary

The results showed that the ferritic specimen was more prone to LME crack initiation with a much higher frequency of smaller cracks observed in the sample. The austenitic microstructure had fewer cracks with a significantly higher LME crack propagation rate resulting in a much larger crack size. The results correspond perfectly with the results observed during the high temperature tensile test (i.e., Chapter 4) where it was shown that ferritic specimen was more sensitive to LME cracks initiation (i.e., the number of LME cracks); however, austenitic specimens exhibited a significantly higher rate of LME crack propagation.

6.3 Relationship between LME mechanism and susceptibility factors

In light of the results presented in previous chapters, Figure 6.4 summarizes the micro-scale events that occur during the initiation and propagation of LME cracks. Numerical modeling and

TEM analysis (Chapter 3) showed that the interdiffusion of Zn-embrittler atoms at grain boundaries resulted in the formation of a stress-induced diffusion wedge (SIDW) at the exposed tip of the grain boundary. The SIDW generated a sinusoidal stress field perpendicular to the length of the grain boundary whose magnitude and amplitude were dependent on time and temperature. The formation of the SIDW provided the thermodynamic driving force needed to trigger a critical degree of diffusion of the Zn-embrittler atoms, resulting in the subsequent melting of the SIDW. The wedge-induced stress field caused an expansion in the size of the wedge which eventually led to the initiation of LME. Following crack initiation, Zn atoms diffused from the crack tip to the grain boundary network based on the stress-assisted grain boundary diffusion mechanism (Chapter 4). Furthermore, the segregation of alloying elements such as Cr at grain boundaries, along with the co-segregation of other alloying elements, made the grain boundary region more susceptible to cracking and contributed to LME crack propagation.

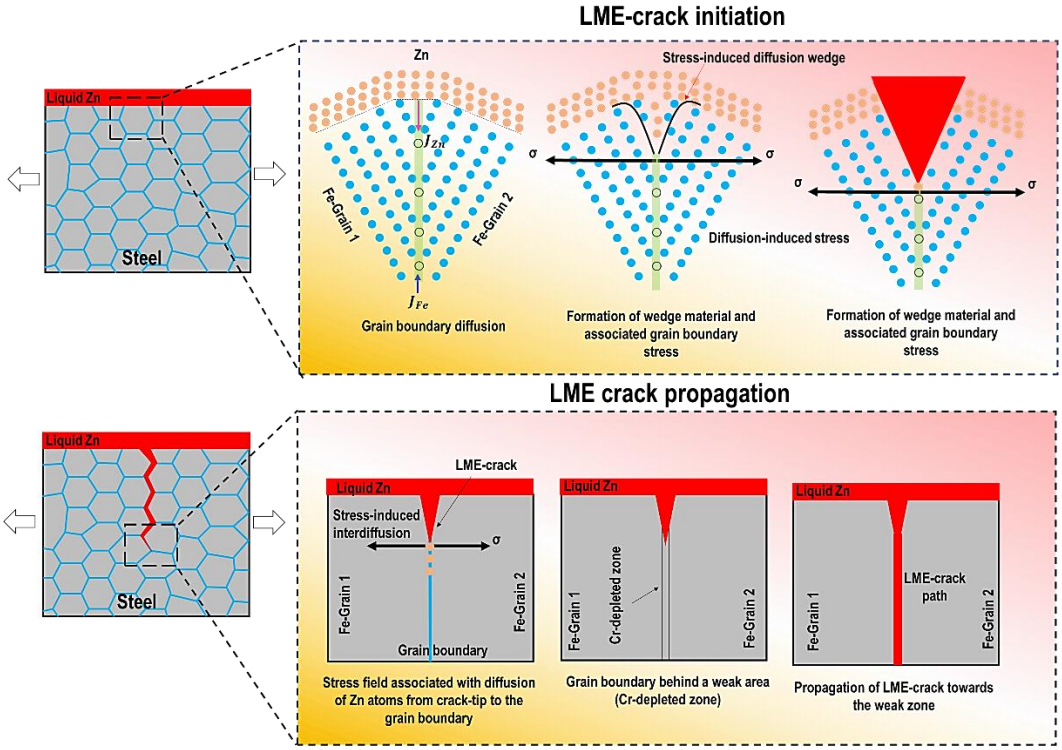

Figure 6.4 Schematic illustration of microscale events during liquid metal embrittlement crack initiation and propagation.

The results presented in this study show that the proposed model can be used as an effective tool to predict the impact of factors such as grain boundary diffusivity, stress, and temperature on LME crack susceptibility which can help mitigate LME-related issues in mass production applications. Based on the model presented in this study, it is evident that by increasing the grain boundary diffusivity of Zn, the susceptibility to LME cracking in the Fe-Zn couple increases. As shown in Figure 6.5, decreasing D_{gb}^{Fe}/D_{gb}^{Zn} (by increasing D_{gb}^{Zn}) or increasing

temperature can result in the generation of a high tensile stress applied to the grain boundary plane which would eventually increase the likelihood of an LME crack event. Therefore, the occurrence of LME cracking during the RSW process in the investigated austenitic and ferritic specimens can be effectively explained by the proposed mechanism in this study. Indeed, the austenitic microstructure has a higher grain boundary diffusion coefficient of Zn than the ferritic microstructure [7,28,65], resulting in a higher crack propagation rate in this sample compared to the ferritic specimen. Additionally, the austenitic microstructure has a higher thermal expansion coefficient (TEC) compared to the ferritic specimen [168], which leads to a generation of higher tensile stresses during the RSW process after non-equilibrium cooling, which ultimately contributed to an increase in the likelihood of LME crack formation. The results clearly showed that the effect of the contributing factors on the LME crack susceptibility predicted by the model was highly consistent with observations made under different thermomechanical conditions, including the high temperature tensile test (i.e., Chapter 4) and the RSW process (i.e., Chapter 6).

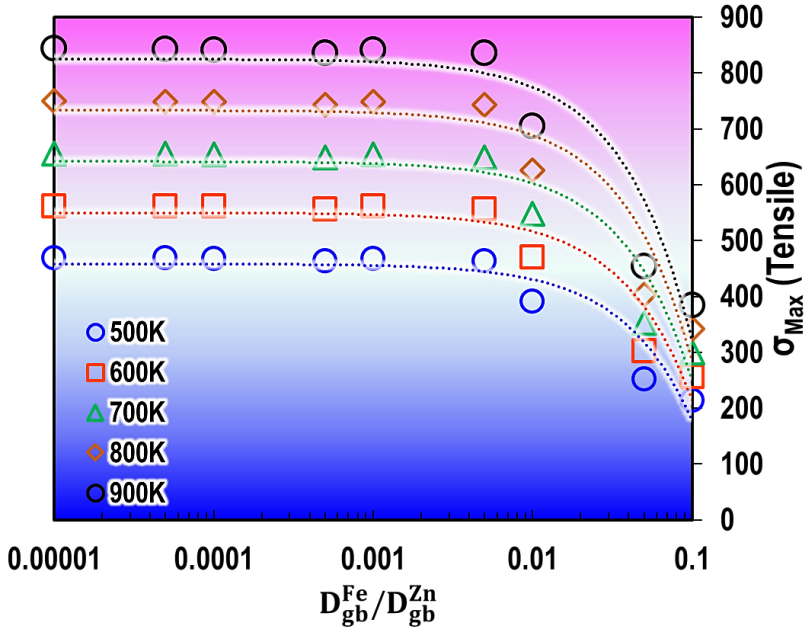

Figure 6.5 The calculated maximum tensile stress acting on the grain boundary plane with respect to the grain boundary coefficient ratio ($\theta = D_{gb}^{Fe}/D_{gb}^{Zn}$) for a common Fe-based for different temperatures ranging from 500K to 900K (Copied from Figure 3.3 (c)).

This study also contributed to explaining the contradictory results regarding the influence of initial microstructure on LME cracking. Considering the low LME-induced crack propagation rate within ferrite (due to the lower grain boundary diffusion coefficient of Zn compared with austenite), a fully ferritic decarburization layer may be an effective method of reducing LME. In the presence of aggressive thermomechanical conditions during RSW, however, numerous cracks may propagate rapidly, resulting in increased LME susceptibility as shown in this section and as discussed in Chapter 2 and Chapter 4 regarding the possibility of LME occurring in the

decarburization layer [45]. Furthermore, the diffusion nature of the LME cracking phenomenon and the Fe-Zn reaction at high temperatures can be an effective method to develop strategies for mitigating LME at high temperatures. According to the results presented in Chapter 5, the segregation of alloying elements in the Zn coating can result in the formation of the α-Fe (Al, Zn) layer which effectively prevented the direct contact between liquid metal and Fe substrate, thus preventing the formation of the LME cracks.

Chapter 7 : Conclusions and potential areas of future research

7.1 Conclusions

The present study provided new insight into the precursor events leading to liquid metal embrittlement (LME) cracking in the Fe-Zn system. In addition, the study provided a systematic analysis of the LME crack propagation path in two ferritic and austenitic microstructures and established a correlation between the underlying mechanism of LME crack propagation and the influence of metallurgical factors such as initial microstructure, grain boundary characteristics, and grain boundary chemistry on the severity of LME cracking. Lastly, this thesis provided a detailed investigation into the LME cracking behavior of the ZnAlMg coating and provided a roadmap that can be used in the future to design and produce ZnAlMg coatings that are resistant to LME cracking. Based on a thorough understanding of the LME mechanism and factors affecting its susceptibility, this study examined effective solutions to mitigate LME cracking in the Fe-Zn system. The following conclusions can be made from the present study:

(1) The results presented in Chapter 4 showed that the LME crack initiation happens through the stress-assited grain boundary diffusion mechanism. The diffusion of Zn atoms along the grain boundaries of the Fe-substrate led to the formation of a stress-induced diffusion wedge (SIDW) along the grain boundary. The formation of the SIDW generated a sinusoidal distribution stress field perpendicular to the grain boundary plane. Atomic-scale analysis of the early stages of LME formation showed that the interface between the Zn-penetration layer and the Fe-substrate exhibited curvature and the penetration layer appeared to have a clear wedge-shaped profile along the grain boundary. The results of numerical simulations and the experimental observations revealed that LME initiation entails several steps, including (i) solid-state grain boundary diffusion, (ii) formation of the SIDW, (iii) eventual melting of the SIDW, and (iv) opening of the liquid wedge due to interdiffusion and the application of externally applied stresses.

(2) A comprehensive analysis of the LME-induced fracture surfaces and LME crack morphology revealed that stress-induced grain boundary diffusion was the most probable underlying mechanism for LME crack propagation in both ferritic and austenitic microstructures. Additionally, the results showed that both Zn-coated ferritic and austenitic microstructures were found to be sensitive to the formation of LME cracking. The ferritic microstructure was more prone to LME crack initiation with a relatively low LME crack propagation rate. The austenitic microstructure was resistant to crack initiation but had a significantly higher LME crack propagation rate. The failure analysis revealed that the ferritic specimen exhibited a hybrid failure mechanism with a ductile fracture mode from one side and LME-induced failure from the Zn-coated side. The austenitic specimen displayed a completely brittle failure mode, as a result of LME-induced cracking. It was found that the depletion and

co-segregation of alloying elements such as Cr, Mn, and Ni result in a decrease in grain boundary cohesive energy and lead to LME crack propagation. The results obtained in this study resolved contradictions regarding the role of initial microstructure on LME cracking and also defined a new perspective for the term "LME susceptibility" in the iron-zinc (Fe-Zn) system. The results also provided a new pathway for advancing LME-resistant materials using microstructural modification techniques.

(3) The present study evaluated the LME crack susceptibility of ZnAlMg coated steel and established a correlation between high-temperature phase evolution and the LME cracking severity. The results revealed that the susceptibility to LME cracking in ZnAlMg coating decreased with increasing high temperature testing temperature. The microstructure near the fracture surface of the sample tested at 700 ˚C revealed a non-uniform and thin layer of α-Al/Al_2Fe_5 layer at the interface between steel and coating. Due to the absence of a coherent inhibition layer at the coating/steel interface, severe LME cracking was observed at this testing temperature, which resulted in a loss of ductility in the sample. In the samples tested at 800 ˚C, a uniform and thin layer of FeAl was observed that provided some resistance to LME. However, despite the improved resistance to LME cracking at 800 ˚C compared to 700 ˚C, LME cracking occurred due to the ease with which the FeAl layer broke down under the application of the tensile load. Finally, the LME behavior of the coating at 900 ˚C showed that a uniform α-Fe(Zn, Al) layer was developed at the interfacial area which successfully mitigated the LME problem by inhibiting the direct contact of liquid metal with the steel substrate, which represented a novel observation that contributes to the body of knowledge regarding LME mitigation strategies.

7.2 Potential areas of future research

(1) While the present study provided a detailed understanding of the micro-scale events involved in LME crack formation, further research is necessary to shed light on the atomic-scale events involved in the initiation and propagation of LME cracks. However, due to the extremely rapid nature of LME cracking in the Fe-Zn system and the presence of intermetallic compounds within the cracks and interfacial region, it is exceedingly complicated to detect and characterize the atomic scale events occurring during crack initiation and propagation. It is therefore possible to use molecular dynamics (MD) simulations and density functional theory (DFT) calculations in conjunction with empirical analysis to investigate the underlying mechanisms of the occurrence of LME cracks in the Fe-Zn system. While the LME crack formation mechanism and the impact of alloying elements on the susceptibility of the grain boundary to embrittlement phenomenon have been notably investigated by DFT calculations [55,169,170], further investigation should be conducted, particularly with MD simulations, in order to better comprehend the atomistic mechanisms of LME cracking in Fe-Zn.

(2) Alloying elements such as B, Mn, V, Nb, etc. play an influential role in the microstructure and mechanical properties of steel substrates. Despite this, the impact of these alloying elements on the susceptibility to LME cracking is not adequately addressed in the literature. The clarification of this issue is critical since LME occurs at high temperatures in the Fe-Zn system, which implies that the segregation of alloying elements like B at grain boundaries can affect the alloy's susceptibility to intergranular cracking and zinc penetration. Consequently, a systematic study is required to investigate the impact of alloying elements on microstructural characteristics, mechanical properties, and their consequent effects on the severity of LME cracking. Advanced characterization techniques such as TEM-EELS and APT analysis are required to investigate the role of alloying elements on grain boundary cohesion/decohesion behavior.

(3) According to the results of this study, ternary ZnAlMg coating systems are capable of mitigating LME cracking at high temperatures. However, the effect of alloying elements of the Zn coating (e.g., Al, Mg, etc.) on LME cracking behavior at different temperatures has not been well investigated. A comprehensive investigation in this area can assist in developing a Zn-based coating that exhibits excellent corrosion behavior and is resistant to LME cracking under a wide variety of thermomechanical conditions.

(4) Recently, a novel approach known as "grain boundary segregation engineering (GBSE)" has been employed for the manipulation of internal interfaces of metallic materials to improve the materials' mechanical response to intergranular cracking. Grain boundary segregation is characterized by the inhomogeneous distribution of solute atoms between the grain boundaries and/or phase boundaries [171]. In this approach, the alloy is subjected to a diffusion heat treatment at temperatures below Ac_1 for different annealing times ranging from a few minutes to several hours. This specific heat treatment procedure leads to severe segregation of Mn to the grain boundaries and the associated martensite to austenite reverse transformation. This would lead to the formation of thin austenitic layers between the martensitic laths which might act as a soft barrier against crack propagation [171]. This manipulation of grain boundary chemistry can be employed as the mitigation technique to decrease the sensitivity of grain boundaries to cracking. The technique can be applied particularly in developing third-generation advanced high strength steels (3G-AHSS) such as medium-Mn TRIP steels or Q&P steels for the development of materials that are resistant to LME cracking.

References

[1] M. López Freixes, X. Zhou, H. Zhao, H. Godin, L. Peguet, T. Warner, B. Gault, Revisiting stress-corrosion cracking and hydrogen embrittlement in 7xxx-Al alloys at the near-atomic-scale, Nat. Commun. 13 (2022) 1–9. https://doi.org/10.1038/s41467-022-31964-3.

[2] G. Duscher, M.F. Chisholm, U. Alber, M. Rühle, Bismuth-induced embrittlement of copper grain boundaries, Nat. Mater. 3 (2004) 621–626. https://doi.org/10.1038/nmat1191.

[3] M. Yamaguchi, T. Tsuru, M. Itakura, E. Abe, Atomistic weak interaction criterion for the specificity of liquid metal embrittlement, Sci. Rep. 12 (2022) 1–7. https://doi.org/10.1038/s41598-022-10593-2.

[4] M. Seita, J.P. Hanson, S. Gradečak, M.J. Demkowicz, The dual role of coherent twin boundaries in hydrogen embrittlement, Nat. Commun. 6 (2015). https://doi.org/10.1038/ncomms7164.

[5] J. Song, W.A. Curtin, Atomic mechanism and prediction of hydrogen embrittlement in iron, Nat. Mater. 12 (2013) 145–151. https://doi.org/10.1038/nmat3479.

[6] H. Zhao, P. Chakraborty, D. Ponge, T. Hickel, B. Sun, C.H. Wu, B. Gault, D. Raabe, Hydrogen trapping and embrittlement in high-strength Al alloys, Nature. 602 (2022) 437–441. https://doi.org/10.1038/s41586-021-04343-z.

[7] M.H. Razmpoosh, C. DiGiovanni, Y.N. Zhou, E. Biro, Pathway to understand liquid metal embrittlement (LME) in Fe-Zn couple: From fundamentals toward application, Prog. Mater. Sci. 121 (2021) 100798. https://doi.org/10.1016/j.pmatsci.2021.100798.

[8] M.H. Razmpoosh, A. Macwan, F. Goodwin, E. Biro, Y. Zhou, Suppression of liquid-metal-embrittlement by twin-induced grain boundary engineering approach, Materialia. 11 (2020) 100668. https://doi.org/10.1016/j.mtla.2020.100668.

[9] M.H. Razmpoosh, A. Macwan, E. Biro, D.L. Chen, Y. Peng, F. Goodwin, Y. Zhou, Liquid metal embrittlement in laser beam welding of Zn-coated 22MnB5 steel, Mater. Des. 155 (2018) 375–383. https://doi.org/10.1016/j.matdes.2018.05.065.

[10] H.S. Nam, D.J. Srolovitz, Effect of material properties on liquid metal embrittlement in the Al-Ga system, Acta Mater. 57 (2009) 1546–1553. https://doi.org/10.1016/j.actamat.2008.11.041.

[11] B. Joseph, F. Barbier, M. Aucouturier, Embrittlement of copper by liquid bismuth, Scr. Mater. 40 (1999) 893–897. https://doi.org/10.1016/S1359-6462(99)00030-5.

[12] A. Ghatei-Kalashami, M.S. Khan, M.Y. Lee, Y.N. Zhou, High-temperature phase evolution of the ZnAlMg coating and its effect on mitigating liquid-metal-embrittlement cracking, Acta Mater. 229 (2022) 117836. https://doi.org/10.1016/j.actamat.2022.117836.

[13] J. Kang, G.C. Glatzmaier, S.H. Wei, Origin of the bismuth-induced decohesion of nickel and copper grain boundaries, Phys. Rev. Lett. 111 (2013) 1–5. https://doi.org/10.1103/PhysRevLett.111.055502.

[14] A.G. Kalashami, C. DiGiovanni, M.H. Razmpoosh, F. Goodwin, N.Y. Zhou, The Role of Internal Oxides on the Liquid Metal Embrittlement Cracking During Resistance Spot Welding of the Dual Phase Steel, Metall. Mater. Trans. A Phys. Metall. Mater. Sci. 51

(2020) 2180–2191. https://doi.org/10.1007/s11661-020-05702-7.

[15] A. Ghatei-Kalashami, S. Zhang, M. Shojaee, A.R.H. Midawi, F. Goodwin, N.Y. Zhou, Failure behavior of resistance spot welded advanced high strength steel: The role of surface condition and initial microstructure, J. Mater. Process. Technol. 299 (2022) 117370. https://doi.org/10.1016/j.jmatprotec.2021.117370.

[16] A. Ghatei Kalashami, X. Han, F. Goodwin, N.Y. Zhou, The influence of modified annealing during the galvanizing process on the resistance spot welding of the CMn1.8Si advanced high strength steel, Surf. Coatings Technol. 381 (2020) 125181. https://doi.org/10.1016/j.surfcoat.2019.125181.

[17] A. Ghatei Kalashami, A. Kermanpur, A. Najafizadeh, Y. Mazaheri, Effect of Nb on Microstructures and Mechanical Properties of an Ultrafine-Grained Dual Phase Steel, J. Mater. Eng. Perform. 24 (2015). https://doi.org/10.1007/s11665-015-1539-5.

[18] A.G. Kalashami, A. Kermanpur, A. Najafizadeh, Y. Mazaheri, Development of a high strength and ductile Nb-bearing dual phase steel by cold-rolling and intercritical annealing of the ferrite-martensite microstructures, Mater. Sci. Eng. A. 658 (2016) 355–366. https://doi.org/10.1016/j.msea.2016.02.028.

[19] A. Ghatei Kalashami, A. Kermanpur, E. Ghassemali, A. Najafizadeh, Y. Mazaheri, Correlation of microstructure and strain hardening behavior in the ultrafine-grained Nb-bearing dual phase steels, Mater. Sci. Eng. A. 678 (2016). https://doi.org/10.1016/j.msea.2016.09.108.

[20] A. Ghatei Kalashami, A. Kermanpur, E. Ghassemali, A. Najafizadeh, Y. Mazaheri, The effect of Nb on texture evolutions of the ultrafine-grained dual-phase steels fabricated by cold rolling and intercritical annealing, J. Alloys Compd. 694 (2017). https://doi.org/10.1016/j.jallcom.2016.10.148.

[21] M.H. Razmpoosh, A. Macwan, F. Goodwin, E. Biro, Y. Zhou, Role of Random and Coincidence Site Lattice Grain Boundaries in Liquid Metal Embrittlement of Iron (FCC) -Zn Couple, Metall. Mater. Trans. A. 51 (2020) 3938–3944. https://doi.org/10.1007/s11661-020-05857-3.

[22] A. Ghatei-Kalashami, E. Ghassemali, C. Digiovanni, F. Goodwin, N.Y. Zhou, Occurrence of liquid-metal-embrittlement in a fully ferritic microstructure, Materialia. (2021) 101036. https://doi.org/10.1016/j.mtla.2021.101036.

[23] S.M.A. Shibli, B.N. Meena, R. Remya, A review on recent approaches in the field of hot dip zinc galvanizing process, Surf. Coatings Technol. 262 (2015) 210–215. https://doi.org/10.1016/j.surfcoat.2014.12.054.

[24] A. Azimi, F. Ashrafizadeh, M.R. Toroghinejad, F. Shahriari, Metallurgical assessment of critical defects in continuous hot dip galvanized steel sheets, Surf. Coatings Technol. 206 (2012) 4376–4383. https://doi.org/10.1016/j.surfcoat.2012.04.062.

[25] C.W. Lee, D.W. Fan, I.R. Sohn, S.J. Lee, B.C. De Cooman, Liquid-metal-induced embrittlement of Zn-coated hot stamping steel, Metall. Mater. Trans. A Phys. Metall. Mater. Sci. 43 (2012) 5122–5127. https://doi.org/10.1007/s11661-012-1316-0.

[26] L. Cho, H. Kang, C. Lee, B.C. De Cooman, Microstructure of liquid metal embrittlement cracks on Zn-coated 22MnB5 press-hardened steel, Scr. Mater. 90 (2014) 25–28. https://doi.org/10.1016/j.scriptamat.2014.07.008.

[27] C.W. Lee, W.S. Choi, L. Cho, Y.R. Cho, B.C. De Cooman, Liquid-Metal-Induced

Embrittlement Related Microcrack Propagation on Zn-coated Press Hardening Steel, 55 (2015) 264–271.

[28] M. Takahashi, M. Nakata, K. Imai, N. Kojima, N. Otsuka, Liquid Metal Embrittlement of Hot Stamped Galvannealed Boron Steel Sheet – Effect of Heating Time on Crack Formation –, ISIJ Int. (2017) 1–8. https://doi.org/10.2355/isijinternational.ISIJINT-2016-730.

[29] V. Janik, Y. Lan, P. Beentjes, D. Norman, G. Hensen, S. Sridhar, Zn Diffusion and α-Fe(Zn) Layer Growth During Annealing of Zn-Coated B Steel, Metall. Mater. Trans. A Phys. Metall. Mater. Sci. 47 (2016) 400–411. https://doi.org/10.1007/s11661-015-3203-y.

[30] N. Shajan, K.S. Arora, M. Shome, P. Singh, Effect of boron in suppressing the liquid metal embrittlement in drawable grade of steel, Sci. Technol. Weld. Join. 26 (2020) 130–135. https://doi.org/10.1080/13621718.2020.1848980.

[31] M.H. Razmpoosh, E. Biro, D.L. Chen, F. Goodwin, Y. Zhou, Liquid metal embrittlement in laser lap joining of TWIP and medium-manganese TRIP steel: The role of stress and grain boundaries, Mater. Charact. 145 (2018) 627–633. https://doi.org/10.1016/j.matchar.2018.09.018.

[32] M.H. Razmpoosh, A. Macwan, F. Goodwin, E. Biro, Y. Zhou, Crystallographic study of liquid-metal-embrittlement crack path, Mater. Lett. 267 (2020) 127511. https://doi.org/10.1016/j.matlet.2020.127511.

[33] Y. Zhu, H. Wang, Y. Wang, Y. Hao, B.E. Carlson, F. Lu, Formation mechanism of liquid metal embrittlement in laser lap welding of zinc-coated GEN3 steels, Mater. Sci. Eng. A. 800 (2021) 140229. https://doi.org/10.1016/j.msea.2020.140229.

[34] Y.G. Kim, I.J. Kim, J.S. Kim, Y. Il Chung, D.Y. Choi, Evaluation of surface crack in resistance spot welds of Zn-coated steel, Mater. Trans. 55 (2014) 171–175. https://doi.org/10.2320/matertrans.M2013244.

[35] R. Ashiri, M.A. Haque, C.W. Ji, M. Shamanian, H.R. Salimijazi, Y. Do Park, Supercritical area and critical nugget diameter for liquid metal embrittlement of Zn-coated twining induced plasticity steels, Scr. Mater. 109 (2015) 6–10. https://doi.org/10.1016/j.scriptamat.2015.07.006.

[36] L. He, C. Digiovanni, X. Han, C. Mehling, E. Wintjes, E. Biro, N.Y. Zhou, C. Digiovanni, X. Han, C. Mehling, E. Wintjes, E. Biro, N.Y. Zhou, Suppression of liquid metal embrittlement in resistance spot welding of TRIP steel, Sci. Technol. Weld. Join. 1718 (2019). https://doi.org/10.1080/13621718.2019.1573011.

[37] C. Digiovanni, L. He, U. Pistek, F. Goodwin, E. Biro, N.Y. Zhou, Role of spot weld electrode geometry on liquid metal embrittlement crack development, 49 (2020) 1–9. https://doi.org/10.1016/j.jmapro.2019.11.015.

[38] S.P. Murugan, J.B. Jeon, C. Ji, Y. Park, Liquid zinc penetration induced intergranular brittle cracking in resistance spot welding of galvannealed advanced high strength steel, Weld. Word. 64 (2020) 1957–1969.

[39] S.P. Murugan, K. Mahmud, C. Ji, I. Jo, Y. Park, Critical design parameters of the electrode for liquid metal embrittlement cracking in resistance spot welding, Weld. World. 63 (2019) 1613–1632.

[40] J. Frei, M. Biegler, M. Rethmeier, C. Böhne, J. Frei, M. Biegler, Investigation of liquid

metal embrittlement of dual phase steel joints by electro-thermomechanical spot-welding simulation electro-thermomechanical spot-welding simulation, Sci. Technol. Weld. Join. 24 (2019) 624–633. https://doi.org/10.1080/13621718.2019.1582203.

[41] Z. Ling, T. Chen, L. Kong, M. Wang, H. Pan, M. Lei, Liquid Metal Embrittlement Cracking During Resistance Spot Welding of Galvanized Q&P980 Steel, Metall. Mater. Trans. A. 50 (2019) 5128–5142. https://doi.org/10.1007/s11661-019-05388-6.

[42] C. Böhne, G. Meschut, M. Biegler, M. Rethmeier, C. Böhne, G. Meschut, M. Biegler, M. Rethmeier, C. Böhne, Avoidance of liquid metal embrittlement during resistance spot welding by heat input dependent hold time adaption heat input dependent hold time adaption, (2020). https://doi.org/10.1080/13621718.2020.1795585.

[43] C. Böhne, G. Meschut, M. Biegler, J. Frei, C. Böhne, Prevention of liquid metal embrittlement cracks in resistance spot welds by adaption of electrode geometry adaption of electrode geometry, Sci. Technol. Weld. Join. 0 (2019) 1–8. https://doi.org/10.1080/13621718.2019.1693731.

[44] Z. Ling, M. Wang, L. Kong, K. Chen, Towards an explanation of liquid metal embrittlement cracking in resistance spot welding of dissimilar steels, Mater. Des. 195 (2020) 109055. https://doi.org/10.1016/j.matdes.2020.109055.

[45] A. Ghatei Kalashami, C. Digiovanni, M.H. Razmpoosh, F. Goodwin, N.Y. Zhou, The effect of silicon content on liquid-metal-embrittlement susceptibility in resistance spot welding of galvanized dual-phase steel, J. Manuf. Process. 57 (2020) 370–379. https://doi.org/10.1016/j.jmapro.2020.07.008.

[46] R. Ashiri, M. Shamanian, H.R. Salimijazi, M.A. Haque, J.H. Bae, C.W. Ji, K.G. Chin, Y. Do Park, Liquid metal embrittlement-free welds of Zn-coated twinning induced plasticity steels, Scr. Mater. 114 (2016) 41–47. https://doi.org/10.1016/j.scriptamat.2015.11.027.

[47] D. Bhattacharya, Liquid metal embrittlement during resistance spot welding of Zn-coated high-strength steels, Mater. Sci. Technol. (United Kingdom). 34 (2018) 1809–1829. https://doi.org/10.1080/02670836.2018.1461595.

[48] D.Y. Choi, A. Sharma, S.H. Uhm, J.P. Jung, Liquid Metal Embrittlement of Resistance Spot Welded 1180 TRIP Steel: Effect of Electrode Force on Cracking Behavior, Met. Mater. Int. 25 (2019) 219–228. https://doi.org/10.1007/s12540-018-0180-x.

[49] J. Frei, M. Rethmeier, Susceptibility of electrolytically galvanized dual-phase steel sheets to liquid metal embrittlement during resistance spot welding, Weld. World. 62 (2018) 1031–1037. https://doi.org/10.1007/s40194-018-0619-1.

[50] C. DiGiovanni, S. Bag, C. Mehling, K.W. Choi, A. Macwan, E. Biro, N.Y. Zhou, Reduction in liquid metal embrittlement cracking using weld current ramping, Weld. Word. 63 (2019) 1583–1591.

[51] C. DiGiovanni, E. Biro, N.Y. Zhou, Impact of liquid metal embrittlement cracks on resistance spot weld static strength strength, Sci. Technol. Weld. Join. 24 (2019) 218–224. https://doi.org/10.1080/13621718.2018.1518363.

[52] E. Wintjes, C. DiGiovanni, L. He, E. Biro, N.Y. Zhou, Quantifying the Link Between Crack Distribution and Resistance Spot Weld Strength Reduction in Liquid Metal Embrittlement Susceptible Steels, Weld. World. 63 (2019) 807–814.

[53] C. Digiovanni, A.G. Kalashami, F. Goodwin, E. Biro, N.Y. Zhou, Occurrence of sub-

critical heat affected zone liquid metal embrittlement in joining of advanced high strength steel, J. Mater. Process. Tech. 288 (2021) 116917. https://doi.org/10.1016/j.jmatprotec.2020.116917.

[54] X. Gong, M.P. Short, T. Auger, E. Charalampopoulou, K. Lambrinou, Environmental degradation of structural materials in liquid lead- and lead-bismuth eutectic-cooled reactors, Prog. Mater. Sci. 126 (2022) 100920. https://doi.org/10.1016/j.pmatsci.2022.100920.

[55] K.D. Bauer, M. Todorova, K. Hingerl, J. Neugebauer, A first principles investigation of zinc induced embrittlement at grain boundaries in bcc iron, Acta Mater. 90 (2015) 69–76. https://doi.org/10.1016/j.actamat.2015.02.018.

[56] C. Beal, X. Kleber, D. Fabregue, M. Bouzekri, Embrittlement of a zinc coated high manganese TWIP steel, Mater. Sci. Eng. A. 543 (2012) 76–83. https://doi.org/10.1016/j.msea.2012.02.049.

[57] C. Beal, X. Kleber, M. Bouzekri, Liquid zinc embrittlement of twinning-induced plasticity steel, Scr. Mater. 66 (2012) 1030–1033. https://doi.org/10.1016/j.scriptamat.2011.12.040.

[58] J. Kang, S. Hong, J. Kim, S. Kim, Zn-induced liquid metal embrittlement of galvanized high-Mn steel : Strain-rate dependency, Mater. Sci. Eng. A. 793 (2020) 139996. https://doi.org/10.1016/j.msea.2020.139996.

[59] A.R. Marder, The metallurgy of zinc-coated steel, Prog. Mater. Sci. 45 (2000) 191–271. https://doi.org/10.1081/E-EPCS.

[60] P. Pokorny, J. Kolisko, L. Balik, P. Novak, Reaction kinetics of the formation of intermetallic Fe–Zn during hot-dip galvanizing of steel, Metalurgija. 55 (2016) 111–114.

[61] N.L. Okamoto, D. Kashioka, M. Inomoto, H. Inui, Compression deformability of Γ and ζ Fe–Zn intermetallics to mitigate detachment of brittle intermetallic coating of galvannealed steels, Scr. Mater. 69 (2013) 307–310. https://doi.org/10.1016/j.scriptamat.2013.05.003.

[62] M.H. Kamdar, Embrittlement by liquid metals, Prog. Mater. Sci. 15 (1973) 289–374.

[63] P.J.L. Fernandes, D.R.H. Jones, Mechanisms of liquid metal induced embrittlement, Int. Mater. Rev. 42 (1997) 251-261. https://doi.org/10.1179/imr.1997.42.6.251.

[64] M.G.G. Nicholas, C.F.F. Old, M.D. Division, Review Liquid metal embrittlement, J. Mater. Sci. 14 (1979) 1–18. https://doi.org/10.1007/BF01028323.

[65] H. Kang, L. Cho, C. Lee, B.C. De Cooman, Zn Penetration in Liquid Metal Embrittled TWIP Steel, Metall. Mater. Trans. A Phys. Metall. Mater. Sci. 47 (2016) 2885–2905. https://doi.org/10.1007/s11661-016-3475-x.

[66] S.P. Lynch, Environmentally assisted cracking: Overview of evidence for an adsorption-induced localised-slip process, Acta Metall. 36 (1988) 2639–2661.

[67] A.R.C. Westwood, M.H. Kamdar, Concerning liquid metal embrittlement , particularly of zinc monocrystals by mercury, Philos. Mag. 8 (1963) 787–804. https://doi.org/10.1080/14786436308213836.

[68] N.S. Stoloff and T.L Johnston, Crack propagation in a liquid metal environment, Acta Metall. 11 (1963) 251–256.

[69] W.M. Robertson, Propagation of a crack filled with liquid metal, North Am. Aviat. Sci.

Center, Thousand Oaks, Calif. (1966).

[70] E.E. Glickman and Y.V. Goryunov, Mechanism of embrittlement by liquid metals and other manifestations of the Rebinder effect in metal systems, Sov Mater Sci. 14 (1978) 355–364.

[71] E.E. Glickman, Dissolution Condensation Mechanism of Stress Corrosion Cracking in Liquid Metals : Driving Force and Crack Kinetics, Metall. Mater. Trans. A. 42 (2011) 250–266. https://doi.org/10.1007/s11661-010-0429-6.

[72] M.J Kelly and N.S. Stoloff, Analysis of Liquid Metal Embrittlement from a Bond Energy Viewpoint, Metall. Trans. A. 6 (1975) 159–166.

[73] E.E Glickman, Grain Boundary Grooving Accelerated by Local Plasticity as a Possible Mechanism of Liquid Metal Embrittlement, Interface Sci. 11 (2003) 451–459.

[74] S.G. Keller, A.P. Gordon, Experimental study of liquid metal embrittlement for the aluminum 7075-mercury couple, Eng. Fract. Mech. 84 (2012) 146–160. https://doi.org/10.1016/j.engfracmech.2012.02.005.

[75] P.C. Hancock, M.B. Ives, The role of plastic deformation in liquid metal embrittlement The role of plastic deformation liquid metal embrittlement, Can. Metall. Q. 10 (1971) 207–211. https://doi.org/10.1179/cmq.1971.10.3.207.

[76] V.V Popovich and I.G. Dmukhovskaya, Rebinder effect under armco iron fracture in liquid metals, Fiz. Mekhanika Mater. 14 (1978) 30–36.

[77] M.A. Krishtal, The formation of dislocations in metals on diffusion of surface-active substances in connection with the effect of adsorption embrittlement, Sov. Phys. Dokl. 15 (1970).

[78] P. Gordon, H.H. An, The Mechanisms of Crack Initiation and Crack Propagation in Metal-Induced Embrittlement of Metals, Metall. Trans. A. 13 (1982) 457–472.

[79] M.H. Razmpoosh, B. Langelier, E. Marzbanrad, H.S. Zurob, N. Zhou, E. Biro, Atomic-scale Investigation of Liquid-Metal-Embrittlement Crack-path : Revealing Mechanism and Role of Grain Boundary Chemistry, Acta Mater. 204 (2021) 116519. https://doi.org/10.1016/j.actamat.2020.116519.

[80] L. Klinger, E. Rabkin, The effect of stress on grain boundary interdiffusion in a semi-infinite bicrystal, Acta Mater. 55 (2007) 4689–4698. https://doi.org/10.1016/j.actamat.2007.04.039.

[81] L. Klinger, E. Rabkin, Theory of the Kirkendall effect during grain boundary interdiffusion, Acta Mater. 59 (2011) 1389–1399. https://doi.org/10.1016/j.actamat.2010.10.070.

[82] S.P. Lynch, Liquid-metal embrittlement in an Al 6% Zn3% Mg alloy., Acta Metall. 29 (1981) 325–340.

[83] S.P. Lynch, Metallographic contributions to understanding mechanisms of environmentally assisted cracking, Metallography. 23 (1989) 147–171. https://doi.org/10.1016/0026-0800(89)90016-5.

[84] S.P. Lynch, Mechanisms and kinetics of environmentally assisted cracking: Current status, issues, and suggestions for further work, Metall. Mater. Trans. A. 44 (2013) 1209–1229. https://doi.org/10.1007/s11661-012-1359-2.

[85] J.C. Fisher, Calculation of diffusion penetration curves for surface and grain boundary

diffusion, J. Appl. Phys. 22 (1951) 74–77. https://doi.org/10.1063/1.1699825.

[86] D. Kim, J. Kang, S. Kim, Heating rate effect on liquid Zn-assisted embrittlement of high Mn austenitic steel, Surf. Coat. Technol. 347 (2018) 157–163. https://doi.org/10.1016/j.surfcoat.2018.04.081.

[87] A. Sabet Ghorabaei, M. Nili-Ahmadabadi, Effects of prior austenite grain size and phase transformation temperature on bainitic ferrite formation in multi-constituent microstructures of a strong ultra-low-carbon steel, Mater. Sci. Eng. A. 815 (2021) 141300. https://doi.org/10.1016/j.msea.2021.141300.

[88] M. Gómez, S.F. Medina, G. Caruana, Modelling of Phase Transformation Kinetics by Correction of Dilatometry Results for a Ferritic Nb-microalloyed Steel, ISIJ Int. 43 (2003) 1228–1237. https://doi.org/10.2355/isijinternational.43.1228.

[89] C. DiGiovanni, A. Ghatei Kalashami, E. Biro, N.Y. Zhou, Liquid metal embrittlement transport mechanism in the Fe/Zn system: Stress-assisted diffusion, Materialia. 18 (2021) 101153. https://doi.org/10.1016/j.mtla.2021.101153.

[90] H. Lee, M.C. Jo, S.S. Sohn, S.H. Kim, T. Song, S.K. Kim, H.S. Kim, N.J. Kim, S. Lee, Microstructural evolution of liquid metal embrittlement in resistance-spot-welded galvanized TWinning-Induced Plasticity (TWIP) steel sheets, Mater. Charact. 147 (2019) 233–241. https://doi.org/10.1016/j.matchar.2018.11.008.

[91] A. Ghatei-Kalashami, E. Ghassemali, C. Digiovanni, F. Goodwin, N. Zhou, Liquid metal embrittlement cracking behavior in iron-zinc (Fe / Zn) couple : Comparison of ferritic and austenitic microstructures, Mater. Lett. 324 (2022) 132780. https://doi.org/10.1016/j.matlet.2022.132780.

[92] J. Kang, D. Kim, D.H. Kim, S. Kim, Fe-Zn reaction and its influence on microcracks during hot tensile deformation of galvanized 22MnB5 steel, Surf. Coat. Technol. 357 (2019) 1069–1075. https://doi.org/10.1016/j.surfcoat.2018.08.010.

[93] C. Beal, X. Kleber, D. Fabregue, M. Bouzekri, Liquid zinc embrittlement of a high-manganese- content TWIP steel, Philos. Mag. Lett. 91 (2011) 297–303. https://doi.org/10.1080/09500839.2011.559177.

[94] J. Kim, S.P. Murugan, J. Kim, W. Yook, C. Lee, C. Ji, J.B. Jeon, Y. Park, Liquid metal embrittlement during the resistance spot welding of galvannealed steels: synergy of liquid Zn, α-Fe(Zn) and tensile stress, Sci. Technol. Weld. Join. 26 (2021). https://doi.org/10.1080/13621718.2021.1880816.

[95] Y. Ma, Y. Yu, P. Geng, R. Ihara, K. Maeda, R. Suzuki, T. Suga, N. Ma, Fracture modeling of resistance spot welded ultra-high-strength steel considering the effect of liquid metal embrittlement crack, Mater. Des. 210 (2021) 110075. https://doi.org/10.1016/j.matdes.2021.110075.

[96] Z. Ling, T. Chen, M. Wang, L. Kong, Reducing liquid metal embrittlement cracking in resistance spot welding of Q & P980 steel, Mater. Manuf. Process. 35 (2020) 1392–1399. https://doi.org/10.1080/10426914.2020.1779935.

[97] D. Bhattacharya, L. Cho, E. van der Aa, A. Pichler, N. Pottore, H. Ghassemi-Armaki, K.O. Findley, J.G. Speer, Influence of the starting microstructure of an advanced high strength steel on the characteristics of Zn-Assisted liquid metal embrittlement, Mater. Sci. Eng. A. 804 (2021) 140391. https://doi.org/10.1016/j.msea.2020.140391.

[98] S. Prasad, J. Kim, J. Kim, Y. Wan, C. Lee, J. Bae, Y. Park, Role of liquid Zn and α-Fe

(Zn) on liquid metal embrittlement of medium Mn steel: an ex-situ microstructural analysis of galvannealed coating during high temperature tensile test, Surf. Coat. Technol. 398 (2020) 126069. https://doi.org/10.1016/j.surfcoat.2020.126069.

[99] S.P. Murugan, V. Vijayan, C. Ji, Y.D. Park, Four types of LME cracks in RSW of Zn-coated AHSS, Weld. J. 99 (2020) 75–92.

[100] S. Zhang, A. Ghatei-Kalashami, A.R.H. Midawi, N.Y. Zhou, A Comparison Between Hardness-Scaling and Ball-Indentation Techniques on Predicting Stress/Strain Distribution and Failure Behavior of Resistance Spot Welded Advanced High Strength Steel, J. Manuf. Sci. Eng. 144 (2022) 1–10. https://doi.org/10.1115/1.4053730.

[101] A. Ghatei Kalashami, X. Han, F. Goodwin, N.Y. Zhou, The influence of modified annealing during the galvanizing process on the resistance spot welding of the CMn1.8Si advanced high strength steel, Surf. Coatings Technol. 381 (2020) 125181. https://doi.org/10.1016/j.surfcoat.2019.125181.

[102] W. Dong, H. Pan, M. Lei, K. Ding, Y. Gao, Zn penetration and its coupled interaction with the grain boundary during the resistance spot welding of the QP980 steel, Scr. Mater. 218 (2022) 114832. https://doi.org/10.1016/j.scriptamat.2022.114832.

[103] W. Dong, K. Ding, H. Pan, M. Lei, L. Wang, Y. Gao, Role of Si Content in the Element Segregation of Galvanized QP980 Advanced High Strength Steel, Jom. (2022) 2–9. https://doi.org/10.1007/s11837-022-05284-2.

[104] S.H. Hong, J.H. Kang, D. Kim, S.J. Kim, Si effect on Zn-assisted liquid metal embrittlement in Zn-coated TWIP steels: Importance of Fe-Zn alloying reaction, Surf. Coatings Technol. 393 (2020) 125809. https://doi.org/10.1016/j.surfcoat.2020.125809.

[105] C. Beal, X. Kleber, D. Fabrègue, M. Bouzekri, Embrittlement of a High Manganese TWIP Steel in the Presence of Liquid Zinc, Mater. Sci. Forum. 706–709 (2012) 2041–2046. https://doi.org/10.4028/www.scientific.net/MSF.706-709.2041.

[106] D. Bhattacharya, L. Cho, J. Colburn, D. Smith, D. Marshall, E. van der Aa, A. Pichler, H. Ghassemi-Armaki, N. Pottore, K.O. Findley, J.G. Speer, Influence of Selected Alloying Variations on Liquid Metal Embrittlement Susceptibility of Quenched and Partitioned Steels, Mater. Des. 224 (2022) 111356. https://doi.org/10.1016/j.matdes.2022.111356.

[107] W. Zhang, J. Xu, Advanced lightweight materials for Automobiles: A review, Mater. Des. 221 (2022) 110994. https://doi.org/10.1016/j.matdes.2022.110994.

[108] G. Agarwal, A. Kumar, I.M. Richardson, M.J.M. Hermans, Evaluation of solidification cracking susceptibility during laser welding in advanced high strength automotive steels, Mater. Des. 183 (2019) 108104. https://doi.org/10.1016/j.matdes.2019.108104.

[109] H. Gao, L. Zhang, W.D. Nix, C. V. Thompson, E. Arzt, Crack-like grain-boundary diffusion wedges in thin metal films, Acta Mater. 47 (1999) 2865–2878. https://doi.org/10.1016/S1359-6454(99)00178-0.

[110] T.K. Bhandakkar, E. Chason, H. Gao, Formation of crack-like diffusion wedges and compressive stress evolution during thin film growth with inhomogeneous grain boundary diffusivity, Int. J. Appl. Mech. 1 (2009) 1–19. https://doi.org/10.1142/S1758825109000071.

[111] C. Herring, Diffusional viscosity of a polycrystalline solid, J. Appl. Phys. 21 (1950) 437–445. https://doi.org/10.1063/1.1699681.

[112] W. Sigle, G. Richter, M. Rühle, S. Schmidt, Insight into the atomic-scale mechanism of liquid metal embrittlement, Appl. Phys. Lett. 89 (2006) 87–90. https://doi.org/10.1063/1.2356322.

[113] W. Ludwig, E. Pereiro-López, D. Bellet, In situ investigation of liquid Ga penetration in Al bicrystal grain boundaries: Grain boundary wetting or liquid metal embrittlement?, Acta Mater. 53 (2005) 151–162. https://doi.org/10.1016/j.actamat.2004.09.012.

[114] H.S. Nam, D.J. Srolovitz, Molecular dynamics simulation of Ga penetration along grain boundaries in Al: A dislocation climb mechanism, Phys. Rev. Lett. 99 (2007) 1–4. https://doi.org/10.1103/PhysRevLett.99.025501.

[115] N. Lu, S. Moniri, M.R. Wiltse, J. Spielman, N. Senabulya, A.J. Shahani, Dynamics of Ga penetration in textured Al polycrystal revealed through multimodal three-dimensional analysis, Acta Mater. 217 (2021) 23–26. https://doi.org/10.1016/j.actamat.2021.117145.

[116] D. Sage, C. Fink, Understanding temperature and dwell time dependence of liquid metal embrittlement in austenitic stainless steel by liquid zinc and copper, Materialia. 24 (2022) 101502. https://doi.org/10.1016/j.mtla.2022.101502.

[117] J.S. Dohie, J.R. Cahoon, W.F. Caley, The grain-boundary diffusion of Zn in α-Fe, J. Phase Equilibria Diffus. 28 (2007) 322–327. https://doi.org/10.1007/s11669-007-9093-y.

[118] G.B. Stephenson, Deformation during interdiffusion, Acta Metall. 36 (1988) 2663–2683. https://doi.org/10.1016/0001-6160(88)90114-9.

[119] Y.R. Kolobov, G.P. Grabovetskaya, I. V. Ratochka, K.V. Ivanov, Diffusion—Induced creep of polycrystalline and nanostructured metals, Nanostructured Mater. 12 (1999) 1127–1130.

[120] I. Daruka, I.A. Szabó, D.L. Beke, C. Cserháti, A. Kodentsov, F.J.J. Van Loo, Diffusion-induced bending of thin sheet couples: Theory and experiments in Ti-Zr system, Acta Mater. 44 (1996) 4981–4993. https://doi.org/10.1016/S1359-6454(96)00099-7.

[121] ASTM, ASTM. "A240/A240M-17, Standard Specification for Chromium and Chromium-Nickel Stainless Steel Plate, Sheet, and Strip for Pressure Vessels and for General Applications.," (2017).

[122] D. Mainprice, F. Bachmann, R. Hielscher, H. Schaeben, Descriptive tools for the analysis of texture projects with large datasets using MTEX: Strength, symmetry and components, Geol. Soc. Spec. Publ. 409 (2015) 251–271. https://doi.org/10.1144/SP409.8.

[123] B.C. Nzogang, J. Bouquerel, P. Cordier, A. Mussi, J. Girard, S. Karato, Characterization by Scanning Precession Electron Diffraction of an Aggregate of Bridgmanite and Ferropericlase Deformed at HP-HT, Geochemistry, Geophys. Geosystems. 19 (2018) 582–594. https://doi.org/10.1002/2017GC007244.

[124] E.D. Merson, P.N. Myagkikh, V.A. Poluyanov, D.L. Merson, A. Vinogradov, Quasi-cleavage hydrogen-assisted cracking path investigation by fractographic and side surface observations, Eng. Fract. Mech. 214 (2019) 177–193. https://doi.org/10.1016/j.engfracmech.2019.04.042.

[125] J.K. Kim, B. Lee, H. Lee, H. Kim, K. Young, Intergranular segregation of Cr in Ti-stabilized low-Cr ferritic stainless steel, Scr. Mater. 61 (2009) 1133–1136.

https://doi.org/10.1016/j.scriptamat.2009.08.045.

[126] X. Li, L. Chang, C. Liu, B. Leng, X. Ye, F. Han, X. Yang, Effect of thermal aging on corrosion behavior of type 316H stainless steel in molten chloride salt, Corros. Sci. 191 (2021) 109784. https://doi.org/10.1016/j.corsci.2021.109784.

[127] T. Liu, S. Xia, T. Shoji, Intergranular stress corrosion cracking in simulated BWR water of 316L stainless steels manufactured with different procedures, Corros. Sci. 183 (2021) 109344. https://doi.org/10.1016/j.corsci.2021.109344.

[128] C.L. Lai, L.W. Tsay, W. Kai, C. Chen, The effects of cold rolling and sensitisation on hydrogen embrittlement of AISI 304L welds, Corros. Sci. 52 (2010) 1187–1193. https://doi.org/10.1016/j.corsci.2009.11.029.

[129] T. Fujii, M. Suzuki, Y. Shimamura, Susceptibility to intergranular corrosion in sensitized austenitic stainless steel characterized via crystallographic characteristics of grain boundaries, Corros. Sci. 195 (2022) 109946. https://doi.org/10.1016/j.corsci.2021.109946.

[130] S.P. Tsai, S.K. Makineni, B. Gault, K. Kawano-Miyata, A. Taniyama, S. Zaefferer, Precipitation formation on $\sum 5$ and $\sum 7$ grain boundaries in 316L stainless steel and their roles on intergranular corrosion, Acta Mater. 210 (2021) 116822. https://doi.org/10.1016/j.actamat.2021.116822.

[131] J. Kil, Y. Ho, J. Sub, K. Young, Effect of chromium content on intergranular corrosion and precipitation of Ti-stabilized ferritic stainless steels, Corros. Sci. 52 (2010) 1847–1852. https://doi.org/10.1016/j.corsci.2010.01.037.

[132] S. Hu, E.H. Han, X. Liu, Atomic-scale evidence for the intergranular corrosion mechanism induced by co-segregation of low-chromium ferritic stainless steel, Corros. Sci. 189 (2021) 109588. https://doi.org/10.1016/j.corsci.2021.109588.

[133] I.M. Neklyudov, V.N. Voyevodin, Features of structure-phase transformations and segregation processes under irradiation of austenitic and ferritic-martensitic steels, J. Nucl. Mater. 212–215 (1994) 39–44. https://doi.org/10.1016/0022-3115(94)90031-0.

[134] L.E. Murr, A. Advani, S. Shankar, D.G. Atteridge, Effects of deformation (strain) and heat treatment on grain boundary sensitization and precipitation in austenitic stainless steels, Mater. Charact. 24 (1990) 135–158. https://doi.org/10.1016/1044-5803(90)90032-F.

[135] L.A. Giannuzzi, J.L. Drown, S.R. Brown, R.B. Irwin, F.A. Stevie, Applications of the FIB lift-out technique for TEM specimen preparation, Microsc. Res. Tech. 41 (1998) 285–290. https://doi.org/10.1002/(SICI)1097-0029(19980515)41:4<285::AID-JEMT1>3.0.CO;2-Q.

[136] M.A. Gibson, C.A. Schuh, Segregation-induced changes in grain boundary cohesion and embrittlement in binary alloys, Acta Mater. 95 (2015) 145–155. https://doi.org/10.1016/j.actamat.2015.05.004.

[137] J.R. Trelewicz, C.A. Schuh, Grain boundary segregation and thermodynamically stable binary nanocrystalline alloys, Phys. Rev. B - Condens. Matter Mater. Phys. 79 (2009) 1–13. https://doi.org/10.1103/PhysRevB.79.094112.

[138] Z. Li, Z. Li, W. Tian, Strengthening effect of nb on ferrite grain boundary in x70 pipeline steel, Materials (Basel). 14 (2021) 1–14. https://doi.org/10.3390/ma14010061.

[139] M. Koyama, E. Akiyama, T. Sawaguchi, D. Raabe, K. Tsuzaki, Hydrogen-induced

cracking at grain and twin boundaries in an Fe-Mn-C austenitic steel, Scr. Mater. 66 (2012) 459–462. https://doi.org/10.1016/j.scriptamat.2011.12.015.

[140] D. Gorse, S. Goryachev, T. Auger, Liquid metal embrittlement. From basic concepts to recent results related to structural materials for liquid metal spallation targets, Proc. 3 Int. Symp. Mater. Chem. Nucl. Environ. 1 (2003) 63–71.

[141] P. Volovitch, T.N. Vu, C. Allély, A. Abdel Aal, K. Ogle, Understanding corrosion via corrosion product characterization: II. Role of alloying elements in improving the corrosion resistance of Zn-Al-Mg coatings on steel, Corros. Sci. 53 (2011) 2437–2445. https://doi.org/10.1016/j.corsci.2011.03.016.

[142] B.W. Çetinkaya, F. Junge, G. Müller, F. Haakmann, K. Schierbaum, M. Giza, Impact of alkaline and acid treatment on the surface chemistry of a hot-dip galvanized Zn–Al–Mg coating, J. Mater. Res. Technol. 9 (2020) 16445–16458. https://doi.org/10.1016/j.jmrt.2020.11.070.

[143] D. Thierry, D. Persson, G. Luckeneder, K.H. Stellnberger, Atmospheric corrosion of ZnAlMg coated steel during long term atmospheric weathering at different worldwide exposure sites, Corros. Sci. 148 (2019) 338–354. https://doi.org/10.1016/j.corsci.2018.12.033.

[144] N. Wint, A.D. Malla, N. Cooze, T. Savill, S. Mehraban, T. Dunlop, J.H. Sullivan, D. Penney, G. Williams, H.N. McMurray, The ability of Mg2Ge crystals to behave as 'smart release' inhibitors of the aqueous corrosion of Zn-Al-Mg alloys, Corros. Sci. 179 (2021). https://doi.org/10.1016/j.corsci.2020.109091.

[145] X. Gao, J.F. Nie, Structure and thermal stability of primary intermetallic particles in an Mg-Zn casting alloy, Scr. Mater. 57 (2007) 655–658. https://doi.org/10.1016/j.scriptamat.2007.06.005.

[146] J.N. Kim, C.S. Lee, Y.S. Jin, Structure and Stoichiometry of MgxZny in Hot-Dipped Zn–Mg–Al Coating Layer on Interstitial-Free Steel, Met. Mater. Int. 24 (2018) 1090–1098. https://doi.org/10.1007/s12540-018-0119-2.

[147] M. Ahmadi, B. Salgın, M. Ahmadi, B.J. Kooi, Y. Pei, Unraveling dislocation mediated plasticity and strengthening in crack-resistant ZnAlMg coatings, Int. J. Plast. 144 (2021) 103041. https://doi.org/10.1016/j.ijplas.2021.103041.

[148] F. Julian, the Metallurgy of Steel., J. Am. Chem. Soc. 26 (1904) 880–881. https://doi.org/10.1021/ja01997a020.

[149] S. Hong, J. Kang, D. Kim, S. Kim, Si effect on Zn-assisted liquid metal embrittlement in Zn-coated TWIP steels: importance of Fe-Zn alloying reaction, Surf. Coat. Technol. 393 (2020) 125809. https://doi.org/10.1016/j.surfcoat.2020.125809.

[150] M.A. Dayananda, An Analysis of Concentration Profiles for Fluxes, Diffusion Depths, and Zero-Flux Planes in Multicomponent Diffusion, Metall. Trans. A. 14 (1983) 1851–1858.

[151] V.D. Divya, U. Ramamurty, A. Paul, Interdiffusion and solid solution strengthening in Ni–Co–Pt and Ni–Co–Fe ternary systems, Philos. Mag. 93 (2013) 2190–2296. https://doi.org/10.1080/14786435.2013.765987.

[152] M.A. Dayananda, Y.H. Sohn, Average effective interdiffusion coefficients and their applications for isothermal multicomponent diffusion couples, Scr. Mater. 35 (1996) 683–688.

[153] M.L. Martin, T. Auger, D.D. Johnson, I.M. Robertson, Liquid-metal-induced fracture mode of martensitic T91 steels, J. Nucl. Mater. 426 (2012) 71–77. https://doi.org/10.1016/j.jnucmat.2012.03.040.

[154] T. Truglas, J. Duchoslav, C. Riener, M. Arndt, C. Commenda, D. Stifter, G. Angeli, H. Groiss, Correlative characterization of Zn-Al-Mg coatings by electron microscopy and FIB tomography, Mater. Charact. 166 (2020) 110407. https://doi.org/10.1016/j.matchar.2020.110407.

[155] T. Min, Y. Gao, L. Chen, Q. Kang, W.Q. Tao, Mesoscale investigation of reaction-diffusion and structure evolution during Fe-Al inhibition layer formation in hot-dip galvanizing, Int. J. Heat Mass Transf. 92 (2016) 370–380. https://doi.org/10.1016/j.ijheatmasstransfer.2015.08.083.

[156] G.M. Song, T. Vystavel, N. Van Der Pers, J.T.M. De Hosson, W.G. Sloof, Relation between microstructure and adhesion of hot dip galvanized zinc coatings on dual phase steel, Acta Mater. 60 (2012) 2973–2981. https://doi.org/10.1016/j.actamat.2012.02.003.

[157] M. Dutta, S.B. Singh, Effect of strip temperature on the formation of an Fe2Al5 inhibition layer during hot-dip galvanizing, Scr. Mater. 60 (2009) 643–646. https://doi.org/10.1016/j.scriptamat.2008.12.033.

[158] Y. Wang, P. Chao, S. Moniri, J. Gao, T. Volkenandt, V. De Andrade, A.J. Shahani, Integrated three-dimensional characterization of reactive phase formation and coarsening during isothermal annealing of metastable Zn–3Mg–4Al eutectic, Mater. Charact. 170 (2020) 110685. https://doi.org/10.1016/j.matchar.2020.110685.

[159] X. Li, A. Scherf, M. Heilmaier, F. Stein, The Al-Rich Part of the Fe-Al Phase Diagram, J. Phase Equilibria Diffus. 37 (2016) 162–173. https://doi.org/10.1007/s11669-015-0446-7.

[160] I. Lee, K. Han, I. Ohnuma, R. Kainuma, Experimental determination of phase diagram at 450 °C in the Zn–Fe–Al ternary system, J. Alloys Compd. 854 (2021) 157163. https://doi.org/10.1016/j.jallcom.2020.157163.

[161] N.L. Okamoto, H. Inui, A. Yasuhara, S. Yamaguchi, Crystal structure determination of the Γ2 phase in the Fe-Zn-Al system by single-crystal synchrotron X-ray diffraction combined with scanning transmission electron microscopy, J. Alloys Compd. 644 (2015) 287–296. https://doi.org/10.1016/j.jallcom.2015.04.119.

[162] P.G. An, Metal-Induced Embrittlement of Metals An Evaluation of Embrittler Transport Mechanisms, Metall. Trans. A. 9 (1978) 267–273.

[163] M.A. Dayananda, C.W. Kim, Zero-flux planes and flux reversals in Cu− Ni− Zn diffusion couples, Metall. Trans. A. 10 (1979) 1333–1339.

[164] C.W. Kim, M.A. Dayananda, Identification of zero-flux planes and flux reversals in several studies of ternary diffusion, Metall. Trans. A. 14 (1983) 857–864.

[165] C.W. Kim, M.A. Dayananda, Zero-flux planes and flux reversals in the Cu-Ni-Zn system at 775 C, Metall. Trans. A. 15 (1984) 649–659.

[166] G.M. Song, W.G. Sloof, Effect of alloying element segregation on the work of adhesion of metallic coating on metallic substrate: Application to zinc coatings on steel substrates, Surf. Coatings Technol. 205 (2011) 4632–4639. https://doi.org/10.1016/j.surfcoat.2011.04.014.

[167] D.F.R. Boer, W. Mattens, R. Boom, A.R. Miedema, A.K. Niessen, Cohesion in metals.

Transition metal alloys, (1988).

[168] L. Wei, J. Zheng, L. Chen, R. Devesh, K. Misra, High temperature oxidation behavior of ferritic stainless steel containing W and Ce, Corros. Sci. 142 (2018) 79–92. https://doi.org/10.1016/j.corsci.2018.07.017.

[169] D. Scheiber, K. Prabitz, L. Romaner, W. Ecker, The influence of alloying on Zn liquid metal embrittlement in steels, Acta Mater. 195 (2020) 750–760. https://doi.org/10.1016/j.actamat.2020.06.001.

[170] W. Peng, H. Peng, G. Wu, J. Zhang, Effect of zinc-doping on tensile strength of Σ5 bcc Fe symmetric tilt grain boundary, Comput. Mater. Sci. 171 (2020) 109204. https://doi.org/10.1016/j.commatsci.2019.109204.

[171] D. Raabe, M. Herbig, S. Sandlöbes, Y. Li, D. Tytko, M. Kuzmina, D. Ponge, P.P. Choi, Grain boundary segregation engineering in metallic alloys: A pathway to the design of interfaces, Curr. Opin. Solid State Mater. Sci. 18 (2014) 253–261. https://doi.org/10.1016/j.cossms.2014.06.002.

[172] F.Y. Genin, W. W. Mullins, P. Wynblatt, The effect of stress on grain boundary grooving, Acta Metall. Mater. 41 (1993) 3541–3547.

[173] J. Chakraborty, Diffusion in stressed thin films, 2005.

Appendix A

The chemical potential gradient is considered the driving force for governing the grain boundary diffusion equations.

$$\mu^i - \mu^0 = kTln\ a^i \qquad \text{A (1)}$$

In the case of applied tensile stress (σ), the chemical potential of any atom of volume Ω would be changed as [172]:

$$\mu^i - \mu^0 = kTln\ a^i + \sigma\Omega \qquad \text{A (2)}$$

Considering the activity coefficient, $\gamma_i = \frac{a_i}{C_i}$ where C_i is the concentration and substituting in Eq. A (2):

$$J_i \propto \frac{\partial \mu_i}{\partial y} \qquad \text{A (3)}$$

$$J_i = -\frac{\delta D_{gb}}{kT} C_i \frac{\partial \mu}{\partial y} = -\frac{\delta D_{gb}}{kT}\ C_i \frac{\partial}{\partial y}\ (\mu^0 + kTln\ (\gamma_i C_i) + \sigma\Omega) \qquad \text{A (4)}$$

Where D_{gb} and δ are grain boundary (GB) diffusivity and thickness of GB, respectively. It has been assumed that the activity coefficient and atomic volume do not depend on stress or concentration, i.e.:

$$\boldsymbol{\gamma_i\ or\ \Omega\ \neq f(C_i, \sigma) \neq\ f(x, t)} \qquad \text{A (5)}$$

Differentiating the second part in the bracket of the right-hand side of Eq. A (4) gives the following equation:

$$\frac{\partial \mu_i}{\partial y} = kT\eta_i \frac{1}{C_i}\frac{\partial C_i}{\partial y} + \Omega \frac{\partial \sigma}{\partial y} \qquad \text{A (6)}$$

Where $\eta_i = \left(1 + \frac{\partial ln\gamma_i}{\partial lnC_i}\right)$ is the thermodynamic factor [173]. Therefore, the flux equation in the presence of tensile stress can be described by the following equation:

$$J_i = -\delta\eta_i D_{gb} \frac{\partial C_i}{\partial y} - \frac{\delta D_{gb}\Omega}{kT} C_i\ \frac{\partial \sigma}{\partial y} \qquad \text{A (7)}$$

Based on the Gibbs-Duhem relationship, the thermodynamic factor for both chemical species is the same [173]:

$$\eta_{Fe} = \eta_{Zn} = \eta \qquad \text{A (8)}$$

The thermodynamic factor is different in each binary system and depends on the composition and temperature. It is known that $\eta > 1$ for systems with a negative heat of mixing and $\eta < 1$ for the ones with positive heat mixing. The η can be calculated using thermodynamic data. For simplicity, the thermodynamic factor has been taken as a constant equal to 1.0. It should be noted that this assumption will not affect the concentration profiles [173]. Therefore, the atomic fluxes along with grain boundary associated with the diffusion of Zn atoms into Fe-substrate (J_{Zn}) and the diffusion of Fe-atom towards zinc layer (J_{Fe}) can be represented as:

$$J_{Zn} = -\delta D_{gb}^{Zn} \frac{\partial C_{gb}^{Zn}}{\partial y} - \frac{\Omega \delta D_{gb}^{Zn}}{kT} C_{gb}^{Zn} \frac{\partial \sigma}{\partial y} \qquad \text{A (9)}$$

$$J_{Fe} = -\delta D_{gb}^{Fe} \frac{\partial C_{gb}^{Fe}}{\partial y} - \frac{\Omega \delta D_{gb}^{Fe}}{kT} C_{gb}^{Fe} \frac{\partial \sigma}{\partial y} \qquad \text{A (10)}$$

Where D_{gb}^{Zn} and D_{gb}^{Fe} are grain boundary diffusivities of Zn and Fe atoms, respectively. In this model, the dependence of grain boundary diffusivities on pressure (p) and concentration is neglected, e.g.:

$$\frac{\partial D(\sigma)}{\partial p} \equiv 0 \qquad \text{A (11)}$$

$$\frac{\partial D(C)}{\partial C} \equiv 0 \qquad \text{A (12)}$$

Fick's second law can be written down as follows:

$$\frac{\partial C_i}{\partial t} = -\frac{\partial J_i}{\partial y} \qquad \text{A (13)}$$

$$\frac{\partial C_{gb}^i}{\partial t} = \delta D_{gb}^i \frac{\partial^2 C_{gb}^i}{\partial y^2} + \frac{\Omega \delta D_{gb}^i}{kT} \frac{\partial}{\partial y}\left(C_{gb}^i \frac{\partial \sigma}{\partial y}\right), i = Zn \; and \; Fe \qquad \text{A (14)}$$

$$\frac{\partial C_{gb}^{i}}{\partial t} = \delta D_{gb}^{i} \frac{\partial^2 C_{gb}^{i}}{\partial y^2} + \frac{\Omega \delta D_{gb}^{i}}{kT} \frac{\partial C_{gb}^{i}}{\partial y} \frac{\partial \sigma}{\partial y} + \frac{\Omega \delta D_{gb}^{i}}{kT} C_{gb}^{i} \frac{\partial^2 \sigma}{\partial y^2} \quad , \qquad \text{A (15)}$$

$$i = Zn \; and \; Fe$$

The stress profile along GB, $\sigma\,(y,t)$, can be represented as:

$$\sigma_{gb}\,(y,t) = \; E^{*} \int_{0}^{\infty} K\,(y,x) \frac{\partial w(x,t)}{\partial x} dx \qquad \text{A (16)}$$

$$(y,z) = \; \frac{1}{y-z} - \frac{1}{y+z} - \; \frac{2z(y-z)}{(y+z)^3} \qquad \text{A (17)}$$

$$E^{*} = \frac{E}{2\pi(1-\nu^2)} \qquad \text{A (18)}$$

It should be noted that the presence of SIDW with the width of w (x, y) must be considered in the continuity equation. Therefore, Eq. A (13) is rewritten as:

$$\frac{\partial C_i}{\partial t} = \; -\frac{\partial J_i}{\partial y} - C_i^{gb} \frac{\partial w}{\partial t} \qquad \text{A (19)}$$

Where the second term of RHS of Eq. A (19) describes the role of the SIDW dimension on the diffusion flux. Therefore, Eq. A (15) is written as:

$$\frac{\partial C_{gb}^{Zn}}{\partial t} = \delta D_{gb}^{Zn} \frac{\partial^2 C_{gb}^{Zn}}{\partial y^2} + \frac{\Omega \delta D_{gb}^{Zn}}{kT} \frac{\partial C_{gb}^{Zn}}{\partial y} \frac{\partial \sigma}{\partial y} + \frac{\Omega \delta D_{gb}^{Zn}}{kT} C_{gb}^{Zn} \frac{\partial^2 \sigma}{\partial y^2} \qquad \frac{\partial w\,(x,y)}{\partial t} > 0 \qquad \text{A (20)}$$

$$- C_{gb}^{Zn} \frac{\partial w}{\partial t}$$

$$\frac{\partial C_{gb}^{Fe}}{\partial t} = \delta D_{gb}^{Fe} \frac{\partial^2 C_{gb}^{Fe}}{\partial y^2} + \frac{\Omega \delta D_{gb}^{Fe}}{kT} \frac{\partial C_{gb}^{Fe}}{\partial y} \frac{\partial \sigma}{\partial y} + \frac{\Omega \delta D_{gb}^{Fe}}{kT} C_{gb}^{Fe} \frac{\partial^2 \sigma}{\partial y^2} \qquad \frac{\partial w\,(x,y)}{\partial t} > 0 \qquad \text{A (21)}$$

$$- C_{gb}^{Fe} \frac{\partial w}{\partial t}$$

Assuming $C_{gb}^{Zn} + \; C_{gb}^{Fe} = 1$, Eq. A (21) can be rewritten as the following equations:

$$\frac{\partial}{\partial t}\left(1-\ C_{gb}^{Zn}\right)=\delta D_{gb}^{Fe}\frac{\partial^2}{\partial y^2}\left(1-\ C_{gb}^{Zn}\right)+\frac{\Omega\delta D_{gb}^{Fe}}{kT}\frac{\partial}{\partial y}\left(1-\ C_{gb}^{Zn}\right)\frac{\partial\sigma}{\partial y}+\frac{\Omega\delta D_{gb}^{Fe}(1-\ C_{gb}^{Zn})}{kT}\frac{\partial^2\sigma}{\partial y^2}-(1-\ C_{gb}^{Zn})\frac{\partial w\ (y,z)}{\partial t} \quad \text{A (22)}$$

$$\frac{\partial C_{gb}^{Zn}}{\partial t}=\ \delta D_{gb}^{Fe}\frac{\partial^2 C_{gb}^{Zn}}{\partial y^2}+\frac{\Omega\delta D_{gb}^{Fe}}{kT}\frac{\partial C_{gb}^{Zn}}{\partial y}\frac{\partial\sigma}{\partial y}-\frac{\Omega\delta D_{gb}^{Fe}\left(1-\ C_{gb}^{Zn}\right)}{kT}\frac{\partial^2\sigma}{\partial y^2}+\frac{\partial w}{\partial t}-\frac{\partial w}{\partial t}C_{gb}^{Zn} \quad \text{A (23)}$$

Combining Eq. 19 and Eq. 23 yields the following equation:

$$\frac{\partial w\ (y,z)}{\partial t}=\delta\frac{\partial^2 C_{gb}^{Zn}}{\partial y^2}\left(D_{gb}^{Zn}-D_{gb}^{Fe}\right)+\frac{\Omega\delta}{kT}\frac{\partial C_{gb}^{Zn}}{\partial y}\frac{\partial\sigma}{\partial y}\left(D_{gb}^{Zn}-D_{gb}^{Fe}\right)+\frac{\Omega\delta}{kT}\frac{\partial^2\sigma}{\partial y^2}\left(D_{gb}^{Zn}C_{gb}^{Zn}+D_{gb}^{Fe}C_{gb}^{Fe}\right) \quad \text{A (24)}$$

Eq. A (24) illustrates the instantaneous dimension of the extra wedge material. Substituting Eq. A (24) into Eq. A (19) yields the following equation:

$$\frac{\partial C_{gb}^{Zn}}{\partial t}=\ \left(D_{gb}^{Zn}C_{gb}^{Fe}+D_{gb}^{Fe}C_{gb}^{Zn}\right)\frac{\partial^2 C_{gb}^{Zn}}{\partial y^2}+\frac{\Omega\left(D_{gb}^{Zn}C_{gb}^{Fe}+D_{gb}^{Fe}C_{gb}^{Zn}\right)}{kT}\frac{\partial C_{gb}^{Zn}}{\partial y}\frac{\partial\sigma}{\partial y}+\frac{\Omega C_{gb}^{Zn}C_{gb}^{Fe}\left(D_{gb}^{Zn}-\ D_{gb}^{Fe}\right)}{kT}\frac{\partial^2\sigma}{\partial y^2} \quad \text{A (25)}$$

Appendix *B*

The finite difference method (FDM) was employed to solve equations 9 (a)-(c). First, $C_{i,j}$ is expanded in *T* direction while $X_i = i\Delta$ keeps constant.

$$C_{i,j+1} = C_{i,j} + \delta T\left(\frac{\partial C}{\partial T}\right)_{i,j} + \frac{\left(\frac{\partial^2 C}{\partial T^2}\right)_{i,j}}{2!}(\delta T)^2 + \frac{\left(\frac{\partial^3 C}{\partial T^2}\right)_{i,j}}{3!}(\delta T)^3 + \cdots \quad \text{Eq. (B1)}$$

With neglecting the higher-order terms, Eq. (B1) can be written as:

$$\left(\frac{\partial C}{\partial T}\right)_{i,j} = \frac{C_{i,j+1} - C_{i,j}}{\delta T} \quad \text{Eq. (B2)}$$

Similarly, Taylor's series is applied for the $C_{i,j}$ in *X* direction while $T_j = j\Delta$ keep constant.

$$C_{i-1,j} = C_{i,j} - \delta X\left(\frac{\partial C}{\partial X}\right)_{i,j} + \frac{\left(\frac{\partial^2 C}{\partial X^2}\right)_{i,j}}{2!}(\delta X)^2 + \frac{\left(\frac{\partial^3 C}{\partial X^2}\right)_{i,j}}{3!}(\delta X)^3 + \cdots \quad \text{Eq. (B3)}$$

$$C_{i+1,j} = C_{i,j} + \delta X\left(\frac{\partial C}{\partial X}\right)_{i,j} + \frac{\left(\frac{\partial^2 C}{\partial X^2}\right)_{i,j}}{2!}(\delta X)^2 + \frac{\left(\frac{\partial^3 C}{\partial X^2}\right)_{i,j}}{3!}(\delta X)^3 + \cdots \quad \text{Eq. (B4)}$$

Combining Eq. (B3) and Eq. (B4) with neglecting higher orders yields the following set of equations:

$$\frac{C_{i-1,j} + C_{i+1,j} - 2C_{i,j}}{(\delta X)^2} = \left(\frac{\partial^2 C}{\partial X^2}\right)_{i,j} \quad \text{Eq. (B5)}$$

$$\frac{C_{i-1,j} - C_{i+1,j}}{\delta X} = \left(\frac{\partial C}{\partial X}\right)_{i,j} \quad \text{Eq. (B6)}$$

By substituting Eqs. (B5) and (B6) into Eqs. 9 (a)-(b) the following equations are obtained:

$$\begin{aligned}\frac{\partial \mathrm{W_i}}{\partial \mathrm{T}} = {} & (1 - \theta)(\mathrm{C_{i+1}} - 2\mathrm{C_i} + \mathrm{C_{i-1}}) \\ & + 0.25(1 - \theta)(\mathrm{C_{i+1}} - \mathrm{C_{i-1}})(\mathrm{S_{i+1}} - \mathrm{S_{i-1}}) + (\mathrm{C_i} + \theta(1 \\ & - \mathrm{C_i}))(\mathrm{S_{i+1}} - 2\mathrm{S_i} + \mathrm{S_{i-1}})\end{aligned} \quad \text{Eq. (B7)}$$

$$\frac{\partial C_i}{\partial T} = [(\theta C_i + (1 - C_i))(C_{i+1} - 2C_i + C_{i-1})] + 0.25[(\theta C_i + (1 - C_i))(C_{i+1} - C_{i-1})(S_{i+1} - S_{i-1})] + [C_i(1 - C_i)(1 - \theta)(S_{i+1} - 2S_i + S_{i-1})] \quad \text{Eq. (B8)}$$

As mentioned by Klinger and Rabkin [81], for solving Eq. 9 (c), the entire intergro-differentiate equation is discretized using a uniform grid $X_i = i\Delta x$ and $Y_i = i\Delta y$ as follows:

$$S_i = \sum_{k \neq i, i-1} \left[(W_{k+1} - W_k)F_{i,k} + 0.5\,(W_{i+1} - W_{i-1})G_i^{(0)} + (W_{i+1} - W_{i-1} - 2W_i)G_i^{(1)}\right] \quad \text{Eq. (B9)}$$

The first term of the right-hand side (RHS) of Eq. (B9) is a linear approximation and the second part of RHS of Eq. (B9) is a parabolic approximation of W_i. Therefore, Eq. (B9) can be rewritten as follows:

$$S_i = \sum_{k \neq i, i-1} \left[(W_{k+1} - W_k)F_{i,k} + 0.5\,(W_{i+1} - W_{i-1})G_i^{(0)} + (W_{i+1} - W_{i-1} - 2W_i)G_i^{(1)}\right] \quad \text{Eq. (B10)}$$

$$F_{i,k} = \ln\left|\frac{(i + k + 1)(i - k)}{(i - k - 1)(i + k)}\right| - \frac{6i}{(i + k + 1)(i + k)} + \frac{2i^2(2k + 2i + 1)}{(i + k + 1)^2(i + k)^2} \quad \text{Eq. (B11)}$$

$$G_i^{(0)} = \int_{i-1}^{i+1} \left(\frac{1}{y - z} - \frac{1}{y + z} - \frac{2z(y - z)}{(y + z)^3}\right)dZ = \ln\left|\frac{2i + 1}{2i - 1}\right| - \frac{12i}{(4i^2 - 1)} + \frac{16i^3}{(4i^2 - 1)^2} \quad \text{Eq. (B12)}$$

$$G_i^{(1)} = \int_{i-1}^{i+1} \left(\frac{1}{y - z} - \frac{1}{y + z} - \frac{2z(y - z)}{(y + z)^3}\right)(z - y)dZ = -8i \ln\left|\frac{2i + 1}{2i - 1}\right| + \frac{32i^2}{4i^2 - 1} - \frac{32i^4}{(4i^2 - 1)^2} \quad \text{Eq. (B13)}$$

Eqs. (B7), (B8), (B10-13) were solved by coding in MATLAB.

Appendix *C*

This appendix contains the material copy permission for the figures that were adopted/printed from references in Chapter 2. The first two pages of each permission are added. A copy of the entire document will be provided upon request.

ELSEVIER LICENSE
TERMS AND CONDITIONS

Mar 06, 2023

This Agreement between University of Waterloo -- Ali Ghatei ("You") and Elsevier ("Elsevier") consists of your license details and the terms and conditions provided by Elsevier and Copyright Clearance Center.

License Number	5503110575861
License date	Mar 06, 2023
Licensed Content Publisher	Elsevier
Licensed Content Publication	Progress in Materials Science
Licensed Content Title	The metallurgy of zinc-coated steel
Licensed Content Author	A.R. Marder
Licensed Content Date	Jun 1, 2000
Licensed Content Volume	45
Licensed Content Issue	3
Licensed Content Pages	81
Start Page	191
End Page	271
Type of Use	reuse in a thesis/dissertation

Portion	figures/tables/illustrations
Number of figures/tables/illustrations	2
Format	both print and electronic
Are you the author of this Elsevier article?	No
Will you be translating?	No
Title	An integrative investigation of liquid metal embrittlement in the Fe-Zn system: From responsible mechanisms to mitigation strategies
Institution name	University of Waterloo
Expected presentation date	Apr 2023
Portions	Figure 6 and Figure 7 on pages 200 and 201, respectively.
Requestor Location	University of Waterloo 200 University Avenue West Waterloo, ON N2L 3G1 Canada Attn: University of Waterloo
Publisher Tax ID	GB 494 6272 12
Total	0.00 USD
Terms and Conditions	

INTRODUCTION

ELSEVIER LICENSE
TERMS AND CONDITIONS

Mar 07, 2023

This Agreement between University of Waterloo -- Ali Ghatei ("You") and Elsevier ("Elsevier") consists of your license details and the terms and conditions provided by Elsevier and Copyright Clearance Center.

License Number	5503791020117
License date	Mar 07, 2023
Licensed Content Publisher	Elsevier
Licensed Content Publication	Scripta Materialia
Licensed Content Title	Compression deformability of Γ and ζ Fe–Zn intermetallics to mitigate detachment of brittle intermetallic coating of galvannealed steels
Licensed Content Author	Norihiko L. Okamoto,Daisuke Kashioka,Masahiro Inomoto,Haruyuki Inui,Hiroshi Takebayashi,Shu Yamaguchi
Licensed Content Date	Aug 1, 2013
Licensed Content Volume	69
Licensed Content Issue	4
Licensed Content Pages	4
Start Page	307

End Page	310
Type of Use	reuse in a thesis/dissertation
Portion	figures/tables/illustrations
Number of figures/tables/illustrations	1
Format	both print and electronic
Are you the author of this Elsevier article?	No
Will you be translating?	No
Title	An integrative investigation of liquid metal embrittlement in the Fe-Zn system: From responsible mechanisms to mitigation strategies
Institution name	University of Waterloo
Expected presentation date	Apr 2023
Portions	Figure 1 (b) on Page 308
Requestor Location	University of Waterloo 200 University Avenue West Waterloo, ON N2L 3G1 Canada Attn: University of Waterloo
Publisher Tax ID	GB 494 6272 12
Total	0.00 USD

Terms and Conditions

ELSEVIER LICENSE
TERMS AND CONDITIONS

Mar 07, 2023

This Agreement between University of Waterloo -- Ali Ghatei ("You") and Elsevier ("Elsevier") consists of your license details and the terms and conditions provided by Elsevier and Copyright Clearance Center.

License Number	5503660915679
License date	Mar 07, 2023
Licensed Content Publisher	Elsevier
Licensed Content Publication	Acta Metallurgica
Licensed Content Title	Crack propagation in a liquid metal environment
Licensed Content Author	N.S Stoloff,T.L Johnston
Licensed Content Date	Apr 1, 1963
Licensed Content Volume	11
Licensed Content Issue	4
Licensed Content Pages	6
Start Page	251
End Page	256
Type of Use	reuse in a thesis/dissertation

Portion	figures/tables/illustrations
Number of figures/tables/illustrations	2
Format	both print and electronic
Are you the author of this Elsevier article?	No
Will you be translating?	No
Title	An integrative investigation of liquid metal embrittlement in the Fe-Zn system: From responsible mechanisms to mitigation strategies
Institution name	University of Waterloo
Expected presentation date	Apr 2023
Portions	Figure 1 on Page 252 and Figure 2 on Page 252
Requestor Location	University of Waterloo 200 University Avenue West Waterloo, ON N2L 3G1 Canada Attn: University of Waterloo
Publisher Tax ID	GB 494 6272 12
Total	0.00 USD
Terms and Conditions	

INTRODUCTION

1. The publisher for this copyrighted material is Elsevier. By clicking "accept" in connection with completing this licensing transaction, you agree that the following terms and conditions

ELSEVIER LICENSE
TERMS AND CONDITIONS

Mar 06, 2023

This Agreement between University of Waterloo -- Ali Ghatei ("You") and Elsevier ("Elsevier") consists of your license details and the terms and conditions provided by Elsevier and Copyright Clearance Center.

License Number	5503141418247
License date	Mar 06, 2023
Licensed Content Publisher	Elsevier
Licensed Content Publication	Engineering Fracture Mechanics
Licensed Content Title	Experimental study of liquid metal embrittlement for the aluminum 7075–mercury couple
Licensed Content Author	Scott G. Keller,Ali P. Gordon
Licensed Content Date	Apr 1, 2012
Licensed Content Volume	84
Licensed Content Issue	n/a
Licensed Content Pages	15
Start Page	146
End Page	160

Type of Use	reuse in a thesis/dissertation
Portion	figures/tables/illustrations
Number of figures/tables/illustrations	1
Format	both print and electronic
Are you the author of this Elsevier article?	No
Will you be translating?	No
Title	An integrative investigation of liquid metal embrittlement in the Fe-Zn system: From responsible mechanisms to mitigation strategies
Institution name	University of Waterloo
Expected presentation date	Apr 2023
Portions	Figure 1 (c) on Page 148
Requestor Location	University of Waterloo 200 University Avenue West Waterloo, ON N2L 3G1 Canada Attn: University of Waterloo
Publisher Tax ID	GB 494 6272 12
Total	0.00 USD
Terms and Conditions	

INTRODUCTION

SPRINGER NATURE LICENSE
TERMS AND CONDITIONS

Mar 07, 2023

This Agreement between University of Waterloo -- Ali Ghatei ("You") and Springer Nature ("Springer Nature") consists of your license details and the terms and conditions provided by Springer Nature and Copyright Clearance Center.

License Number	5503670451366
License date	Mar 07, 2023
Licensed Content Publisher	Springer Nature
Licensed Content Publication	Metallurgical and Materials Transactions A
Licensed Content Title	Dissolution Condensation Mechanism of Stress Corrosion Cracking in Liquid Metals: Driving Force and Crack Kinetics
Licensed Content Author	Evgeny E. Glickman
Licensed Content Date	Dec 1, 2010
Type of Use	Thesis/Dissertation
Requestor type	academic/university or research institute
Format	print and electronic
Portion	figures/tables/illustrations
Number of figures/tables/illustrations	1

Will you be translating?	no
Circulation/distribution	1 - 29
Author of this Springer Nature content	no
Title	An integrative investigation of liquid metal embrittlement in the Fe-Zn system: From responsible mechanisms to mitigation strategies
Institution name	University of Waterloo
Expected presentation date	Apr 2023
Portions	Figure 5 on Page 253
Requestor Location	University of Waterloo 200 University Avenue West Waterloo, ON N2L 3G1 Canada Attn: University of Waterloo
Billing Type	Invoice
Billing Address	University of Waterloo 200 University Avenue West Waterloo, ON N2L 3G1 Canada Attn: University of Waterloo
Total	0.00 USD
Terms and Conditions	

Springer Nature Customer Service Centre GmbH Terms and Conditions

SPRINGER NATURE LICENSE
TERMS AND CONDITIONS

Mar 07, 2023

This Agreement between University of Waterloo -- Ali Ghatei ("You") and Springer Nature ("Springer Nature") consists of your license details and the terms and conditions provided by Springer Nature and Copyright Clearance Center.

License Number	5503670924407
License date	Mar 07, 2023
Licensed Content Publisher	Springer Nature
Licensed Content Publication	Metallurgical transactions, A, Physical metallurgy and materials science
Licensed Content Title	The mechanisms of crack initiation and crack propagation in metal-induced embrittlement of metals
Licensed Content Author	Paul Gordon et al
Licensed Content Date	Dec 31, 1969
Type of Use	Thesis/Dissertation
Requestor type	academic/university or research institute
Format	print and electronic
Portion	figures/tables/illustrations
Number of figures/tables/illustrations	3

Will you be translating?	no
Circulation/distribution	1 - 29
Author of this Springer Nature content	no
Title	An integrative investigation of liquid metal embrittlement in the Fe-Zn system: From responsible mechanisms to mitigation strategies
Institution name	University of Waterloo
Expected presentation date	Apr 2023
Portions	Figure 13 on Page 465, Figure 14 and Figure 15 on Page 466
Requestor Location	University of Waterloo 200 University Avenue West Waterloo, ON N2L 3G1 Canada Attn: University of Waterloo
Total	0.00 USD

Terms and Conditions

Springer Nature Customer Service Centre GmbH Terms and Conditions

The following terms and conditions ("Terms and Conditions") together with the terms specified in your [RightsLink] constitute the License ("License") between you as Licensee and Springer Nature Customer Service Centre GmbH as Licensor. By clicking 'accept' and completing the transaction for your use of the material ("Licensed Material"), you confirm your acceptance of and obligation to be bound by these Terms and Conditions.

1. Grant and Scope of License

1. 1. The Licensor grants you a personal, non-exclusive, non-transferable, non-sublicensable, revocable, world-wide License to reproduce, distribute, communicate to

ELSEVIER LICENSE
TERMS AND CONDITIONS

Mar 07, 2023

This Agreement between University of Waterloo -- Ali Ghatei ("You") and Elsevier ("Elsevier") consists of your license details and the terms and conditions provided by Elsevier and Copyright Clearance Center.

License Number	5503651289167
License date	Mar 07, 2023
Licensed Content Publisher	Elsevier
Licensed Content Publication	Acta Materialia
Licensed Content Title	The effect of stress on grain boundary interdiffusion in a semi-infinite bicrystal
Licensed Content Author	L. Klinger,E. Rabkin
Licensed Content Date	Aug 1, 2007
Licensed Content Volume	55
Licensed Content Issue	14
Licensed Content Pages	10
Start Page	4689
End Page	4698

Type of Use	reuse in a thesis/dissertation
Portion	figures/tables/illustrations
Number of figures/tables/illustrations	3
Format	both print and electronic
Are you the author of this Elsevier article?	No
Will you be translating?	No
Title	An integrative investigation of liquid metal embrittlement in the Fe-Zn system: From responsible mechanisms to mitigation strategies
Institution name	University of Waterloo
Expected presentation date	Apr 2023
Portions	Figure 1 on Page 4690 Figure 4 on Page 4693 Figure 5 on Page 4693
Requestor Location	University of Waterloo 200 University Avenue West Waterloo, ON N2L 3G1 Canada Attn: University of Waterloo
Publisher Tax ID	GB 494 6272 12
Total	0.00 USD
Terms and Conditions	

ELSEVIER LICENSE
TERMS AND CONDITIONS

Mar 07, 2023

This Agreement between University of Waterloo -- Ali Ghatei ("You") and Elsevier ("Elsevier") consists of your license details and the terms and conditions provided by Elsevier and Copyright Clearance Center.

License Number	5503660187954
License date	Mar 07, 2023
Licensed Content Publisher	Elsevier
Licensed Content Publication	Acta Materialia
Licensed Content Title	Theory of the Kirkendall effect during grain boundary interdiffusion
Licensed Content Author	L. Klinger,E. Rabkin
Licensed Content Date	Feb 1, 2011
Licensed Content Volume	59
Licensed Content Issue	4
Licensed Content Pages	11
Start Page	1389
End Page	1399

Type of Use	reuse in a thesis/dissertation
Portion	figures/tables/illustrations
Number of figures/tables/illustrations	2
Format	both print and electronic
Are you the author of this Elsevier article?	No
Will you be translating?	No
Title	An integrative investigation of liquid metal embrittlement in the Fe-Zn system: From responsible mechanisms to mitigation strategies
Institution name	University of Waterloo
Expected presentation date	Apr 2023
Portions	Figure 1 on Page 1390 and Figure 3 on Page 1392
Requestor Location	University of Waterloo 200 University Avenue West Waterloo, ON N2L 3G1 Canada Attn: University of Waterloo
Publisher Tax ID	GB 494 6272 12
Total	0.00 USD
Terms and Conditions	

INTRODUCTION

ELSEVIER LICENSE
TERMS AND CONDITIONS

Mar 07, 2023

This Agreement between University of Waterloo -- Ali Ghatei ("You") and Elsevier ("Elsevier") consists of your license details and the terms and conditions provided by Elsevier and Copyright Clearance Center.

License Number	5503660467245
License date	Mar 07, 2023
Licensed Content Publisher	Elsevier
Licensed Content Publication	Scripta Materialia
Licensed Content Title	Microstructure of liquid metal embrittlement cracks on Zn-coated 22MnB5 press-hardened steel
Licensed Content Author	Lawrence Cho,Heeseung Kang,Changwook Lee,Bruno C. De Cooman
Licensed Content Date	Nov 1, 2014
Licensed Content Volume	90
Licensed Content Issue	n/a
Licensed Content Pages	4
Start Page	25
End Page	28

Type of Use	reuse in a thesis/dissertation
Portion	figures/tables/illustrations
Number of figures/tables/illustrations	2
Format	both print and electronic
Are you the author of this Elsevier article?	No
Will you be translating?	No
Title	An integrative investigation of liquid metal embrittlement in the Fe-Zn system: From responsible mechanisms to mitigation strategies
Institution name	University of Waterloo
Expected presentation date	Apr 2023
Portions	Figure 1 on Page 26 and Figure 3 on Page 27
Requestor Location	University of Waterloo 200 University Avenue West Waterloo, ON N2L 3G1 Canada Attn: University of Waterloo
Publisher Tax ID	GB 494 6272 12
Total	0.00 USD
Terms and Conditions	

INTRODUCTION

SPRINGER NATURE LICENSE
TERMS AND CONDITIONS

Mar 07, 2023

This Agreement between University of Waterloo -- Ali Ghatei ("You") and Springer Nature ("Springer Nature") consists of your license details and the terms and conditions provided by Springer Nature and Copyright Clearance Center.

License Number	5503790591805
License date	Mar 07, 2023
Licensed Content Publisher	Springer Nature
Licensed Content Publication	Metallurgical and Materials Transactions A
Licensed Content Title	Zn Penetration in Liquid Metal Embrittled TWIP Steel
Licensed Content Author	Heeseung Kang et al
Licensed Content Date	Apr 11, 2016
Type of Use	Thesis/Dissertation
Requestor type	academic/university or research institute
Format	print and electronic
Portion	figures/tables/illustrations
Number of figures/tables/illustrations	3

Will you be translating?	no
Circulation/distribution	1 - 29
Author of this Springer Nature content	no
Title	An integrative investigation of liquid metal embrittlement in the Fe-Zn system: From responsible mechanisms to mitigation strategies
Institution name	University of Waterloo
Expected presentation date	Apr 2023
Portions	Figure 2 (b) on Page 2888 Figure 10 on Page 2895 Figure 11 (a)-(f) on Page 2896
Requestor Location	University of Waterloo 200 University Avenue West Waterloo, ON N2L 3G1 Canada Attn: University of Waterloo
Total	0.00 USD

Terms and Conditions

Springer Nature Customer Service Centre GmbH Terms and Conditions

The following terms and conditions ("Terms and Conditions") together with the terms specified in your [RightsLink] constitute the License ("License") between you as Licensee and Springer Nature Customer Service Centre GmbH as Licensor. By clicking 'accept' and completing the transaction for your use of the material ("Licensed Material"), you confirm your acceptance of and obligation to be bound by these Terms and Conditions.

1. Grant and Scope of License

1. 1. The Licensor grants you a personal, non-exclusive, non-transferable, non-sublicensable, revocable, world-wide License to reproduce, distribute, communicate to

ELSEVIER LICENSE
TERMS AND CONDITIONS

Mar 05, 2023

This Agreement between University of Waterloo -- Ali Ghatei ("You") and Elsevier ("Elsevier") consists of your license details and the terms and conditions provided by Elsevier and Copyright Clearance Center.

License Number	5502741374662
License date	Mar 05, 2023
Licensed Content Publisher	Elsevier
Licensed Content Publication	Materialia
Licensed Content Title	Liquid metal embrittlement transport mechanism in the Fe/Zn system: Stress-assisted diffusion
Licensed Content Author	C. DiGiovanni,A. Ghatei Kalashami,E. Biro,N.Y. Zhou
Licensed Content Date	Aug 1, 2021
Licensed Content Volume	18
Licensed Content Issue	n/a
Licensed Content Pages	1
Start Page	101153
End Page	0

Type of Use	reuse in a thesis/dissertation
Portion	figures/tables/illustrations
Number of figures/tables/illustrations	1
Format	both print and electronic
Are you the author of this Elsevier article?	No
Will you be translating?	No
Title	An integrative investigation of liquid metal embrittlement in the Fe-Zn system: From responsible mechanisms to mitigation strategies
Institution name	University of Waterloo
Expected presentation date	Apr 2023
Portions	Figure 4 on page 4
Requestor Location	University of Waterloo 200 University Avenue West Waterloo, ON N2L 3G1 Canada Attn: University of Waterloo
Publisher Tax ID	GB 494 6272 12
Total	0.00 USD
Terms and Conditions	

INTRODUCTION

ELSEVIER LICENSE
TERMS AND CONDITIONS

Mar 07, 2023

This Agreement between University of Waterloo -- Ali Ghatei ("You") and Elsevier ("Elsevier") consists of your license details and the terms and conditions provided by Elsevier and Copyright Clearance Center.

License Number	5503660645582
License date	Mar 07, 2023
Licensed Content Publisher	Elsevier
Licensed Content Publication	Acta Materialia
Licensed Content Title	Atomic-scale Investigation of Liquid-Metal-Embrittlement Crack-path: Revealing Mechanism and Role of Grain Boundary Chemistry
Licensed Content Author	M.H. Razmpoosh,B. Langelier,E. Marzbanrad,H.S. Zurob,N. Zhou,E. Biro
Licensed Content Date	Feb 1, 2021
Licensed Content Volume	204
Licensed Content Issue	n/a
Licensed Content Pages	1
Start Page	116519
End Page	0

Type of Use	reuse in a thesis/dissertation
Portion	figures/tables/illustrations
Number of figures/tables/illustrations	1
Format	both print and electronic
Are you the author of this Elsevier article?	No
Will you be translating?	No
Title	An integrative investigation of liquid metal embrittlement in the Fe-Zn system: From responsible mechanisms to mitigation strategies
Institution name	University of Waterloo
Expected presentation date	Apr 2023
Portions	Figure 2 on Page 3
Requestor Location	University of Waterloo 200 University Avenue West Waterloo, ON N2L 3G1 Canada Attn: University of Waterloo
Publisher Tax ID	GB 494 6272 12
Total	0.00 USD

Terms and Conditions

INTRODUCTION

SPRINGER NATURE LICENSE
TERMS AND CONDITIONS

Mar 07, 2023

This Agreement between University of Waterloo -- Ali Ghatei ("You") and Springer Nature ("Springer Nature") consists of your license details and the terms and conditions provided by Springer Nature and Copyright Clearance Center.

License Number	5503790762335
License date	Mar 07, 2023
Licensed Content Publisher	Springer Nature
Licensed Content Publication	Metallurgical and Materials Transactions A
Licensed Content Title	Role of Random and Coincidence Site Lattice Grain Boundaries in Liquid Metal Embrittlement of Iron (FCC)-Zn Couple
Licensed Content Author	M. H. Razmpoosh et al
Licensed Content Date	Jun 14, 2020
Type of Use	Thesis/Dissertation
Requestor type	academic/university or research institute
Format	print and electronic
Portion	figures/tables/illustrations
Number of figures/tables/illustrations	1

Will you be translating?	no
Circulation/distribution	1 - 29
Author of this Springer Nature content	no
Title	An integrative investigation of liquid metal embrittlement in the Fe-Zn system: From responsible mechanisms to mitigation strategies
Institution name	University of Waterloo
Expected presentation date	Apr 2023
Portions	Figure 8 on Page 3944
Requestor Location	University of Waterloo 200 University Avenue West Waterloo, ON N2L 3G1 Canada Attn: University of Waterloo
Total	0.00 USD

Terms and Conditions

Springer Nature Customer Service Centre GmbH Terms and Conditions

The following terms and conditions ("Terms and Conditions") together with the terms specified in your [RightsLink] constitute the License ("License") between you as Licensee and Springer Nature Customer Service Centre GmbH as Licensor. By clicking 'accept' and completing the transaction for your use of the material ("Licensed Material"), you confirm your acceptance of and obligation to be bound by these Terms and Conditions.

1. Grant and Scope of License

1. 1. The Licensor grants you a personal, non-exclusive, non-transferable, non-sublicensable, revocable, world-wide License to reproduce, distribute, communicate to the public, make available, broadcast, electronically transmit or create derivative